ENHANCEMENT IN THERMOELECTRIC PROPERTIES OF FLEXIBLE ANTIMONY TELLURIDE FILMS DEPOSITED BY DIRECT CURRENT MAGNETRON SPUTTERING

PRASOPPORN JUNLABHUT

A THESIS SUBMITTED IN PARTIAL FULFILLMENT OF THE REQUIREMENT FOR
THE DEGREE OF DOCTOR OF PHILOSOPHY IN APPLIED PHYSICS
DEPARTMENT OF PHYSICS SCHOOL OF SCIENCE
KING MONGKUT'S INSTITUTE OF TECHNOLOGY LADKRABANG
2021

KMITL-2021-SC-D-030-054

Thesis Title	Enhancement in thermoelectric properties of flexible antimony telluride films deposited by direct current magnetron sputtering
Student Name	Prasopporn Junlabhut
Student ID	60605093
Degree	Doctor of Philosophy (Applied Physics)
Department	Physics
Year	2021
Thesis Advisor	Assoc. Prof. Dr. Aparporn Sakulkalavek

Abstract

Thermoelectric technology has been utilized for energy harvesting in the microwatt power range. *P*-type Sb_2Te_3 is a narrow band gap semiconductor with a rhombohedral layered crystal structure and is a well-known thermoelectric material for near room temperature applications. To date, the preparation of these chalcogenide materials in film form is required to fabricate on a flexible substrate. For energy harvesting applications, the maximum output power is proportional to the film thickness. This thesis, P-type Sb_2Te_3 films with different thicknesses were deposited on polyimide substrates via heat treatment-assisted DC magnetron sputtering. The annealing temperature and annealing time were optimized to enhance thermoelectric properties. The correlations between the thickness variance and the structure, dislocation density, surface morphology, thermoelectric properties and output power are investigated. As a result, the film thickness and the heat treatment process during growth are related to the diffusion of deposited atoms on the substrate surface, leading to imperfection defects inside the films. The structure revealed that the preferred orientation plane along the (00l) plane was changed to the (015) plane as the thickness dimension of the film increased, indicating that the atomic interactions between atoms and substrate can obstruct nucleation in the vertical direction. This texture change had a significant impact on electrical transportation. The residual stress typically accumulates as the thick layer increases, which is related to the diffusion of deposited atoms on the substrate surface and to the appearance of microstructure and morphology. The thermal energy of the thick dimension is not enough cause diffusion and agglomeration. The resultant surface morphology showed small compact grains as the film thickness increased. All imperfections inside the films are affected by the thermoelectric properties. The maximum power output factor of 2.73 mW/mK^2 for a film thickness of 9.0 μm was obtained following annealing at 350°C for 30 min. Experimental characterization showed that increasing the film thickness to 9.0 μm at a

deposition time of 60 min can produce an output power of 0.032 μW at a temperature difference of 58 K.

Keywords: Antimony telluride, Flexible substrate, Thermoelectric, Sputtering, Annealing condition

Acknowledgements

This thesis was successfully completed by supporting my advisor Assoc. Prof. Dr. Aparporn Sakulkalavek for her guidance and support throughout my thesis. I would like to thanks Assoc. Prof. Dr. Wisanu Pechara for his inspiration and suggestion in my study. I would like to thank Rajabhat Rajanagarindra University (RRU) for their scholarship support. This research and innovation activity is funded by National Research Council of Thailand (NRCT).

Special thanks to Professor Prof. Dr. Pichet Limsuwan, Dr. John Morris and Assoc. Prof. Dr. Rachsak Sakdanuphab who review and comment and proofreading several chapters of this manuscript. I also would like to thank the lab group members and all those who helped me to stay focused on completing the thesis and who have provided me with the encouragement to continue when the going got tough.

The author gratefully acknowledges the support Optical Thin-Film Technology Laboratory, NSTDA, Thailand, for carrying out Hall measurements, the Rajamangala University of Technology Suvarnabhumi for ZEM-3 measurements.

Prasopporn Junlabhut

Table of Contents

List of Tables

List of Figures

List of Figures

List of Figures

List of Figures

List of Figures

List of Figures

Figure **Page**

Chapter 1
Introduction

1.1 Research Motivation

Global warming and climate change are major problems for the world. Strategies for dealing with these problems include increasing the use of renewable energy (solar, wind, water and biomass) and improving energy efficiency. One way to improve energy efficiency and minimize wasted heat is to use energy harvesting technology. This technology can directly convert thermal energy to electrical energy through thermoelectric materials, based on the Seebeck and Peltier effects. The conversion efficiency of thermoelectrics is expressed by the thermoelectric figure of merit (ZT). Antimony telluride, based on the general formula Sb_2Te_3, is a well-known TEs that has attracted much attention for its thermoelectric application with a narrow bandgap, $E_g < 0.2$ eV [1]. Sb_2Te_3 compounds have the rhombohedral crystal structure Sb_2Te_3 lattice consists of layers. Each layer comprises five atomic planes oriented perpendicular to the c-axis according to ...Te^1-Sb-Te^2-Sb-Te^1... Te^1-Sb-Te^2-Sb-Te^1. There is the van der Waals gap between Te^1 atoms [2]. Typically, the excellence ZT of Sb_2Te_3 is achieved at near room temperature [3-4] which is conveniently close to the human body temperature. Low temperature waste heat (35-200°C) is the most interesting because it can be found the thermal waste heat when doing the activities. Since waste heat tends to be accessible all day and night, it may become an attraction for the energy harvesting applications.

As the adhesion problems and limited flexibility between waste heat and the thermoelectric devices, Two dimensional atomic are the basic plane structures of bulk layered materials and have attracted attention to improving the thermoelectric performance through the rational nanostructure design [54]. The flexible film can be manufactured into a variety of shapes and sizes to fit the needs of various areas. To form a flexible thermoelectric device, a polyimide substrate was chosen due to its low thermal conductivity (0.12 W/Km and its thermal expansion coefficient ($12\times10^{-6}K^{-1}$) closely matching the thermal expansion coefficient of Sb_2Te_3 film, which reduces

residual stress and increasing adhesion [5]. Generally, Screen printing [6-8], electrochemical [9], thermal evaporation [10], and magnetron sputtering [11] have been extensively investigated to deposit the Sb_2Te_3 film on a polyimide substrate. Screen printing has been commonly used due to the short process time, low fabrication cost and large coating area. However, these are requiring a mixing powder, binder, glass powder and solvent along with a precursor, which leads to weak contact between particles and highly porous products. Thermal evaporation is a common method of film deposition. The material is evaporated in a vacuum by the thermal process and travels directly to the substrate. However, this method is performed at high temperature and low vacuum. Among the film deposition techniques, Direct current (DC) magnetron sputtering has been widely used because it produces high-quality films, extremely high adhesion and excellent uniformity over a large substrate area. Moreover, the Sb_2Te_3 films were sputtered onto polyimide substrates using a single compound target. Many reports were shown that the compositional, structural, electrical and thermoelectric properties of the Sb_2Te_3 thermoelectric films were controlled by sputtering parameters such as sputtering pressure, sputtering power, deposition temperature, deposition time and heat treatment [12-16]. It is affected by the enhancing of the properties of the Sb_2Te_3 film which leads to the increase of the energy efficiency of thermoelectric applications.

In this study, the Sb_2Te_3 thin- and thick- film were directly deposited on flexible polyimide by DC magnetron sputtering using a single compound target. The influence of sputtering parameters on the structural, electrical and thermoelectric properties of Sb_2Te_3 flexible films was investigated. The sputtering parameters and heat treatment processes were optimized to improve thermoelectric properties. For practical use, thin- and thick- film of Sb_2Te_3 are interesting to compare the output performance on a single leg Sb_2Te_3.

1.2 Objectives of the study

The objective of this thesis is conducted in order to:

1. study the influence of sputtering power on thermoelectric properties of *P*-type Sb_2Te_3 flexible thin-film deposited by DC magnetron sputtering

2. study the enhancement of thermoelectric properties of *P*-type Sb_2Te_3 flexible thick-films via heat-treatment process.

3. study the thickness effect on the thermoelectric properties of *P*-type Sb_2Te_3 flexible thin- and thick-films deposited by thermal treatment-assisted DC magnetron sputtering.

4. compare the output performance of a planar single-leg *P*-type Sb_2Te_3 with different thicknesses.

1.3 Scopes of the study

The scopes of this thesis are expressed as follows:

1. The *P*-type Sb_2Te_3 thin films were deposited on flexible polyimide substrates using DC magnetron sputtering with sputtering power density in the range of 30-50 W. The effect of sputtering power density on thermoelectric properties were studies.

2. The structural, chemical electrical and thermoelectric properties of Sb_2Te_3 thin films were characterized and investigated.

3. The *P*-type Sb_2Te_3 thick-films were deposited on flexible polyimide substrates using thermal treatment assisted DC magnetron sputtering at temperatures of 0, 150, 250 and 350 °C for 30 min. To investigate the effect of annealing time, the thick films were also annealed at 350 °C for 15, 30 and 60 min, respectively.

4. The structural, chemical electrical and thermoelectric properties of Sb_2Te_3 thick films were characterized and investigated.

5. Thin- and thick- Sb_2Te_3 films were deposited with various deposition times of 2, 30, 60 and 120 min with optimized thermal treatment conditions.

6. The structural, chemical electrical and thermoelectric properties of Sb_2Te_3 thin- and thick- films were characterized and investigated.

7. Compare the output performance of a planar single leg with different thicknesses.

1.4 Expected results

1. The relevant parameters of the deposited thin-and thick-films such as suitable sputtering parameters, thermoelectric properties, thermal treatment conditions and thickness will be notified.

2. The suitable conditions of the planar thin- and thick-film *P*-type Sb_2Te_3 in a single leg were achieved for thermoelectric application.

Chapter 2
Theory and literature reviews

In overview, the objective of this chapter is to investigate the fundamental of thermoelectric, thermoelectric applications, antimony telluride thermoelectric material, thin- and thick-film deposition techniques, and the characterization technique. In this chapter, the relevant theories and literature reviews are explained.

2.1 Thermoelectric phenomena and their parameters

The advent of thermoelectric devices was discovered in 1821 when Thomas Johann Seebeck found the deviation of a compass needle due to two junctions of two dissimilar materials at different temperatures. This now called the Seebeck effect was caused by the formation of an electric potential difference due to a temperature difference. In 1834 Jean Peltier discovered that an electric current passes through two dissimilar materials alter the temperature at the junction. It is called the Peltier effect. Some years later, Thomson explained found that the connection between the Seebeck effect and the Peltier effect within the framework of thermodynamics, known as the Thomson effect. All thermoelectric phenomena are described. These effects are the phenomenological foundations for the description of thermoelectric materials and the functioning of thermoelectric devices and thermoelectric applications.

2.1.1 Seebeck Effect

The Seebeck effect is the relation between electrical potential and a temperature gradient. The increase of the electrical potential is occurred due to a temperature difference. Seebeck gave an overview of several material combinations applicable in thermocouples. A thermocouple consists of two junctions of two dissimilar materials. The two junctions are held at the temperatures T_C and T_H experiencing a temperature difference (ΔT) and thus exhibit a temperature gradient along with the materials.

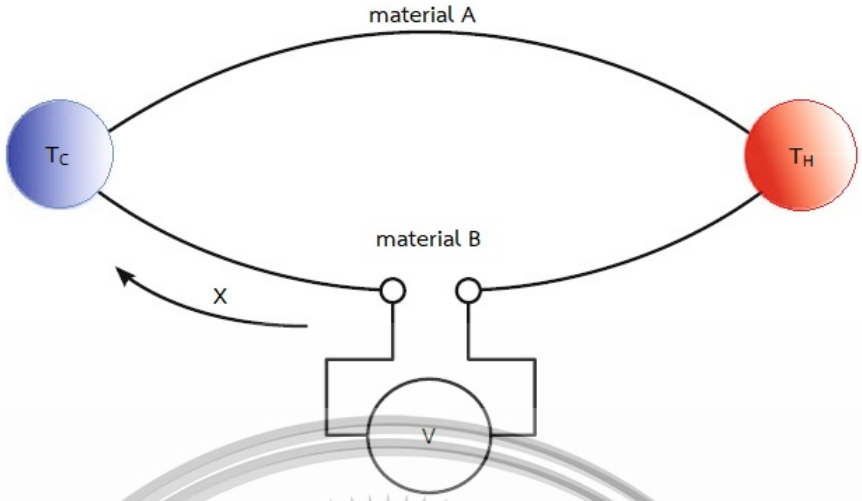

Figure 2.1 A temperature difference creates a potential difference in the junction between material A and B.

The minority carriers are left on the hot side thus giving rise to a thermoelectric voltage. The buildup of charge carriers on the cold side eventually ceases when an equal amount of charge carriers drift back to the hot side as a result of the electric field created by the charge separation. At this point, the materials reach a steady state. The given temperatures difference generates a thermoelectric voltage difference (ΔV) measured at the device contacts:

$$\Delta V \propto \Delta T \tag{2.1}$$

The Seebeck coefficient (S) is defined via the limit at infinitesimal temperatures difference:

$$S(T) = \lim_{\Delta T \to 0} \frac{\Delta V}{\Delta T} \tag{2.2}$$

The total thermoelectric voltage is obtained.

$$dV = \int_{T_C}^{T_H} S(T) dT \tag{2.3}$$

The temperature dependence Seebeck coefficient along two different materials allows expressing a combined coefficient for the material couple under given thermal conditions.

$$\Delta V = (S_A - S_B)\int_{T_C}^{T_H} dT = (S_A - S_B)\Delta T \tag{2.4}$$

Where S_A and S_B are a Seebeck coefficient of material A and B. while *P*-type materials possess a positive Seebeck coefficient, *N*-type materials offer negative ones. The thermoelectric voltages drive current flowing through the materials when their junction kept the temperature difference [17-18].

2.1.2 Peltier Effect

The Peltier effect is a phenomenological effect reverse to the Seebeck effect. When an electric current passes through two dissimilar materials are connected at two junctions, heat can be absorbed in the junction, while it is released at the other one. As a result, heat flux through the materials is induced. The heat flux at the junction will be interpreted as energy conservation within the junctions and the change of total energy of the carriers when electrical current passing. The Peltier coefficients represent how much heat current is carried per unit change through a material. The Peltier heat (Q) absorbed by the cold junction per unit time is given by [17-18]

$$dQ \ \alpha \ IdT \tag{2.5}$$

$$\frac{dQ}{dT} = (\prod_A - \prod_B)I \tag{2.6}$$

In this equation, $\prod_A$ and $\prod_B$ are the Peltier coefficients of the materials A and B. The unit of the Peltier coefficient is W/A or V. Furthermore, the Peltier coefficients are also temperature dependent like the Seebeck coefficients. The Peltier coefficient and the Seebeck coefficient are related to each other by the first Kelvin relation. The relation is given by:

$$(\prod_A - \prod_B) = (S_A - S_B)T \tag{2.7}$$

$$\Pi_{AB} = S_{AB}T \tag{2.8}$$

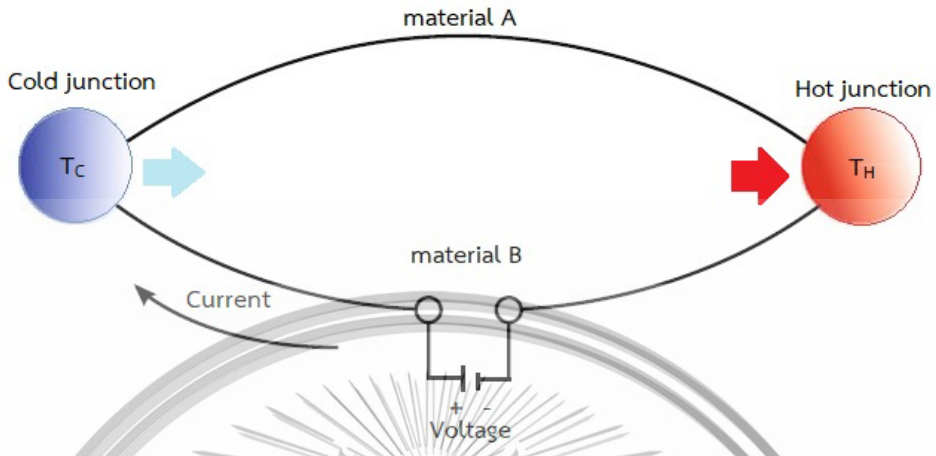

Figure 2.2 A thermal gradient exists at the junction of dissimilar materials when an electrical current flows.

2.1.3 Thomson Effect

The Thomson effect was predicted and observed the third thermoelectric effect by William Thomson (Lord Kelvin). It refers to the emission or absorption of heat by the current caring conductor exposed to a temperature gradient. The heat generated by the Thomson effect is called Thomson heat. Thomson heat is proportional to the current and time can be expressed as : [17-19].

$$dQ = \chi I dt \frac{dT}{dx} \tag{2.9}$$

In which Q is Thomson heat, χ denoted the Thomson coefficient, I is the current intensity, t is time, and dT/dx is the temperature gradient along with the material.

Thomson coefficient is different from the two main thermoelectric coefficients because it can be determined by direct measurement on an individual material.

As mention before, three thermoelectric coefficients are related by the Kelvin equations:

$$\chi = T\frac{dS}{dT} \tag{2.10}$$

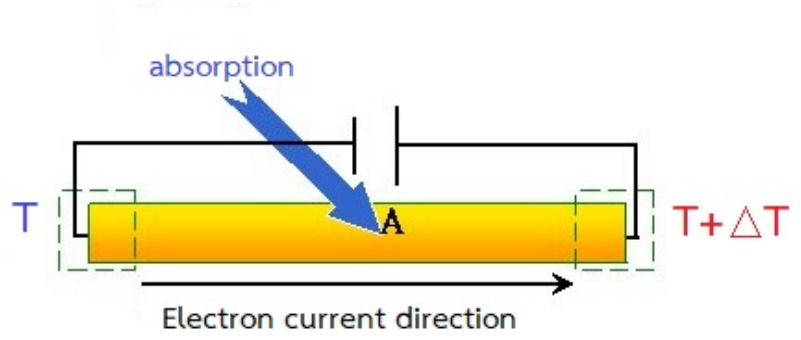

Figure 2.3 Absorption of heat by current caring conductor exposed to a temperature gradient.

2.1.4 Figure of Merit

The efficiency of thermoelectric material can be determined by the figure of merit (ZT), defined as:

$$ZT = \frac{S^2 T}{\rho\kappa} \tag{2.11}$$

In which S is the Seebeck coefficient, T is temperature, ρ is electrical resistivity and κ is thermal conductivity. A good candidate thermoelectric material should have low ρ to minimize Joule heating, low κ to maintain a large temperature gradient, and a large Seebeck coefficient for maximum conversion of heat to electrical power or electrical power to cooling performance.

The optimization ZT is not simply because the material properties are interrelated, so optimizing one can have a negative effect on the others. Especially, thermal conductivity and electrical resistivity are related to carrier concentrations as well as carrier mobility. A given temperature has a constant ratio based on the Wiedemann-Franz law.

$$\frac{\kappa}{\sigma} = LT \tag{2.12}$$

$$L = \frac{\pi^2}{3}\left(\frac{\kappa_B}{e}\right)^2 = 2.45\times10^{-8} \quad (\frac{W\Omega}{K^2}) \tag{2.13}$$

Where κ_B is the Boltzmann constant and e is the electron charge. The semiconductor materials have a high power factor (S^2/ρ) and a low thermal conductivity, which makes a high ZT materials.

However, the Seebeck coefficient and electrical resistivity of semiconductors are related to the separation between the conduction band in N-type (valence band in *P*-type) and the Fermi level of the material. It is indicated that the increase of the Seebeck coefficient by manipulating the Fermi level also increases the electrical resistivity as well. In order to reduce thermal conductivity, the common approach is to introduce additional short-range disorders into the crystalline structure. On the other hand, the distortion inevitably blocks transport, which may reduce the electrical conductivity.

In general, the Fermi level is used to describe the average energy of a crystal in a material at a given temperature. In the Fermi function of a semiconductor, the band theory is a gap between the Fermi level and the conduction band. At above zero temperature, some electrons can bridge the gap and participate in electrical conduction. The electron population depends on the product of the Fermi function and the electron density of states. The band structure of the thermoelectric material has a sharp band or high density of states near the Fermi level to enhance Seebeck and dispersive bands to enhance the electrical conductivity. For a good thermoelectric material, there should be a high density of states (DOS) near the Fermi level but the dispersive bands should not be cut by the Fermi level nor should be touching. The Semiconductors are suitable for thermoelectric materials with relatively low carrier concentration and can have large Seebeck coefficients and high mobility. The relation of carrier and Seebeck can be determined from a relatively simple model of electron transport. Two-dimensionally confined carriers in quantum well exhibits quantum effects whereby the Seebeck can be increased due to increase the DOS without the other properties decreasing. The effective mass of carriers is governed by the energy surface shape in the valence and conduction bands, which can, along with the carrier and phonon scattering behavior, strongly affect electronic phenomena [52-53].

2.1.5 Seebeck Coefficient

The Seebeck coefficient (S) of thermoelectric material is a measure of the induced thermoelectric voltage produced by a temperature difference across the

material. A good thermoelectric should have an absolute value of S in the range of hundreds of $\mu V / K$. For semiconductors, the parabolic band, energy-independent scattering approximation is used to derive the Seebeck coefficient shown in Equation 2.14.

$$S(T) = \frac{8\pi^2 \kappa_B^2}{3eh^2} m^* T \left(\frac{\pi}{3n}\right)^{2/3} \tag{2.14}$$

$$S(T) \ \alpha \ \frac{m^*}{n^{2/3}} \tag{2.15}$$

Where, h is the Plank's constant, m^* is the effective mass and n is the carrier concentration. Based on the equation, the Seebeck coefficient is negative if carriers are the electron, positive if carriers are holes. A maximum Seebeck coefficient can be achieved for large effective mass and low carrier concentration. On the other hand, a high Seebeck coefficient can result in low electrical conductivity. Generally, a high Seebeck coefficient is always found in semiconductors (*N*-type and *P*-type). This relation can be described based on the band model [18-19]:

$$S(T) = \pm \frac{\kappa_B}{e} \left[\left(\frac{5}{2} + s \right) + \ln \frac{2(2\pi m^* \kappa_B T)^{3/2}}{h^3 n} \right] \tag{2.16}$$

In which s is the scattering parameter, assuming that the carrier relaxation time can be expressed in terms of carrier energy $\left(\tau = \tau_0 E^s\right)$, τ is the carrier relaxation time, τ_0 is a constant and E is the carrier energy. It can be expressed as:

$$S(T) = \pm \frac{\kappa_B}{\sigma} n\mu \left[\left(\frac{5}{2} + s \right) + \ln \frac{2(2\pi m^* \kappa_B T)^{3/2}}{h^3 n} \right] \tag{2.17}$$

As a result, the Seebeck coefficient, carrier concentration electrical conductivity and carrier mobility are interrelated in a semiconductor.

2.1.6 Electrical resistivity and Electrical conductivity

Electrical resistivity (ρ) is a measure of the ability of thermoelectric material to conduct the transport of an electrical current which can influence the value of ZT. Electrical conductivity (σ) is a measure of the ability of thermoelectric material to carry the transport of the charge carriers (electrons or holes). The charge carrier transport occurs due to the thermal energy and the associated random motion of carriers. In semiconductors, the carrier concentration depends strongly on the temperature. At zero temperature, the conductivity is zero. Also, the scattering processes and thus the relaxation time constant exhibit a temperature dependence. The conductivity of semiconductors spans a wide range from insulating to almost metallic conduction.

The electrical conductivity is inversely proportional to the electrical resistivity. SI unit of time the electrical resistivity is $\Omega.m$ while the electrical conductivity is per $\Omega.m$ or (S/m). The electrical conductivity and mobility can be related to relaxation time as equations

$$\sigma = \frac{1}{\rho} = \frac{ne^2\tau}{m^*} \tag{2.18}$$

In an intrinsic semiconductor, the carrier mobility (μ) is determined by scattering with phonons. Further scattering is introduced by impurities, defects or alloy disorder. The electrical conductivity is proportional to the carrier concentration (n), the electron charge (e) and the carrier mobility (μ), which is given by:

$$\sigma = en\mu \tag{2.19}$$

For each carrier type, the mobility in the relaxation time approximation is given by:

$$\mu = \frac{e\tau}{m^*} \tag{2.20}$$

In the presence of both electrons and holes,

$$\sigma = \sigma_e + \sigma_h = -en\mu_e + en\mu_h \tag{2.21}$$

Where τ is the charge carrier relaxation time which depends on the charge carrier scattering, μ_e and μ_h is the mobility for electrons and holes, respectively. These are given by $\mu_e = -e\tau/m^*$ and $\mu_h = +e\tau/m^*$. As the unit for mobility, usually cm^2/Vs is used. In small bandgap semiconductors, high mobility is caused by its small effective mass [18-21]. The majority carriers greatly outnumber minority carriers, so that Equation (2.21) can be reduced to a single term involving the majority carrier. [22]

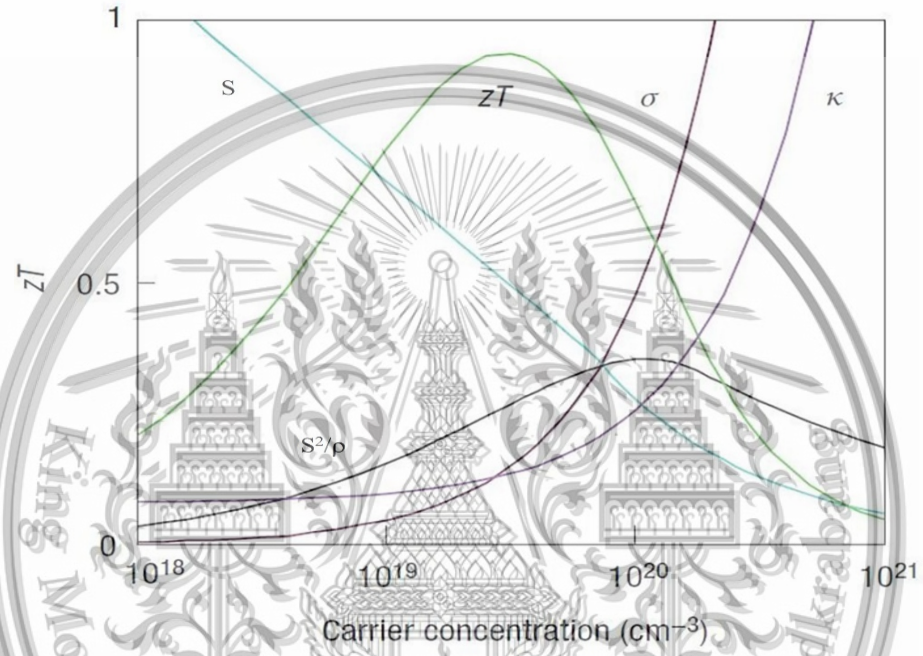

Figure 2.4 Carrier concentration on thermoelectric properties of a material [19].

According to equation (2.11), a high ZT requires as increasing carrier concentration. Both electrical conductivity and electronic thermal conductivity increase with increasing the carrier concentration, as shown in Figure. 2.4. since there are more carriers to transport electron charges and heat energy, through the Wiedemann–Franz relation. The maximum ZT has occurred with a carrier concentration of $n \approx 10^{19}$ cm^{-3}.

2.1.7 Carrier mobility

According to equation (2.19), the electrical conductivity is proportional to the carrier concentration and carrier mobility. The carrier mobility is a measure of how well the carrier will flow through the material. Generally, if the mobility is high and the carrier density is moderate, the Seebeck coefficient remains high, resulting in good

thermoelectric material. In a semiconductor, the carrier concentration and carrier mobility are temperature-dependent. The role of scatters and the effect on mobility can be considered by considering the two main types of scattering mechanisms, lattice scattering and impurity scattering. The mobility due to these scattering mechanisms is illustrated.

1. Lattice scattering

Lattice scattering is a thermal motion of lattice atoms at above-zero temperatures. The carrier scattering is mainly due to the thermal vibration of the lattice at high temperatures. The acoustic waves can be generated in terms of phonons. In metals, carrier-carrier scattering affects the electrical conductivity, but the carrier concentration in semiconductors is low. As a result, carrier-carrier scattering can be ignored in a semiconductor. For lattice scattering, the scattering time (τ) in terms of a scattering cross-section (S) is given by:

$$\tau = \frac{1}{S\upsilon_{th}N_s} \tag{2.22}$$

Where υ_{th} is the mean speed of the carriers (thermal velocity) and N_s is the number of scatters per unit volume.

If a is the amplitude of lattice vibration of two-dimension scattering, $S = \pi a^2$. The a increases with increasing temperature and hence the S increases. In terms of υ_{th}, an electron in the conduction band is equal to its kinetic energy so that

$$\frac{1}{2}m_e^*\upsilon_{th}^2 = \frac{3}{2}k_BT \tag{2.23}$$

$$\upsilon_{th} \propto \sqrt{T} \tag{2.24}$$

The N_s is a constant and is independent of temperature. As a result, the lattice scattering time (τ_L) on temperature is given by:

$$\tau_L = \frac{1}{(\pi a^2)\upsilon_{th}N_s} \propto \frac{1}{(T)\left(T^{\frac{1}{2}}\right)} \propto T^{-\frac{3}{2}} \tag{2.25}$$

Since the scattering time is directly proportional to the mobility. This means that μ due to lattice scattering varies as $T^{-\frac{3}{2}}$. As increasing in temperature, the lattice scattering is influenced to reduce carrier mobility. This means, as the temperature increase, the atomic vibrations increases the electrons moves faster leading to reduce the carrier mobility. A similar argument is valid for *P*-type semiconductors (hole). Despite the decrease of carrier mobility, the electrical conductivity increases with temperature due to the exponential increase in carrier concentration.

2. Impurity scattering

Impurity scattering is based on the ionized donor and acceptor impurities. At room temperature the impurities are ionized, there is an electrostatic attraction between the carriers traveling in the lattice and the impurities. The probability of impurities scattering is independent of the doping density and the ionized impurities. As seen in Figure. 2.5, as a donor, the scattering cross-section is calculated from the balance between the KE and the PE of the carrier due to the ionized impurities. The carrier will be scattered if PE dominated. The scattering radius (r_c) is the distance at which both effects are equal.

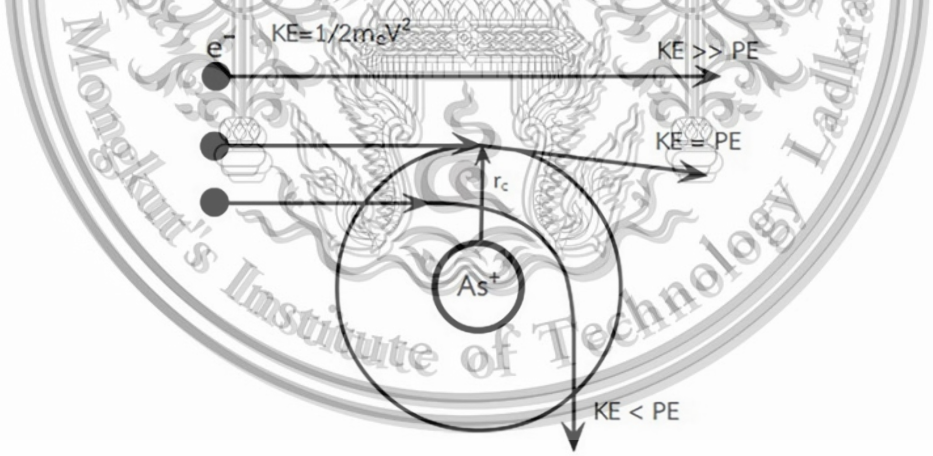

Figure 2.5 Carrier scattering from an ionized As donor.

$$\frac{3}{2}k_BT = \frac{e^2}{4\pi\varepsilon_0\varepsilon_r r_c} \tag{2.26}$$

$$S = \pi r_c^2 \quad \propto \quad T^{-2} \tag{2.27}$$

The scattering time due to impurities (τ_I) is given by:

$$\tau_I = \frac{1}{(\pi r_c^2)\upsilon_{th} N_I} \propto \frac{1}{(T^{-2})\left(T^{\frac{1}{2}}\right)} \propto T^{\frac{3}{2}} \tag{2.28}$$

Since the scattering time is directly related to mobility, the mobility due to impurities increases with temperature. It opposites to the lattice scattering behavior. At low temperatures, the carriers can travel slower and this makes it easier to ionized impurities. Also with increasing temperature, the charge carriers are moving faster and this makes the interaction with the impurity for a shorter time. The carrier mobility due to impurity scattering decreases as $T^{\frac{3}{2}}$.

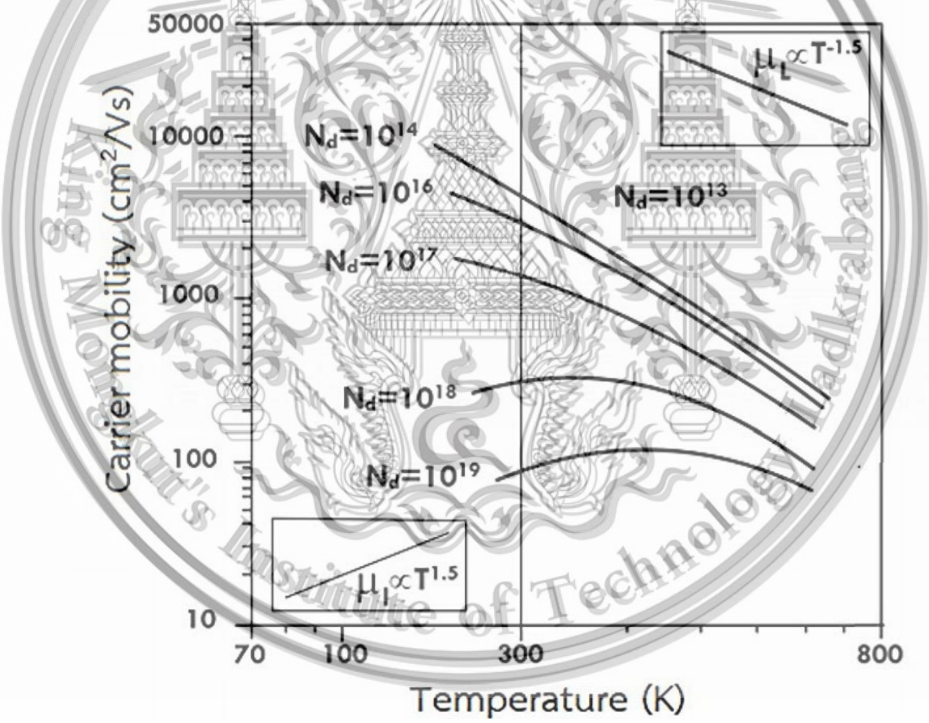

Figure 2.6 Temperature dependence on carrier mobility due to lattice and impurity scattering with various donor concentrations of semiconductor.

At low temperature, the carrier mobility increases due to impurity scattering dominated, while at high-temperature lattice scattering dominated, as seen in Figure 2.6 [23]. At low donor concentrations, lattice scattering dominates over the entire temperature range. As increasing donor concentrations impurity scattering starts to

dominate at low temperatures. In acceptor concentration is also the same behavior, the carrier mobility decreases with increasing carrier concentration. The temperature dependence of conductivity is seen in Figure 2.7 [23]. The dominating term is still the carrier concentration, due to its exponential dependence on temperature but the mobility term also plays a role, especially in the extrinsic region (or saturation region in n). The optimal temperature range σ is nearly the saturation region n.

The carrier concentration in a semiconductor is affected by temperature, as seen:

$$\sigma \propto \exp\left(-\frac{E}{k_B T}\right) \tag{2.29}$$

Where, E is the conduction energy. At low temperatures, the carrier is small while at the high-temperature donor or acceptor atoms are increasingly ionized.

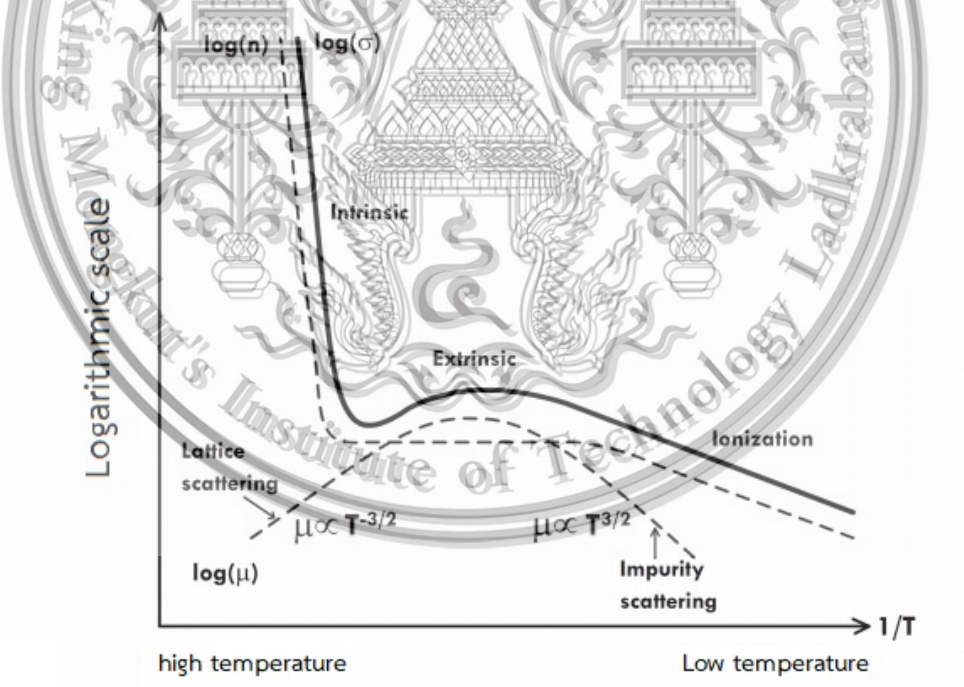

Figure 2.7 Temperature dependence on electrical conductivity, carrier concentration and carrier mobility.

During the ionization, carrier concentrations become saturated. At this time a further temperature increase generated the intrinsic carriers by thermal. In the intrinsic region, carrier concentration increases with increasing temperature. In this case, the influence of lattice scattering ($\mu \propto T^{-3/2}$) can be expected. At high-temperature measurement, E is the energy gap (E_g) and at low-temperature measurement, E is the activation energy (E_a).

2.1.8 Thermal conductivity

Thermal conductivity (κ) is the ability of thermoelectric material to describe the heat transfer via mainly two transporters such as charge carriers and lattice waves (phonons). Thermal conductivity is measure in units of W/mK . According to Equation (2.11), low thermal conductivity is required. It is an important factor to be controlled when optimizing for a high ZT . The total thermal conductivity in semiconductors is classified into two main components, electronic thermal conductivity (κ_e) and lattice thermal conductivity (κ_l) based on the contribution of charge carriers transporting heat and lattice waves (phonons), respectively.

The thermal conductivity of semiconductors is temperature-dependent. Total thermal conductivity is given by:

$$\kappa = \kappa_e + \kappa_l \tag{2.30}$$

1. Electrical thermal conductivity

The electrical thermal conductivity is mainly related to carriers transporting heat. The ratio of the electronic transporting heat to the electrical conductivity of a metal is directly proportional to the temperature through the Wiedemann-Franz law, in Equation (2.12). In theory, the value $L = 2.45 \times 10^{-8}$ $(W\Omega/K^2)$ is defined that the electrons do not interact with each other. The electron can be scattered with impurities or lattice vibrations. The Wiedemann and Franz law is valid at low temperatures. At high temperature $(T \geq \theta_D)$, the carried are elastically scattered, which θ_D is Debye temperature (θ_D = 160 K for Sb_2Te_3).

The κ_e is sensitive to carrier concentration and mobility. If the concentration increases, the electrical conductivity increases leading to the electron thermal conductivity increases linearly. However, the carrier mobility has less influence on electrical thermal

conductivity due to a small proportion of total thermal conductivity generated by electrical thermal conductivity, the impact of κ_e can be neglected at low temperatures [19, 22, 24].

2. Lattice thermal conductivity

The lattice thermal conductivity is mainly related to the crystal structure, grain boundary, lattice defects, imperfections, dislocations, anharmonicity of the lattice oscillations, carrier concentration, and interactions between the carriers and lattice waves. Lattice thermal conductivity based on classical kinetic energy theory of gases is defined as follows:

$$\kappa_l = \frac{1}{3} C_v \bar{d} \bar{v} \tag{2.31}$$

In which, C_v is the specific heat at constant volume, $\bar{d}$ is the average phonon mean free path and $\bar{v}$ is the average phonon velocity. At above Debye temperature, C_v approaches the classical value of $3R$, where R is a gas constant. At low temperature, C_v is proportional to T^3, following the law of Debye $\left(C_v \propto T^3\right)$.
Since Equation. (2.31) is not valid for a wide range of materials. Then, the lattice thermal conductivity, using the Callaway formalism, as seen:

$$\kappa_l = \frac{k_B}{2\pi^2 v_s}\left(\frac{k_B T}{\bar{h}}\right)^3 \int_0^{\frac{\theta_D}{T}} \tau_c(x) \frac{x^4 e^x}{\left(e^x - 1\right)} dx \tag{2.32}$$

In which, $\bar{h}$ is the reduced Plank's constant $\left(\bar{h} = \frac{h}{2\pi}\right)$, x is the dimensionless parameter with $x = \frac{h\omega}{2\pi k_B T}$, ω is the frequency of phonon and v_s is the speed of sound and τ_c is the combined phonon relaxation time.

The relation between the phonon scattering mechanisms and the combined phonon relaxation time can be obtained according to Matthiessen's rule [20], can be written as

$$\tau_c^{-1} = \tau_p^{-1} + \tau_D^{-1} + \tau_B^{-1} + \tau_{EP}^{-1} \tag{2.33}$$

In which, τ_C^{-1} is the total probability of scattering, τ_p^{-1} is the probability for phonon-phonon scattering, τ_D^{-1} is the probability for point defect scattering, τ_B^{-1} is the probability for grain boundary scattering and τ_{EP}^{-1} is the probability for electron-phonon scattering. The total phonon scattering mechanisms are described [19-24].

2.1. Phonon-phonon scattering

The phonon-phonon scattering has occurred at a high temperature $(T \gg \theta_D)$ because there is more phonon. The scattering is given by:

$$\tau_p^{-1} = B\omega^2 T \exp\left(-\frac{\theta_D}{3T}\right) \tag{2.34}$$

The effect of phonon-phonon scattering to temperature dependence on thermal conductivity is expressed by

$$\kappa \propto \exp\left(\frac{\theta_D}{2T} - 1\right) \tag{2.35}$$

At the above Debye temperature, the thermal conductivity is inversely proportional to temperature. As the temperature below, the thermal conductivity should be raised exponentially until other scattered predominate.

2.2. Point defect phonon scattering

The point defect such as vacancies, dislocations, uncharged impurity sites and different isotopes of the host constituents is an atom with different forms. There has little effect on the long-wavelength (low energy of phonon). But short wavelength, high energy phonons are strongly scattered by point defects. The Point defect phonon scattering is given by:

$$\tau_D^{-1} = A\omega^4 \tag{2.36}$$

2.3. Grain boundary phonon scattering

The grain phonon boundary scattering is mainly significant to the crystalline size at low temperatures and thus should not be important limitations at high temperatures. The Boundary scattering can be written in terms of grain size (d) and film thickness (t) as:

$$\tau_B^{-1} = \frac{v_s}{d} + \frac{v_s}{t} \tag{2.37}$$

2.4. Carrier-phonon scattering

The charge carrier-phonon scattering is much more effective at low temperatures. The long-wavelength of phonon can interact with all charge carriers. Carrier phonon scattering can be increased when the carrier concentration of material increases. The carrier-phonon scattering is given by:

$$\tau_{EP}^{-1} = C\omega \tag{2.38}$$

Therefore, good thermoelectric materials are crystalline materials that manage to scatter phonon without significantly disrupting the electrical conductivity.

2.2 Thermoelectric Applications

Thermoelectric technology is widely used due to increasing renewable energy and improving energy efficiency. It was stated that thermoelectric devices directly convert heat into a temperature difference and heat flow and vice versa which is made up of three different effects: the Seebeck effect, the Peltier effect and Thomson effect. A recent development in theoretical studies on the thermoelectric provides new opportunities for wide applications such as equipment used by the military, medical, industrial, and scientific.

Generally, thermoelectric devices contain more than one thermoelectric couples consist of N-type and *P*-type semiconductors, which are different charge carriers. The voltage for the Seebeck effect and the cooling and heating power for the Peltier effect is increased directly proportional to the number of couples.

The Seebeck and Peltier effects occur due to the charge carrier movement in the thermoelectric materials. In N-type semiconductors, the major carriers are electrons. In *P*-type semiconductors, the major carriers are holes. Holes are vacancies in a crystal structure in which an electron could occupy. In the Seebeck effect, the charge carriers can be diffuse from hot side to cold side. The buildup of charge at the cold produces a voltage potential. The electrical voltage will drive the electrical current in a completed circuit and produce electrical power. In the Peltier effect, rather

than having a resistive load in the circuit, the direct current source is used to move the carriers by an electric field. When the charge carriers transport, the heat was taken with them. The electrons moving to the higher energy absorb heat and electrons that move to a lower energy release heat. This charge carrier movement can be used to pump heat against the direction it naturally flows and produce cooling and heating.

Thermoelectric devices are usually called thermoelectric modules. It consists of thermoelectric couples. The thermoelectric couples are wired electrically in series and thermally in parallel and connected on the top by an electrode. The couples are sandwiched between a substrate that is sometimes ceramic. This provides structural rigidity, a flat surface for good thermal contact and electrical insulation for the electrical interconnects between the *P*-type and N-type semiconductors, as seen in the figure. 2.8.

Thermoelectric devices will provide advantages over alternative technologies. The significant features of thermoelectric modules include: there are no moving parts lead to increased reliability and long life. There are much smaller and lighter than a comparable mechanical system, depending on the application requirement. The systems are silent operation and environmentally friendly. The fast response time of thermoelectric happens depending on the speed of electrons.

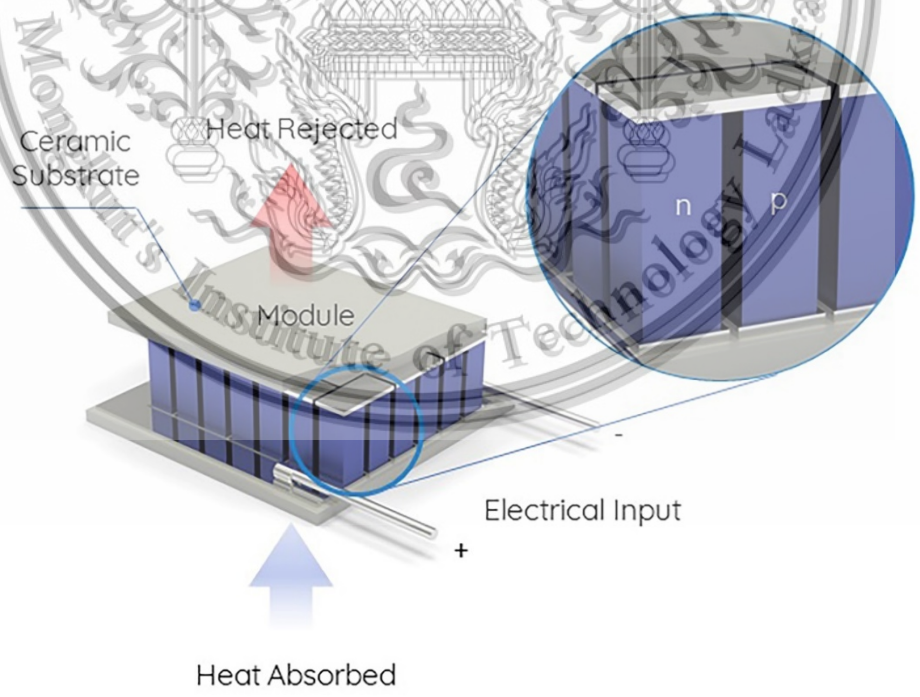

Figure 2.8 Schematic of the thermoelectric module.

2.2.1 Thermoelectric power generator (TEG)

Thermoelectric generators directly convert heat into electrical power based on the Seebeck effect. Figure. 2.9 (a) is the mechanism of TEG. The thermoelectric couples are wired electrically in series and thermally in parallel. Heat is pumped into the hot side, transported through thermocouples and rejected to other sides. The charge carriers can be diffuse from hot to cold sides. The buildup of charge at the cold produces a voltage potential. The electrical voltage will drive the electrical current in a completed circuit and produce electrical power. The output voltage is increased directly proportional to the number of couples (n)

The output voltage (V) can be generated as:

$$V = n(S_p - S_n)\Delta T \tag{2.39}$$

Where, $S_p - S_n$ is the Seebeck coefficients of TEG, ΔT is the temperature gradient between hot and cold junctions.

The output power (P) of the TEG can be calculated as:

$$P = I^2 R_L = \frac{V^2}{(R_p + R_n)^2} R_L \tag{2.40}$$

Where $R_p + R_n$ is the internal resistance of TEG and R_L is the external load. When $R_p + R_n$ equals R_L, the maximum power $(P_{\max})$ can be obtained:

$$P_{\max} = \frac{n^2 (S_p - S_n)^2 \Delta T^2}{4R} \tag{2.41}$$

The efficiency of TEG (η) is defined as the ratio of the generated power to the power drawn from a heat source (Q_H).

$$\eta = \frac{P}{Q_H} \tag{2.42}$$

If the R_L is chosen to maximize the maximum output, the maximum efficiency $(\eta_{\max})$, is given by:

$$\eta_{\max} = \frac{\Delta T}{T_h} \times \frac{\sqrt{1+ZT}-1}{\sqrt{1+ZT}+\frac{T_c}{T_h}} \tag{2.43}$$

Equation (2.43) show that the power generation efficiency is depending on the ZT of materials, the temperatures of the hot and cold junctions and the external load resistance.

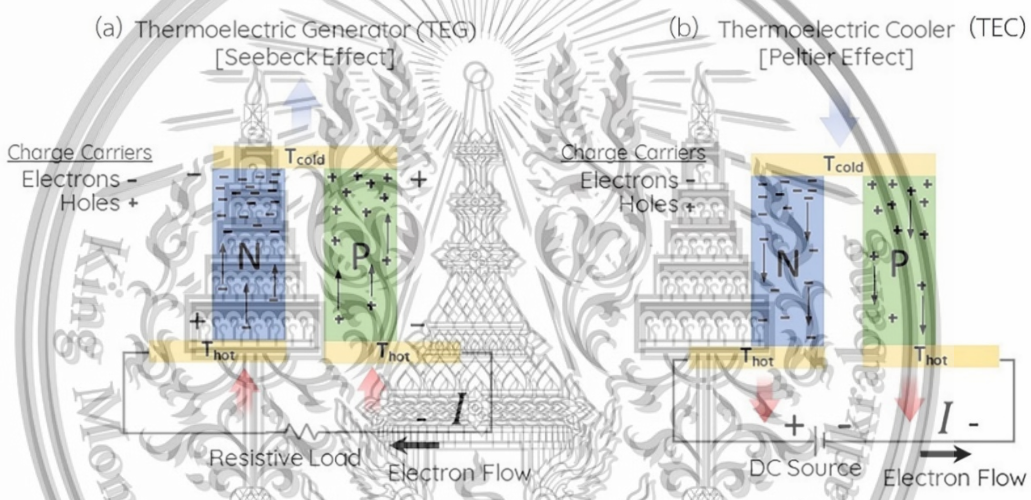

Figure 2.9 The schematics of (a) thermoelectric generator and (b) thermoelectric cooling.

2.2.2 Thermoelectric cooling (TEC)

Thermoelectric cooling or thermoelectric refrigeration directly converts an electrical current to heat based on the Peltier effect to create a heat flux between the junctions of two different types of materials, as seen in the figure. 2.9 (b). This effect is typically used in portable coolers and cooling in electronic circuits. The direct current source is used to move the carriers by an electric field. When the charge carriers transport, the heat was taken with the carriers.

The electrons moving to the higher energy absorb heat and electrons that move to a lower energy release heat. This charge carrier movement can be used to pump heat against the direction it naturally flows and produce cooling and heating.

The coefficient of performance $(COP:\varphi)$ for a TEC is defined as the ratio of the cooling capacity Q_C to the total power consumption (P).

$$\varphi = \frac{Q_C}{P} \tag{2.44}$$

The maximum COP is given by:

$$\varphi_{\max} = \frac{T_h}{\Delta T} \times \frac{\sqrt{1+ZT} - \frac{T_c}{T_h}}{\sqrt{1+ZT}+1} \tag{2.45}$$

Equation (2.45) shows that the maximum coefficiency of the performance of TEC is depending on the ZT of materials, the temperatures of the hot and cold junctions.

2.3 Antimony telluride thermoelectric material

Antimony telluride (Sb_2Te_3) is a promising *P*-type thermoelectric material from the $V-VI$ group. The atomic arrangement is based on general formula $A_2^V B_3^{VI}$ (A =Sb and B =Te) with a narrow bandgap (Eg< 0.2 eV). Sb_2Te_3 compounds have the a rhombohedral crystal structure with five atoms per unit cell belonging to the space group $R\bar{3}m$. The Sb and Te atoms consist of a sequence of layers, each layer comprising five atomic planes oriented perpendicular to the c-axis according to the scheme: ...$Te^{(1)}$-Sb-$Te^{(2)}$-Sb-$Te^{(1)}$... $Te^{(1)}$-Sb-$Te^{(2)}$-Sb-$Te^{(1)}$..., as seen in Figure. 2.10. Such a sequence is repeated in parallel layers and a single sequence known as quintuple. The subscript of Te refers to various types of bonding with antimony. The $Te^{(1)}$-Sb and Sb-$Te^{(2)}$ were bonded by a covalent and ionic bond and there are the van der Waals gap between $Te^{(1)}$ and $Te^{(1)}$ atoms.

Because of weak van der Waals bonding, this compound has a layer structure, the crystal can easily cleavage along the *c*-direction. Typically, the Sb_2Te_3 compound is excellent thermoelectric properties due to the large mean molecular mass, low melting temperature and partial degeneracy of the conduction and valence bands of V-VI chalcogenide [18]. The non-cubic structure of Sb_2Te_3 contributed to anisotropic in thermoelectric properties, the electrical and thermal conductivities are higher along a plane parallel to the cleavage than perpendicular to them.

Recently, tuning the carrier conduction or lowering the phonon conductivity through a reduction in the dimension of the structure have been studied to enhance thermoelectric efficiency. In nanostructured materials, grain boundary scattering plays an important role to suppress the lattice thermal conductivity with phonon, while the electronic thermal conductivity can be controlled efficiently by carrier concentration [26].

Typically, the excellence ZT of Sb_2Te_3 is achieved approximately near room temperature ($300\ K$), which corresponding to the human body heat source [27-28].

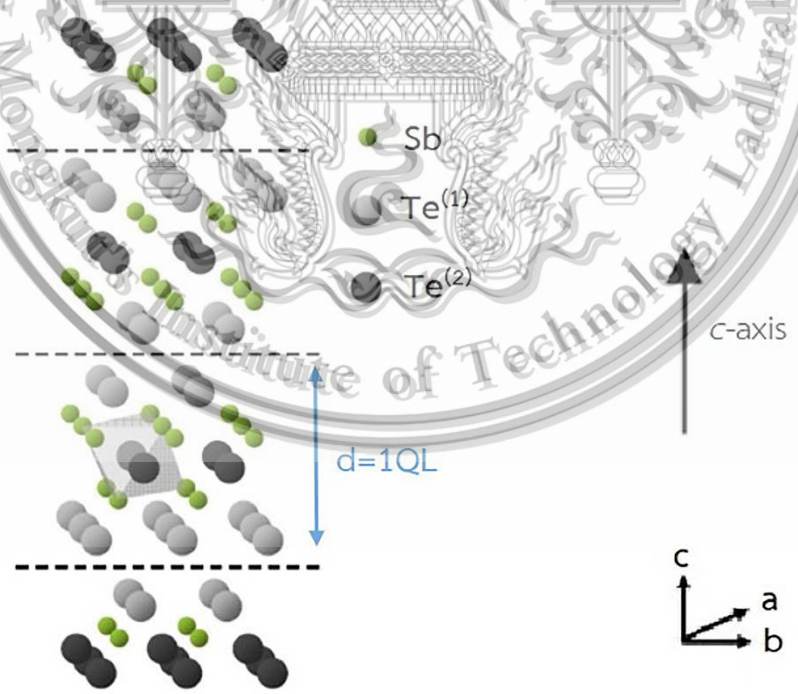

Figure 2.10 Atomic layers of Sb_2Te_3 crystal structure. Dash line indicates van der Waals gap of one quintuple layer (QL).

2.4 The film deposition process

The film depositions using vacuum technologies are typically classified into two main categories: depending on whether the process is primarily chemical and physical processes. Several processes exhibit unique material properties resulting in the growth process and deposition parameters. The film deposition using vacuum processes contains three main steps:

1. Creation of the appropriate atomic, molecular or ionic depositing species
2. Transport of the species from the source to the substrate
3. Condensation of the depositing species on the substrate directly or via a chemical reaction with reactive constituents, forming a solid deposit.

In atomic processes, the solid film is formed by condensation of the atoms in the vapor phase onto the substrate and migration to nucleation and growth sites. The adsorbed atoms require enough energy to occupy their lowest energy configurations avoiding structural imperfections. The microstructure and morphology of the deposited film are a result of the energy of the atoms which is dependent on the deposition process deposition parameters [29].

Table 2.1 Several techniques of the film deposition

Chemical vapor deposition (CVD) techniques	Physical vapor deposition (PVD) techniques
• Plasma-enhanced CVD (PECVD)	• Thermal evaporation
• Atmospheric pressure CVD	• Sputtering
• Low-pressure CVD (LPCVD)	• Molecule beam epitaxy
• Very low-pressure CVD (VLPCVD)	

2.4.1 Chemical Vapor Deposition (CVD)

In chemical vapor deposition, the films are deposited via a chemical reaction between heat substrate and inert gas in the chamber at low pressure. The precursor is introduced into a reaction chamber and is controlled by balanced flow regulators and control valves. The precursor molecules pass by the substrate, are drawn into the boundary layer, and are deposited on the surface of the substrate.

2.4.2 Physical Vapor Deposition (PVD)

In physical vapor deposition, the precursors (solid, liquid or, vapor) are released and moved to the surface of the substrate. The physical vapor deposition consists of different methods such as thermal evaporation, molecular beam epitaxy, and sputtering.

- Evaporation: Material is heated to a gas phase, where it then diffuses through a vacuum to the substrate.
- Molecular beam epitaxy: The substrate is cleaned and loaded into a chamber that is evacuated and heated to remove the surface contaminants and to roughen the surface of the substrate. The molecular beams emit a small amount of material through a shutter, which then collects on the substrate.
- Sputtering: Plasma is generated; this plasma contains argon ions and electrons. The atoms from the target are ejected after being struck by argon ions. Atoms from the target travel through the plasma and form a layer on the substrate [30].

2.4.3 Advantages and Disadvantages of film deposition

Depending on the applications, there are sound arguments for the use of either process (PVD or CVD). One reason to use a physical vapor deposition process (such as sputtering) instead of chemical vapor deposition is the temperature requirement.

CVD processes run at a much higher temperature than PVD processes. A furnace, RF coil, or laser always generates substrate temperature. Substrates that cannot tolerate this temperature must have films deposited by the physical form of vapor deposition instead. The benefit of the substrate temperature in some CVD processes is that there is less waste deposition, especially in cold-wall reactors, because only the heated surfaces are coated. With the use of a laser heating system, the CVD process becomes selective to the path of the laser; this is a distinct advantage over PVD methods.

The molecular beam epitaxy (PVD process) has a distinct advantage of atomic-level control of the chemical composition, the film thickness, and the transition sharpness. This process is relatively more expensive but is worth the added cost for applications that demand higher precision.

Sputtering (PVD process) does not require the use of a specialized precursor as used in CVD. Sputtering has a wide range of materials readily available for deposition.

Another advantage of PVD over CVD is the safety issue of the materials that are used for CVD.

However, the researcher could easily select CVD or PVD for research based on criteria such as the cost, the film thickness, the precursor availability, and the compositional control. In this work, sputtering was selected due to a wide range of materials. Further, the sputtering process is environmentally friendly and safe compared to other processes. Among these deposition techniques, sputtering has been widely used because it produces high-quality films, extremely high adhesion and excellent uniformity over a large substrate area.

2.5 Sputtering process

The sputtering process is a wildly used technique for deposition of the films, defined as the removal of surface atoms of the target by energetic ion bombardment. Momentum transfer theory and Thermal vaporization theory have been proposed for sputtering. Sputter atoms are emitted when kinetic moments of incident ions are transferred to the target surface.
The surface of the target is heated to be vaporized due to the bombardment of energetic ions.

Direct current (DC) sputtering system is composed of a pair of planar electrodes. One is a cathode and another one is an anode. The top of plasma-facing surface is covered with a sputtering target and the reverse side is water-cooled. The substrate is placed on the anode. The sputtering chamber is set to vacuum and filled with inert gas, mostly Argon. The glow discharge is generated under the applied of DC voltage between two electrodes. The Ar^{+} ions generated in the glow discharge are accelerated at the cathode fall and sputter the target resulting in the deposition of the film on the substrate at the anode. The target is always conduction material because the glow discharge (current flow) is maintained between metallic electrodes. The advantage of the DC system is simply set up. It is the standard sputter device.

The deposition rates are almost constant in various materials. The film thickness can be controlled with proportional with the current. The deposition rates of the DC are higher than the RF mode. And adhesion strength is high because of the high energy process. However, the main disadvantage of the DC system is required high

Ar pressure. The sputtering target is restricted to metal. Non-conductive materials cannot be deposited by DC system since the non-conductive coating on the substrate prevents the electron flow through the anode.

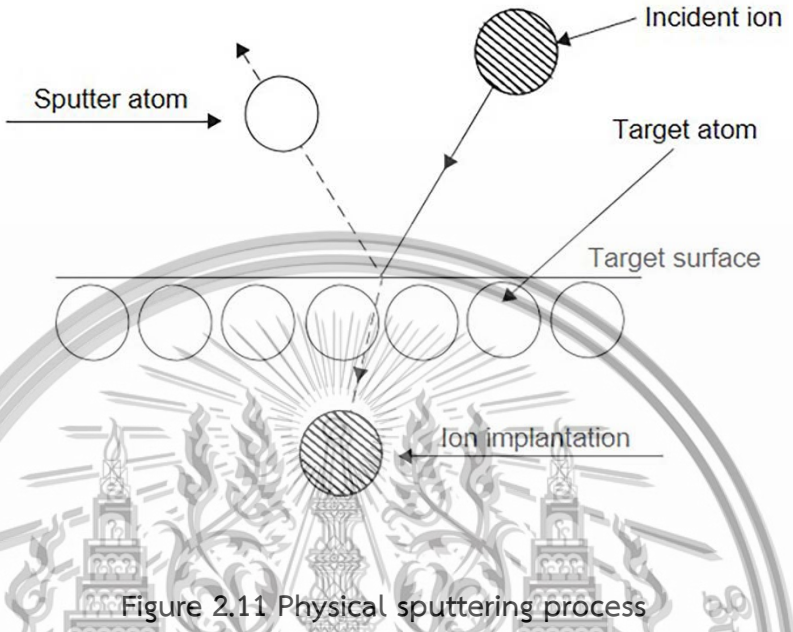

Figure 2.11 Physical sputtering process

Sputtered atoms collide with Ar gas and diffuse to the substrate since the gas pressure is high and the mean free path of the sputtered atoms is less than the electrode spacing. The amount of sputtered atoms deposited on a unit substrate area (W) is determined by deposition rates (R).

$$W = \frac{k_1 W_0}{pl} \tag{2.46}$$

$$R = \frac{W}{t} \tag{2.47}$$

Where, k_1 is a constant, W_0 is the amount of sputtered atoms from the unit cathode area, p is the discharge gas pressure, l is the electrode spacing and t is the sputtering time.

The amount of sputtered particles from the unit cathode area W_0 is given by:

$$W_0 = \left(\frac{j_+}{e}\right) St \left(\frac{A}{N}\right) \tag{2.48}$$

The j_+ is nearly equal to the discharge current I_s, and the sputter yield is proportional to the discharge voltage V_s, the total amount of sputtered particles becomes $V_s I_s t/pl$. Thus, the sputtered deposit is proportional to discharge voltage, discharge current and sputtering time $(V_s I_s t)$.

The deposition rates of the sputtering are lower than other vacuum deposition. In general, lower sputtering pressure increases deposition rates. Low-pressure sputtering is a promising process for film production but fewer ions to bombard for deposition, which reduced the deposition rate process. Magnetron sputtering system is used to improve the ions bombarding by installing of the magnet in the rear of the sputtering target. The magnetic flux on the cathode surface is terminated to the magnetic core. A magnetic field is assumed on the cathode which parallels to the surface of the target. The electron in the glow discharge shows cycloid motion and the center of orbit drifts in a direction of $\mathrm{E}\times\mathrm{B}$ with the drift velocity of E/B, where E and B denotes the electric field and the magnetic field, respectively. The magnetic field lines trap the escaping energetic electrons, and the trapped electrons make ionizing collisions.

The increasing of the ionization increases the ion current to the cathode target and lowers the operating gas pressure resulting in higher deposition rates. The incident flux of ionized particles increases in the magnetron increasing deposition rates. The incident ionized flux modifies the growth process. Moreover, high ion current density will enhance the chemical reaction at the substrate during the film growth [31].

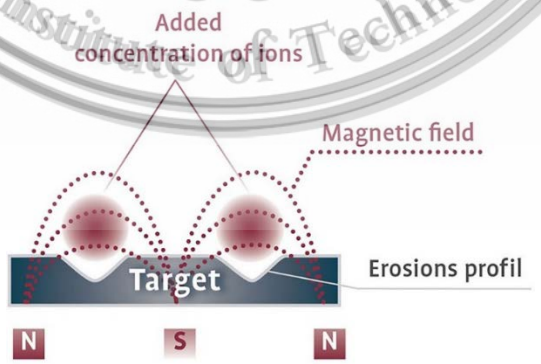

Figure 2.12 Schematic of the magnetron sputtering system.

2.5.1 Sputtered atoms

A glow discharge is a plasma formed by ionizing sputtering gas (Ar). The sputtering gas bombards the target and sputters off the target to deposit. Ions can be generated by the collision of the neutral atoms with the high-energy electrons. The interaction of the ions and target are controlled by ions energy and ions velocity. The magnetic and electric field can be used to control ions.

The process begins with applying a voltage between two electrodes. The electron near the cathode is accelerated towards the anode and collides with a neutral Ar atom converting it to a positively charged ion.

$$\bar{e} + Ar \rightarrow 2\bar{e} + Ar^{+} \tag{2.49}$$

The interaction result exhibits two atoms of the electron which can collide with other gas atoms and ionize by creating a cascading process until the gas breaks down. The breakdown voltage depends on the pressure and the distance between the anode and the cathode. The interactions between the incident ions and the target are not only the sputtered atoms but also cause the generation of secondary electrons and reflected ion and neutrals. Ions bombardment may be implanted into the target material [20]. The secondary electron is maintained the glow discharge process. The sputtered atoms are coated onto the substrate in the form of neutral atoms.

The sputtered atoms are sputtered by bombardment with ions having a few hundred electron volts. These sputtered atoms are partially ionized, i.e., a few percents of the sputtered atoms, in the discharge region of the sputtering system. An alloy target, if low energy of incident ions have interacted, most of the sputtered atoms are composed of the alloy.

The principle of ions collision with the target is energy and momentum conservation. In any collision, momentum is typically conserved. If the collision is elastic, kinetic energy is also conserved. The energies required for sputtering are higher than lattice bonding which are the causes of inelastic interactions. Therefore, sputtering collisions can be considered elastic.

1. Momentum and Energy

Momentum (P)

$$P = m v \tag{2.50}$$

Kinetic energy (K)

$$K = \frac{1}{2} m v^2 \tag{2.51}$$

Momentum conservation, total momentum before = total momentum after

$$m_1 v_{1i} + m_2 v_{2i} = m_1 v_{1f} + m_2 v_{2f} \tag{2.52}$$

Kinetic energy conservation, total kinetic energy before = total kinetic energy after

$$\frac{1}{2}(m_1 v_{1i}^2 + m_2 v_{2i}^2) = \frac{1}{2}(m_1 v_{1f}^2 + m_2 v_{2f}^2) \tag{2.53}$$

As seen in figure 2.13, the maximum energy transfer between two masses in the forward direction in such a collision occurs when the masses are equal.

$$\frac{K_2}{K_1} \propto \frac{4 m_1 m_2}{(m_1 + m_2)} \cos^2 \theta \tag{2.54}$$

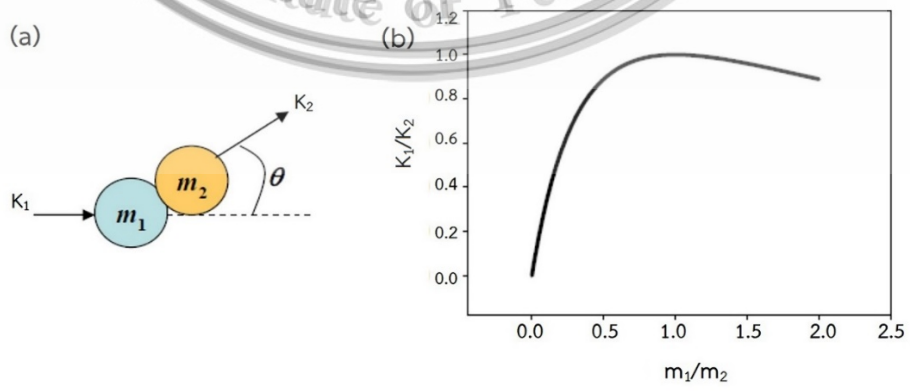

Figure 2.13 (a) Kinetic energy transfer (b) kinetic energy transfer between two masses in the forward direction.

2. Mean free path

The energy of sputtered atoms is typically higher than that of thermally evaporated atoms in a vacuum. The energy of sputtered atoms depends on the incident ion species and the incident bombardment angles.

The mean free path of the sputtered atoms, which pass through the glow discharge space, is given by

$$\lambda_1 \cong \frac{c_1}{\nu_{12}} \tag{2.55}$$

Where c_1 is the sputtered atoms velocity and ν_{12} is the collision frequency between sputtered atoms and sputtering gas. The sputtered atoms velocity is larger than the sputtering gas, ν_{12}, as given by:

$$\nu_{12} \cong \pi (r_1 + r_2)^2 c_1 n_2 \tag{2.56}$$

Where r_1 and r_2 are the atomic radius of sputtered atoms and sputtering gas, respectively, n_2 is the density of discharge gas. The mean free path is given by:

$$\lambda_1 \cong \frac{1}{\pi (r_1 + r_2)^2 n_2} \tag{2.57}$$

2.5.2 Sputtering yield

The sputtering yield (S) is defined as the mean number of atoms removed from the target due to bombardment per incident ions and is given by:

$$S = \frac{\text{Sputtered atoms}}{\text{Incident ions}} \tag{2.58}$$

The sputtering is the interaction of incident ions with target atoms. The sputtering yield will be influenced by these factors:

- The energy of incident ions
- The incident angle of ions
- The masses of the ions and target atoms

Sputtering target: the binding energy of the target atoms and relative mass of ions

The sputtering yield can be measured by the following methods: Weight loss of sputtering target, Decrease of thickness target, Collection of the sputtered material and Detection of sputtered ions.

The momentum transfer theory and thermal vaporization theory have been proposed for sputtering. The sputtering process is initiated by the collision between incident ions and target atoms. The displacement of target atoms will be more isotropic due to successive collisions and atoms may finally move from the target. The sputtering yield is insensitive to the temperature of the target except at a very high temperature. It will be shown the increase in the sputtering rates due to accompanying the thermal evaporation. The mechanism of sputtering is considered in detail for the following three different energy regions of the incident ions.

1. Threshold region (E < 100 eV)
2. Low-energy region (E > 100 eV)
3. High-energy region (E = 10-100 keV)

The threshold region is the energy for ejecting target atoms. The sputtering yield increases with increasing the higher energies in the low-energy region. The saturation of sputtering yield has occurred at the high-energy region for heavier bombarding

According to the elastic-collision theory, the possible energy transferred in the collision process (T_m) is followed by:

$$T_m = \frac{4M_1M_2}{(M_1+M_2)^2}E \tag{2.59}$$

Where, M_1 and M_2 are the mass of the incident ions and target atoms, respectively. E is the kinetic energy of incident ions. In the first order of approximation, the sputtering yield is proportional to T_m. The sputtering yield (S) of the target material bombarded with different element is given by:

$$S = k\frac{1}{\lambda(E)\cos\theta}\frac{M_1M_2}{(M_1+M_2)^2}E \tag{2.60}$$

Where k is a constant which depends on the target material, λ is the mean free path for elastic collisions near the target, θ is the direction of incidence ions. The mean free path is given by:

$$\lambda = \frac{1}{\pi R^2 n_0} \tag{2.61}$$

Where n_0 are the numbers of lattice atoms per unit volume. R is the collision radius in the sphere model.

Finally, the sputtering yield is expressed by the relationships where

1. <1 keV

$$S(E) = (3/4\pi^2)\alpha T_m / U_0 \tag{2.62}$$

2. 1-10 keV

$$S(E) = 0.420\alpha S_n(E)/U_0 \tag{2.63}$$

Where, T_m is the possible energy transferred in the collision process, U_0 is a heat of sublimation and α is the function of M_2/M_1.

However, the sputtering yield is depending on the energy of the incident ions, target materials and angle of incidence ions. Sputter yields increase as the mass of incident ion increases due to a process of momentum transfer and also tends to increase as the kinetic energy of incident ions above the threshold energy [20].

2.5.3 The practical aspect of sputtering systems

For the operation of the sputtering system, many equipments are prepared including the sputtering target, sputtering gas, substrate and monitor systems.

1. Sputtering target

The sputtering target is typically made from metal or alloy compound disks. Typically, the diameter is 5-8 cm for research and 15-30 cm for production. A rectangular is used for production. In the sputtering process, the sputtering target is mounted on a water-cooled backing plate by mechanical support. It is surrounded by a dark space, known as a ground shield. When input the power appears as target heating. Rotation of the substrate holder is often used to obtain a uniform composition.

Typically, the compound target is widely used in a single target system. It can be deposited by direct sputtering from the sintered powder of the compounds material. The thickness distribution of the sputtered film is governed by the construction of a magnetic core. The magnetron cathode comprised a permanent magnet. The magnetic flux density of the magnetic core has occurred on the target surface. The magnetron is covered by a permalloy sheet which confines the leakage magnetic flux.

However, the thickness distribution of sputtered films is governed by several factors such as the angular distribution of the sputtered atom, the collisions between sputtered atoms and sputtering gas and the construction of the target shield.

2. Sputtering gas

Typically, the deposition process of the film is affected by the deposition rates (the power density) and the gas pressure. The sputtering gas is widely used as an inert gas (generally a heavy gas, Ar). In the sputtering process, a plasma is created by ionizing a sputtering gas. The sputtering gas bombards the target and sputters off the material to deposit.

At low pressures, higher ions energy increases the deposition rate/sputtering yield. There are not enough collisions between ions and sputtering target atoms to contribute a plasma which deposition rate. On the other hand, at high pressures, there are many collisions that electrons do not have enough time to gather energy between collisions to be able to ionize the atoms. Therefore, the sputtering gas was optimized for providing the deposition rate of the film production. The optimum pressure depends on target-substrate configurations.

3. Substrate

In this work, Sb_2Te_3 films were directly deposited on a flexible polyimide substrate. Polyimide is widely used as a dielectric substrate for its high-temperature resistance, self-extinguishing burn characteristics, toughness and flexibility. It has been used successfully in applications at temperatures as low as -269°C and as high as 400°C. Moreover, to form a flexible thermoelectric device, polyimide used as a substrate was chosen due to its low thermal conductivity (0.12 $Wm^{-1}K^{-1}$) and thermal expansion coefficient (12×10^{-6} K^{-1}) which closely matches that of the Sb_2Te_3 films. Besides, polyimide can reduce residual stress and increase adhesion in the film.

The substrate temperature is the most important thing and yet difficult to control. In convention sputtering system, the substrate is mounted on a temperature-controlled. However, the heat of surface target and the bombardment by high-energy secondary electrons heat the substrate surface. To reduce the effect of the heat of the substrate, the surface of the target must be cooled. Bombardment by the secondary electrons are avoided by negatively biasing the substrate. The temperature rise at magnetron is reduced because the secondary electrons from the target are trapped by the magnetic field near the surface of the cathode target.

4 monitoring systems

The monitoring of sputtering conditions is important to control the properties of the film production. The parameters to be monitored are as follows:

1. Sputtering discharge
   - Voltage
   - Current
   - Power density
2. Sputtering gas in the sputtering chamber
   - Residual gas
   - Total/partial pressure of the sputter gas
3. Substrate temperature

4.1 Sputtering discharge

The discharge parameters (the sputtering voltage and the sputtering current) can be easily measured by a conventional high impedance voltmeter and a low impedance current meter for DC sputtering.

Figure 2.14 DC power of the sputtering system.

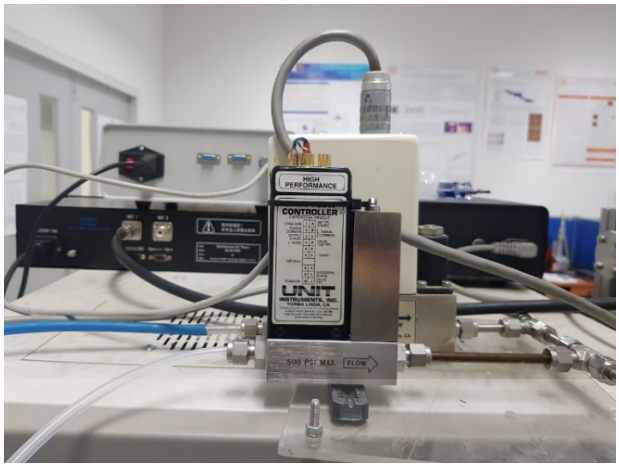

Figure 2.15 Mass flow controller.

4.2 Sputtering gas

The gas composition and sputtering pressure in the chamber are measured by a vacuum gauge. When the sputtering gas is introduced into the ion source chamber, the sputtering gas is ionized and resulting ions are accelerated. The concentration of the total/partial pressure of sputtering gas is generally fed to the system through a stainless steel pipe. The non-uniformity in partial gas density during sputter results in non-uniformity in the chemical composition of film production. The gas flow is controlled by a leaking valve. The gas flow is controlled by a mass flow controller.

4.3. Substrate temperature

The substrate temperature is measured by a thermocouple. A 1000 W quartz lamp was used to heating the substrate. The position of the thermocouple was fixed nearly the glass slide as shown by the schematic diagram in the figure. 2.16. This reading temperature is from a thermocouple called reference temperature (T_{ref}). The temperature control unit was used for setting the T_{ref}. It can be assumed that the T_{ref} is the substrate temperature (T_{sub}) from the calibration. The relationship between T_{ref} and T_{sub} was measured. The thermocouple was contacted under of the polyimide substrate.

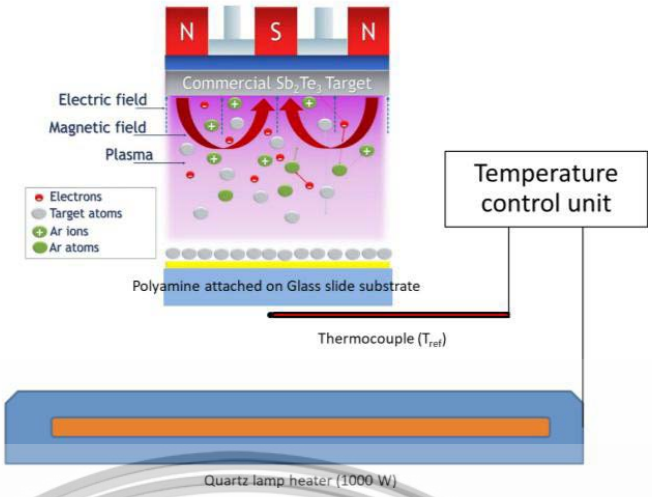

Figure 2.16 Schematic diagram of substrate temperature.

In the sputtering process, sputtered atoms are transported and diffused on the surface of the substrate are called adatoms. The interactions of adatoms and substrate are delicate. The control of film quality is necessary for both scientific research and applications. Fundamentals of the controlling film quality are described in the following sections which are governed by chemical composition, crystal structure, phase structure, uniformity and film stress. The chemical composition is governed by the chemical composition of a material, composition of sputtered atoms, gas atoms, the surface reaction of adatoms, and Interdiffusion between adatoms and substrate. The crystal structure properties are governed by stoichiometry, Impurity atoms and phase separation. Their physical, chemical, electrical and mechanical properties are affected by the growth process. In the growth process, it is important to understand the relation between the film properties and the sputtering parameters.

2.6 Thin/thick-film growth process

In term of thin-film are not only defined by the thickness but also by the way they are deposited. Thin-film is mostly deposited on a substrate by vacuum deposition. The smooth surface and the fine structure are obtained. The thickness of thin-film can vary from 50 angstroms to several thousands of angstroms. In term of thick-film is defined from the fact that the fired film is fairly thick, varying from 1-50 μm. There are considerable possibilities for building multilayer structures [54].

The growth processes of thin- and thick- film consist of a statistic process of nucleation, a surface-diffusion-controlled growth of the three-dimensional nuclei, and a formation of a network structure leading to give a continuous film. The formation of the films occurs via nucleation and growth processes. The step by step growth process can be presented as follows: [32-33]

When sputtered atoms are transported to a substrate, their velocity is lost and is physically adsorbed on the substrate surface. The adsorbed are not in thermal equilibrium with the substrate initially and move over the substrate surface. In this process, the bigger clusters are formed. The adatoms are thermodynamically unstable and may tend to desorb in time, depending on the deposition parameters. If the adatoms collide with others, it will be getting desorbed, then starts growing in size. After reaching a certain critical size, the cluster becomes thermodynamically stable. This step related to the formation of stable, chemisorbed, critical-sized nuclei is called the nucleation stage.

The critical nucleus grows continuously until a saturation nucleation density is obtained. The nucleation density and the average size are depending on the energy of the impinging materials, the rate of impingement, the activation energies of adsorption, desorption, thermal diffusion, temperature, topography, and chemical reaction of the substrate.

A nucleus can grow both parallel to the substrate by surface diffusion, and perpendicular to direct impingement of the incident atoms. The rate of lateral growth is generally much higher than the perpendicular growth. The grown nuclei are called islands.

The next stage in the process of film growth is the coalescence stage, in which the small islands start coalescing with each other in an attempt to reduce the substrate surface area. This tendency to form bigger islands is called agglomeration, which is enhanced by increasing surface mobility. The increasing of substrate temperature affects the formation of new nuclei which may occur on areas exposed as a consequence of coalescence. Larger islands grow together. The porosity of the film structure has occurred. A completely continuous film was obtained by filling the porous.

Depending on the thermodynamic parameters of the deposition process and the substrate, the initial nucleation and growth stages were described by (a) island type, called the Volmer-Weber model, (b) layer type, called Frank-van der Merwe model, and (c) mixed type, called Stranski-Krastanov model.

In the Vomer-Weber model, equilibrium exists in a three-dimensional crystal of the film in contact with the substrate. The mechanism of island growth happens when the interaction between the atoms is stronger than the interaction with the substrate surface. Nucleation occurs in the form of discrete nuclei on the substrate. The number of nuclei and the size of the nucleus increase leads to intersperse with each other to form a continuous film.

In the Frank-van der Merwe model, nucleation occurs in the form of a monolayer island. The monolayer grows together to form a layer-by-layer to complete the continuous of the deposit. The interaction between the atom and the substrate is stronger than neighboring layer atoms.

The Stransky-Krastanov model combines the features of layer-by-layer growth and discrete three-dimensional nucleation. This model is deposited at a low temperature in which the surface mobility is low. The conditions of growth are explained in terms of thermodynamics and surface energy. The nucleation and growth occur as in the layer-by-layer mode, so a finite number of the monolayer is produced. The film growth occurs by the formation of discrete nuclei.

The lattice mismatch between the substrate and the deposit cannot be accommodated when the film thickness increases. Alternatively, the orientation of the overlayers concerning the substrate might be responsible for the production of this model. [20]

The growth model of the films is conducted by the surface energy of thin films (γ_f), the surface energy of substrates (γ_s), and the interfacial energy between films and substrates (γ_{fs}). The island growth or the Volmer-Weber model will be predominant at $\gamma_f > \gamma_s - \gamma_{fs}$ and the layer-by-layer growth or the Frank-van der Merwe model at $\gamma_f < \gamma_s - \gamma_{fs}$. In this growth, the surface energy of the substrate shows the minimum free energy [34-35].

2.6.1 Microstructure and Temperature

When the sputtered atoms are transported to the substrate. All atoms diffuse on the surface of the substrate. Diffusion of adatoms on the surface depending on the energy of adatoms and interactions at the substrate. The adatoms form chemical bonding with the other adatoms or the substrate. The formation of the films is related to the mobility of adatoms during growth. The energy supply to the adatoms is provided by the following mechanism:

- Thermal effect
- Ionic bombarding
- The chemical reaction at the substrate

These effects can be explained by the structure zone model (SZM). The SZM model can determine the microstructure and the morphology of the films as a function of the adatoms. The parameters that the SZM model includes for determining the microstructure and the morphology of the films are the substrate temperature, the working pressure, the voltage applied and the thermal characteristics of the target.

In the grain growth and recrystallization studies, one expects useful relations in terms of T_s/T_m. where T_s is the substrate temperature and T_m is the material melting point. After examining film coatings, Movchan and Demchisshim 1969 divided the T_s/T_m into three zones.

The first zone is $T_s/T_m < 0.3$. This zone is formed by small grains that form a columnar structure with porous morphology and weakly binding grains. The columnar structure was produced by a low diffusion, low mobility of the adatoms adsorbed by the surface of the substrate, which is produced by varying velocity. The various incidence angles of sputtered atoms arrive at the substrate.

The secondary zone is $0.3 \leq T_s/T_m \leq 0.45$. The substrate temperature increasing homogeneous which leads to a higher diffusion of the adatoms. The dense structure with a higher degree of binding between the columns is produced. The grain size of the film can be increased and the grains extended in equiaxed form.

In the third zone, $T_s/T_m > 0.45$, the volumetric diffusion size has a great influence on the film morphology due to the increase in the diffusion into the grains, which produces grain growth. The formation of the equiaxed grain and re-crystallization. In this zone, a greater crystalline structure is produced [32].

Moreover, the growth parameters can change the kinetic energy of the adatoms that arrived at the substrate and the mean free path of the particles. Sputtering pressure allows an increase or decrease in the ion bombardment of the surface, which in turn determines the mobility of the adatoms at the surface. The bias voltage of the substrate has the same effect on mobility and adsorption of the atoms as increasing temperature. When it is increased resulting in denser films and a high degree of crystallinity.

The bias voltage also influences the mechanical properties of the films. At a high voltage, the deformation of the lattice at the substrate increases due to the high residual efforts and the low adhesion between film and substrate.

Furthermore, the growth parameters that affect the microstructure are the power supply and the gas flows. Changing the gas flow rate during film growth changes the preferred orientation.

The deposition with well-defined large grains is formed at high temperature (substrate and source), which results in high surface mobility. The effect of temperature has exhibited the increases the kinetic energy of the incident atom and also increases in the surface mobility.

However, with the sufficiently kinetic energies, the surface mobility is reduced due to the penetration of the incident ions into the substrate, resulting in small grain. This effect of the kinetic energy of the ions on grain size is more pronounced at high substrate temperature. The effect of substrate temperature on grain size is prominent relatively with the film thickness. The post-annealing may also improve the larger grain size. The grain growth is obtained during post-annealing because of the high activation energy process of thermal diffusion of the condensate adatoms.

The effect of annealing temperature on grain size is prominent relatively with the film thickness. The effect of substrate temperature, post-annealing temperature, kinetic energy, and thickness on the grain size is summarized in Figure 2.18. It can be seen that the grain size cannot be increased indefinitely because of the limitation on surface mobility.

The parameters of grain growth are high surface mobility as obtained at high substrate temperature, low supersaturation, clean, smooth, and inert of substrate surfaces and crystallographic compatibility between the substrate and the material [32, 36].

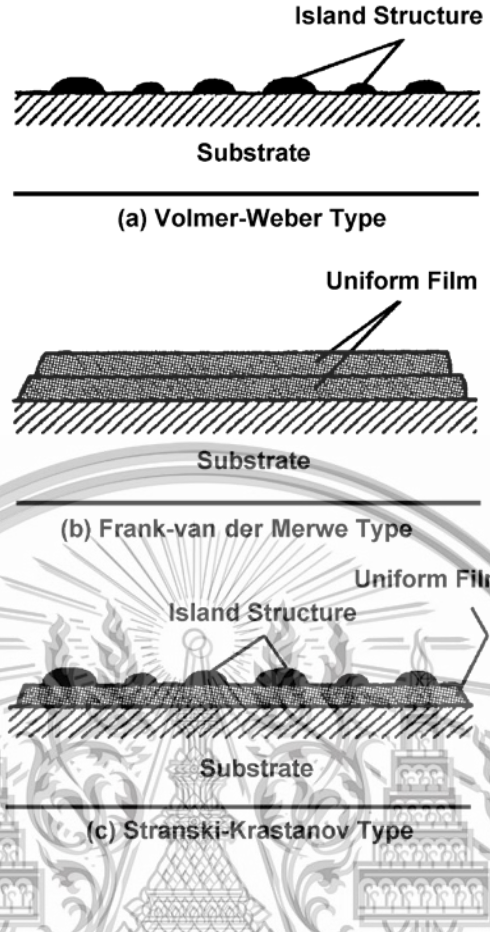

Figure 2.17 Three modes of film growth processes.

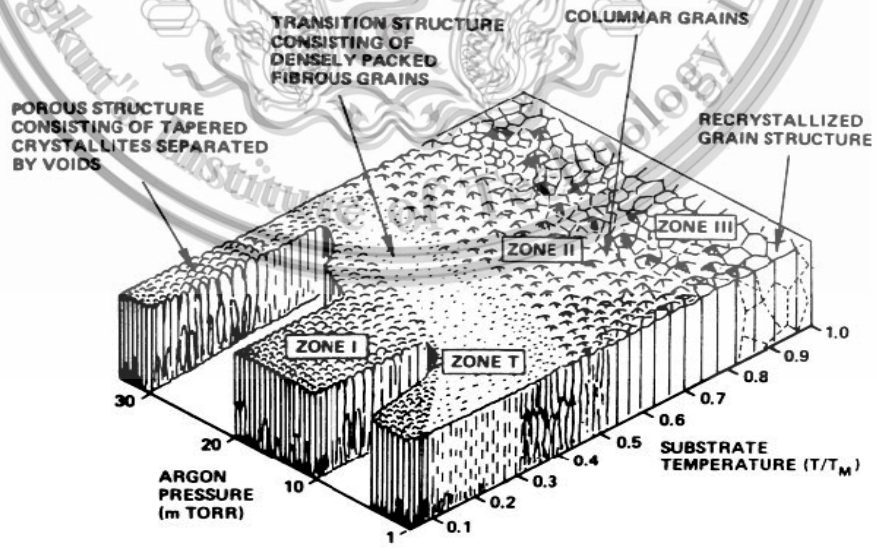

Figure 2.18 Structure zone model on substrate temperature and argon pressure.

2.6.2 Surface roughness and density

The small grain size and smooth surface of the film deposited have become when the low nucleation barrier, the high supersaturation and the high nucleation density occur, leading to small film thickness. On the other hand, if the nucleation barrier is large and the supersaturation is low, few nuclei are formed, resulting in larger grain and rough surface which become a large thickness. The surface roughness occurs when the incident ions are not falling normally on the substrate during the deposition process. The Frank-van der Merwe model provides the smooth surface and the Volmer-Weber model provides the rough surface. The strains due to the thermal expansion mismatch between film and substrate affect the surface microstructure and roughness [37].

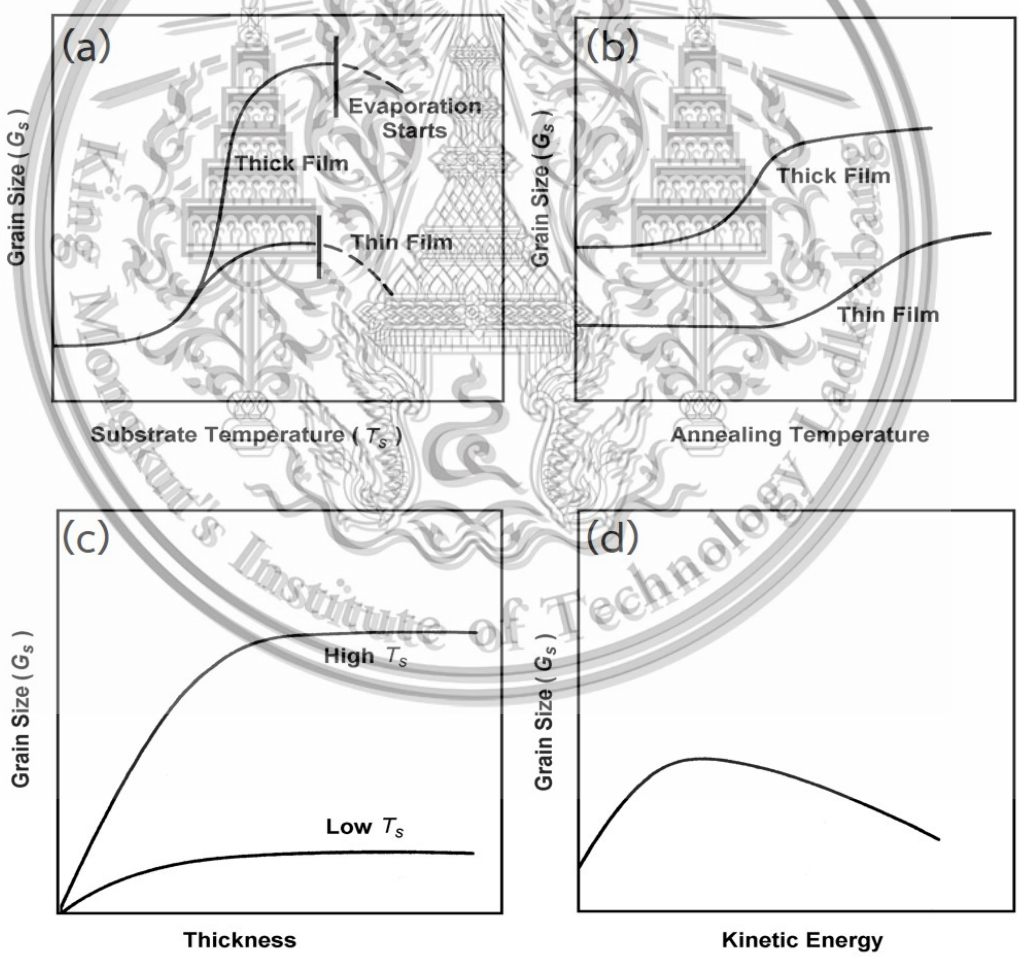

Figure 2.19 The effect of (a) substrate temperature, (b) annealing temperature, (c) thickness and (d) kinetic energy on the grain size of the films.

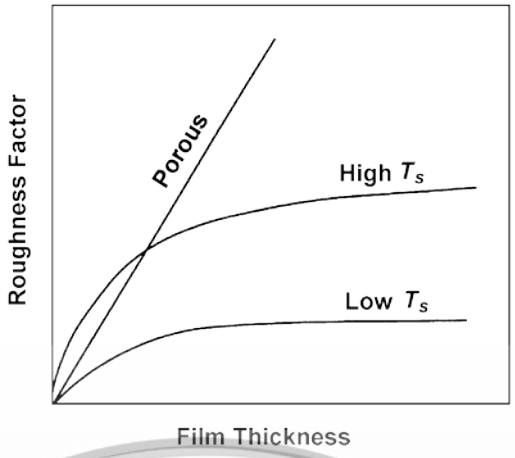

Figure 2.20 The variation of the roughness factor as a function of film thickness.

2.6.3 Adhesion

The adhesion of the film is typically depending on the chemical structure of a material, the cleanliness, and the substrate surface. Moreover, the adhesion is obtained in high values of 1) kinetic energy of the incident ions, 2) adsorption energy of the deposit and 3) initial nucleation density. The contaminated substrate surface may decrease the adhesion. Porous formed may cause under the high supersaturation and poor vacuum is less adherent than compact formed. The adhesion of the film is improved by providing the nucleation on the substrate by using a fine-grained substrate or pre-coated surface with suitable material.

The internal stress has occurred during the deposition process. The elastic energy is stored in the film due to stress. The elastic energy (u_v in J/m^3) is expressed by:

$$u_v = \frac{\sigma^2}{2Y} \tag{2.64}$$

Where Y denotes the Young's modulus of the film. The store energy in the unit area of the film (u_s) becomes:

$$u_s = u_v d = \frac{\sigma^2}{2Y} d \tag{2.65}$$

Where d is the film thickness. When u_s is higher than the adhesive energy, the film deposited will peel off from the substrate. Under an adhesive condition, the critical film thickness is obtained. Stress can be introduced by the thermal expansion between films and substrates. The internal stress (σ) is expressed by measuring the strain (ε) using an XRD analysis.

$$\sigma = \frac{\varepsilon Y}{2v} \tag{2.66}$$

Where ε denotes the strain and v is the Poisson's ratio of the film [32].

2.6.4 Two-dimension material

Two-dimension (2D) material is characterized by compressing of electrons and holes inside the highly limited space of nano-size resulting from quantum confinement. Quantum well, thin film and superlattice are classified into 2D material.

Quantum effects obtains in 2D material which can be confined carriers during the physical size of the confinement potential is comparable to the de Broglie wavelength. The Fermi energy is used to describe the average energy of a crystal in a material at a given temperature and the corresponding Fermi wavelength is the de Broglie wavelength of the electrons present near the Fermi energy level. In bulk material (3D), the charge carriers are free in three directions which exhibit a continuous energy spectrum. In thin film (2D), the charge carriers are free in two directions and confine in one direction. When the length along one of these directions becomes comparable to Fermi wavelength, the corresponding momentum is quantized. The quantized energy (E_n) can be calculated by:

$$E_n = \frac{\bar{h}^2 k^2}{2m^*}, k = \frac{n\pi}{L} \tag{2.67}$$

Where k is the wavenumber in z direction and n is the quantum number. The calculation of the wave function in quantum well with an infinite quantum well potential of barriers and a finite width of the well (L). The energy level in x and y direction are continuous and z direction is discrete energy.

The band theory is a gap between the Fermi level and the conduction band. At above zero temperature, some electrons can bridge the gap and participate in

electrical conduction. The electron population depends on the product of the Fermi function and the electron density of states. The band structure of the thermoelectric material has a sharp band or high density of states near the Fermi level to enhance Seebeck and dispersive bands to enhance the electrical conductivity. For a good thermoelectric material, there should be a high density of states (DOS) near the Fermi level but the dispersive bands should not be cut by the Fermi level nor should be touching [52-53].

The DOS is defined as the number of different states at a particular energy level that electrons are allowed to occupy, within k space. It can be expressed by:

$$D(E)=\frac{dN}{dE} \tag{2.68}$$

Where $D(E)$ is the DOS as a function of energy, N is the number of states and E is the energy of different states.

In the case of 2D material, the carriers are free on the surface of the film structure (parallel to the quantum well plane). The quantization of the carriers occurs in the perpendicular direction to the quantum well plane. The thickness of the well is inverse proportional to the confinement energy $(L_z << L_x; L_y)$. Moreover, decreasing the width of the wall caused the quantized energy increases of carriers [20].

The semiconductor is suitable for thermoelectric materials with relatively low carrier concentration and can have large Seebeck coefficients and high mobility. The relation of carrier and Seebeck can be determined from a relatively simple model of electron transport. Two-dimensionally confined carriers in quantum well exhibits quantum effects whereby the Seebeck can be increased due to increase the DOS without the other properties decreasing. The effective mass of carriers is governed by the energy surface shape in the valence and conduction bands, which can, along with the carrier and phonon scattering behavior, strongly affect electronic phenomena [52-53].

2.7 Characterization techniques

In this study, characterization techniques of sputtered thin/thick Sb_2Te_3 films are described. The experimental techniques to analyze thermoelectric film properties including physical, chemical, electrical and thermoelectric are presented.

2.7.1 X-ray diffraction (XRD)

X-ray diffraction technique is used for phase identification of a crystal structure and atomic spacing of materials which can be obtained through electron and neutron diffraction and determined of unit cell dimension. In typical, X-rays are generated by a cathode tube, filtered to produce monochromatic radiation, collimated and directed to the materials. The interaction between the incident rays and sample material produces constructive interference and diffraction rays when the condition satisfies Bragg's law, as seen in the figure. 2.21.

$$2d \sin\theta = n\lambda \tag{2.69}$$

Where d is the spacing of the atomic plane measured perpendicular to the planes, θ is Bragg's angle measured between the incident direction and the planes, n is an integer that presents the order of reflection and λ is the wavelength of X-rays.

Bragg's law relates to the diffraction angle of X-rays radiation and the lattice spacing in a crystalline material. The X-rays diffraction were obtained by scanning sample material in the range of 2θ angles, all diffraction direction of the lattice are attained due to the random orientation of the materials [32].

The diffraction patterns have conversed with d-spacing leads to the identification of the mineral because each mineral has a unique d-spacing. The standard reference pattern (JCPDS card) is achieved by comparison of d-spacing.

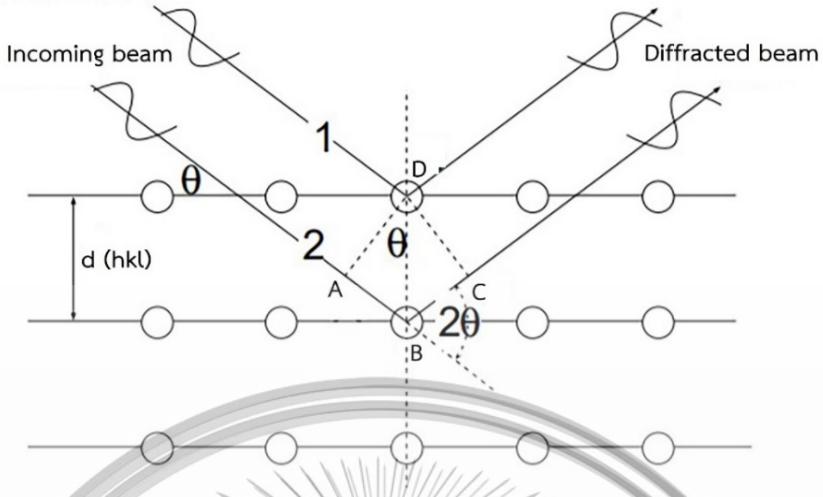

Figure 2.21 Bragg's law

X-ray diffractometers consist of an X-ray tube, sample holder and X-ray detector. Cathode tube generates X-ray by the heating filament to introduce electrons. The acceleration of electrons toward a target material was done by applying a high voltage, then the bombarding occurred. When electrons have sufficient energy to dislodge inner shell electrons of the target material, characteristic X-ray spectra are produced. In typical, Copper is a common target material to produce monochromatic radiation with Cu- K_α radiation (λ =1.5418 Å). Then, the collimated X-rays are directed to the sample. The intensity of reflected X-rays is recorded by rotating the detector. When the incident X-rays impinging the sample satisfies the Bragg Equation, constructive interference occurs and a peak intensity occurs. A detector records the signal data and converts it to a count rate which is then output to a monitor.

The Scherer equation is a formula that relates the crystalline size in a sample to the broadening of a diffraction peak. The Scherer equation can be written as:

$$D = \frac{k\lambda}{\beta \cos\theta} \tag{2.70}$$

Where D is a crystalline size, k is the Scherer constant (0.94), λ is the X-ray wavelength, β is the line broadening at half the maximum intensity (FWHM) and θ is the Bragg angle.

Many factors may contribute to the observed diffraction peak profile such as instrument, crystalline size, temperature and microstrain. The most important factor is the microstrain. In general, microstrain corresponds to atom displacements concerning their position in crystals that are free of any defects including non-uniform lattice distortion, dislocation, antiphase domain boundaries and grain surface relaxation.

The diffraction peaks can be apparent to the crystalline size by the Scherrer equation. And their microstrain, Williamson and Hall suggested a method for finding both, called the Williamson-Hall (W-H) method [39]. The W-H method is a formula that relates to the effect of crystallite size (β_D) and microstrain (β_ε), as seen in equation (2.71).

$$\beta_T = \beta_D + \beta_\varepsilon \tag{2.71}$$

Where β_T is the total broadening, β_D is the broadening due to crystalline size and β_ε is the broadening due to strain. From the Scherer equation (2.69) known that:

$$\beta_D = \frac{k\lambda}{D\cos\theta} \tag{2.72}$$

The peak broadening due to microstrain is given by:

$$\beta_\varepsilon = 4\varepsilon\tan\theta \tag{2.73}$$

Where ε is the strain and θ is the peak position. So,

$$\beta_T = \frac{k\lambda}{D\cos\theta} + 4\varepsilon\tan\theta \tag{2.74}$$

Or

$$\beta_T \cos\theta = 4\varepsilon \sin\theta + \frac{k\lambda}{D} \tag{2.75}$$

Equation (2.75) represents a straight line, which ε is the slope of the straight line and $\frac{k\lambda}{D}$ is the y-intercept.

2.7.2 Field-emission scanning electron microscopy (FE-SEM)

The field emission scanning electron microscopy provides topographical and elemental information on the specimen. The electron microscope is also limited by the wavelength of the electron. Since the wavelength of the electron is small, the subatomic resolution can be obtained.

The electron microscope that works with an electron in a negative charge instead of visible light in an optical microscope. Therefore, all samples work with FE-SEM must be conductive under vacuum. The electrons were created by a field emission source made from tungsten filament. A direct current is passed through the filament which heats it about 2700 K. At temperature, the filament emits electrons into the surrounding vacuum by the process called thermionic emission. The high energy electron is accelerated from the filament by applied voltage (0.5-30 kV) within the high vacuum column, called primary electrons. The anode has a pinhole to collimate the electrons beam. The collimated electrons pass through a magnetic lens which focuses them to spot on the specimen. The scan coils deflect the electron beam over the object according to a zig-zag pattern. The formation of the image on the monitor occurs in synchrony with the scan movement. The objective lens is the lowest in the column. It can focus the electron beam on the object. After the primary electrons are focused and deflected by electronic lenses to produce a narrow scan beam that bombards the specimen. The atomic electrons ejected from the specimen at low energy (less than 100s of eV) as a result of inelastic scattering are emitted, as known that secondary electrons.

Furthermore, the incident electron with high energy (keV) that scattering in elastic through more than 90° as called backscattering electrons. X-ray is also created when core-shell electrons in the specimen are knocked loose, and valence electrons fall into the vacancies using the EDX detector to provide the elemental information. The angle and velocity of these secondary electrons relate to the surface structure of the specimen. A detector catches the secondary electrons and produces an electronic signal that reflects the surface microstructure morphology of the specimen. The signal

is amplified and transformed into a screen. FE-SEM provides great topological, chemical compositions that come from different detectors.

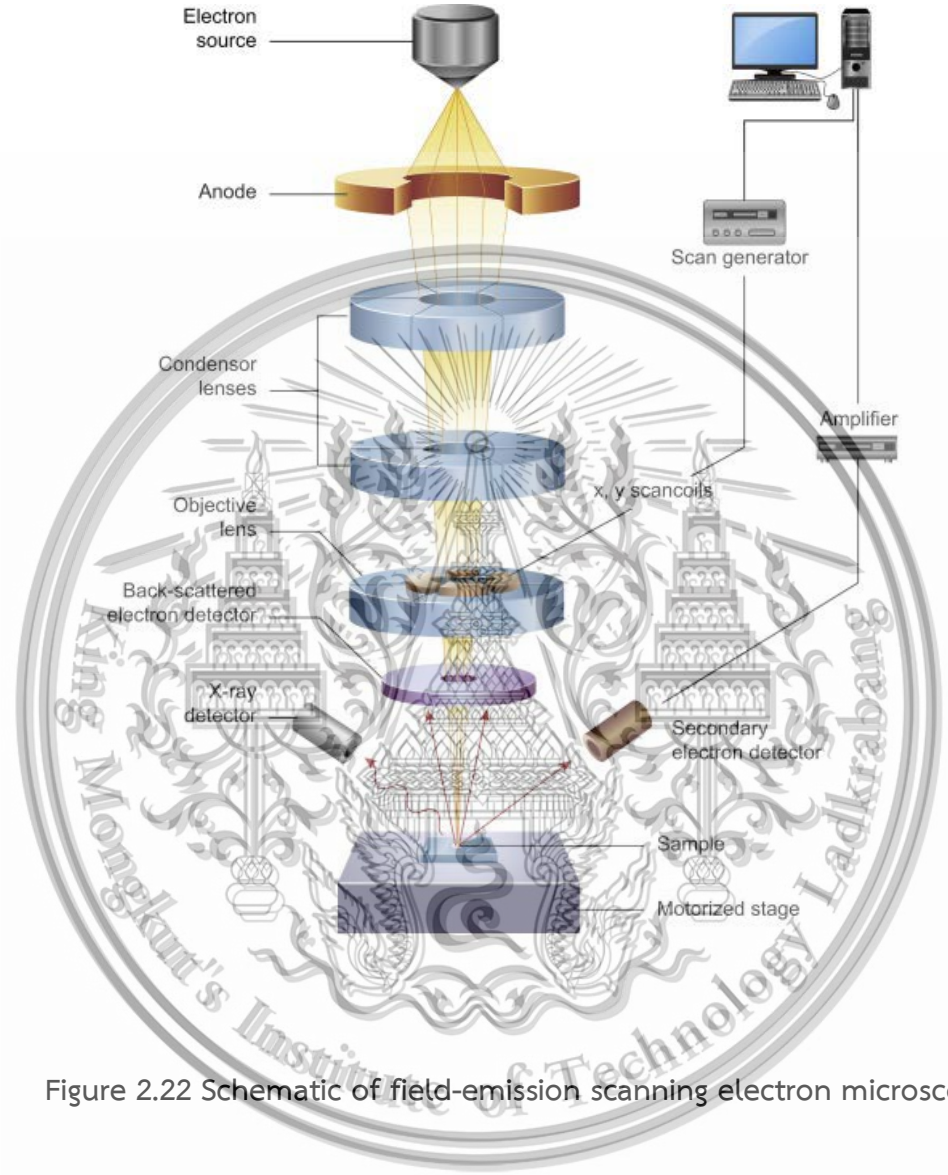

Figure 2.22 Schematic of field-emission scanning electron microscope.

Energy-dispersive X-ray spectroscopy (EDS) is an analytical function used for the elemental detector, the pulse processor and the analyzer. The X-ray detector is used to detect and convert electronic signals. Then, the pulse processor is used to measure the electronic signals for determining the energy of the X-ray detector. After that, the analyzer is used to display and identify the elemental composition.

Finally, the fatigue-cracked specimen surfaces, cross-sections and elemental composition of the specimen were obtained. [20, 40-42]

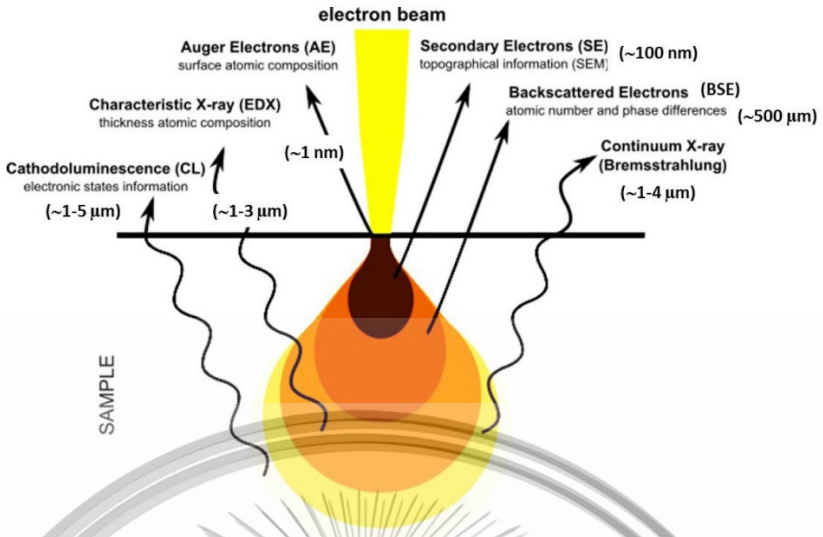

Figure 2.23 Signals generated at electron-specimen interactions

2.7.3 Hall effect measurement

The Hall effect measurement provides the electrical transport properties of conducting materials. For thermoelectric material, carrier types and electrical mobility can be determined by Hall effect measurement. The Hall effect is based on the Lorentz force acting on the charge carriers moving in a magnetic field. When electrical current (I) flows through a conductor material perpendicular to a magnetic field, the magnetic field (B) exerts a Lorentz force on a charge carrier moving, pushing them to one side of the conductor. The combination of the current and the applied magnetic field induces a voltage difference across a conductor, as known as the Hall voltage (V_H). The set up of the Hall effect measurement is shown in the Figure. 2.24. The Hall coefficient (R_H) is defined in equation (2.76).

$$R_H = \frac{E}{jB} \tag{2.76}$$

Where j is the current density of the carrier of electron and E is an electric field. Charge carriers in a magnetic field are subject to the Lorentz force, given by:

$$F = q(v \times B) \tag{2.77}$$

Where q is the charge of carrier and v is the drift velocity of the current. If electric force (qE) is equal to the Lorentz force, the electric field is given by:

$$E = v \times B \tag{2.78}$$

The drift velocity of the current or the velocity of the carriers is related to the current density, expressed as equation (2.79).

$$j = n_c q v \tag{2.79}$$

Where n_c is the charge carrier concentration. So, the electric field can be defined as:

$$E = \frac{jB}{qn_c} \tag{2.80}$$

From the Hall coefficient definition in equation (2.76), the carrier type and the carrier concentration is derived to be:

$$n_c = \frac{1}{R_H q} \tag{2.81}$$

If the Hall coefficient is positive, the carrier type is hole or *P*-type and the Hall coefficient is negative, the carrier type is electron or *N*-type. The carrier mobility (μ) is determined by the electrical resistivity (ρ) and hall coefficient, given by:

$$\mu = \frac{R_H}{\rho} \tag{2.82}$$

In general, a few simple instruments of Hall effect measurement are required a current source (100 mA-10 PA), a voltmeter, a current meter and a magnetic field. The Van der Pawn is the common geometry to determine the electrical resistivity using either a four-point probe. In this case, the film was placed on a square substrate. The

current is applied to two adjacent contacts and voltages are measured between the other two. Van der Pauw equation for material resistivity is given by [44]:

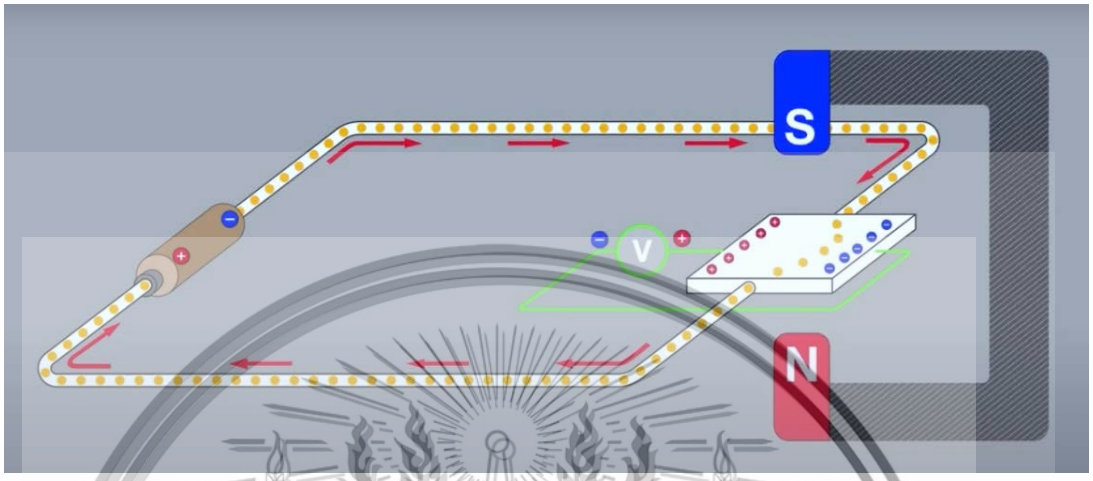

Figure 2.24 Hall effect measurement set up.

$$\rho = \frac{\pi}{\ln 2} ft \frac{\left(R_{1234} + R_{2341}\right)}{2} \tag{2.83}$$

To measure the Hall voltage, the contact configuration will be rearranged. the current source and the measured voltage are applied across opposite contacts. To obtain the precise result of the hall voltage, the recommended technique involves a combination of reversing source current polarity, sourcing on additional terminals, and reversing the direction of the magnetic field [18, 43].

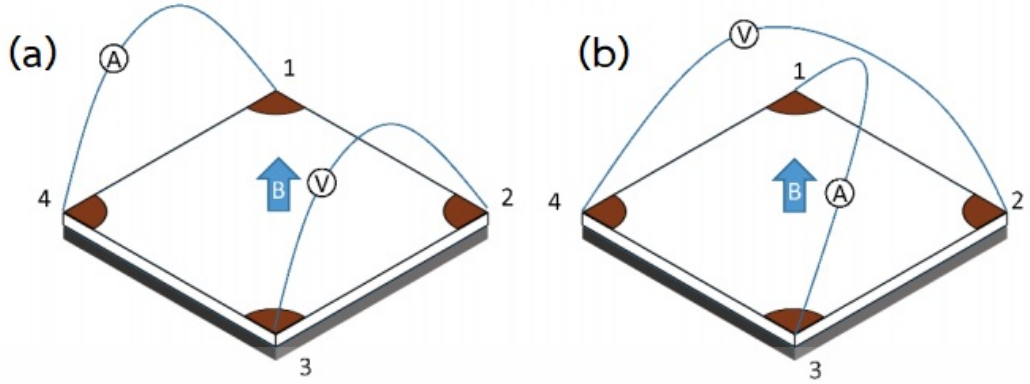

Figure 2.25 Schematic of Van der Pawn set up (a) for material resistivity and (b) for hall voltage measurements.

2.7.4 Seebeck Coefficient/Electrical Resistance Measurement System (ZEM-3)

Seebeck coefficient and electrical resistivity are standards for thermoelectric material measurement which are widely used with materials including metals, semiconductors and oxides. ZEM-3 measurement is to measure the voltage difference of the sample material under the temperature gradient. The schematic of ZEM-3 is shown in figure 2.26 [45]. The electrical arrangement is set the sample in a vertical position in the infrared heating furnace under low-pressure helium ambient. While the sample is heated, the temperature gradient (ΔT) across the sample was measured. Two thermocouples were pressed at the surface of the sample to measure the thermal electromotive force (dE).

Following the Seebeck equation, the Seebeck coefficient is obtained. Electrical resistance (R) is measure via the dc four-terminal method. The electrical current (I) was applied through the sample between current electrodes. The voltage (dV) drop when the current flows between the sample wires were measured. Ohm's law, the dimension of the sample is used the converted the resistance to resistivity (ρ) [20], as seen in equation (2.84).

$$R = \frac{\rho L}{A} \tag{2.84}$$

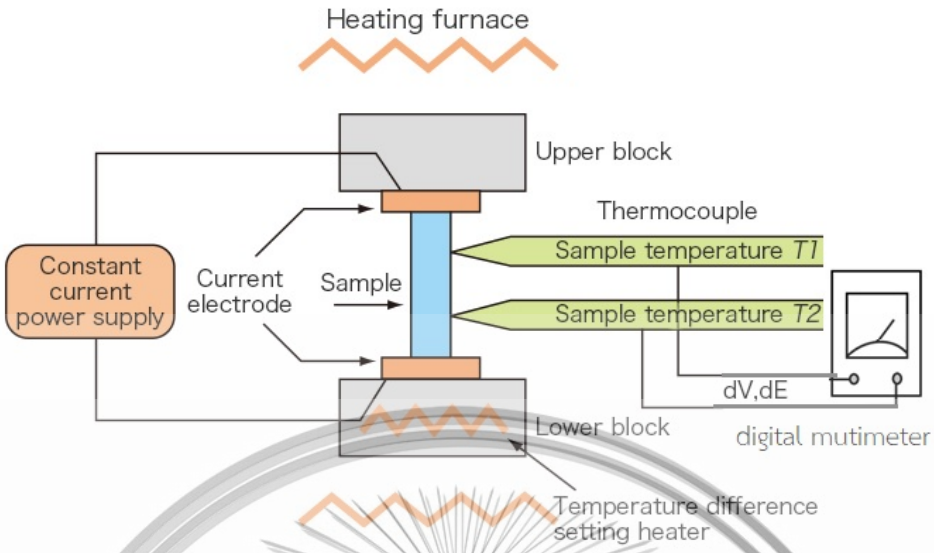

Figure 2.26 Schematic of Seebeck coefficient/electrical resistance measurement system.

2.8 Literature reviews

Previously, many researchers have been reported the influence of the sputtering parameters such as sputtering pressure, substrate temperature, pre-heat substrate, post-annealing treatment and sputtering power of thermoelectric materials using sputtering. It is affected by enhancing the thermoelectric properties of thermoelectric materials which leads to the increase of the output performance of the thermoelectric applications.

Shen *et al.* [12] reported that the enhancing thermoelectric properties of Sb_2Te_3 flexible thin-film through the adjustment of the sputtering pressure (1.0-4.0 Pa). The mechanism of influence of Ar pressure on crystalline, microstructure, grain of the Sb_2Te_3 thin-films have been presented. The growth rate and the binding energy are dependent on the deposition rate and the energy of the particles of the film. In the case of low Ar pressure, the kinetic energy of absorbed atoms on the surface is high lead to a high deposition rate which decreases the diffusion time of atoms on the substrate surface. It can be formed to porous film. On the other hand, when the sputtering pressure is raised, the energy of the particles arriving at the substrate

decrease because the backscattering rate increases lead to obtain the lower deposition rate and kinetic energy. The films will get enough time to diffuse and reach the lattice point to form a crystallized structure. As the result, this work develops a sputtering Ar pressure to improve the thermoelectric properties of Sb_2Te_3 thin films.

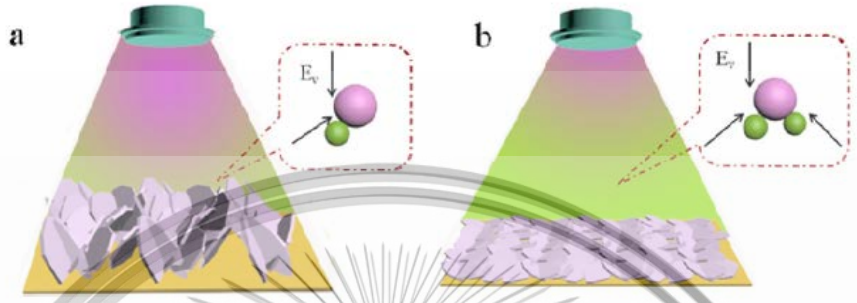

Figure 2.27 Mechanism of the Sb_2Te_3 thin-films deposited under (a) low Ar pressure and (b) high Ar pressure.

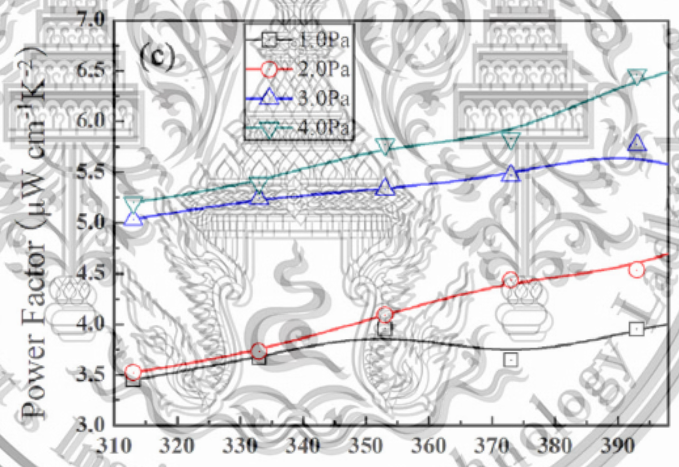

Figure 2.28 In-plane power factor of Sb_2Te_3 thin-film with various sputtering Ar pressure.

Chen *et al.* [13] studied the effects of substrate temperature on the thermoelectric properties of Sb_2Te_3 thin films by RF and DC Co-sputtering. During the sputtering process, the substrate temperature was varied from room temperature to

300ºC while keeping other parameters constant. As a result, Substrate temperature above 250ºC can enhance the crystalline quality and prefer *c*-axis orientation. Larger grain can be obtained due to a diffusion of atoms. Moreover, the substrate temperature can be adjusted the composition at near stoichiometric due to re-evaporation of volatile tellurium during the deposition process. All improvements lead to improve electrical transport and thermoelectric properties of the films. The optimized power factor of samples deposited at 250ºC was 3.26×10^{3} W/mK^{2} which is a high value compared with those obtained by the other techniques such as MBE, pulsed magnetron sputtering Co-sputtering anneal, close space vapor, co-evaporation and ion-beam sputtering.

Khumtong *et al.* [14] reported that the influence of pre-heat temperature on Te content of Sb_2Te_3 thin-films using RF magnetron sputtering. The result indicated that Te content increases near stoichiometric with increasing pre-heat temperature from 200-400ºC. It suggested that the Te atoms accumulation in plasma have occurred at the high substrate temperature. When the temperature is slightly decreased, the Te-enriched plasma redeposits on the substrate. Moreover, the pre-heat temperature can be improved the crystalline quality of the film, as seen in Figure 2.31 (B-C).

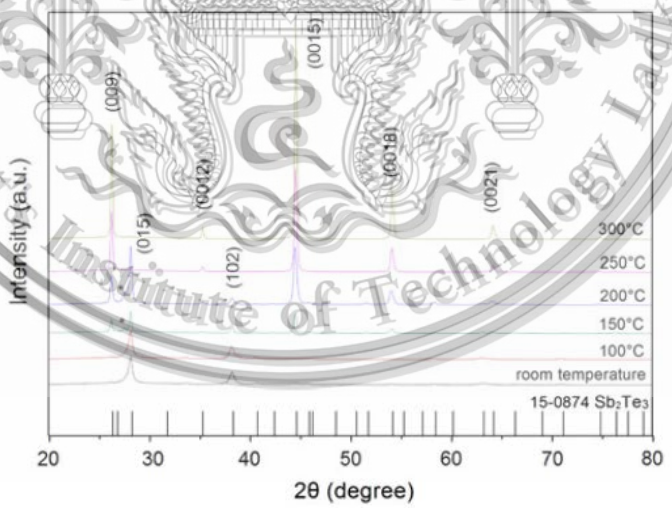

Figure 2.29 XRD patterns of Sb_2Te_3 thin-films with various substrate temperature.

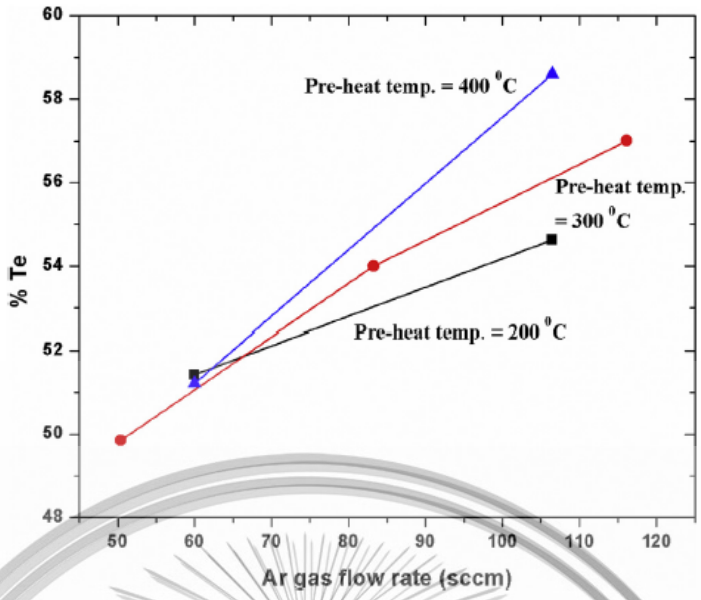

Figure 2.30 Effect of pre-heat temperature on Te content of Sb_2Te_3 thin-films.

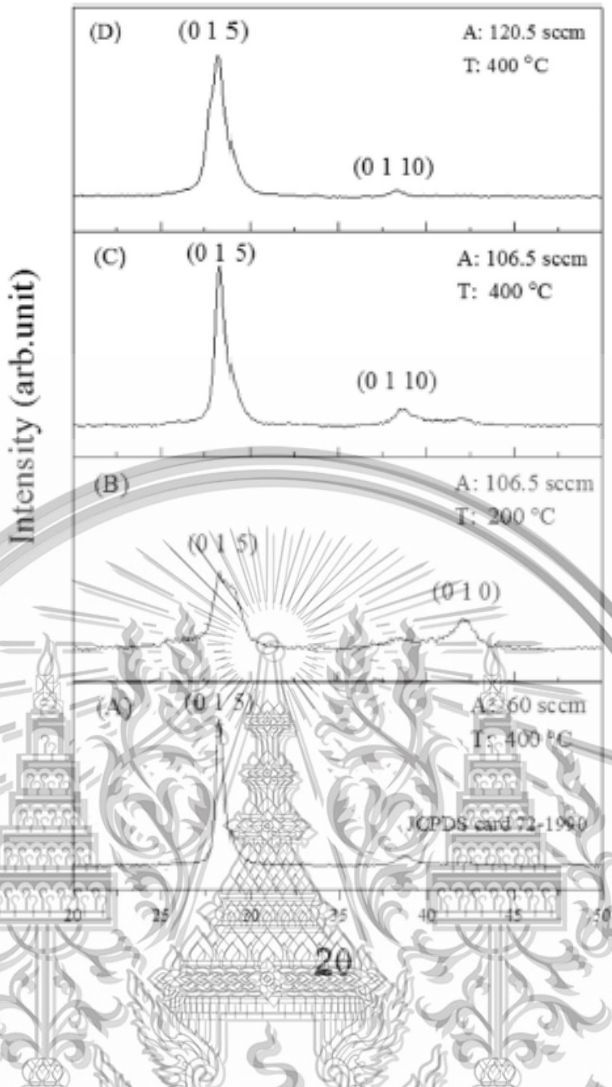

Figure 2.31 XRD patterns of Sb_2Te_3 thin-films prepared with different sputtering Ar gas flow rates and pre-heat temperatures.

Fang *et al.* [56] reported that the effects of annealing temperature on their thermoelectric properties of Sb_2Te_3 thin films prepared by RF magnetron sputtering. In this work, post-annealing temperature were performed at 373, 423, 473, 523 and 573 K for 6 h under N_2 atmosphere and as-deposited films were studied the effect of annealing time by annealed at 523 K for 3, 6, 9 and 12 h, respectively. It can be seen that the annealing temperature is significant to the crystalline quality of the films. In a deposited film, the atoms do not have enough energy to diffuse and agglomerate. After annealing, a hexagonal structure of Sb_2Te_3 was obtained. The peak intensity is intense as the annealing temperature increases to 573K. At above 573K, some phase separation of Sb and Te atoms are exhibited. Moreover, the Seebeck coefficient of the

annealed films increased while annealing temperature was further raised. It is related to the decreasing of carrier concentration due to the decrease in carrier concentration. The increase in electrical transportation may be due to the decrease of defects inside the films and the increase in mobility. In order to optimize the annealing time, an annealing treatment was performed with varying times at 523 K. The results indicated that the highest power factor of the films is obtained of 18.02 μW cm^{-1} K^{-1}, which is annealed at 523K for 6 h. In summary, the annealing treatment may effectively improve the thermoelectric properties of the Sb_2Te_3 thin films.

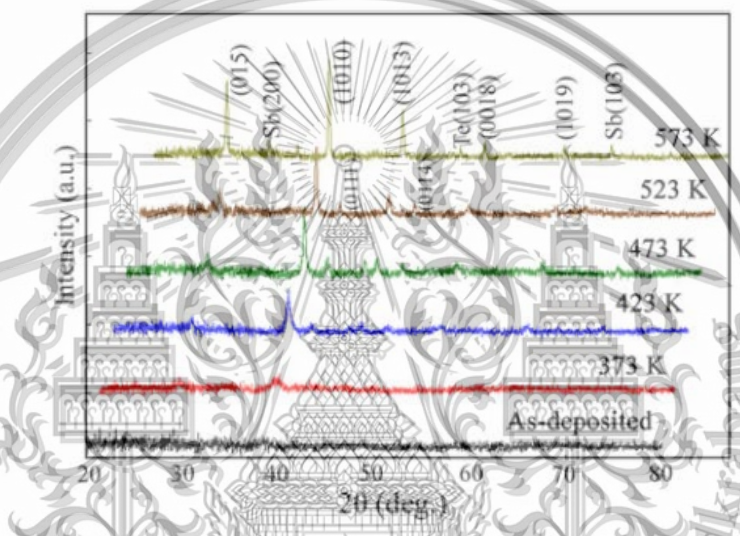

Figure 2.32 XRD patterns of Sb_2Te_3 thin-films annealed at different temperatures for 6 h.

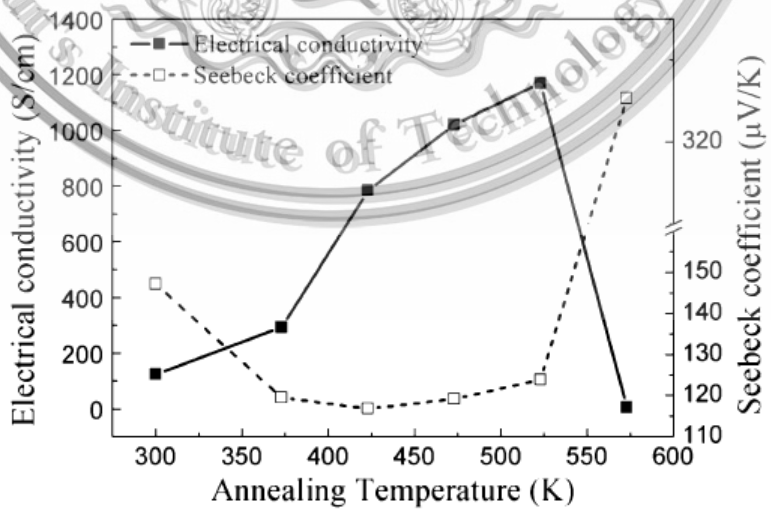

Figure 2.33 The electrical conductivity and the Seebeck coefficient of the Sb_2Te_3 thin-films as a function of annealing temperature

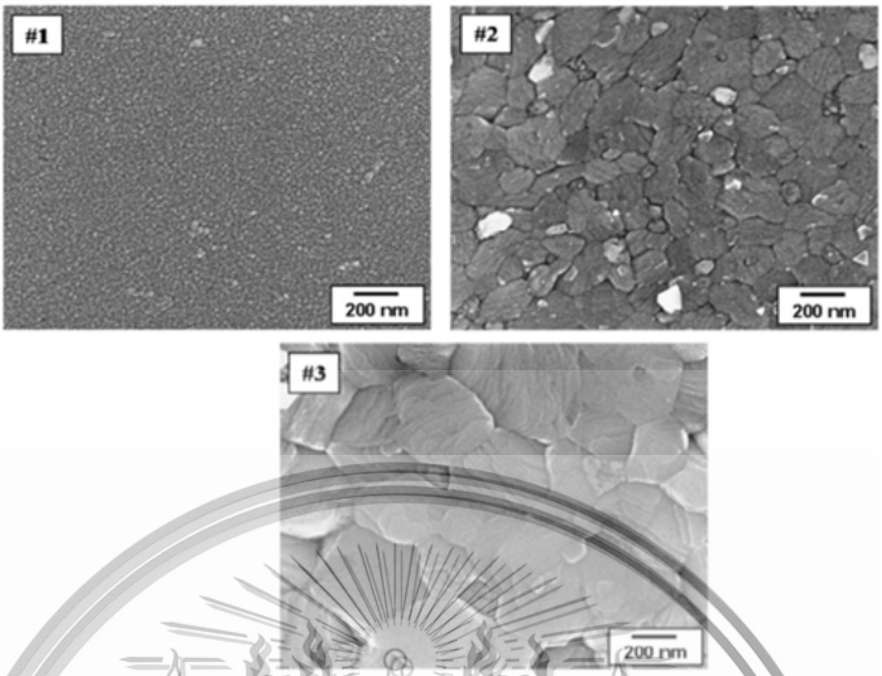

Figure 2.34 Surface morphology of the bismuth antimony telluride thin-films, annealed for (#1) 0 min, (#2) 30 min and (#3) 60 min.

Talashiri et al. [57] also reported the improved thermoelectric performance of bismuth antimony telluride thin-films by annealing treatment. Perfect orientation with c-axis normal to the substrate is achieved by increasing the annealing temperature. As increasing the annealing time, the grain size of the thin films grew further from 50 nm to a maximum of 300 nm, as seen in Figure. 2.34. These results lead to the electrical properties and the thermoelectric performance of the films was also enhanced by the annealing treatment.

In the case of the sputtering power, many researchers [15-16, 58] are reported that sputtering power is the important factor in the deposition process of DC magnetron sputtering, directly affecting film quality, crystalline structure, electrical properties and optical properties. It may be attributed that the sputtering power plays an important role in deposition films, which affect the plasma density and particles energy during deposition. The kinetic energy of the ejected atoms that arrive on the substrate. If atoms have enough kinetic energy, they can rearrange themselves in the growth process resulting in a crystalline film. However, there are few reports of the

sputtering power effect on the deposited Sb_2Te_3 films with a single compound target. This thesis is to optimization the suitable sputtering power density of the Sb_2Te_3 films on the chemical composition, structural and thermoelectric properties which leads to the increase of the energy efficiency of the wearable thermoelectric application.

After achieving the suitable sputtering power density of the films, the wearable thermoelectric applications are continuously studied [59-64]. For practical use, it was found that a temperature difference (ΔT) between both sides of the thermoelectric generator applications can diffuse the charge carriers lead to produces a high voltage potential. In Peltier applications, the heat was also taken with the charge carrier transport. The carriers move to the higher energy to absorb heat and release heat at the lower energy side. The charge carrier movement can be used to pump heat against the direction it naturally flows and produce cooling and heating. In these results, it was found that a temperature difference in the film is a significant factor in increasing the efficiency of the applications. On the other hand, it is challenging to produce a satisfactory temperature difference across the thin film. An attractive strategy is to induce a large temperature difference. A flexible thermoelectric thick-film could potentially induce a large temperature difference to enhance thermoelectric properties, as seen in table 2.2. There is an attractive approach because of their ability and suitability to power miniature electrical devices for thermoelectric applications.

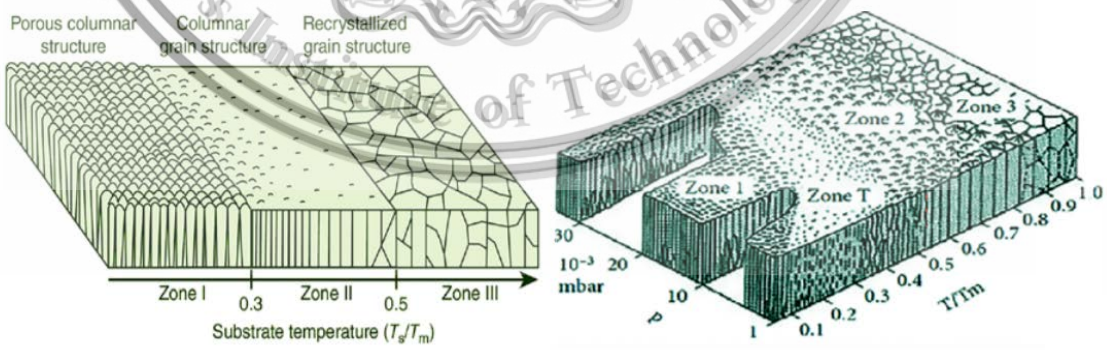

Figure 2.35 Structure zone model of thick-film.

Table 2.2 A review of the thermoelectric Sb_2Te_3 thick-films.

Researchers	Method	Processes	Thickness (μm)	Resistivity (Ω.m)	Power factor (mW/mK^2)
Shen *et al.*	300 nm thick SiO_2 layer, Co evaporation	Deposition temp. at 250°C Deposition time for 40-500 min	1, 6, 10, and 16	1 μm ; $16x10^{-6}$ 10 μm ; $20x10^{-6}$	1 μm ; 3.3
Shen *et al.*	Si/SiO_2 wafer substrate, Co evaporation Bi_2Te_3 films	Deposition temp at250°C Deposition time for 40-600 min	1, 4, 10, and 18	1 μm ; $10x10^{-6}$ 10 μm ; $25x10^{-6}$	1 μm ; 2.8 4 μm ; 2.6
Kim *et al.*	Al_2O_3 substrate, Screen printing (powder, binder, glass powder, solvent)	Paste and dried 100°C for 10 min Annealed 260°C for 10 min, 2 teps annealed at 430°C 20 for min and 500°C for 30 min (TE ambient)	-	-	1
Cao *et al.*	Polyimide, Screen printing (particle, binder, solvent)	Paste and pressing 250 MPa for 3 min Annealed 250°C 3 h	3.5	$5x10^{-3}$	0.212
Vigil-Galan *et al.*	Glass substrate, close space vapor	Keep thermal gradient 300-350°C	15.29	$3x10^{-5}$ (σ=323 S/cm)	0.377
Mizoshiri *et al.*	polyimide, Thermal assisted DC sputtering, alloy target	Ar plasma heating varying from 10-30 mA at 10 Pa	100 (1.6 μm/min)	$2x10^{-5}$ (σ=500 S/cm)	1.6

Table 2.3 Characteristics of structure zone model of thick-film.

Area	Temperature	microstructure
1st Zone	Low temp	- low diffusion, low mobility of the atoms - porous morphology and weakly binding grains
2nd Zone	$0.3 \leq T_s/T_m \leq 0.5$	- higher diffusion, a dense structure - The grain size increase
3rd Zone	$T_s/T_m > 0.5$	- the diffusion into the grains increase - a greater crystalline structure

However, by increasing the thickness of the Sb_2Te_3 material, the maximum amount of heat through the film at a given temperature. Rudez *et al*. [65] reported that the growth process of the thick layer is obtained from the weak contact for the surface layer resulting from a high porosity and consequently, higher resistivity of the thick-films maybe affect to the thermoelectric properties. Wasa *et.al*. [32] reported that the temperature treatments such as substrate temperature and post-annealing process are affected to improve these problems. The treatment process can yield a better connection between the grains. In the structure zone model, as increasing of the substrate temperature, diffusions and agglomeration of atoms are accelerated and hence better densification to achieve a low porosity. In this thesis, strongly carriers transport and thermoelectric properties were studied following annealing. Little effort appears to have been made on the effects of thermal treatment on the structural and electrical transport properties of sputtered Sb_2Te_3 thick films.

Now, the sputtering power density and thermal treatment conditions are optimized to improve the maximum thermoelectric properties of Sb_2Te_3 films. Then, 2D thermoelectric thin- and thick- films Sb_2Te_3 are interesting to compare the output performance on a single leg.

Chapter 3
Research methodology

This chapter is to explain the preparation and enhancement of thermoelectric properties of thin and thick Sb_2Te_3 film deposited on polyimide flexible substrate preparation by the DC magnetron sputtering technique. The preparation of thin- and thick-films was deposited under various sputtering parameters with optimized post-annealing conditions. The study of the output performance of a single leg *P*-type Sb_2Te_3 was achieved.

3.1 Preparation of *P*-type Sb_2Te_3 flexible thin-films via DC magnetron sputtering technique.

As is well known, *P*-type Sb_2Te_3 thermoelectric material has attracted potential applications in wearable thermoelectric devices. In general, the excellence ZT of Sb_2Te_3 is required for thermoelectric material. DC magnetron sputtering technique is commonly used to provide uniform high purity films with large areas with a single alloy target. The compositional, structural, grain growth, electrical and thermoelectric properties of the films were controlled by sputtering parameters (sputtering power, sputtering pressure, electrode distance, deposition time and deposition temperature). However, it has been little discussion on the effect of sputtering power density on flexible Sb_2Te_3 films. Typically, the sputtering power density is an important factor that affects the plasma density and particle energy during the deposition process. Thus, this section is to study the effect of power density (30-50W) on the physical, chemical, electrical and thermoelectric properties of the flexible Sb_2Te_3 thin-films using DC magnetron sputtering technique.

3.1.1 Materials and equipments

1. 25 μm polyimide film Kapton® Dupont
2. Alloy Sb_2Te_3 target (purity: 99.9%, Stanford Advanced Materials)
3. Microscope slide
4. Aluminum tape

5. Ultrasonic bath
6. Methanol and DI-water
7. Nitrogen gas 99.99%
8. Argon gas 99.99%
9. DC Power Supply
10. Diffusion pump
11. Rotary pump
12. Sputtering chamber
13. Mass flow
14. Water cooling system
15. Monitoring system
16. AC Power Supply
17. Halogen lamp
18. Thermocouple

3.1.2 Experimental procedures

Firstly, 25×75 mm of polyimide substrates was cut and attached to a microscope slide with aluminum tape and ultrasonically cleaned in methanol and then de-ionized water (each for 10 min) and then dried with the nitrogen gas flow. The alloy Sb_2Te_3 compound (purity: 99.9%, Stanford Advanced Materials) with a diameter of 3 inches was used as a sputtering single target. The substrate was placed into the sample holder inside the vacuum chamber. Before the deposition process, the electrode distance was set to 50 mm. Secondly, the vacuum chamber was maintained at based pressure below 2.7×10^{-5} mbar using a diffusion pump backed by a rotary vane pump. The rotary pump was used to achieve a medium vacuum (10^{-2} mbar) in the chamber, a higher vacuum (10^{-5} mbar) was obtained by the diffusion pump.

After that, the flow of argon gas was then introduced into the vacuum chamber and the sputtering pressure was controlled at 2.6×10^{-2} mbar by mass flow. Before the shutter was opened to expose the film, the sputtering power density was applied for 10 min to remove the contaminations and the oxide layer on the target surface. Consequently, the substrate pre-heat was applied at 400 °C for 15 min using the halogen lamp which was set under the substrate at the same vacuum chamber.

Thirdly, opens the target shutter. The various sputtering power densities of 30, 35, 40, 45 and 50 W, were applied for 6 min to start the deposition process. After finishing, switch off the vacuum pumps, open the vent valve and removes the sample out of the vacuum chamber. Finally, the flexible Sb_2Te_3 film was obtained

Table 3.1 Sputtering parameters for the preparation of *P*-type Sb_2Te_3 flexible thin-films.

Sputtering parameters	
Target	Alloy compound Sb_2Te_3 purity 99.9%
Electrode distance	40 mm
Substrate	Polyimide
Base pressure	$3.0x10^{-5}$ mbar
Sputtering pressure	$2.6x10^{-2}$ mbar
Pre-heat	400°C 20 min
Deposition time	6 min
Sputtering power	30, 35, 40, 45, 50 W

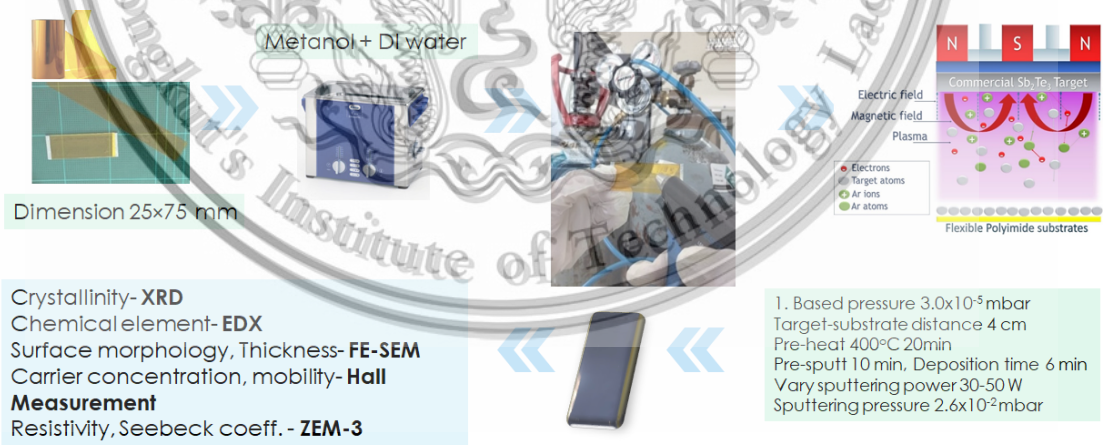

Figure 3.1 Experimental procedures for the preparation of *P*-type Sb_2Te_3 flexible thin-films via DC magnetron sputtering technique.

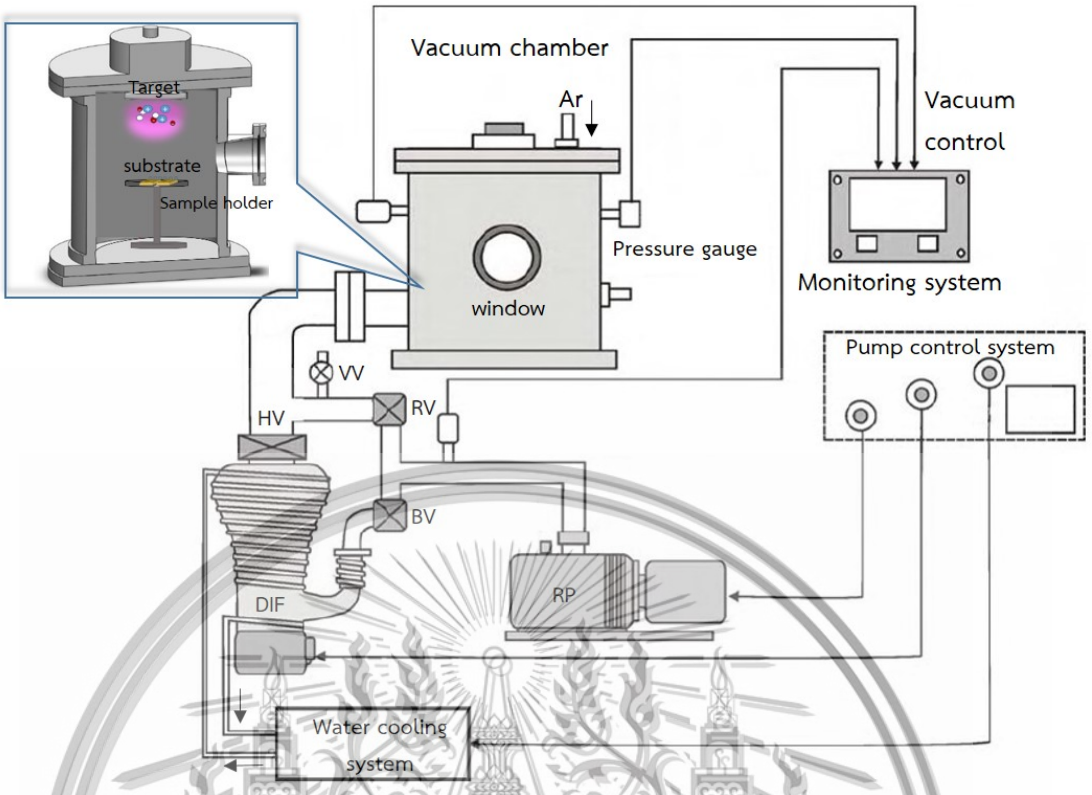

Figure 3.2 Schematic of DC magnetron system.

3.2 Development of thermoelectric properties of *P*-type Sb_2Te_3 flexible thick-films deposited via post-annealing treatment assisted DC magnetron sputtering

In this study, I concern about the flexible thermoelectric devices for practical use. In a typical, they are two kinds: bulk and thin-film. In bulk thermoelectric, a temperature difference (ΔT) between the hot and cold sides can be achieved and results in a relatively high electrical power [48]. The disadvantage of the bulk thermoelectric is that it is difficult to reduce the size of the electronics device. One important thing for wearable thermoelectric, the limitation flexibility design integrates into the human body waste heat. The cost of bulk material is also high because of the batch process requires for their manufacturing. Thin-films thermoelectric is safe cost comparing with bulk due to fewer amounts of the material.

Moreover, it is easy to integrate into compact electronic circuits and can be deposited on flexible heat sources [49]. However, it is difficult to produce a satisfactory temperature difference across the thin films [50]. An attractive strategy is to combine the advantages of bulk and thin-film thermoelectric devices. Flexible thermoelectric thick films could potentially solve this problem to induce a large temperature difference. There is an attractive approach because of their ability and suitability to power miniature electrical devices for wearable applications. Thus, in this section, Sb_2Te_3 thick films were directly deposited on flexible polyimide by heat treatment-assisted DC magnetron sputtering. The post-annealing conditions including annealing temperature and annealing time of thick-films were optimized to enhance the thermoelectric properties.

3.2.1 Materials and equipment

In this study, all equipment is the same for the preparation of *P*-type Sb_2Te_3 flexible thin films. The halogen lamp and thermocouple were added into the sputtering system inside the vacuum chamber under the sample holder, as seen in the figure. 3.3.

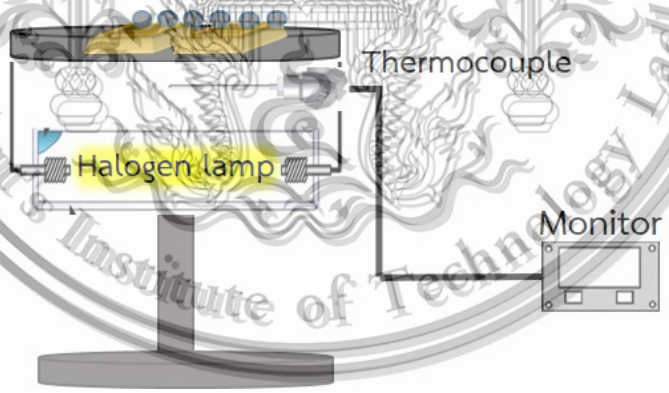

Figure 3.3 Set up of heat treatment system in a vacuum chamber.

Table 3.2 Sputtering parameters of the development of *P*-type Sb_2Te_3 flexible thick-films.

Sputtering parameter	
Target	Alloy Sb_2Te_3 purity 99.9%
Electrode distance	40 mm
Substrate	Polyimide
Base pressure	$3.0x10^{-5}$ mbar
Sputtering pressure	$2.6x10^{-2}$ mbar
Pre-heat	400 °C 15 min
Sputtering power	45 W
Deposition time	60 min
Post-annealing	0, 150, 250, 350 for 30min
Post-annealing time	0, 15, 30, 60 min

3.2.2 Experimental procedures

All experimental procedures of *P*-type Sb_2Te_3 flexible thick-film are the same as for the preparation of thin-film procedures. The difference is that the deposition time was increased to 60 min. In detail, the Sb_2Te_3 films were deposited for 10 min followed by heat treatment with a halogen lamp at 400 °C for 5 min under 2.6×10^{-2} mbar. This process was repeated 6 times to reach the designated film thickness. After finished the deposition process, the flexible Sb_2Te_3 thick-films were post-annealed using a heat treatment system under an argon atmosphere of approximately 2.6×10^{-2} mbar at temperatures of 0, 150, 250 and 350 °C for 30 min to improve the film quality. To investigate the optimized annealing conditions of the thick layer, the annealing time was also varied at 0, 15, 30 and 60 min, respectively.

3.3 Study the thickness effect on the thermoelectric properties of *P*-type Sb_2Te_3 flexible thin- and thick-films deposited by thermal treatment-assisted DC magnetron sputtering

To fabricate a thermoelectric device with high output power, it is important to pay attention to properties of thermoelectric material such as the Seebeck coefficient,

electrical conductivity and thermal conductivity. The thermal resistivity of the substrate is also important [51].

From the above study, it can be found that thick films are significant for practical use compared with thin films. However, the suitable thickness of flexible Sb_2Te_3 thick-films should be optimized before designing the thermoelectric device leads to improve the thermoelectric output performance. This condition is well suited for the fabrication of the wearable thermoelectric device.

3.3.1 Materials and equipment

In this study, all equipment, the sputtering power 45W, the post-annealing temperature and the post-annealing time are maintained like the development of *P*-type Sb_2Te_3 flexible thick-films. The thickness effect on thermoelectric properties was studied by varying the deposition time to obtain the designated film thickness.

3.3.2 Experimental procedures

Several flexible Sb_2Te_3 thin- and thick-films with varying thickness were deposited using thermal treatment-assisted DC magnetron sputtering. The deposition time of sputtering was performed for 2, 30, 60, 120 min, respectively. All samples are coated in the same conditions with the above study followed by post-annealing at 350°C for 30 min. The thickness effect on the thermoelectric properties of *P*-type Sb_2Te_3 flexible thin- and thick-films deposited by thermal treatment assisted DC magnetron sputtering. All deposition process to obtain the designated deposition time and the process were shown in figure 3.4.

Table 3.3 Sputtering parameters of the preparation of the thin- and thick-films *P*-type Sb_2Te_3 with varying film thickness on thermoelectric properties.

Sputtering parameter	
Target	Alloy Sb_2Te_3 purity 99.9%
Electrode distance	40 mm
Substrate	Polyimide
Base pressure	$3.0x10^{-5}$ mbar
Sputtering pressure	$2.6x10^{-2}$ mbar
Pre-heat	300°C 15 min
Sputtering power	45 W
Deposition time	2, 30, 60, 120 min
Post-annealing	350 for 30min

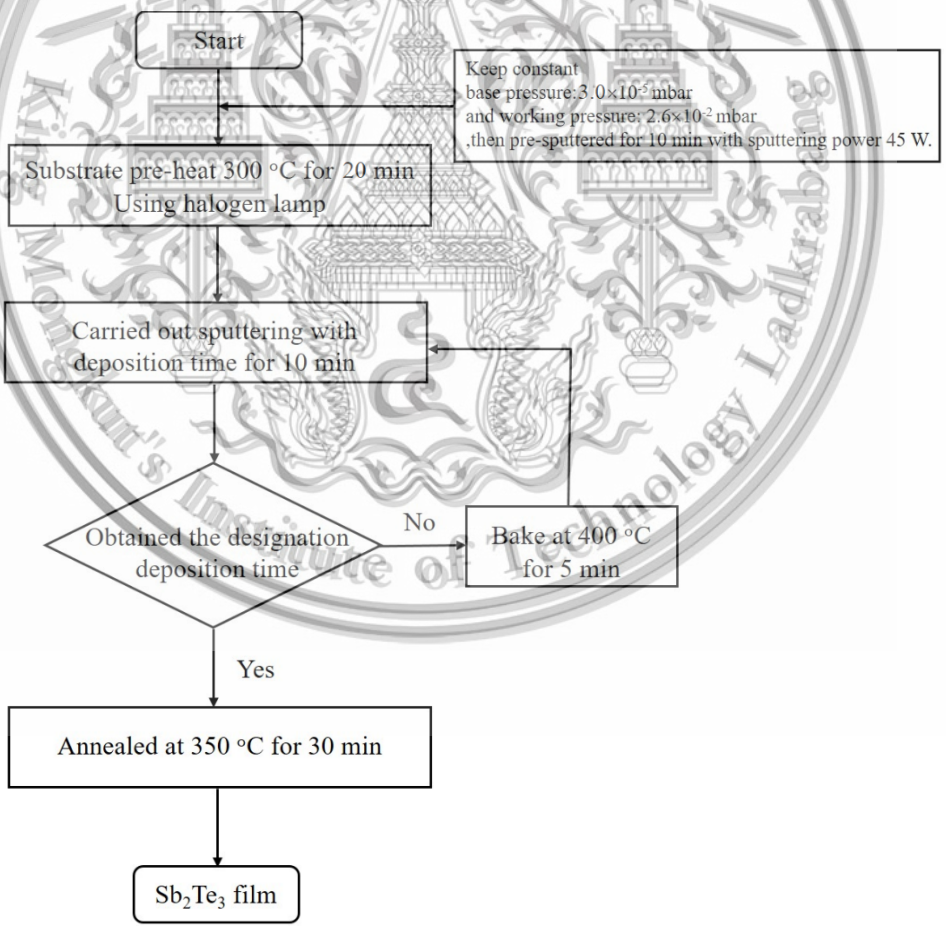

Figure 3.4 Schematic of deposition method.

3.4 The comparison of the output performance of a planar single leg *P*-type Sb_2Te_3 with different thickness

3.4.1 Materials and equipment

Silver paint, heating platform, digital multi-meter (Keithley 2100), and thermal infrared camera have been used for the comparison of the output performance of a planar single leg *P*-type Sb_2Te_3 with different thickness.

3.4.2 Experimental procedures

To obtain the output performance of the single Sb_2Te_3 leg as different film thickness. In the measurement, the deposited films were cut with 1.0 cm× 0.2 cm and tested by placing on the heating platform and the other sides were placed on the cold state to determine the temperature different within the single leg thermoelectric. The heat travels through the thermoelectric leg between the hot and cold junction and the carriers also transport. As the device reached a steady-state, the short circuit current and open circuit voltage measurements were taken by digital multimeter. At the same time, the temperature difference between both sides of single planar was measured by a thermal infrared camera. The schematic set up can be seen in figure 3.5. The thermoelectric output power was then calculated based on the measured voltage and current at different temperatures.

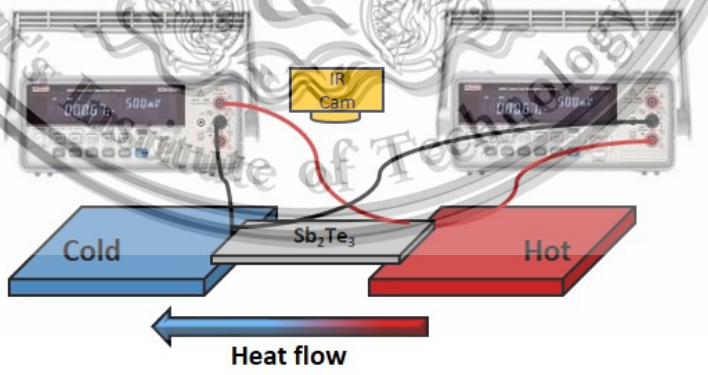

Figure 3.5 Schematic of the measurement of the output performance.

3.5 Characterizations

3.5.1 X-ray Diffraction

The crystal structure, including crystal orientation, crystallite size and strain were characterized by X-ray diffraction using a Rigaku diffractometer (Smartlab), as seen in figure 3.5, operated at 40 kV and 20 mA using Cu-K_α radiation. XRD patterns were recorded in the 2θ range of 10-70° with a scanning rate of 10°/min.

The XRD system consists of three main parts including the main instrument, computer and cooling system. The measured samples are firstly optics set as slits controlled by the SmartLab Studio II software at a computer. After that, the samples were prepared with a dimension of 1x1 cm and attached to the center of the sample holder. Places the sample holder into the main instrument and scans. By the sample scanning, qualitative analysis can be done automatically during X-ray diffraction measurement. The XRD patterns were obtained.

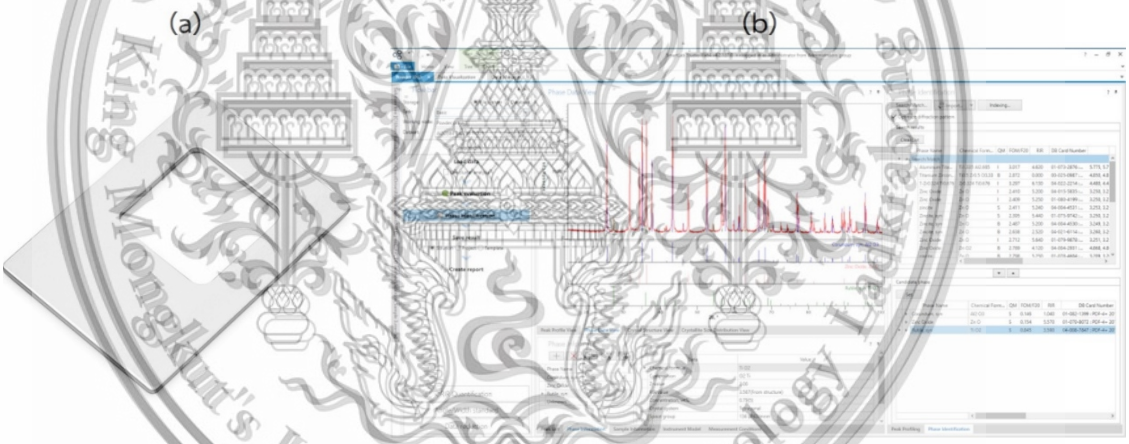

Figure 3.6 (a) Sample holder and (b) SmartLab Studio II software.

Figure 3.7 X-ray diffractometer (Rigaku, Smartlab)

3.5.2 Field-emission scanning electron microscopy

The surface morphology and cross-section of the sample material were observed by field-emission scanning electron microscopy (FE-SEM, JSM-7001F) operated at 10 kV. FE-SEM is the electron microscope at high resolution that uses an electron to illuminate the sample operated at a high vacuum. The samples were cut into small pieces and attached to the holder using carbon tape. The sample holder was placed inside the vacuum chamber and pump out the gas. The samples were moved under the electron column and turn on the electron beam to measure the surface morphology of the samples.

The elemental composition was examined by energy-dispersive X-ray spectroscopy (EDX, Oxford Instruments X-Max 20) over a large film area typically three times to obtain the average data. Additionally, EDX is qualitative and quantitative mapping and line scan element analysis.

Figure 3.8 Field-emission scanning electron microscope (JSM-7001F).

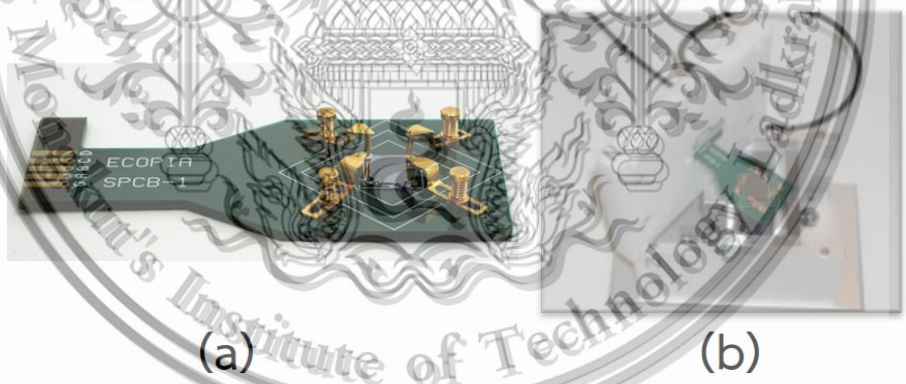

Figure 3.9 (a) Hall measurement stage and (b) sample mounting parts.

3.5.3 Hall effect measurement

The electrical properties and carrier concentration were obtained by a Hall effect measurement system at room temperature (Ecopia, HMS-3000) using Van der Pauw configuration. Before Hall measurement, the samples were prepared in a dimension of 1x1 cm and attached to the microscope slide. Starting with turning on

the Hall system software (HMS-3000) and Swith on the hall system. Places the sample onto the Hall measurement stage and adjust the four probe contacts. Put the Hall measurement stage in the sample mounting parts. Then, input the sample name, IV parameters, and record info for the IV curve and save the graph, respectively. Starting Hall measurement with a magnetic field of 0.55 Tesla, the software was run and automatically calculated the carrier concentration, the electrical mobility and electrical resistivity of the sample.

Figure 3.10 Hall effect measurement system (Ecopia, HMS-3000).

3.5.4 Seebeck Coefficient/Electrical Resistance Measurement System

The temperature-dependent Seebeck coefficient and electrical conductivity were measured using a ZEM-3 apparatus (ULVAC-RIKO) at 50-300 °C. The ZEM-3 system consists of a computer, the main body of the instrument which contains the power distribution safety, interlock, temperature controller, the power supply and digital multimeter, infrared furnace, vacuum pump and quartz chamber. The sample was cut with a dimension of 3×12 mm. Firstly, sliding off the quartz chamber to the left-hand side of the instrument to mount the sample. Taking the thermocouple out of the

nickel cover which is clamped between upper and lower blocks. Before mounting the sample, the width and depth were measured. After that, opening the clamping block, the sample can be mounted and then closing the clamping block. The thermocouple probes are fixed onto the surface of the sample and then the chamber can be closed and pumped. Turn to the measurement software on the computer, input the sample parameters such as sample name, width, depth, probe distance and temperature. Starting the Zem-3 measurement, the measurement system run completes automatically under the helium atmosphere. Finally, analyze the thermoelectric data.

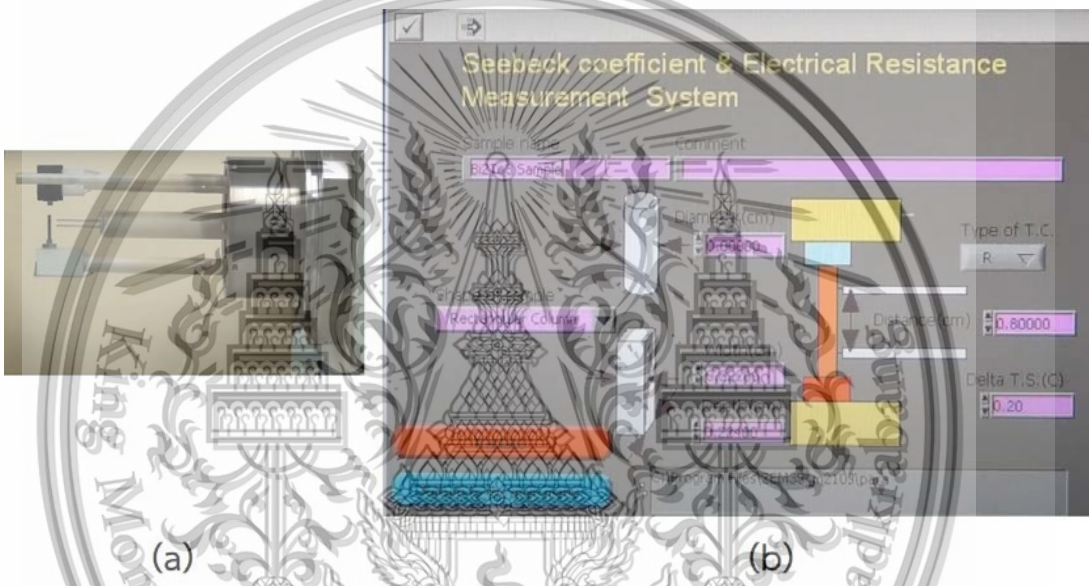

Figure 3.11 (a) Sample clamping block and (b) Seebeck coefficient and electrical resistance measurement system software (V3.5 for SDC35).

Figure 3.12 Seebeck coefficient/electrical resistance measurement system (Ulvac RIKO)

Chapter 4
Results and discussion

4.1 Study the influence of sputtering power on thermoelectric properties of *P*-type Sb_2Te_3 flexible thin-film deposited by DC magnetron sputtering

The formations of *P*-type Sb_2Te_3 thin-films deposited on polyimide substrates with various sputtering power were prepared by DC magnetron sputtering. Interestingly, the sputtering power parameter is important in the magnetron sputtering technique. The effect of the sputtering power associated with the plasma density and particles energy during film formation [66] are investigated.

The x-ray diffraction patterns of the Sb_2Te_3 thin films deposited at various sputtering power, as seen in figure 4.1. After depositing, all films show a polycrystalline structure, belonging to the space group of Sb_2Te_3 (JCPDS No. 15-0874). The four main diffraction peaks at 17.44°, 28.24°, 38.28° and 44.59° corresponded to the (006), (015), (1010) and (1015) planes, respectively. The sharpness intensity of (015) peak increases with increased sputtering power, indicating that the increase of sputtering power is well-defined crystallization of the formation of Sb_2Te_3 films. As the sputtering power is increased, the argon ions become more energetic and could release more energy to the sputtering target [67], led to the higher kinetic energy of the deposited atoms. During ions bombardment, their kinetic energy was dissipated and converted to the vibration of the ions. When the atoms accumulated sufficient vibration energy, they ejected from the target surface, rearranged the crystal structure and increasing surface migration on the surface of the substrate [15,69].

However, when increases the sputtering power up to 50 W, the intensity of (015) peak dropped and the crystallinity dropped further [16,70]. Variation of the power can be correlated with the accumulation of surface and strain energy during the coating process [72]. As the power was increased, a preferred orientation along (015) shifted slightly toward a lower angle. The peak shifting was related to the change in the lattice size, as seen in the figure 4.3. The lattice parameters of the *a*-axis are little changed, while those of the *c*-axis are increased with increasing power. The increase of lattice parameters was described by the antisite defect. Because Sb atom has a larger atomic radius than Te (Sb 1.60 and Te 1.56 Å). When the Sb atoms will enter Te vacancies, lattice parameter is altered, leading to crystal imperfection. [72] The XRD peaks shifted corresponding to Te gradually decrease as the power density increases as seen the elemental composition.

Table 4.1 Electrical and thermoelectric properties of Sb_2Te_3 at different sputtering power at room temperature.

Sputtering power (Watts)	Te content (% at)	Carrier concentration: n ($\times 10^{19}$ cm^{-3})	Carrier mobility: μ (cm^2/Vs)	Electrical conductivity: σ ($\times 10^4$ S/m)	Seebeck Coefficient :S (μ V/K)	Power factor :PF (mW/K^2m)
30	62.3	3.2	50.4	2.57	173	0.77
35	60.0	4.3	47.6	3.28	185	1.12
40	58.7	4.8	54.7	4.18	167	1.16
45	58.6	4.4	61.9	4.32	168	1.22
50	58.5	2.3	36.7	1.35	182	0.43

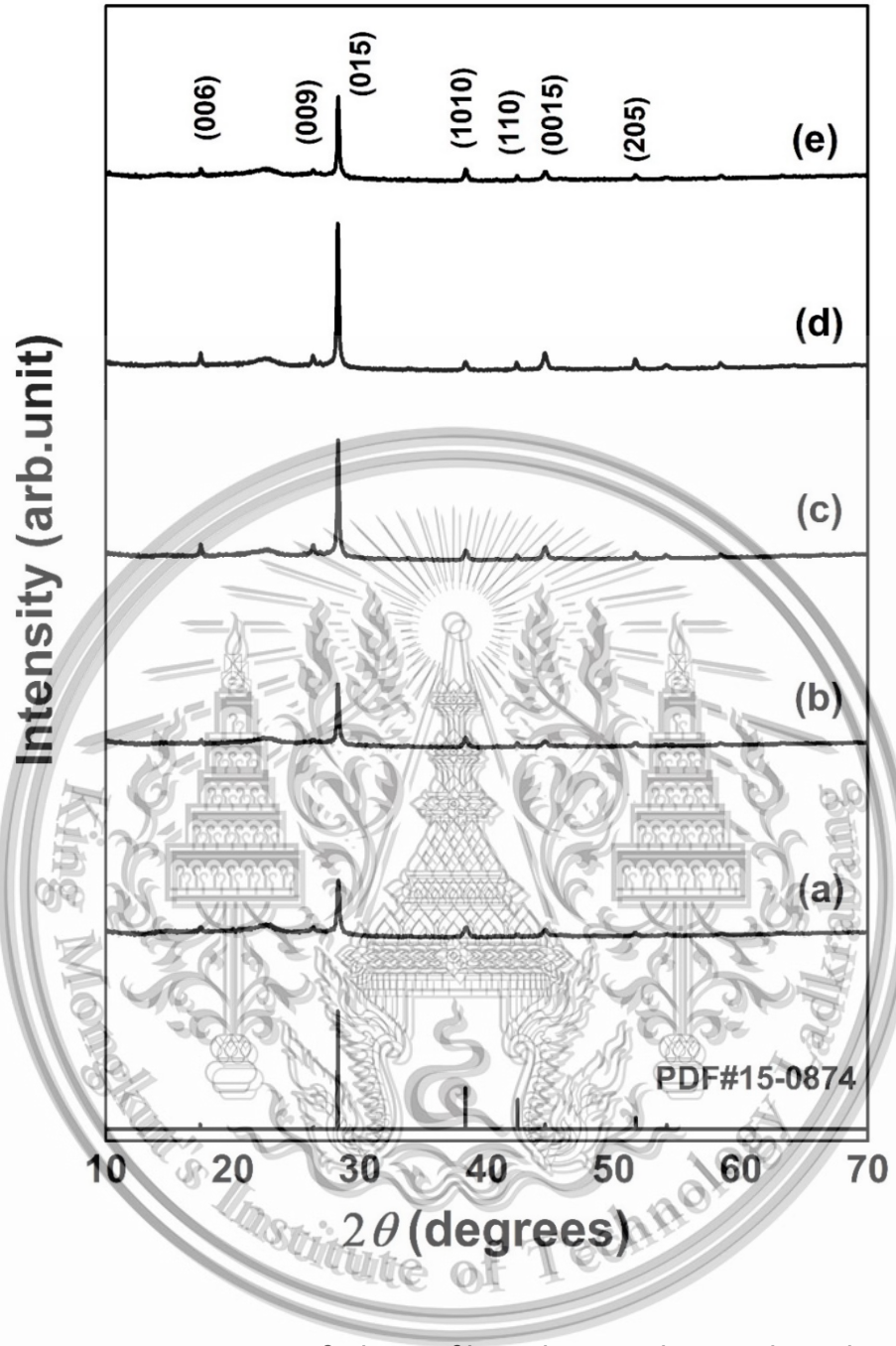

Figure 4.1 XRD patterns of Sb_2Te_3 films deposited on polyimide substrate at different sputtering power (a) 30 (b) 35 (c) 40 (d) 45 and (e) 50 W.

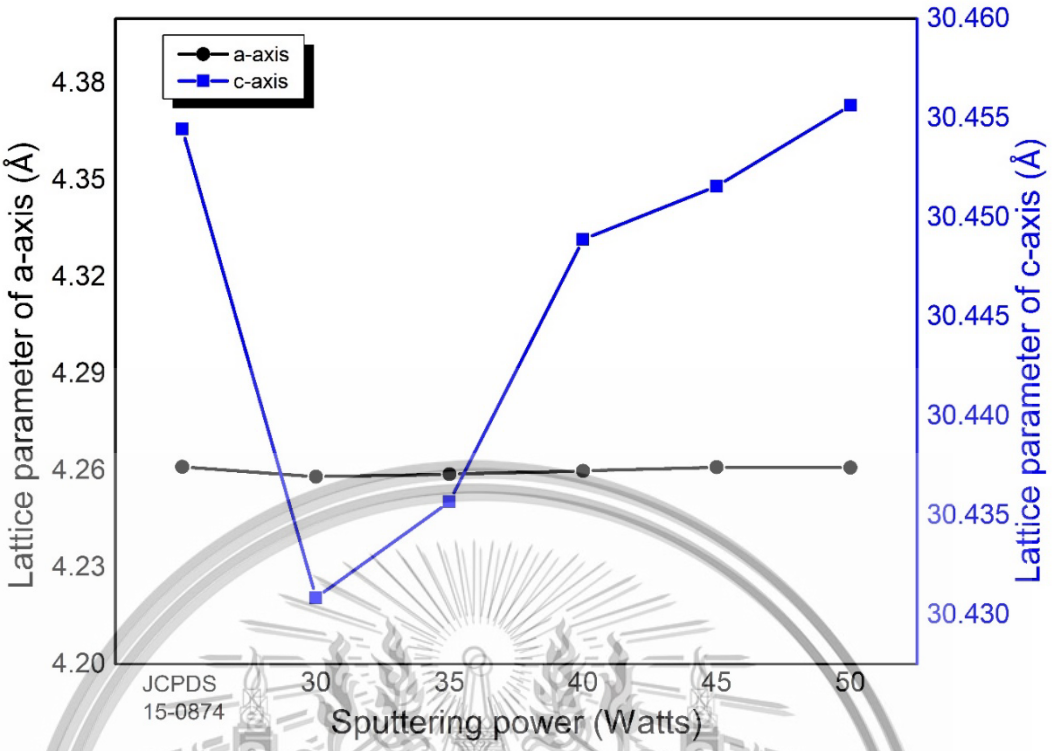

Figure 4.2 Lattice parameter of Sb_2Te_3 films at different sputtering power.

The elemental composition of Te are shown in table 4.1. When the power was increased, the Te vacancy defects in the Sb_2Te_3 films increased. The deviation of Te composition of the films produces holes, which increase the carrier concentration. The surface morphology and atomic concentration of Te in Sb_2Te_3 films deposited at different sputtering power were investigated by SEM and EDS, and the results are shown in figure 4.3. All deposited films exhibited a homogeneous grain distribution which are almost free of cracks. Larger grains formed as the power increased due to coalescence of small grains and diffusion of sputter atoms. The elemental composition of Sb_2Te_3 deposited films was considered to be the stoichiometric relationship of the power. The results indicated that Te content decreased with increasing the power. The stoichiometric film was obtained at a sputtering power of 35 W.

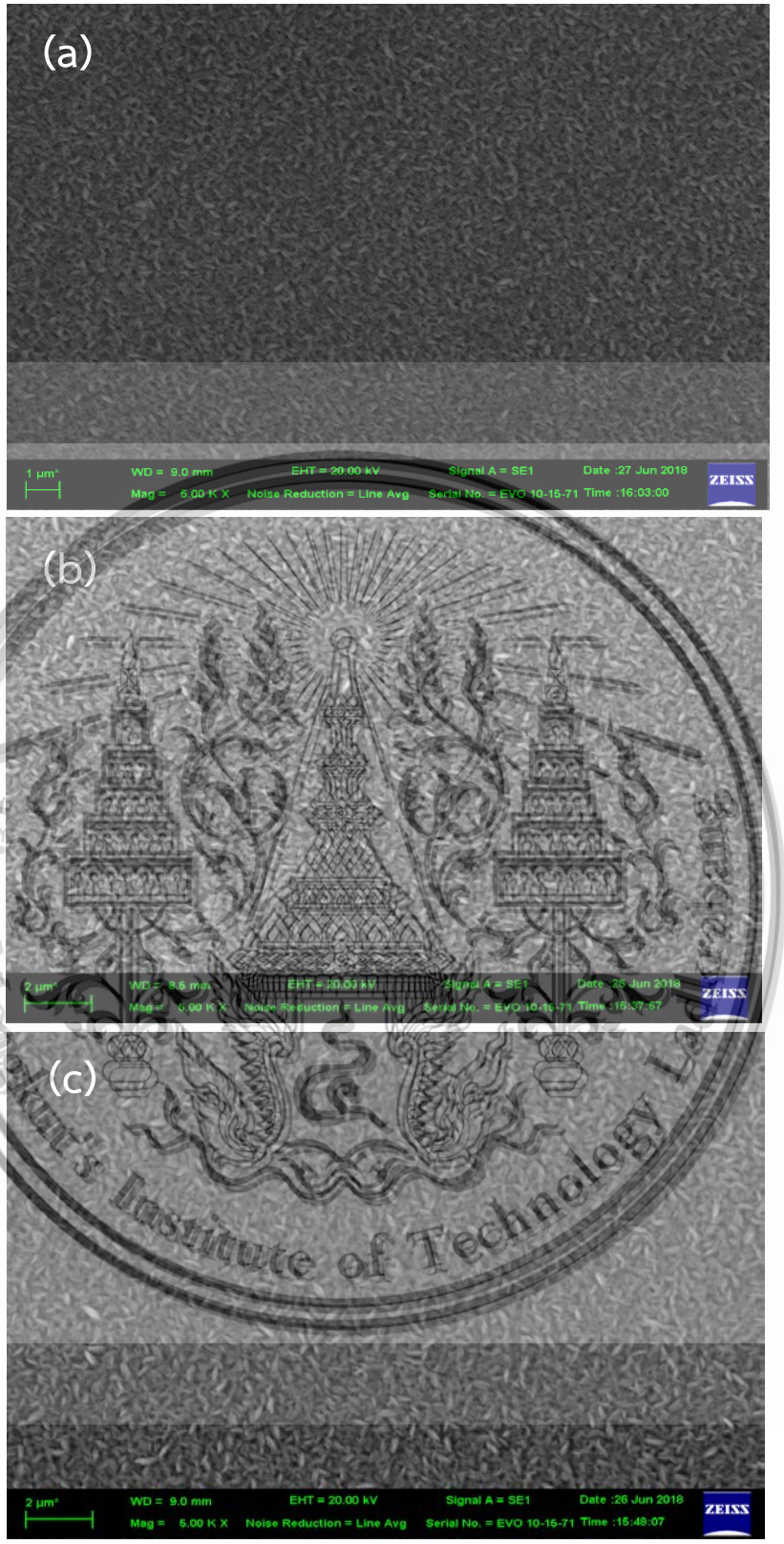

Figure 4.3 Surface morphology of Sb_2Te_3 films at different sputtering power (a) 30 W (b) 35 W (c) 40 W (d) 45 W and (e) 50 W.

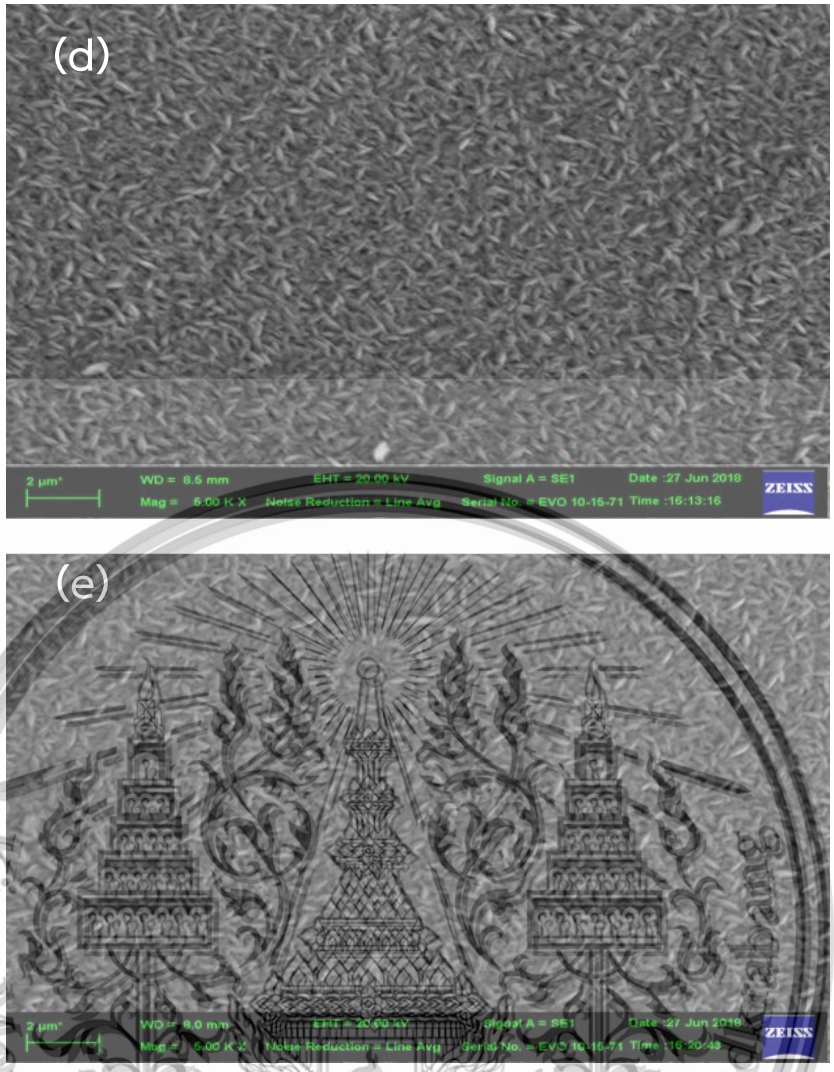

Figure 4.3 Surface morphology of Sb_2Te_3 films at different sputtering power (a) 30 W (b) 35 W (c) 40 W **(d)** 45 W **and (e)** 50 W.

The composition is very important for the electrical property. Te-rich film was observed for low sputtering power (30 W). Excess Te content affects the low conductivity [1]. As the power was increased to 50 W, the deposited films became significantly Te deficient leading to increases the degree of non-stoichiometric. This result indicated that the thermal transport in thin film increased and affected Te evaporation from the surface of the film at high sputtering power due to the differential vapor pressure, Te compared with Sb [16,74].

The film thicknesses were measured by SEM on cross-section. The deposited films have thicknesses between 600 nm and 1000 nm depending on the sputtering power density [66,75]. The deposition rate and thickness of the Sb_2Te_3 films show almost a linear relationship with the sputtering power in the power range from 30-50 W as seen in Figure 4.4. The deposition rate increased with the sputtering power could be associated with increased flux of sputter atoms. An increase in the sputtering power enhances the probability of ejection of atoms from the compound target. It was concluded that the sputtering power was a major factor affecting the sputtering yield of a target, which, in turn, affected the film thickness.

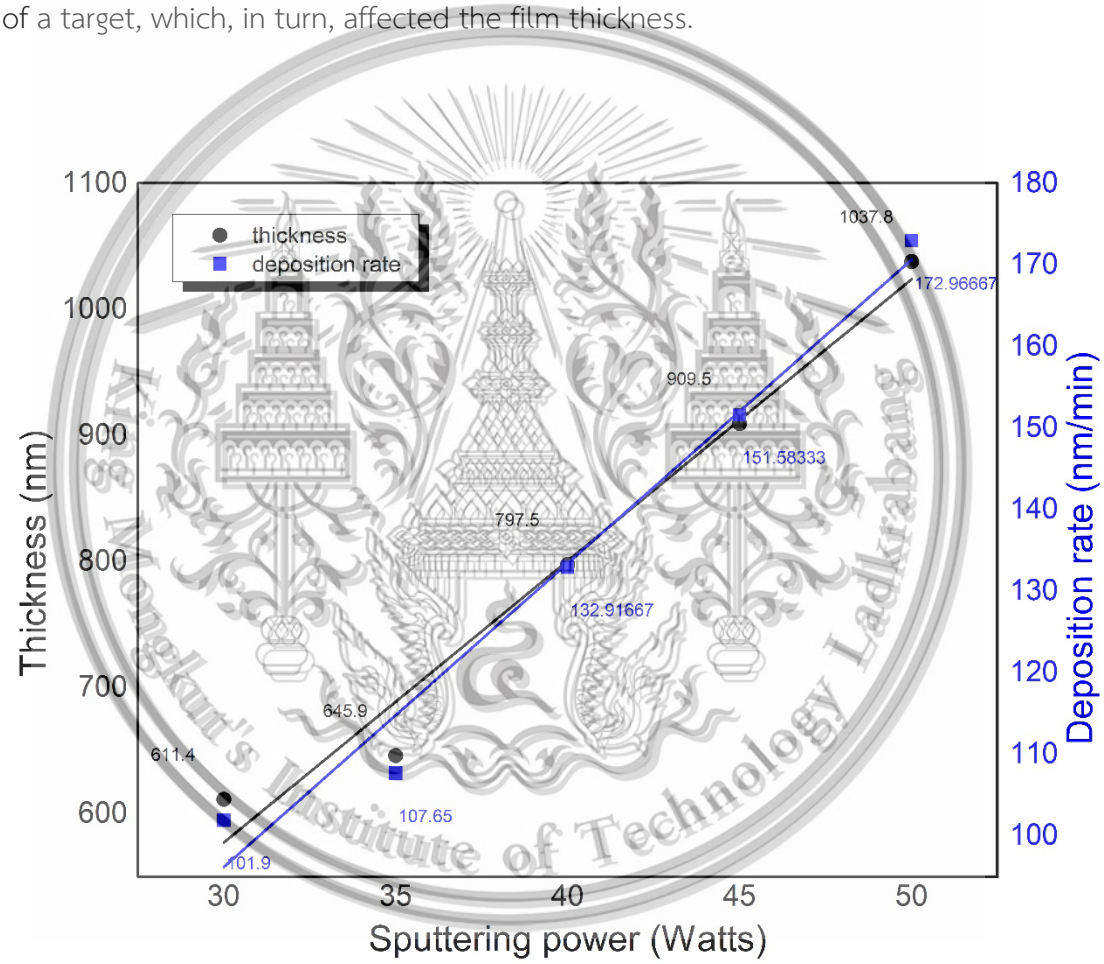

Figure 4.4 Thickness and deposition rate of Sb_2Te_3 films at different sputtering power.

Electrical properties at room temperature of Sb_2Te_3 films are summarized in Table 1. All deposited Sb_2Te_3 films present as *P*-type semiconductors due to the

positive mobility. The carrier concentration (n) increased with increasing sputtering power up to 45 W. Then, it decreased slightly as the sputtering power was increased to 50 W. Typically, the carrier concentration is sensitive to chemical composition and lattice defects: excess Te content led to higher resistivity [74]. Secondly, the Te deficiency led to weak Van der Walls bonding between Te(1) - Te(1) layers - Sb_2Te_3 structure. Te vacancies ($V_{Te}^{\bullet\bullet}$) were produced by increasing sputtering power, which vaporized Te contents. The antisite defects are occupied by Sb atoms. Sb atoms will enter Te vacancies due to the small difference in electronegativity. The antisite defects (Sb'_{Te}) were produced and led to the formation of V'''_{Sb}. The interaction of antisite defects and vacancies is shown by equation 4.1 [76].

$$Sb_2Te_3 = 2Sb'_{Te} + V^{\cdot\cdot}_{Te} + 2V'''_{Sb} + \frac{3}{2}Te_{(g)} \uparrow + 2h^{\cdot} \qquad (4.1)$$

where $h^{\bullet}$ denotes the produced hole and $\uparrow$ denotes the vaporized Te contents in Sb_2Te_3 films. The deviation from stoichiometry of the films produces holes which increase the carrier concentration. The electrical conductivity (σ) of the deposited films increased with sputtering power up to 45 W. Up to this point, the sputtering power affected film crystallinity. The films were more uniform crystallinity with less defects which led to enhanced electrical conductivity. As the sputtering power reached 50 W, the resistivity noticeably increased due to the reduction of carrier concentration and excessive crystallization. The electrical resistivity (ρ) dramatically increased and reaching a maximum of $7.40\times10^{-5}\ \Omega m$. The resistivity is determined by carrier concentration and carrier mobility following, $\rho = 1/\mu qn$. The electrical conductivity increased considerably with increasing the sputtering power. The highest electrical conductivity of 4.32×10^{4} S/cm was obtained with sputtering power 45 W. The change of electrical conductivity with increasing the sputtering power expected to increase the crystallinity, increase the deposition rate and increase the grain size as evidenced from XRD and SEM images [77-78]. A large electrical conductivity of the thermoelectric material is required in thermoelectric efficiency. However, as sputtering power was increased to 50 W, the reduced crystallinity and increased defect concentration caused a decrease of conductivity. The carrier mobility (μ) of the deposited films was increased according to the larger grain growth with increasing sputtering power.

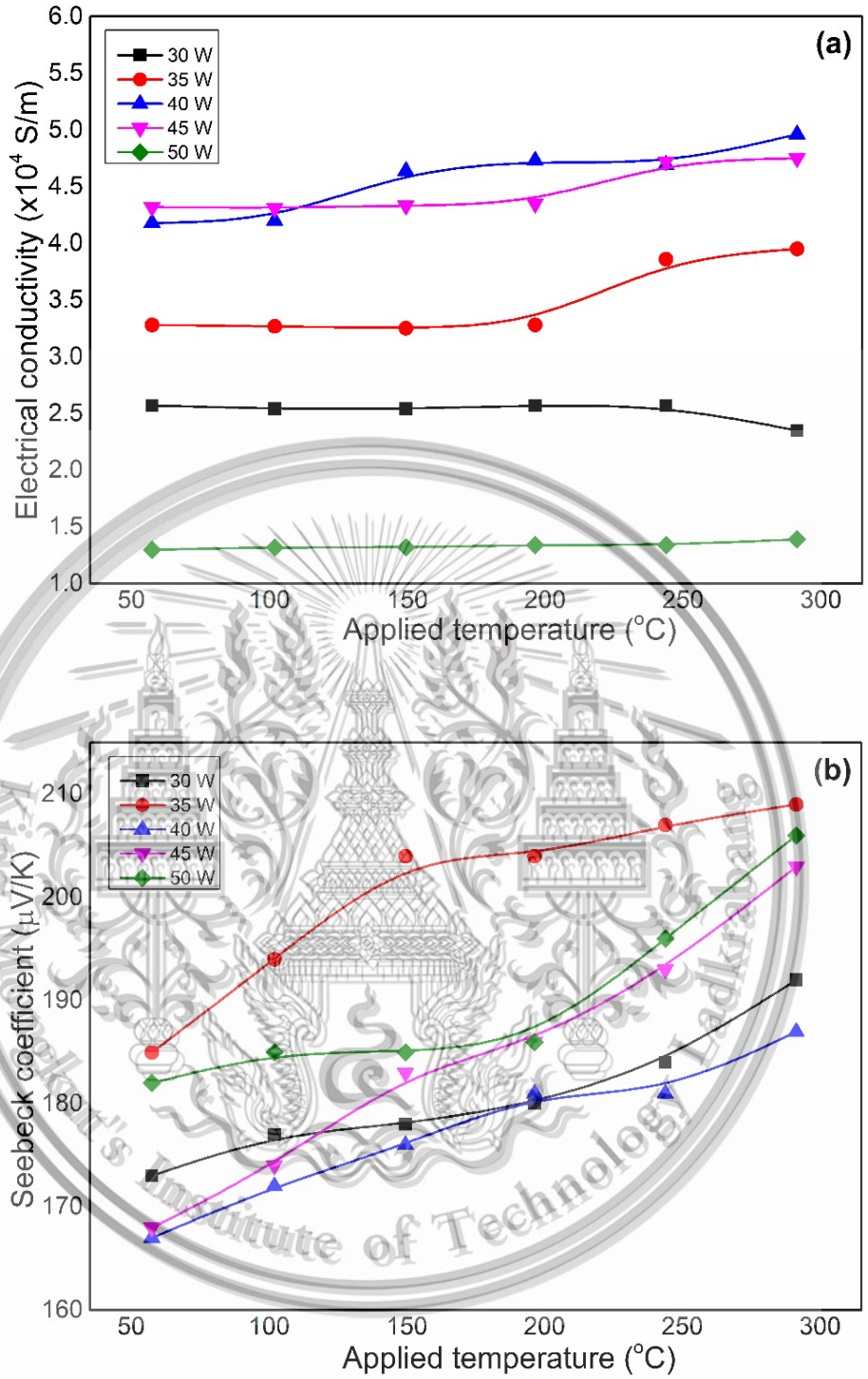

Figure 4.5 Temperature dependence of (a) Electrical conductivity (b) Seebeck coefficient and (c) power factor of the deposited Sb_2Te_3 films at different sputtering power as a function of applied temperature.

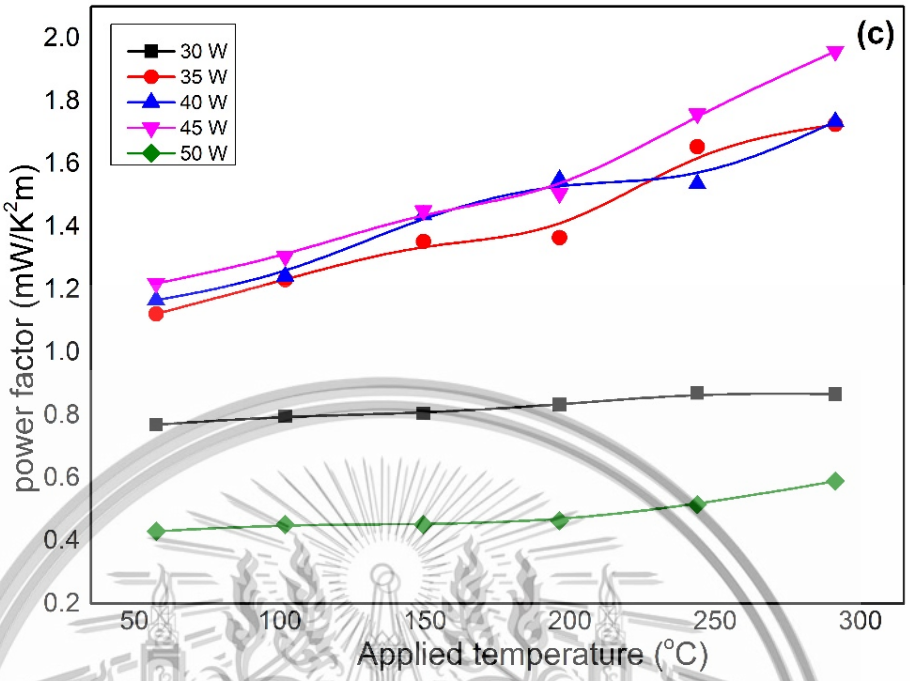

Figure 4.5 Temperature dependence of (a) Electrical conductivity (b) Seebeck coefficient and (c) power factor of the deposited Sb_2Te_3 films at different sputtering power as a function of applied temperature.

The Seebeck coefficient (S) of the Sb_2Te_3 films as increased sputtering power demonstrated that all films are *P*-type semiconductors which confirmed by ZEM-3. The maximum Seebeck coefficient, 185 μV/K, was observed with 35 W sputtering power matching the expected stoichiometric ratio [79]. When the sputtering power density were increased, the Seebeck coefficient declined slightly and then stabilized as seen in Table. 1. According to the theory, the Seebeck coefficient, S, is inversely related to the carrier concentration:

$$S(T) = \frac{8\pi^2 \kappa_B^2}{3eh^2} m^* T \left(\frac{\pi}{3n}\right)^{2/3} \tag{4.2}$$

Where k_B denotes the Boltzmann's constant, e denotes the electron charge, $N(E)$ denotes the density of states, n denotes the carrier concentration and T denotes the temperature. The Seebeck coefficient is inversely proportional to the charge carrier concentration. The power factors of Sb_2Te_3 thermoelectric films was based on two factors, i.e. electrical conductivity and Seebeck coefficient - $PF = S^2\sigma$.

The highest power factor of deposited with sputtering power 45 W was 1.22×10^{-3} W/K^{2}m measured at room temperature. Khumthong et al. reported that the deposited Sb_2Te_3 film fabricated on polyimide substrate using RF magnetron sputtering and obtained *PF*=1.06×10^{-4} W/K^{2}m [80]. Shen et al. reported a maximum *PF*=5.20×10^{-4} W/K^{2}m was obtained for the Sb_2Te_3 film fabricated on polyimide substrate using DC magnetron sputtering with in-situ annealing t in Ar atmosphere for 20 min [81]. This measurements led to the highest power factor with high crystallinity films, which led to high electrical conductivity and high Seebeck coefficient.

The temperature dependence of electrical conductivity, Seebeck coefficient and power factors at different sputtering power of the deposited film are presented in figure 4.5 as a function of applied temperature. In figure 4.5(a) shows the conductivity of the deposited films increased with applied temperature, which indicates a typical semiconductor-like behavior, with a maximum of 4.90×10^4 S/m at 300°C, with the sputtering power in the range of 40 and 45 W. The maximum conductivity corresponded to the maximum crystallinity and consequently the increase of carrier mobility in the film with increasing the sputtering power. The temperature dependence of Seebeck coefficient is shown in figure 4.5(b). A maximum seebeck coefficient of 209 μV/K at sputtering power 35 W (i.e. close to the ideal stoichiometry) at 300°C was obtained. In the theory, the Seebeck coefficient directly depends on the temperature (T) and inversely depends on the carrier concentration [82]. Figure 5(c) shows the temperature dependence of power factors that describe the ability of a material to produce electrical power from a given temperature difference. The results show that the power factors are strongly dominated by electrical conductivity, leading to a maximum PF of 1.95×10^{-3} W/K^{2}m with sputtering power 45 W applied temperature at 300°C.

4.2 Study the enhancement of thermoelectric properties of *P*-type Sb_2Te_3 flexible thick-films via post-annealing treatment assisted DC magnetron sputtering

For the practical use of thermoelectric devices, the flexible thermoelectric materials are important factor to fabricate on flexible heat sources. However, it is difficult to produce a satisfactory temperature difference across the thin-films [50]. Thermoelectric thick-films could potentially solve this problem to induce a large temperature difference and their ability. Thus, in this section, Sb_2Te_3 thick-films were

directly deposited on flexible polyimide by DC magnetron sputtering. Heat treatment process, annealing temperature and annealing time, was optimized the Sb_2Te_3 thick films to enhance their properties. The influence of heat treatment process on the structural, electrical and thermoelectric properties of Sb_2Te_3 flexible thick films were investigated.

The crystal phases of the as-deposited and annealed Sb_2Te_3 thick film are exhibited in the XRD pattern Figure 4.6(a). All diffraction peaks show the characteristic of the rhombohedral crystal structure with a space group of $R\bar{3}m$ with the major peak position at 28.24°, 38.27°, 42.36° and 51.69° which are corresponding to (015), (1010), (110) and (205) plane orientation, respectively. The XRD patterns of all deposited films reveal only the pure Sb_2Te_3. The deposition and heat treatment process are related to the mobility of the adatoms at the substrate surface during growth process. When increasing the substrate temperature, the adatoms have sufficient energy to overcome the surface diffusion barriers to preferential orientation. The sufficient substrate temperature was leading to the nucleation in the in-plane crystal growth along c-axis [83-84]. An increase in annealing temperature results in higher diffusion of the adatoms, which leads to grain growth and higher crystallinity [85]. To achieve the designated film thickness, low mobility atoms arrive at the surface of substrate with various angles of incidence. The annealing process was incorporated with the aim of improving crystal growth. As the annealing temperature increases from 0 to 350°C, the atoms of the Sb_2Te_3 thick film have more energy to diffuse, agglomerate, and finally rearrange into a crystal structure [48]. The intensity of a preferred orientation (015) plane increases with increasing annealing temperature. This implies that thick films are obtained with highly orientated crystallinity following annealing at 350°C for 30 min. XRD patterns of thick films annealed at 350°C for 15, 30 and 60 min are shown in figure 4.6(b). The average crystalline size and the atomic composition are shown in table 4.2. The results suggest that that annealing for 30 min leads to the highest crystal growth, which potentially improves the power factor of the film [87]. The (015) XRD peak of annealed film is sharper and narrower than that of the as-deposited film. This suggests that high quality thick films with good crystallinity and a large grain size are formed as the annealing temperature increases. Crystal imperfection in the film as evidenced from the lattice strain were also examined. Size-induced and strain-induced of Sb_2Te_3 thick

films under the different annealing conditions can be considered by Willianson-Hall formular [88]

$$\beta \cos\theta = \frac{k\lambda}{D} + 4\varepsilon \sin\theta \quad (4.3)$$

Where, D is the average crystalline size, λ is wavelength of X-ray radiation (0.154 nm), β is the integral breadth of the diffraction peak, θ is Bragg diffraction angle, and ε is microscopic strain. The average crystalline size and strain of Sb_2Te_3 thick films increases from 72 to 425 nm with increasing annealing temperature. The highest crystalline size of 425 nm is obtained after annealing at 350°C for 30 min, as shown in table 4.2. The results indicated that post-annealing is significantly related to the lattice strain. The lattice strain decreased slightly with increased annealing temperature. The decreased lattice strain at larger crystalline size were due to reduction of lattice imperfection, which indicated the formation of a high crystalline film. The variation of strain was related to the change in the d-spacing of the film, which indicated a variation of the lattice structure [89].

Table. 4.2 Calculated strain, average crystalline size and percentage of Te of Sb_2Te_3 thick films.

Annealing conditions		$\beta \cos\theta$	Strain (ε) $\times 10^{-3}$	W-H crystalline size (nm)	%Te
Temp. (°C)	Time (min)				
As-dep	-	0.0037	3.29	72	59.28
150°C	30	0.0036	3.21	137	59.21
250°C	30	0.0031	3.08	141	57.34
350°C	30	0.0028	2.29	182	57.10
350°C	15	0.0030	2.22	144	57.30
350°C	30	0.0028	2.29	182	57.10
350°C	60	0.0029	2.37	163	56.22

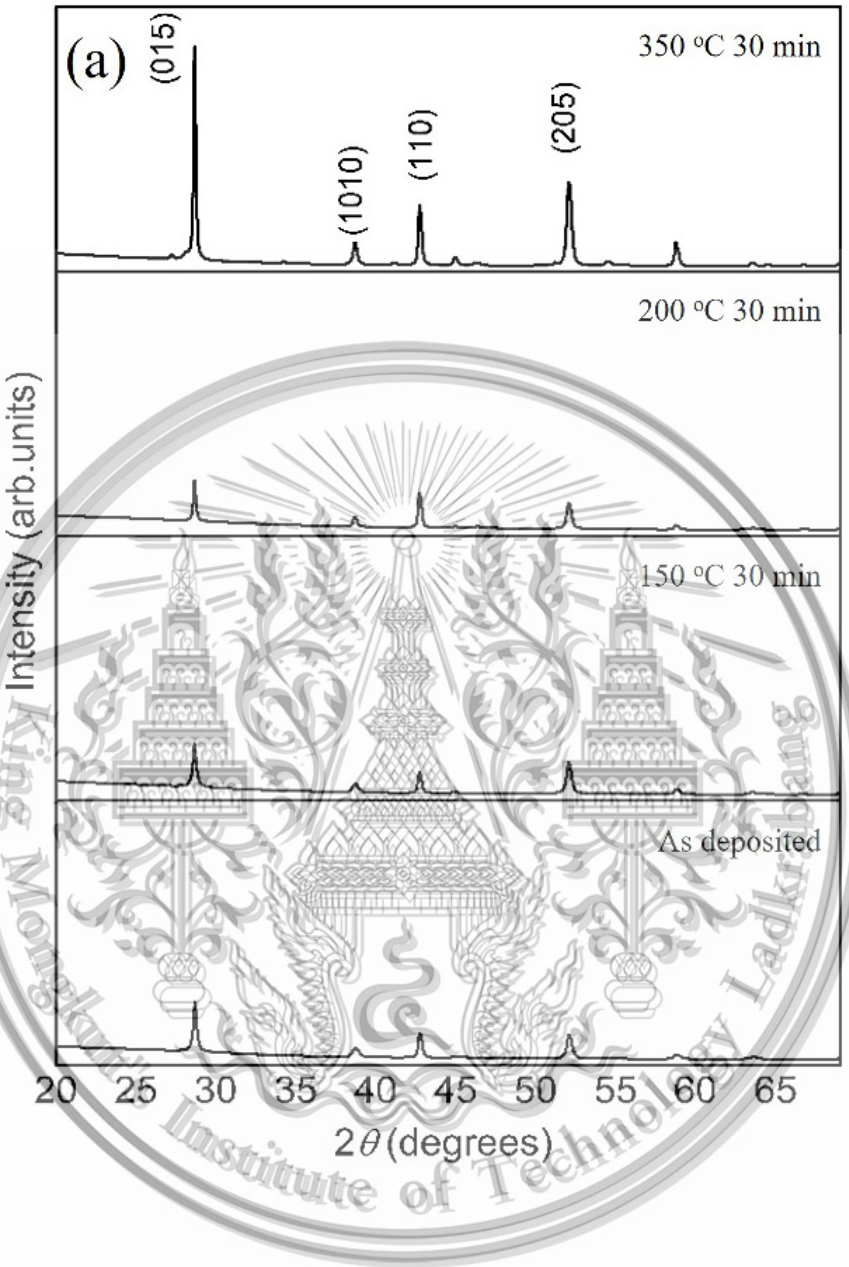

Figure 4.6 XRD patterns of Sb_2Te_3 thick films at different (a) annealing temperature and (b) annealing time

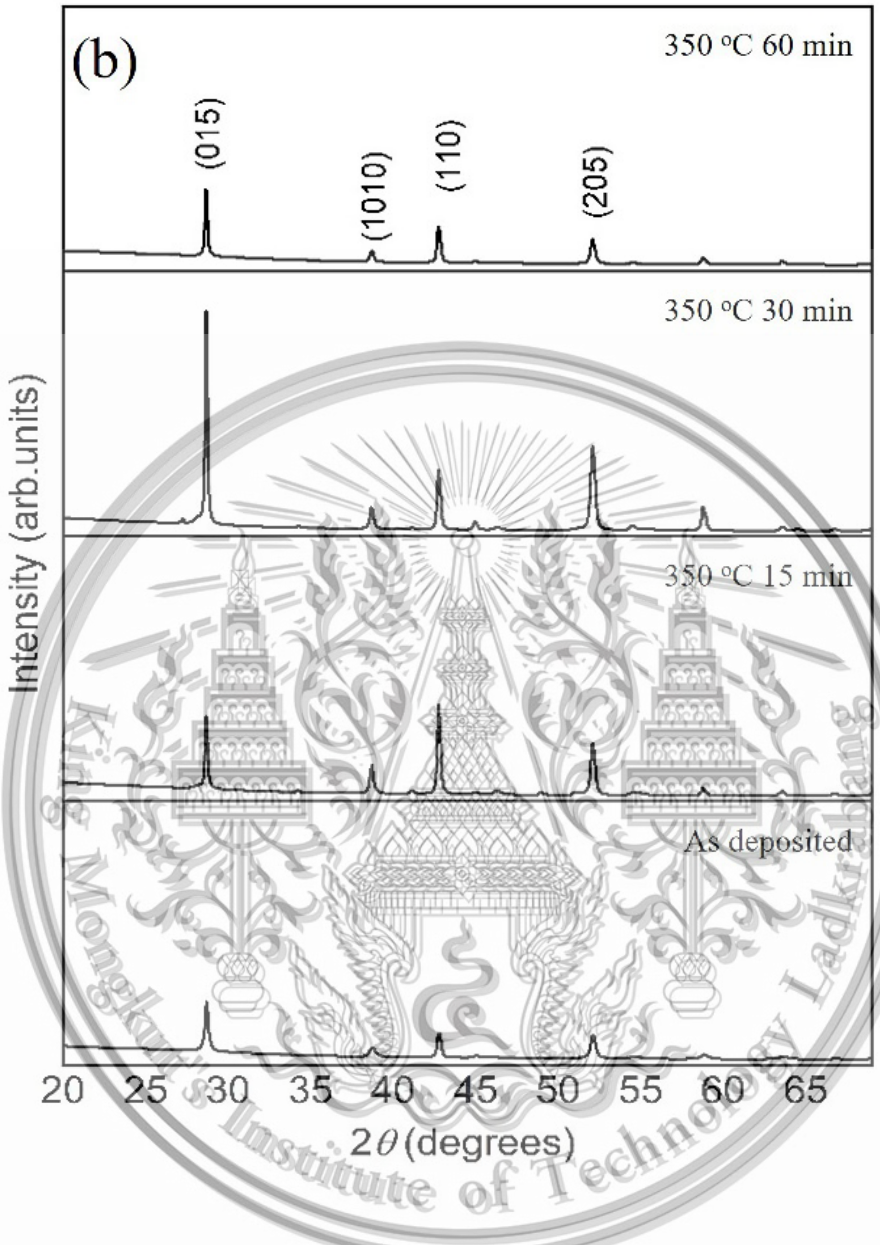

Figure 4.6 XRD patterns of Sb_2Te_3 thick films at different (a) annealing temperature and (b) annealing time

The atomic composition of as-deposition and annealed thick films were measure by EDX, as seen in table 4.2. The %Te slightly decreases from 59.28% to 57.10% as annealing temperature increase. This is caused by the evaporation of volatile element Te during annealing. Atomic bonds of the thick films are not equivalent in all the directions at the surface, which leads to the evaporation of Te [90-91]. In order to further optimize the annealing time, the annealing temperature was performed at 350°C. The %Te slightly decreases with increasing annealing time, this result show that the annealing time do not significantly change the %Te.

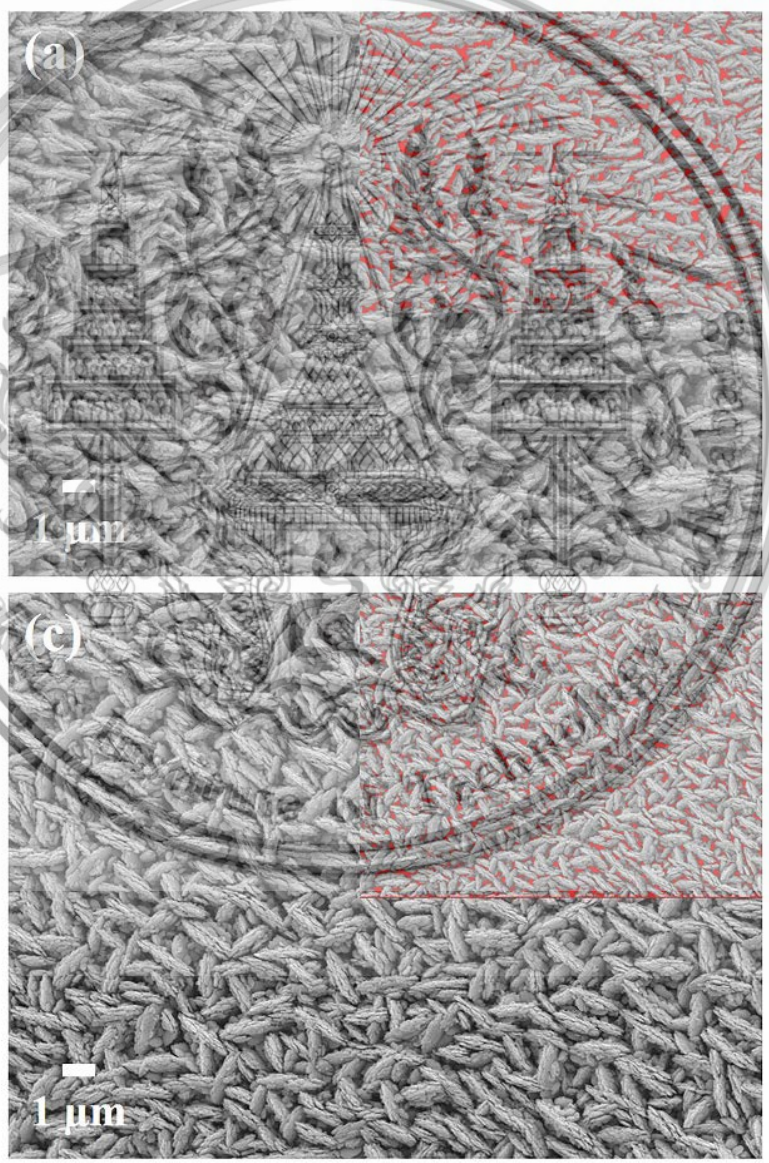

Figure 4.7 Surface morphology of Sb_2Te_3 thick films (a) As-deposited and annealed at (b) 150°C (c) 250°C (d) 350°C for 30 min. Inset show the porosities as red areas.

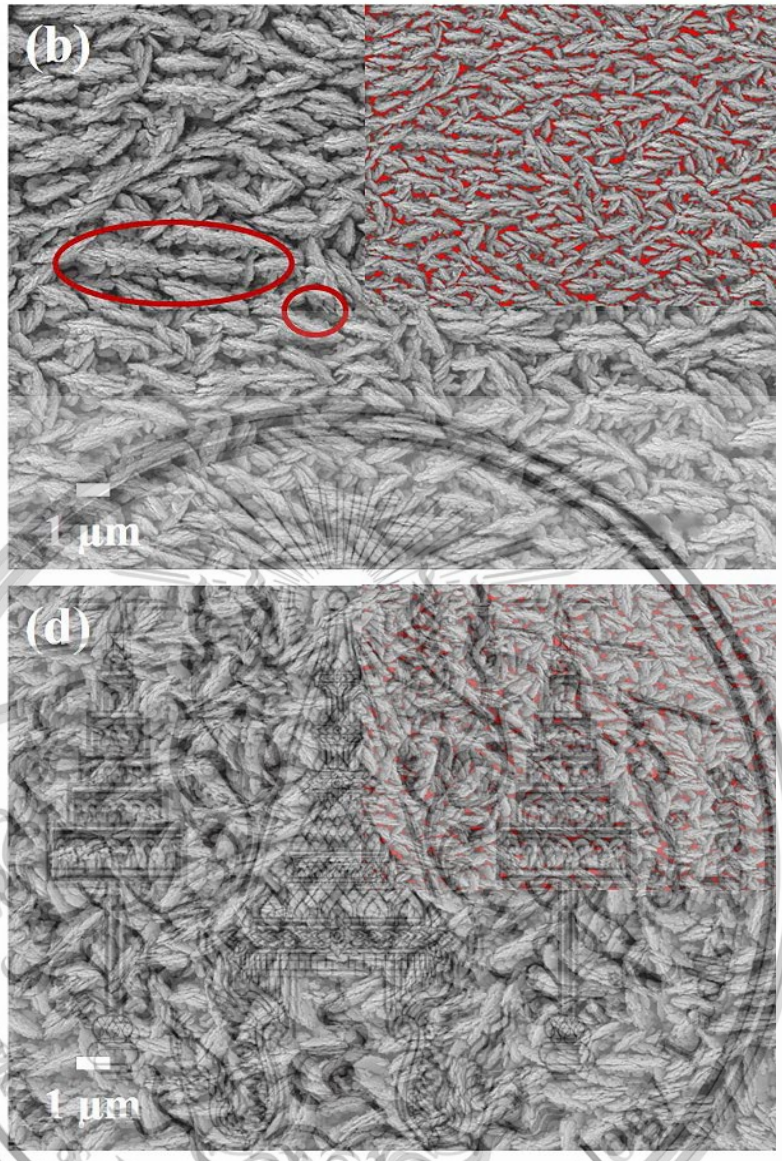

Figure 4.7 Surface morphology of Sb_2Te_3 thick films (a) As-deposited and annealed at (b) 150°C (c) 250°C (d) 350°C for 30 min. Inset show the porosities as red areas.

Surface morphology of Sb_2Te_3 thick films annealed at 0, 150, 250, and 350°C for 30 min are shown in figure 4.7. FE-SEM images of the as-deposited film show loose and vertical flakes, and the surface appears rough and incompact. Flakes with a larger lateral size are observed when the annealing temperature increases to 150°C, as indicated by the red circles in figure 4.7(b). The size distribution, grain density and surface smoothness increase as the annealing temperature increases to 250°C and then to 350°C. The flakes are well crystallized because of the high film surface energy.

Annealing provides sufficient energy to allow the diffusion of condensing particles, leading to lattice points that form an ordered crystalline structure. This is consistent with the XRD results. The film porosity at surface of the film reduces with increasing annealing temperature, which potentially benefits carrier transport and phonon scattering. Figure 4.8 shows FE-SEM images of thick films annealed at 350°C for 15, 30 and 60 min. The size distribution, grain density and surface smoothness of the deposited films increase with increasing annealing time. During the thickness of the deposited films increased, weak contacts between particles generally result in high porosity and higher resistivity [28]. Post-annealing can improve the particle connections. In support of this, FE-SEM images were processed using ImageJ software package to calculate the area ratio of the surface pores [6].

Figure 4.7 insets and figure 4.8 insets show the porosity of the Sb_2Te_3 thick film (as red areas) for the various annealing conditions. The porosities are 15.2, 13.1, 11.7 and 10.3% for the as-deposited thick film and films annealed at 150, 250, and 350°C, respectively. The decrease in number of pores at higher annealing time is also confirmed. The film annealed at 350°C for 15 min has a porosity of 12.1%. However, the porosity of the film slightly decreases to 10.3% after annealing for 30 min and then increases to 13.2% after annealing for 60 min.

Cross-sectional FE-SEM images of the Sb_2Te_3 films annealed for different times are shown in figure 4.9 Columnar-shaped growth is apparent. The thickness slightly decreases with increasing annealing time because of the evaporation of Te. A smooth surface is obtained at higher annealing times. A crack is observed across the columns of the film annealed for 60 min. The crack would lead to an increase in trapped carriers in the grain boundaries, an increase in resistivity. Typically, the intensity of the diffraction peak is proportional to the electron density of the film. For 60 min, the crack would lead to a decrease in the electron density and the intensity also decreases. This result is consistent with the XRD results. The Sb_2Te_3 thick film with a highly orientated crystalline structure is obtained after annealing at 350°C for 30 min. Annealing for 60 min leads to a decrease in film crystallinity, as shown in figure 4.6(b).

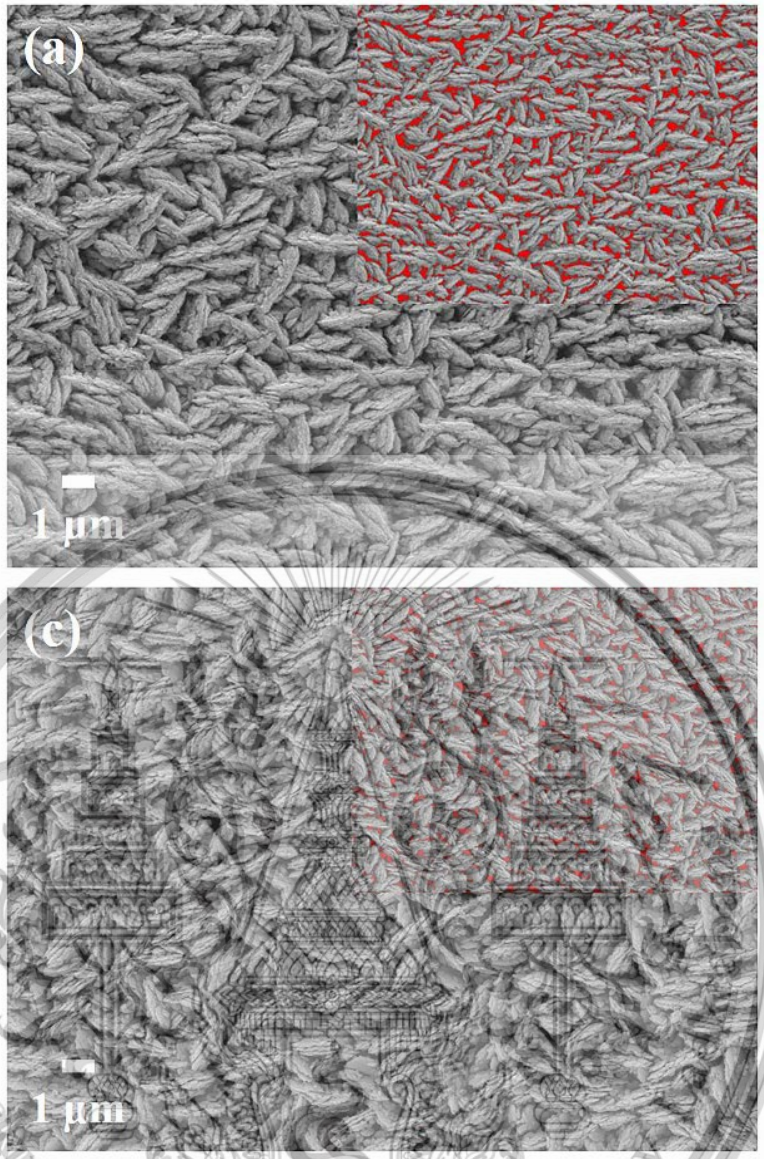

Figure 4.8 Surface morphology of Sb_2Te_3 thick films (a) As-deposited and annealed for (b) 15 min (c) 30 min (d) 60 min at 350°C. Inset shows the porosities as red areas.

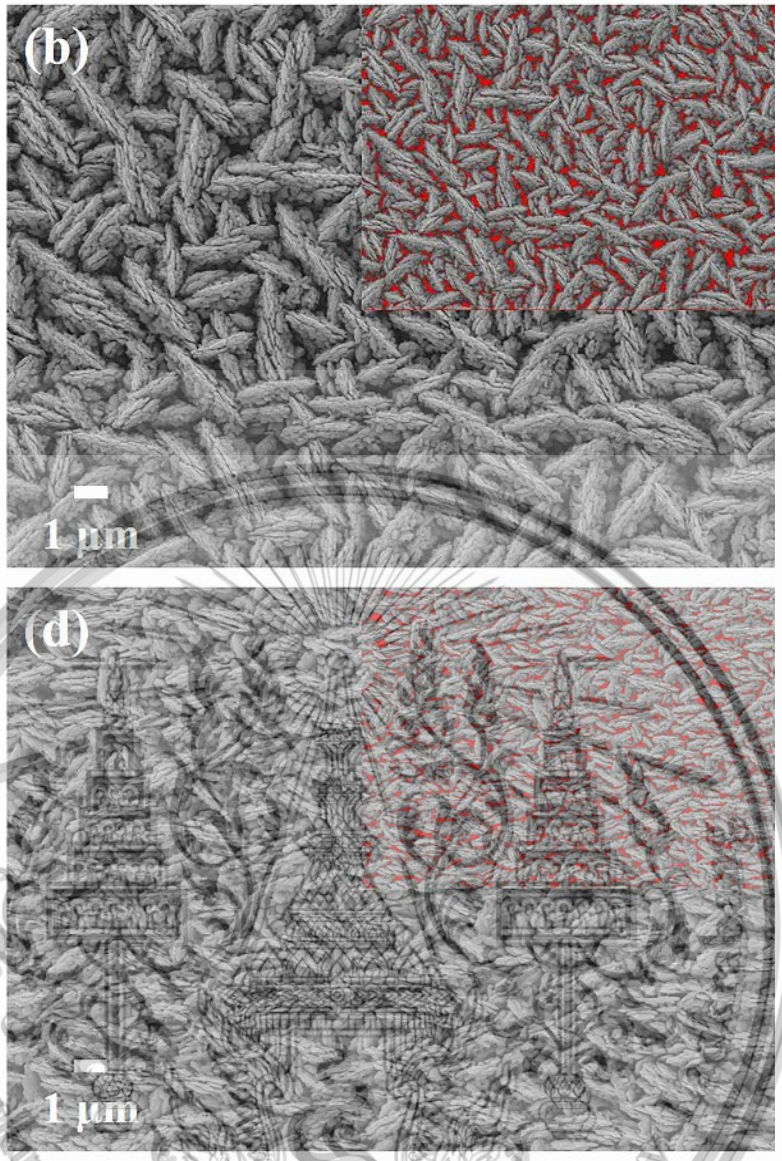

Figure 4.8 Surface morphology of Sb_2Te_3 thick films (a) As-deposited and annealed for (b) 15 min (c) 30 min (d) 60 min at 350°C. Inset shows the porosities as red areas.

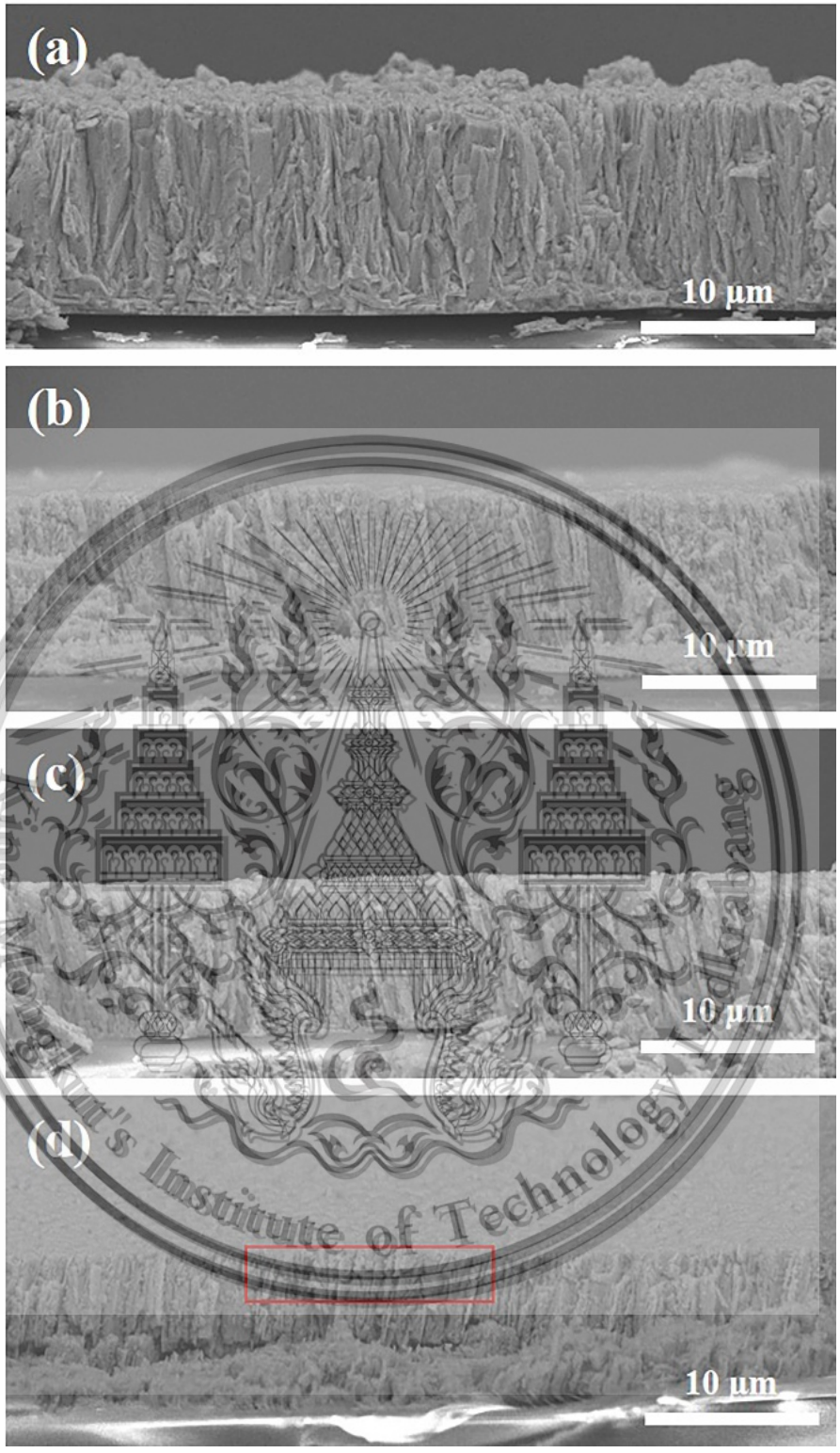

Figure 4.9 Cross-sectional FE-SEM images of Sb_2Te_3 thick films (a) As-deposited and annealed for (b) 15 min (c) 30 min (d) 60 min at 350°C.

Figure 4.10 shows the annealing temperature dependence on the in-plane electrical transport properties and thermoelectric properties of the Sb_2Te_3 films measured at room temperature. All films have a positive carrier concentration, implying that the majority of carriers in the thick films are holes. As seen in figure 4.10(a), the carrier concentration (n) of the films slightly decreases from 4.56×10^{19} to 3.67×10^{19} cm^{-3} and the electrical conductivity (σ) dramatically increased from 237-386 S/cm as annealing temperature increase from 0 to 350ºC. During deposition, the Sb_2Te_3 thick films contain many point defects including vacancies and antisite defects. The carrier concentration is related to defect inside the films. Post-annealing reduces the number of point defects which decreases the carrier concentration [94]. The decrease in carrier concentration with increasing annealing temperature has been previously reported for the Sb_2Te_3 films [95-97]. The results indicated that a significantly reduced amount of carrier concentration in the Sb_2Te_3 films leads to increasing the electrical conductivity of the annealed films.

Besides the reduction of the point defect of the thick films, the increase in carrier mobility (μ) from 27.35 to 55.36 cm^2/Vs with increasing annealing temperature is attributed to grain growth. Post-annealing leads to a slight change in surface morphology, as seen in figure 4.7. The transfer of carriers is mainly affected by grain boundaries leading to an increase in mobility. The low electrical conductivity of the as-deposited films could be attributed to the lower mobility owing to the low crystallinity, small crystalline size and non-compact grain. As increasing the annealing temperature, the Sb_2Te_3 film becomes more compact with better crystallinity leading to improve electrical conductivity. It is assumed that the increased electrical conductivity is largely attributed to the improved crystal orientation, larger crystalline size, low porosities grains and increased carrier mobility. The mean free path of the films is collectively affected by the internal crystal structure, which strongly influences the carrier mobility. According to the value of carrier concentration and carrier mobility, the mean free path of carriers of thick films can be estimated using the formula [81]:

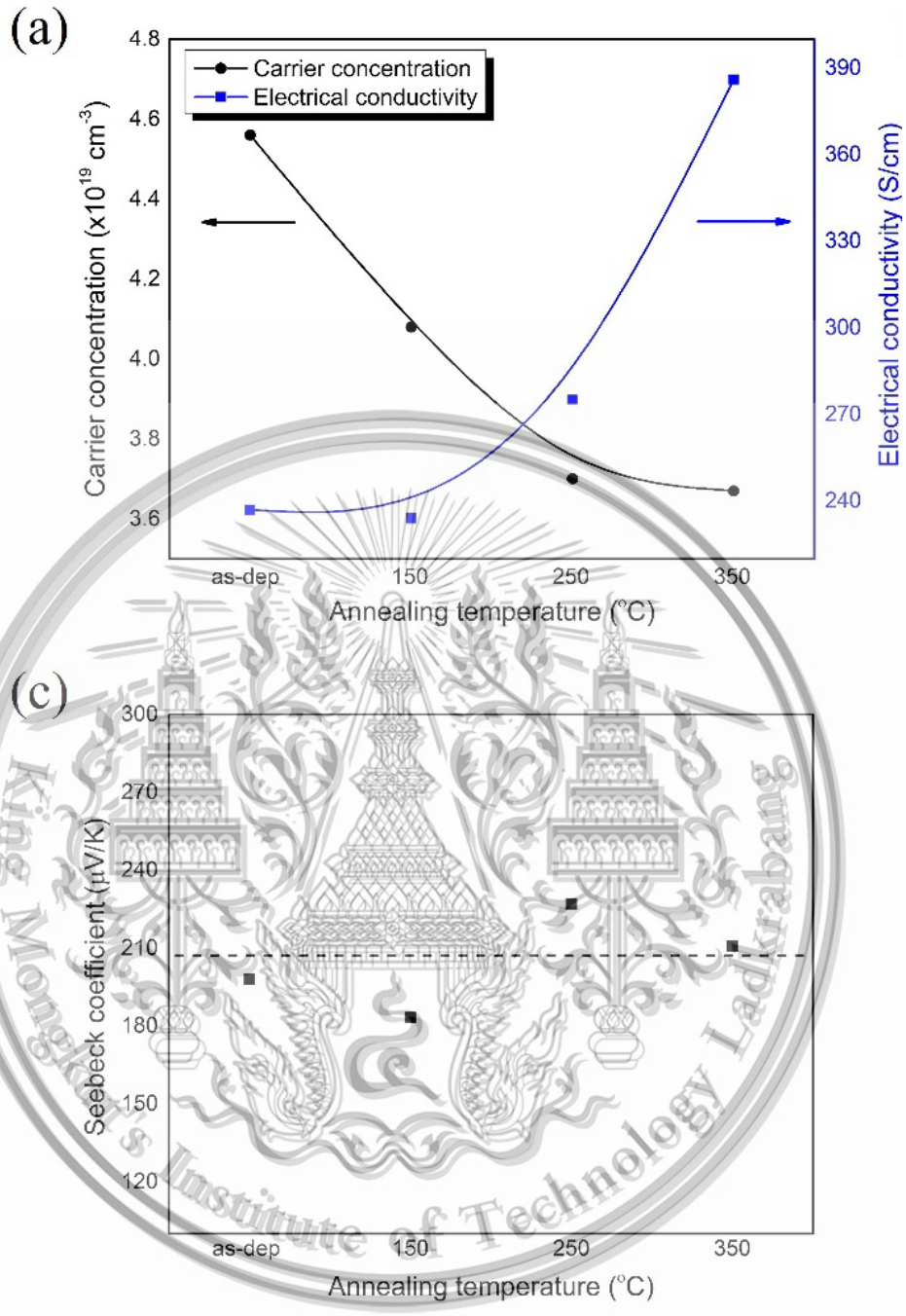

Figure 4.10 Annealing temperature dependence on (a) carrier concentration and electrical conductivity (b) carrier mobility (c) Seebeck coefficient and (d) power factor of the Sb_2Te_3 thick films.

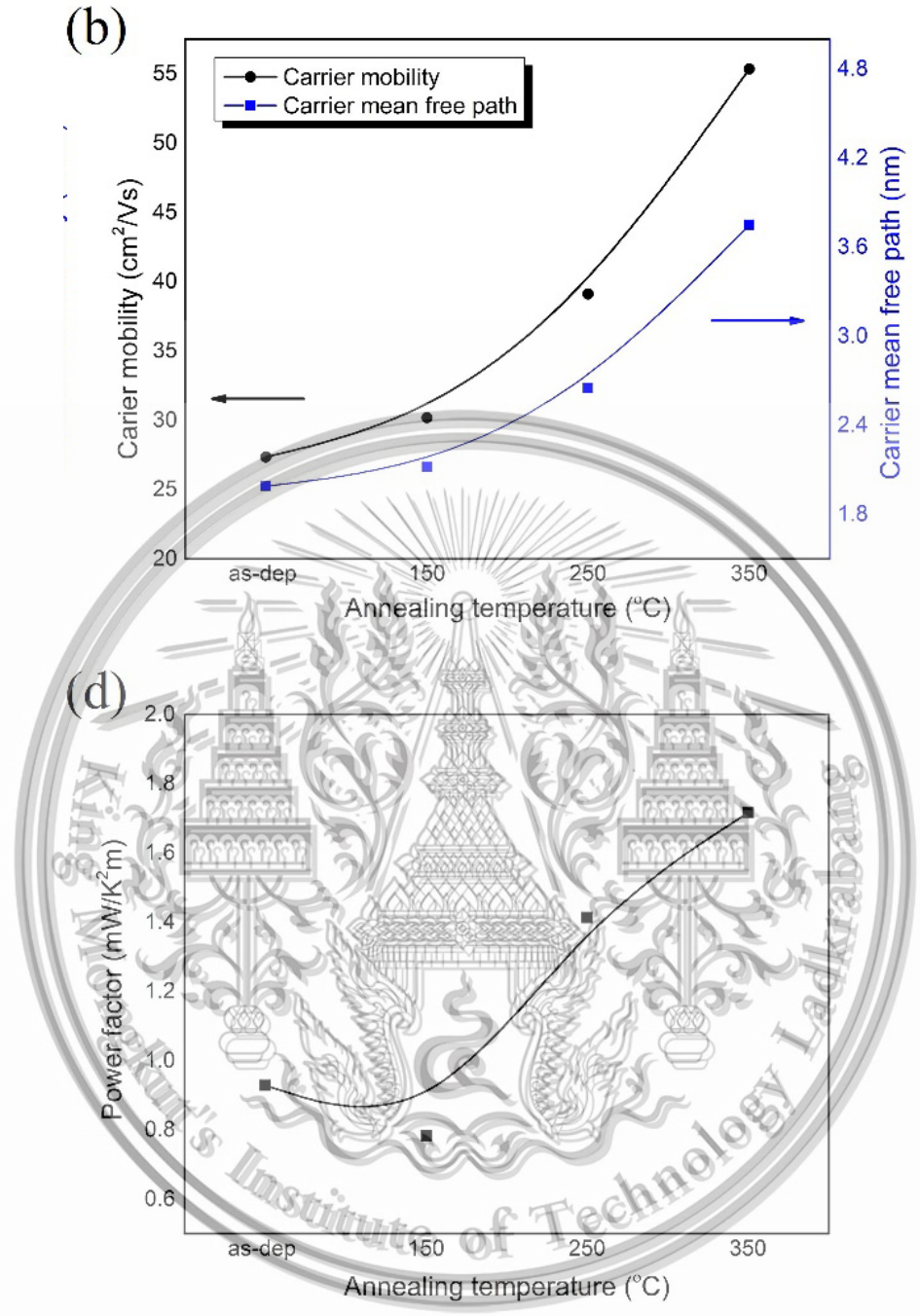

Figure 4.10 Annealing temperature dependence on (a) carrier concentration and electrical conductivity (b) carrier mobility (c) Seebeck coefficient and (d) power factor of the Sb_2Te_3 thick films.

$$l = \frac{h}{2e}\left(\frac{3n}{\pi}\right)^{\frac{1}{3}}\mu \quad (4.4)$$

Where l is the mean free path of the carriers, h is plank's constant and e is the electron charge. The l increases with increasing annealing temperature due to the decreased film porosity, as shown in figure 4.10(b). The in-plane Seebeck coefficients of the Sb_2Te_3 films are positive, indicating that all deposited films are *P*-type. The *S* does not significantly change with increasing annealing temperature, as shown in figure 4.10(c). This is because there is little change in carrier concentration, as shown earlier. The power factor ($PF = S^2\sigma$) is shown in figure 4.10(d). The power factor of the thick film increases with increasing annealing temperature, reaching 1.72 mW/K^{2}m after annealing at 350°C for 30 min. This is attributed to the competition of the decreased carrier concentration, increased mobility and largely constant Seebeck coefficient with increasing annealing temperature.

The thermoelectric properties of the Sb_2Te_3 thick films annealed at 350°C for 15-60 min, as seen in figure 4.11. It shows the electrical conductivity, Seebeck coefficient, and power factor of Sb_2Te_3 thick films annealed at 350°C for different annealing time as a function of applied temperature. The electrical conductivity was slowly decrease with increasing applied temperature range from 50 to 300°C, reaching a maximum of 386 S/cm at 50°C. This indicates typical metallic transport behavior. When at sufficient temperature, the electrical transport across the grain boundaries/interfaces can be expressed by thermionic emission expression:

$$\sigma(T) \approx T^{-\frac{1}{2}} exp\left[-E_B/kT\right] \quad (4.5)$$

Where E_B is the height of the grain boundary/interface potential barrier. For certain temperature and grain boundary/interface potential barriers, $\Delta\sigma/\Delta T$ ratio can become negative or positive, which is consistent with the previous reports [11,28,99]. The conductivity of Sb_2Te_3 thick films increases as increasing annealing time up to 30 min. When the annealing time increase to 60 min, the crystallinity, fracture cross section, and chemical composition of samples decreased, which reduces the electrical conductivity.

The maximum Seebeck coefficient of 237 μV/K is obtained at an applied temperature of 300°C after annealing at 350°C for 30 min. The increase in the Seebeck coefficient of the Sb_2Te_3 thick films could be attributed to the decrease in the carrier concentration [48]. The temperature dependence of thermoelectric power factors of the Sb_2Te_3 films as a function of annealing time is calculated from the value of S and σ. The thermoelectric power factor slightly decreased with increasing applied temperature 50 to 300 °C. A maximum power factor of 1.72 mW/K^{2}m is obtained at an applied temperature of 50 °C. This is lower than that reported by H. Shen et al. [10] 2.5 mW/K^{2}m for co-evaporated 10 μm Sb_2Te_3 thick films at room temperature. The current value is comparable to that reported by M. Mizoshiri et al. [11] of 1.6 mW/K^{2}m for 100 μm thick Sb_2Te_3 Deposited by Thermally Assisted Sputtering Method at room temperature.

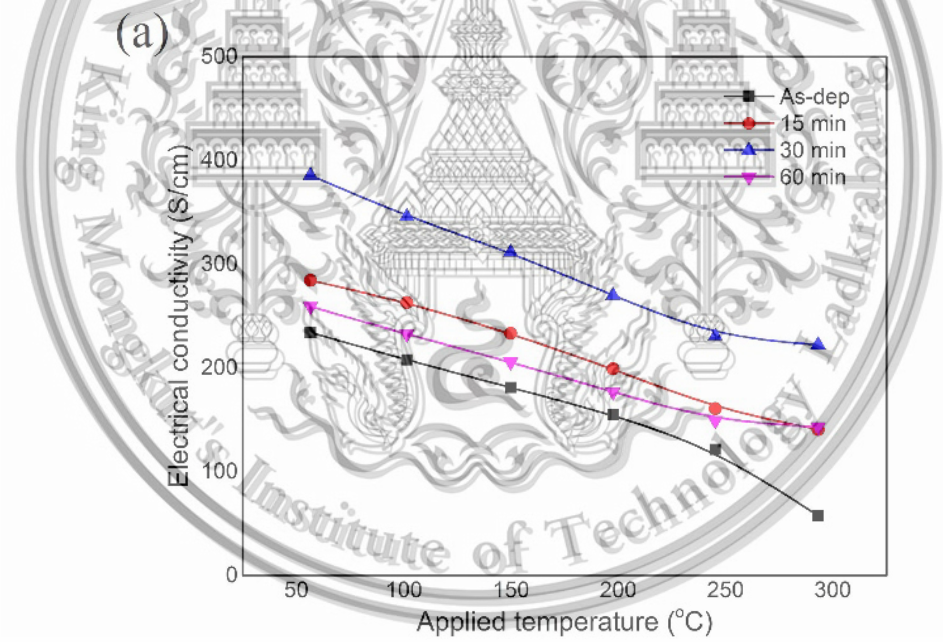

Figure 4.11 Temperature dependence of the in-plane (a) electrical conductivity (b) Seebeck coefficient and (c) power factor of Sb_2Te_3 thick film annealed at 350°C with different annealing time.

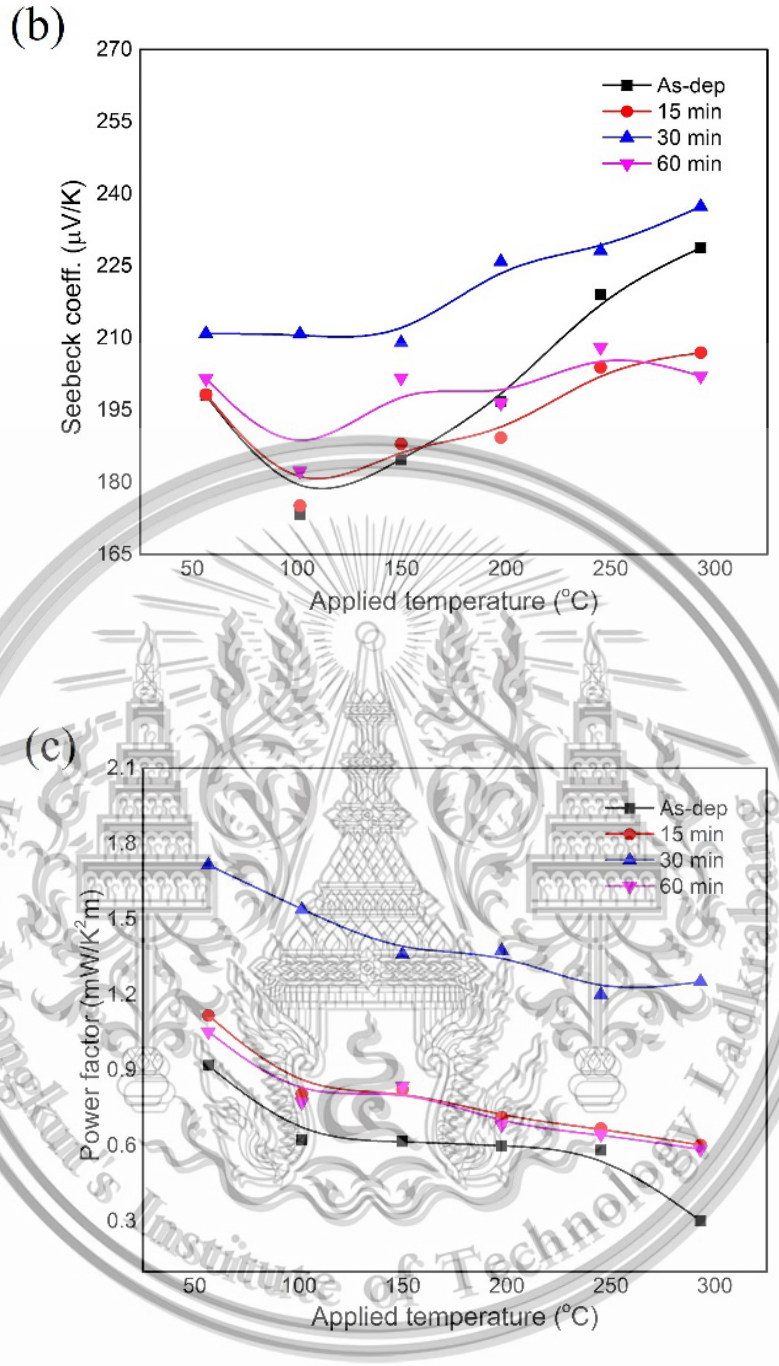

Figure 4.11 Temperature dependence of the in-plane (a) electrical conductivity (b) Seebeck coefficient and (c) power factor of Sb_2Te_3 thick film annealed at 350°C with different annealing time.

The current value is higher than that reported by O. Vigil-Galan et al. [63] of 0.38 mW/K^{2}m for 15 μm Sb_2Te_3 thick films deposited by close space vapor transport

at substrate temperatures 450°C. The results indicated that the suitable Sb_2Te_3 thick films deposited by DC magnetron sputtering at low power density and post-annealed at 350°C for 30 min has enhanced thermoelectric properties.

4.3. Study the thickness effect on the thermoelectric properties of *P*-type Sb_2Te_3 flexible thin- and thick-films deposited by thermal treatment-assisted DC magnetron sputtering

To fabricate a thermoelectric device with high output power, it is important to optimize the properties of Sb_2Te_3 thermoelectric material such as Seebeck coefficient, electrical conductivity and thickness. From the above study, it can be found that thick films can generate the electrical voltage by increasing the temperature difference which is significant for practical use compared with thin films. For thermoelectric generator application, the maximum output power is requested and defined as $P_{max} = \frac{S^2 \Delta T^2 tw}{4\rho l}$, which is proportional to the thickness (t) and width (w) of the thermoelectric device and is inverse to the resistivity (ρ) and the length (l). To obtain the maximum output power, thermoelectric material should be a large power factor and simultaneously reducing the internal resistance that relates to a thick layer of thermoelectric material. The film thickness is one of the key parameters that play important roles in thermoelectric efficiency and generating output power.

However, the suitable thickness of flexible Sb_2Te_3 thick films should be optimized their properties before designing the thermoelectric device leads to improve the thermoelectric output performance. In this work, the designated a suitable thickness layer of flexible Sb_2Te_3 films on their properties is studied. The Sb_2Te_3 films were deposited using thermal treatment-assisted DC magnetron sputtering with different deposition times. The influence of film thickness on their properties is investigated.

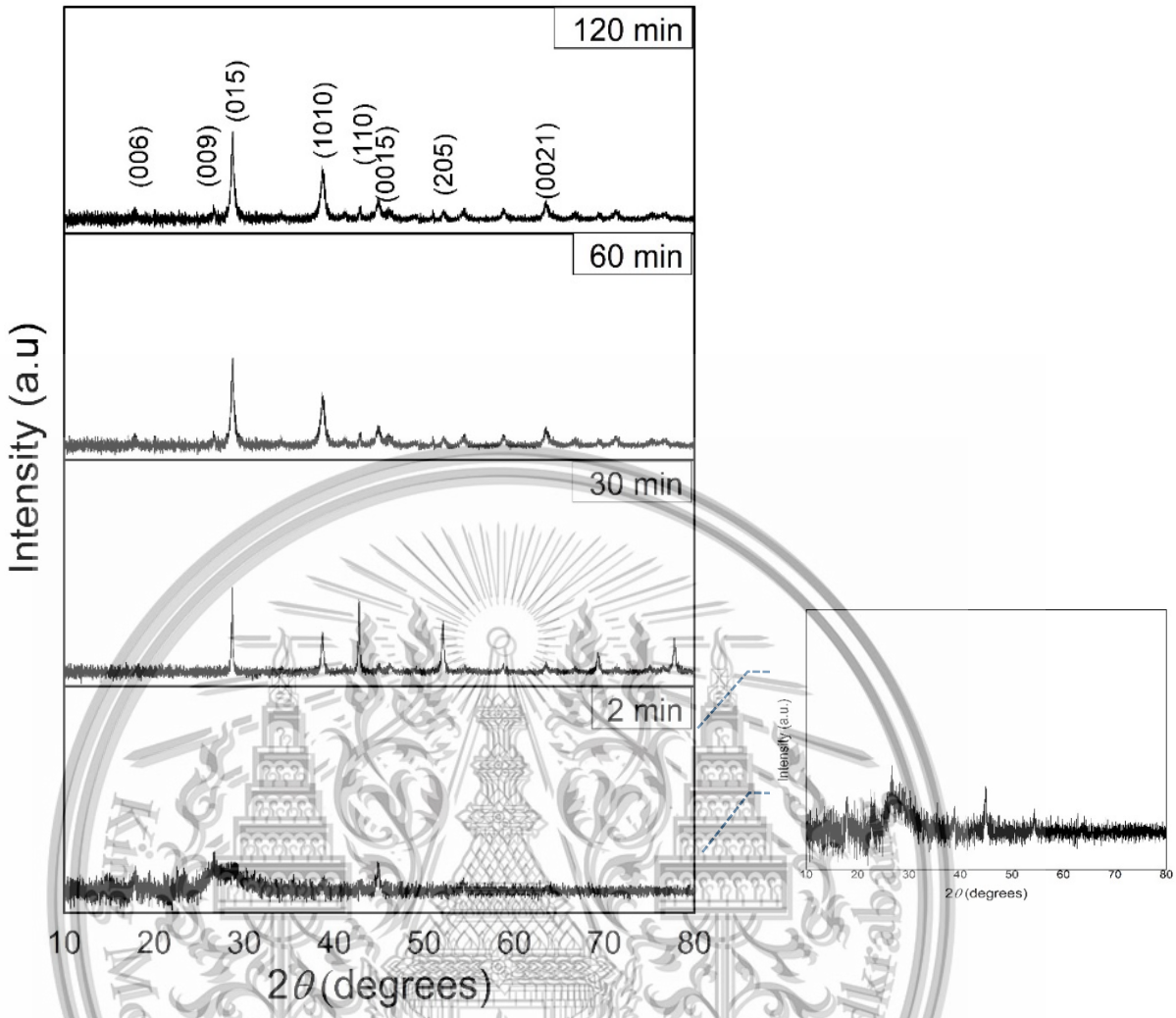

Figure 4.12 XRD patterns of deposited Sb_2Te_3 films with different deposition time. Inset shows the rescaled pattern of 2 min.

XRD patterns of Sb_2Te_3 films with various deposition time are shown in figure 4.12. All films can be indexed to rhombohedral crystal structure that confirms the Sb_2Te_3 pure phase. As the lowest deposition time, there are evident broad diffraction peak. The broad peak should be attributed to the nano scales of the film [68]. It was seen that, the orientation planes (009) and (0015) arose at the lowest deposition time with a relative high substrate temperature during deposition process. The orientation plane along (00l) was observed, indicating the atomic interactions between the Sb_2Te_3 atoms and the substrate can obstruct the nucleation in the vertical direction [3, 33]. Thickness of Sb_2Te_3 films with various deposition time are shown in table. 4.3, monitored by cross-section FE-SEM. Thickness was increased as the deposition time increase. The growth rate of all films are approximately 0.15 μm/min. As increasing the deposition time to 30, 60 and 120 min, the peak positions and their intensities were

change and become shaper. The preferred orientation of the (015), (1010), (110) and (205) lattice plane are observed, which indicated that the atoms of the thick layer cannot obtain enough energy for lateral movement on the surface, leading to random growth in direction vertical to the substrate [3,71]. During growth to the designation thickness, the residual stress is generally accumulated as increasing of the deposition time [73]. Furthermore, the uneven distribution of thermal energy of thick layer affects the growth process leading to surface diffusion of adatoms to growth in ab-plane [3,71]. All results suggest that all films are formed with a high crystallinity in (015) plane. The sharper and intense of the diffraction peaks evidences the grain refinement along with the large strain [78]. The calculated crystalline size, lattice strain and dislocation density are examined by Debye-Scherer's equation. The calculation of crystalline size, dislocation and lattice strain were presented in table 4.3. The crystalline size at (015) orientation plane of deposited Sb_2Te_3 films are N/A, 43, 40 and 18 nm for deposition time 2, 30, 60 and 120 min, respectively. It has been observed that the FWHM increases with increased the deposition time from 30 to 120 min, and thus the average crystalline size decrease. These results indicated that the crystallinity of deposited film are decreased as increasing the deposition time. Consequently, the increasing of the lattice strain (ε) and dislocation (δ) of the deposited films as a function of increasing the deposition time may be due to the generated of the residual stress during deposition leading to obtain the variation in lattice parameters and the change of the imperfection inside the film [72, 85].

EDS provides the average atomic percentage of Te of all annealed Sb_2Te_3 films, as shown in table 4.3. The percentage of Te elements were indicated that all samples are close to the stoichiometric of 2:3 (Sb:Te). A small change of the stoichiometric can be obtained due to thermal treatment process, which caused by the evaporation of Te elements. Considering the vapor pressures of constituent elements [3, 91].

Table 4.3 Thickness, percentage of Te elements, lattice stain, dislocation and crystalline size of deposited Sb_2Te_3 films with different deposition time.

Deposition time	Thickness (μm)	%Te	Crystalline size (D: nm)	Dislocation ($\delta \times 10^{14}$ lines/m^2)	Strain ($\varepsilon \times 10^{-3}$ line^{-2}m^{-4})
2min	0.3	58.73	N/A	N/A	N/A
30min	4.5	58.11	42.6	5.4	0.81
60min	9.0	58.09	40.3	6.2	0.86
120min	16.7	58.51	18.3	30.8	1.89

Table 4.4 Hall measurements of deposited Sb_2Te_3 films with different deposition time.

Deposition time (min)	Thickness (μm)	Carrier concentration ($\times10^{19}cm^{-3}$)	Mobility (cm^2/Vs)	Resistivity ($\times10^{-3}\Omega$.cm)
2	0.3	8.9	58	1.21
30	4.5	4.1	75	2.16
60	9.0	5.6	68	1.50
120	16.7	11.3	42	1.31

Figure 4.13 shows the surface morphologies of Sb_2Te_3 films with various deposition time. It is obvious that the plate structures and smooth surface are obtained in the deposition time of 2 min, as seen in the red circle of figure 4.13(a). The deposited film has a layered microstructure, indicating that the grains grow along the c-axis in a direction parallel to the substrate, which agrees with XRD results. In order for the deposition time to increase 30, 60 and 120 min, the ordinary structure is obtained. As the deposition time increases, the nucleation in the vertical direction is faster occurred comparing to in-plane growth. The deposition atoms cannot have enough energy to lateral movement on the surface leading to random growth. It implies that the distribution of energy leads to surface diffusion of the deposited atoms, which greatly affects the grain growth in the ab-plane and the c-axis direction. However, at high order with thickness at deposition time 120 min, the surface morphology is clearly different. The rougher surface with a small compact grain was obviously observed, as seen in figure 4.13(d). Non-uniformity of the deposited film was occurred in the multi-layers coating due to improper adherent problems between deposited layers.

Figure 4.14 shows the schematic of the growth process of Sb_2Te_3 thick films with different deposition times. All films were grown under the same conditions with different deposition times to carry out the effect of designated films on thermoelectric properties. During the deposition method, the deposition and thermal treatment processes were repeated to reach the designated deposition time. In the sputtering process, the deposited atoms were diffused on the surface of the substrate by giving up their kinetic energy and thermal diffusion. The diffusion and agglomeration between the grains can be yield by thermal treatment. The mobility of the deposited atoms is also related to the appearance of the microstructure [33, 36].

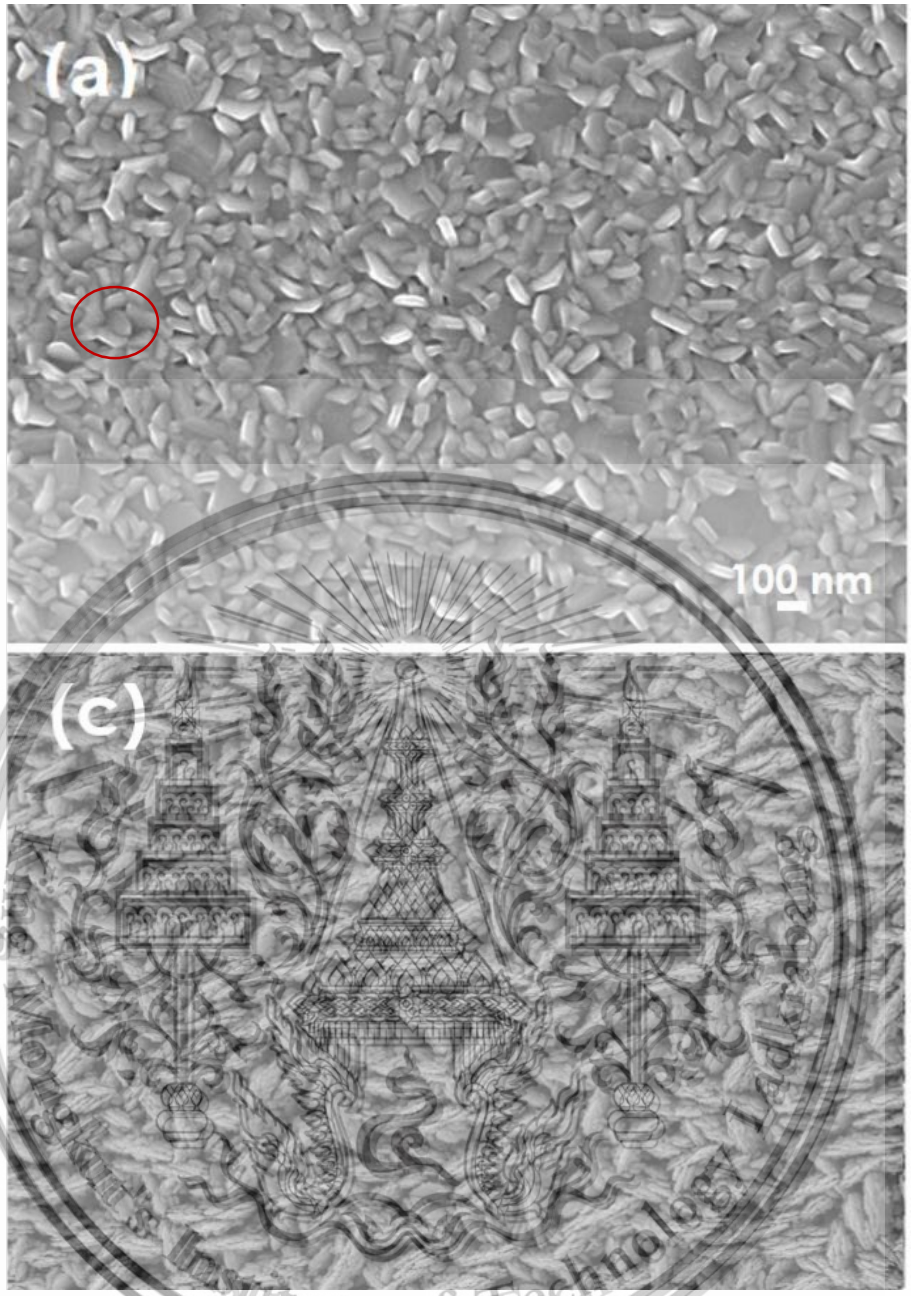

Figure 4.13 Surface morphology of the deposited Sb_2Te_3 films with different deposition time (a) 2 min, (b) 30 min, (c) 60 min and (d) 120 min.

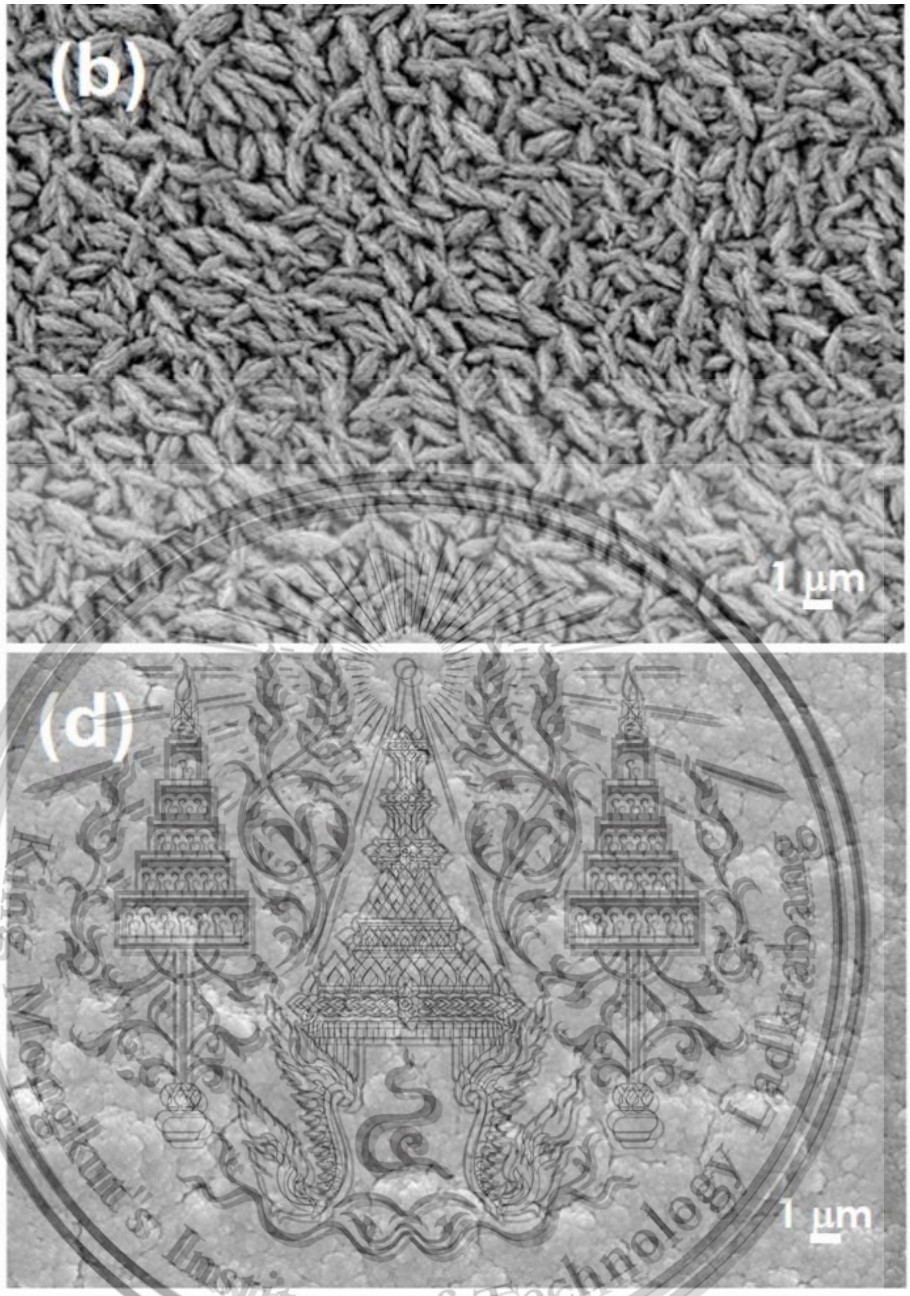

Figure 4.13 Surface morphology of the deposited Sb_2Te_3 films with different deposition time (a) 2 min, (b) 30 min, (c) 60 min and (d) 120 min.

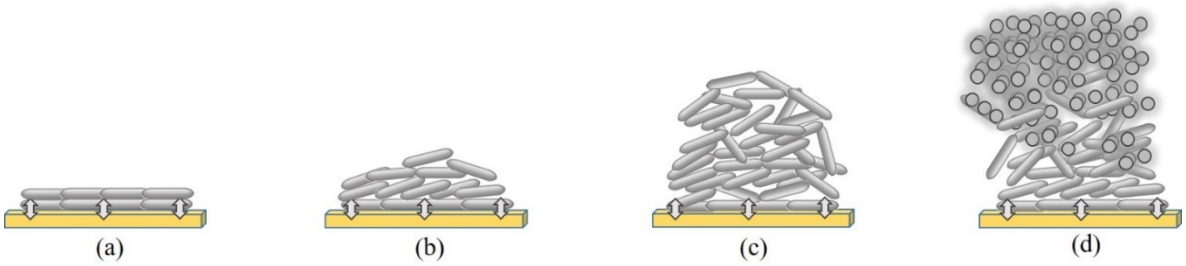

Figure 4.14 Schematic of the growth process of the deposited Sb_2Te_3 films with different deposition time (a) 2 min, (b) 30 min, (c) 60 min and (d) 120 min.

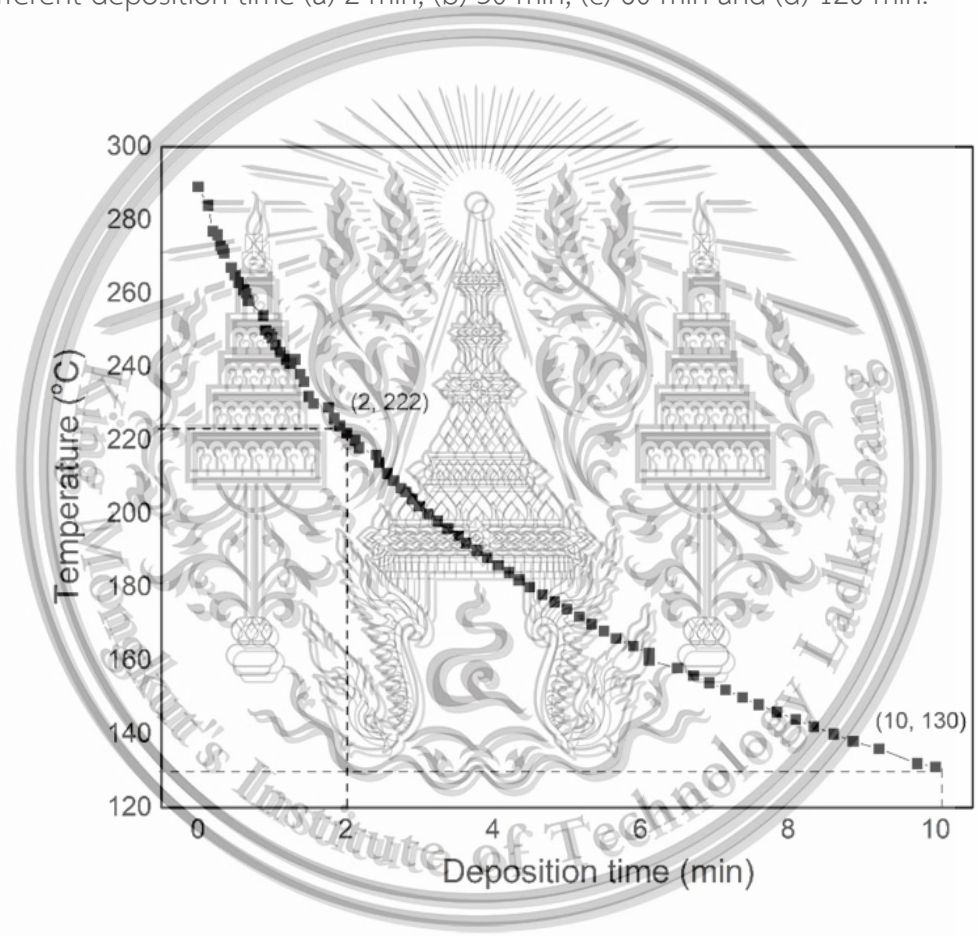

Figure 4.15 Temperature profile of pre-heat treatment of deposited Sb_2Te_3 films as a function of deposition time.

In the case of the low deposition time at 2 min, a relatively high pre-heat temperature of 220°C has remained as seen in the temperature profile in figure 4.15 during the deposition process. The higher diffusion of the deposited atoms is occurred due to thermal diffusion. The interaction between atoms is smaller than their bonding

to the substrate. The layered structure two-dimensional parallel to the substrate is obtained. As increases the deposition time to 30 and 60 min, the effect of pre-heat temperature was decreased due to the decrease of pre-heat temperature to 130 °C during sputtering, as seen in the temperature profile, leading to reduce the surface mobility of the deposited atoms. As the thickness of the film increases, the interaction between their atoms is stronger than the interaction with the substrate surface, causing the atoms to bond strongly to each other and growing into many three-dimensional. Generally, it usually occurs in the case of the generated stress impact after two-dimensional growth. The transition from the layer structure to island growth occurs at a critical layer thickness which is dependent on the physical properties such as surface energy and lattice parameters. It is clarified that the deposition periods and the pre-heat temperature have significantly contributed to the growth process. After increase the deposition time to a relatively high at 120 min, a small grain occurred. It may be thermal energy during growth thick layer is not enough to diffuse and agglomerate the deposited atom on the surface of the film [36] leading to obtaining a small compact grain on the film surface.

The Hall measurements are confirmed that the majority of carriers of the deposited films are holes. Carrier concentration and mobility measurement at room temperature are shown in table 4.4. The carrier concentrations are 8.8×10^{19}, 4.1×10^{19}, 5.6×10^{19} and 11.3×10^{19} cm^{-3} at deposition time 2, 30, 60 and 120 min, respectively. Typically, the carrier concentration of the deposited films is typically sensitive to the chemical composition and the intrinsic defect of the film during the growth process [86]. Less intrinsic led to reducing the carrier concentration. In this work, the chemical composition of all films is nearly stoichiometric. Te contents were slightly disappeared by the thermal process. The change of carrier concentration of the deposited films is quite depending on the intrinsic defect inside the films. From XRD patterns, the broad peak is obtained and the intensity diffraction peak tends to decrease while increases the film thickness. The designated thick layer leads to the deposited atoms are created that constitute small nuclei and clusters which is observed that the crystalline size decreases whereas the increase in lattice strain. The lattice strain is increased due to the prevailing recrystallization during the growth process [89-90]. These results observed that the thickness of the deposited film when increasing the deposition time destroys the crystallinity of the films leading to the variation in lattice parameters and the change of the imperfection inside the films. It can be described by calculated lattice strain and dislocation density from XRD patterns. As increase the deposition time, the lattice strain and dislocation density is relatively increased, as seen in table 4.3. This is attributed to the multilayer in the growth process leads to the presence of the voids at the interface leading to the propagation of the dislocation lines in the

lattice [90, 92]. The variation in lattice parameters has confirmed the change of imperfection inside the film as increase the thickness, as seen in figure 4.16. The a-axis is a little changed while those of the c-axis increased as the deposition time. The lattice parameter is altered when the antisite defect increases leading to crystal imperfection [72]. All results indicated that the variation of lattice parameters, lattice strain and dislocation density could be affected by a high carrier concentration.

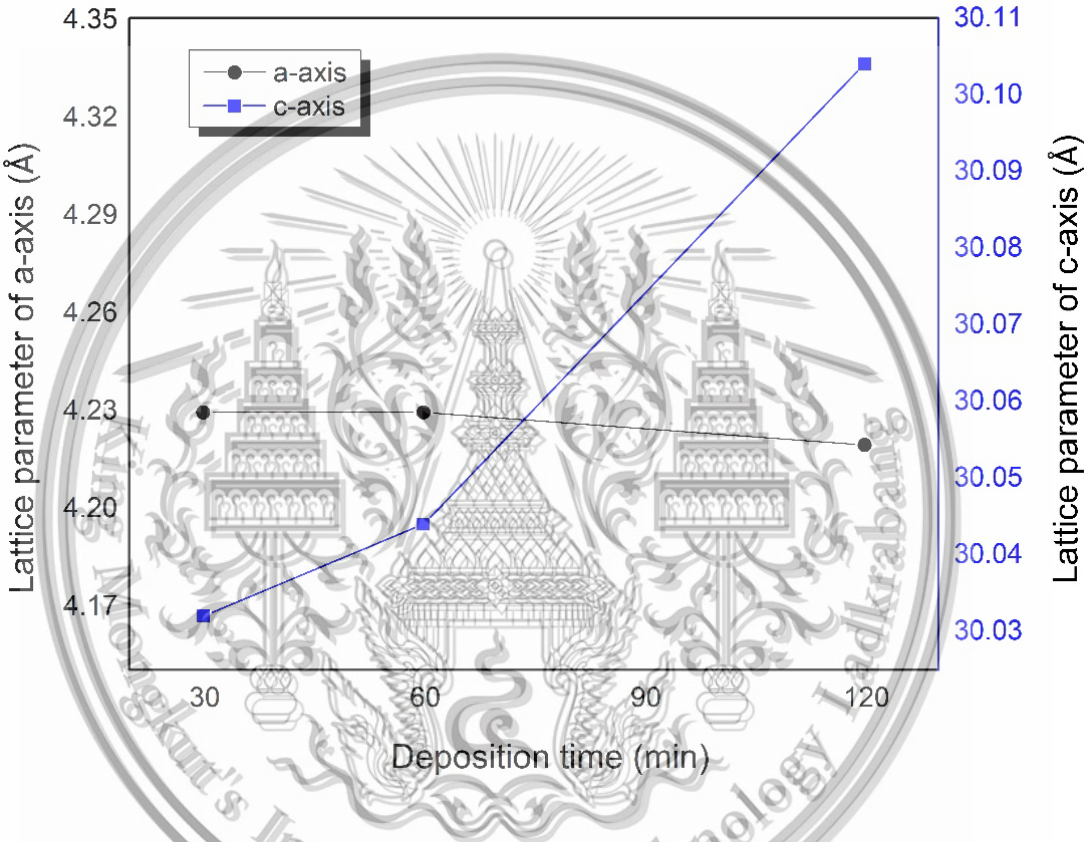

Figure 4.16 Lattice parameters of the deposited Sb_2Te_3 films with different deposition time.

The electrical mobility at room temperature normally depends on the scattering dominated and carrier concentrations. Relatively high mobility can have a moderated carrier concentration [93]. Moreover, the grain of the thick films will grow larger compared with the thin layer, resulting in the reduction of grain boundaries scattering. Thus, the mobility of deposited thick films at a high deposition time is relatively increased. Further increase the deposition time up to 60 min, the mobility slightly decreased, resulting in a rise in carrier concentration. Rougher surface with a small compact grain was obtained as increasing deposition time to 120 min leading to a decreased in electric mobility. As film thickness increased, the variation in the

imperfection inside the crystal is drastically increased [95, 97]. Low electrical mobility was obtained.

The variation of electrical resistivity as a function of deposition time of the Sb_2Te_3 films is exhibited in table 4.4. The results indicated that the electrical resistivity decreases as the film becomes a thin layer. Thin layered structure growth along the in-plane direction (00l) orientation provides a preferential way for carrier transport along the ab-plane as well as gains in the carrier mobility and reduces the electron resistivity [84]. In cases of increasing the film thickness, the electrical resistivity is 2.16×10^{-3}, 1.50×10^{-3} and 1.31×10^{-3} Ω.cm, which decrease with increasing the deposition time 30, 60 and 120, respectively. It is well known that the resistivity is determined by the expression of $\rho = 1/ne\mu$, where n is the carrier concentration, e is the charge unit and μ is the mobility. The decrease resistivity is mainly caused by the increase of the carrier concentration, leading to a rise in electrical resistivity in the films.

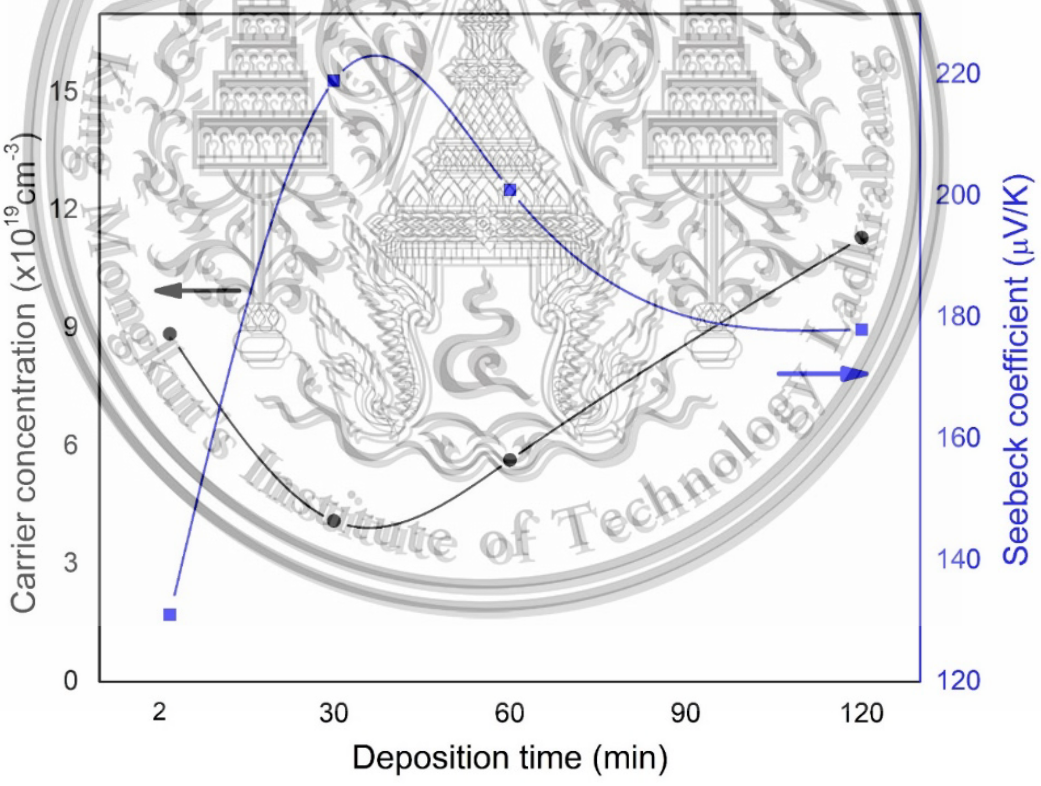

Figure 4.17 Carrier concentration and Seebeck coefficient of deposited Sb_2Te_3 films as a function of deposition time

Carrier concentration and Seebeck coefficient variations as a function of deposition time are exhibited in figure 4.17. The positive Seebeck coefficient of all deposited films is indicated the *P*-type behavior, related to Hall measurements. At near room temperature, the Seebeck coefficient of the layered microstructure film was found at 131 μV/K. This is thought to be related to the deficient of Te that increases the average carrier concentration [98, 101]. The S values are rapidly increased as increasing the thick layer at deposition time 30 min, reached the maximum was 219 μV/K observed. The improvement of crystallinity at a high deposition time leads to an increase in the Seebeck coefficient. Up to increases the deposition time above 30 min, the S values slightly decrease linearly. The variation in S values as a function of deposition time is clearly related inversely to the carrier concentration. The relationship between the Seebeck coefficient and the carrier concentration can be expressed by the Mott relation in equation (4.2). Seebeck coefficient is a factor to reflect the entropy transported per charge carrier and thus decreases as increasing the carrier concentration [102]. As a result, the Seebeck coefficient decreased significantly as the film thickness. This decrease can be explained by the morphology defect inside the films which is observed in lattice strain and dislocation density as the deposition time increases [103].

Temperature dependence of the electrical conductivity of all deposited Sb_2Te_3 films at different deposition times shows in the figure. 4.18(a). The electrical conductivity is slightly decreased during the increase in the applied temperature range of 50-300 °C, which indicated the typical metallic transport behavior. In order to increase the applied temperature, the carrier transport significantly interacts with the impurity inside the film cause to decrease in mobility proportionally to $T^{-3/2}$ [84, 104]. The temperature dependence of the Seebeck coefficient shows an increasing trend in performance as the applied temperature increases, as seen in the figure. 4.18(b). In theory, the Seebeck coefficient is directly dependent on the temperature and inversely depends on the carrier concentration [82]. The maximum Seebeck coefficient was obtained at 240 μV/K at 300°C with a deposition time of 30 min. As the deposition time is above 30 min, the Seebeck coefficient is slightly decrease. The electrical conductivity and the Seebeck coefficient of the deposited films are calculated to obtain the thermoelectric power factor. The temperature dependence of the power factor as a function of deposition time is shown in the figure. 4.18(c). It can be seen that the power factor of layer structure at room temperature is less than 1.5 mW/mK^2. As increasing the deposition time up to 60 min, the maximum power factor is obtained at 2.6 mW/mK^2 due to the enhancement of the electrical conductivity and the Seebeck coefficient. In case of the variation of the applied temperature, the deposited Sb_2Te_3 films exhibit the optimum thermoelectric properties, and the maximum power factor

is raised to 2.73 mW/mK^2, observed at deposition time 60 min with increasing the applied temperature up to 100°C.

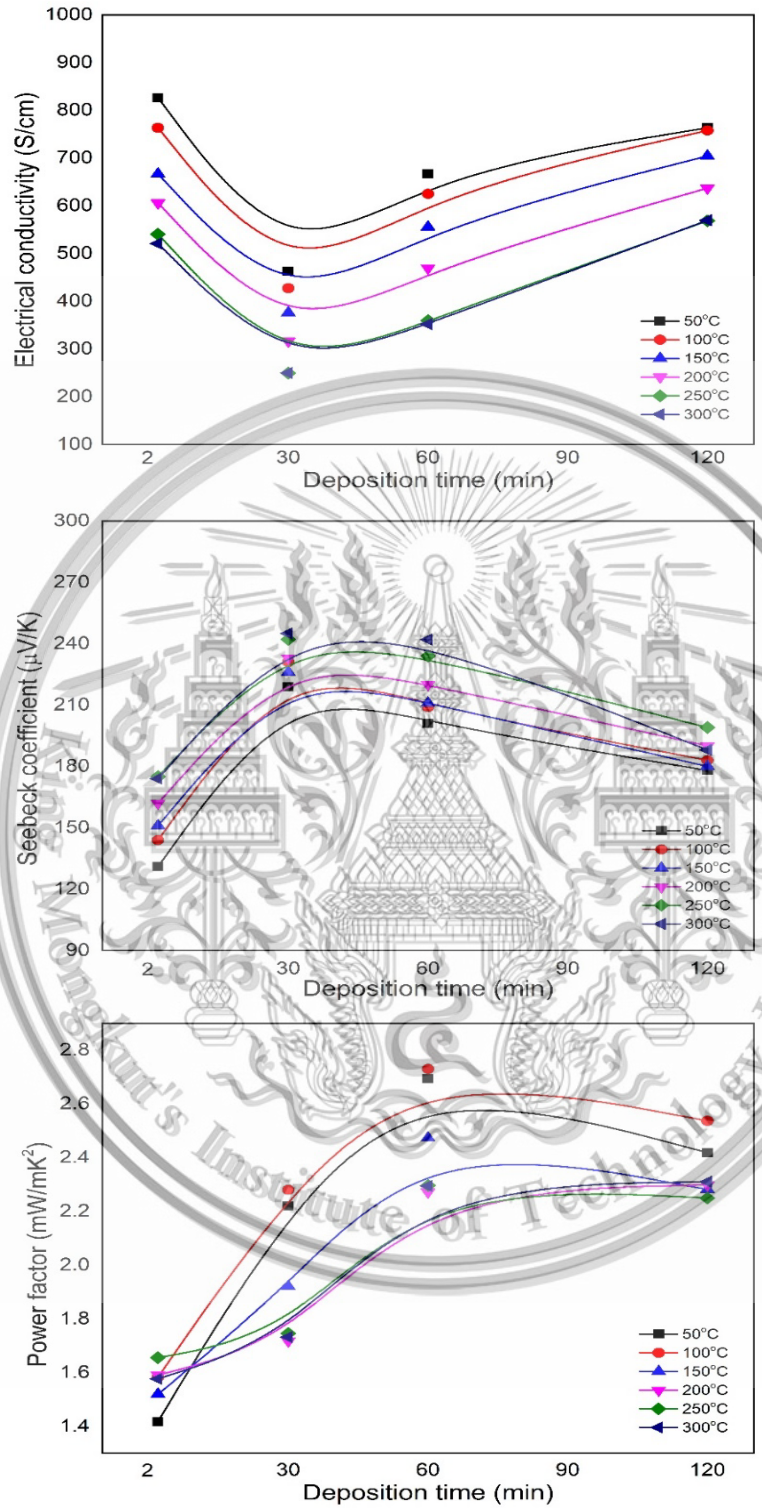

Figure 4.18 Temperature dependence of the thermoelectric properties of Sb_2Te_3 films as a function of deposition time: (a) electrical conductivity, (b) Seebeck coefficient and (c) power factor.

The comparison of thermoelectric properties of deposited Sb_2Te_3 thick film with a few micrometers thickness using various methods is shown in table 4.5. Although this method is a complex and long-term process, the obtained power factor is quite high when compared with another. Thus, it is evident that the selected method with an optimized growth process such as the increase of the deposition time, the change of designated film thickness and the suitable thermal treatment process are important to develop a high efficiency of the deposited Sb_2Te_3 thick films.

Table. 4.5 Comparison of thermoelectric properties of deposited Sb_2Te_3 films in this work and other studies.

Researchers	Method	Thickness (μm)	Resistivity (Ω.m)	PF (mW/mK^2)
H.Shen [43]	co-evaporation	10.0	2.0×10^{-5}	2.5
S.J. Kim [11]	screen printing	-	-	1.0
Z. Cao [6]	screen printing	3.5	5.0×10^{-3}	0.2
O. Vigil-Galan [42]	Close space vapor	15.3	3.0×10^{-5}	0.4
M. Mizoshiri [8]	thermal assisted DC sputtering	100.0	2.0×10^{-5}	1.6
This work	DC sputtering	9.0	1.5×10^{-5}	2.7

4.4 The comparison of the output performance of a planar single leg *P*-type Sb_2Te_3 with different thickness.

In typically, thermoelectric materials are usually characterized by figure of merit. A high figure of merit is an equation to high efficiency of thermoelectric modules (η_{max}), as seen in equation $\eta_{\max} = \frac{\Delta T}{T_h} \times \frac{\sqrt{1+ZT}-1}{\sqrt{1+ZT}+\frac{T_c}{T_h}}$ with an average figure of merit between the hot and cold side temperature. This equation was initially derived by an assumption that the three factors (S, σ, κ) were constants, which were independent of temperature. From this equation, a high-temperature difference and figure of merit

values may produce a high conversion efficiency. In practical use, the efficiency of the design of the thermoelectric generator modules is described by the thermoelectric force, E_T also depends on these factors (S, σ, κ), as seen in the equation.

$$E_T = n \cdot S \cdot \Delta T = n \cdot (S_P - S_n) \cdot (T_H - T_C) \quad (4.6)$$

Where n is the number of thermoelectric modules. To achieve a high thermoelectric force, E_T can effectively be multiplied by connecting the thermoelectric junctions electrically in series and thermally in parallel. Internal resistance $R_i = \frac{\rho \cdot l}{t \cdot w}$ is a key factor to obtain the high efficiency of a thermoelectric material which depends on electrical resistivity and structure dimensions (length: l, thickness: t and width: w). The output electrical power of the thermoelectric materials was described as the efficiency leading to the practical use in a design of thermoelectric generator module. The maximum output power is requested and defined as $P_{max} = \frac{S^2 \Delta T^2 tw}{4\rho l}$. To obtain the maximum output power, thermoelectric material should be a large power factor and simultaneously reducing the internal resistance that relates to the dimension and temperature difference of thermoelectric materials.

The variable of the thickness dimensions and their properties of the deposited Sb_2Te_3 thermoelectric material are measure and compared. The output performance of a planar single leg with different thickness (all samples have the same l and w dimensions) are investigated.

In typically, the practical thermoelectric modules are constructed by the both n- and *P*-type thermoelectric legs. The single leg thermoelectric was only used to evaluate the output characteristics of Sb_2Te_3 with various thickness thermoelectric modules. The measured output characteristic results for the single leg Sb_2Te_3 thermoelectric films on flexible substrate with various thickness dimension are illustrated for five temperature differences ($\Delta T = 18$, 23, 28, 38 and 58 K). The temperature difference on surface of the single leg between hot and cold sides was taken by the IR camera, as shown in figure 4.19. The thermoelectric open circuit voltage (V_{OC}) and current (I_{SC}) of the single leg as a function of temperature difference were measured. The results indicated that the output voltage increased proportionally temperature difference increase. The variable of the electrical potential is derived from the temperature gradient when the sample contact with the heat source [105].

As increases the thickness of the single leg thermoelectric material, the output voltage is increased in linear relationship with the thickness, as illustrated in figure 4.20(a).

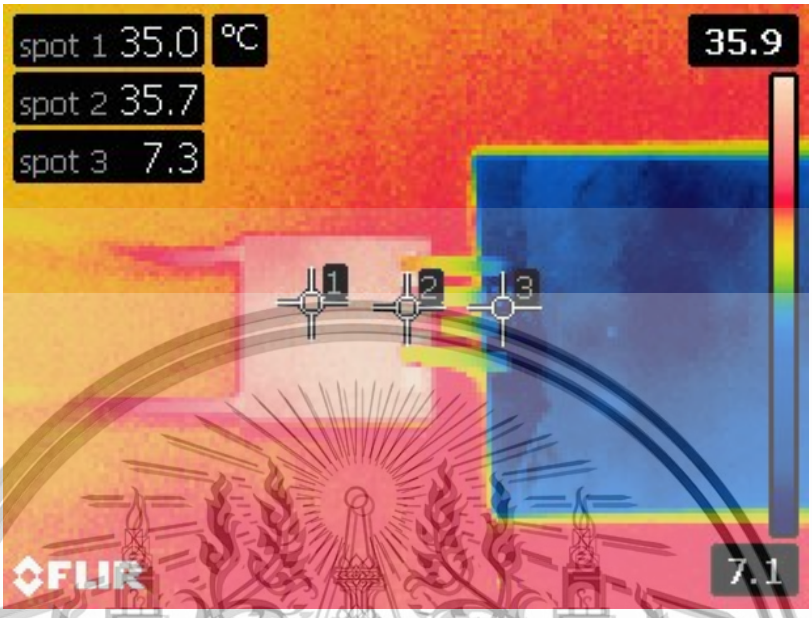

Figure 4.19 Sb_2Te_3 single leg thermoelectric infrared image taken.

Thermoelectric output power curves of the planar single leg Sb_2Te_3 films were calculated depending on the voltage and current as a function of temperature difference. The electrical output power (P_{out}) versus temperature different in the thermoelectric single planar films with a various thickness are measured, as seen in figure 4.20 (b). After applied the temperature difference across the thermoelectric element, the deposited thin film has a relatively low voltage leading to a small forming the thermoelectric power. As increasing the film thickness, the cross-sectional area of the element increases, a high electrical voltage and output power are obtained [41]. As the results, the highest values of planar thermoelectric leg, with thickness 9.0 μm at deposition time 60 min, are 0.75 mV at ΔT = 58 K and the maximum P_{out} are also obtained at 0.032 μW. The results observed that a cross-section areas of the planar single leg and their properties (S,σ) are significantly affect to the output efficiency. When increasing the thickness up to 16.7 μm, the V_{oc} and P_{out} were slightly decreased compare with thickness of 9.0 μm. It may be the reduction of the film properties during growth as increasing the film thickness resulting in the decrease of the output efficiency. The results indicated that the limit of the growth process are

obtained at deposition time of 60 min with film thickness 9.0 μm, which is partially affect to output performance.

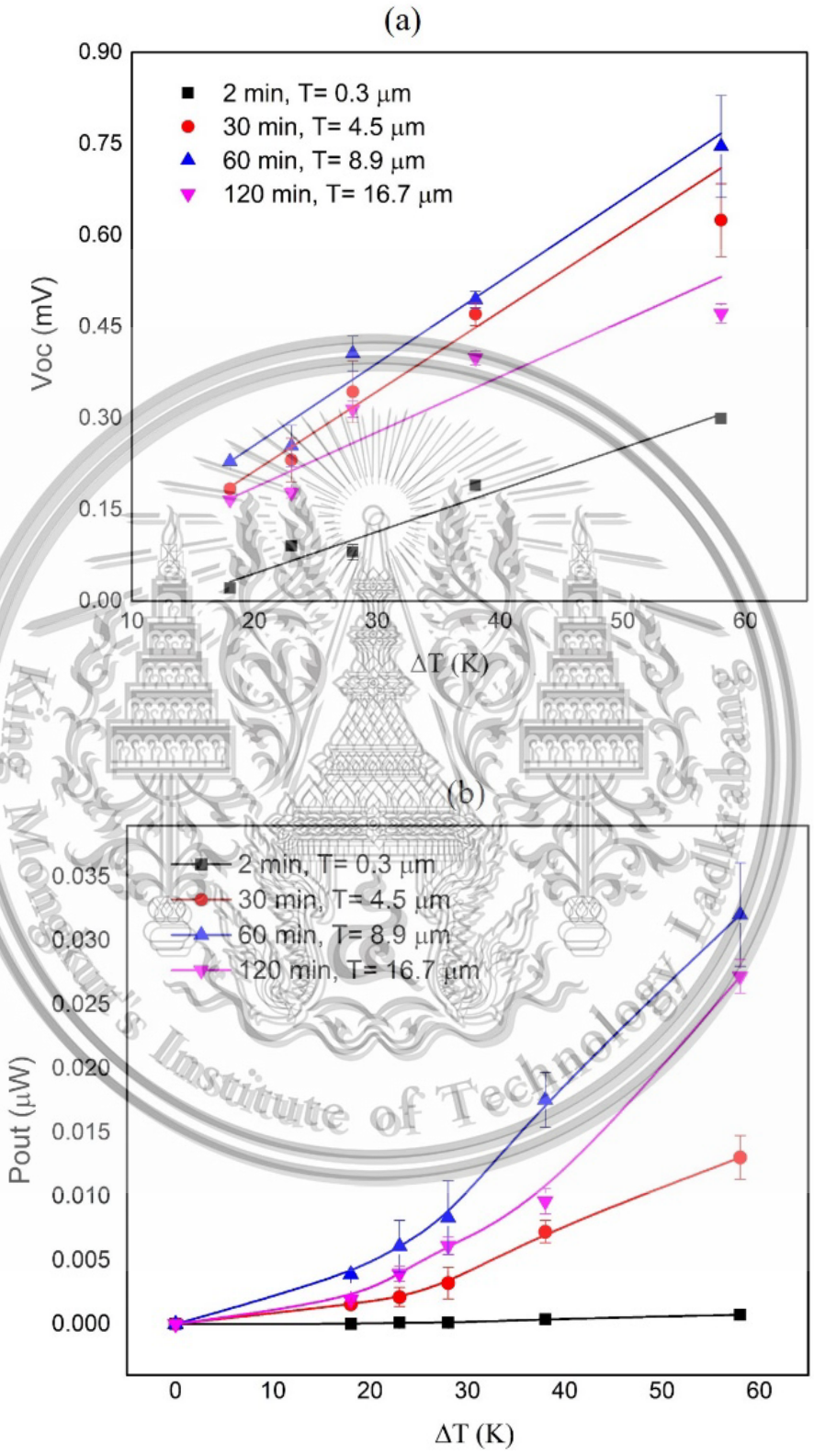

Figure 4.20 (a) the electrical voltage and (b) the calculated output power of single planar Sb_2Te_3 films as different thickness.

Chapter 5
Conclusions and suggestions

5.1 Conclusions

Thermoelectric Sb_2Te_3 thin films were deposited on polyimide flexible substrate by thermal-assisted DC magnetron sputtering operated at the pre-heat substrate of 400°C and sputtering pressure of 2.6×10^{-2} mbar. The various of sputtering power densities of 30, 35, 40, 45 and 50 W were applied. As increase the sputtering power, the argon ions become more energetic and could release more energy to the compound target led to the higher kinetic energy of the deposited atoms. The results show that the sputtering power had a significant effect and controlled the structural, chemical stoichiometry, electrical and thermoelectric properties of the films. The deposited film had larger grains and crystallinity improved as the power increased. However, the stoichiometry of the deposited films slightly changed due to Te evaporation as thermal transport increased. As well as chemical composition, Te evaporation affected carrier concentration and the number of lattice defects which led to a reduced Seebeck coefficient. The largest Seebeck coefficient, 209 μV/K at 300°C, was obtained at a sputtering power of 35 W due to the nearly stoichiometric composition. The maximum power factor, 1.95 mW/K^2m, was found at an optimized sputtering power of 45 W with temperature operated at 300°C.

Sb_2Te_3 thick films more than 10 nm in thickness were deposited by DC magnetron sputtering operated at a pre-heat substrate of 400°C, sputtering pressure of 2.6×10^{-2} mbar and sputtering power 45W. The enhancement of thermoelectric properties of the thick films was developed by the annealing treatment process. Both of deposition and heat treatment processes of the films are related to the mobility of the atoms at the substrate surface during growth. If atoms have sufficient energy to overcome the surface diffusion barriers, the atoms will have more energy to diffuse, agglomerate, and finally rearrange into a fine structure. As the results, the crystalline size and atomic composition of thick films depend on the annealing temperature and annealing time. The largest crystalline size with a slightly decreased %Te is observed for the film annealed at 350°C for 30 min. The correlation between porosity and carrier transport/phonon scattering was illustrated. The pore surface area significantly decreases with increasing annealing temperature and annealing time. A maximum

power factor of 1.72 mW/K^{2}m with annealing of 350ºC for 30 min with temperature operated at 50ºC is obtained.

In order to identify the practical use of the Sb_2Te_3 films, the designated thickness layer is studied with operating conditions at a pre-heat substrate of 400ºC, sputtering pressure of 2.6×10^{-2} mbar, sputtering power 45W and post-annealing temperature of 350ºC for 30 min. To obtain a high output efficiency, thermoelectric material should be a large power factor and simultaneously reducing the internal resistance that relates to the dimension and temperature difference of thermoelectric materials. The designated thickness dimension with different deposition time of 2, 30, 60 and 120 min were prepared. The correlation between the thickness variance with increase deposition time and the structural, grain size, surface morphology and thermoelectric properties are investigated. As increasing the thickness, the atomic ratio of all deposited films is shown a near stoichiometry. The crystallinity, grain size and surface roughness enhance as increasing the deposition time to 60 min. when the deposition time increases to 120 min, the cluster size reduces leading to their structure, grain and thermoelectric properties are relative decreased. As a result, it is cleared that the sputtering growth and the heat treatment process are related to the diffusion of deposited atoms on the substrate surface and related to the appearance of microstructure and morphology. The residual stress is generally accumulated as increasing of the deposition time. It may be thermal energy is not enough to diffuse and agglomerate the deposited atom on the surface of the critical thick layer leading to obtained a small compact grain and increased the imperfection defect inside the films. The imperfections inside the film are affected by their electrical and thermoelectric properties. The obtained maximum power output factor is 2.7 mW/ K^{2}m obtained with deposition time 60 min with applied temperature of 100ºC.

In the case of the measured and compared the output performance of a planar single leg of the Sb_2Te_3 films with different thickness. To obtain the maximum output power, thermoelectric material should be a large power factor and simultaneously reducing the internal resistance that relates to the cross-sectional areas of the planar single leg of the deposited films. The electrical output was generated by the temperature gradient along the single leg, the open-circuit voltage and short circuit current are obtained. Experimental characterization showed that the increased the thickness of the film of 9.0 μm at deposition time 60 min can produce 0.032 μW (0.75 mV) at the temperature difference of 58 K. Up to 16.7 μm thickness at deposition 120 min, the V_{oc} and P_{out} were slightly decreased which may be the reduction of their

properties, resulting in the decrease in the power factor. As the results indicated that the increase of thickness of the planar single leg (cross-sectional area) is partial effect on the output efficiency. The properties of thick films are also expected for the practical use of thermoelectric elements.

The practical thermoelectric modules is constructed by many parts of n- and *P*-type thermoelectric legs which generated the output power from nanowatt to sub-microwatt to use with electronic devices as a temperature sensor or LED lights. The expectation of this thesis implies that the focused on the improvement of the Sb_2Te_3 thermoelectric materials to design the thermoelectric device with efficient energy harvesting abilities in the future.

5.2 Suggestions

1. Long-term stability of flexible Sb_2Te_3 planar single leg should carried out with the human body waste heat.

2. Thick film thermocouples and a systematic measurement should be studied to comprehensively study the stability and reliability of the fabricated devices.

References

[1] X. Duan and Y. Jiang "Annealing effects on the structural and electrical transport properties of n-type $Bi_2Te_{2.7}Se_{0.3}$ thin films deposited by flash evaporation" Applied Surface Science 256 (2010) 7365–7370.

[2] T. Plechacek and J. Horak "Point defects in Pb-doped Sb_2Te_3 single crystals" J. Solid State Chem. 145 (1999) 197–203.

[3] M. Tan, Y. Deng and Y. Hao "Enhanced thermoelectric properties and layered structure of Sb_2Te_3 films induced by special (00l) crystal plane" Chem. Phys. Lett. 584 (2013) 159–164.

[4] K. Rajasekar, L. Kungumadevi, A. Subbarayan and R. Sathyamoorthy "Thermal sensors based on Sb_2Te_3 and $(Sb_2Te_3)_{70}(Bi2Te_3)_{30}$ thin films" Ionics 14 (2008) 69–72.

[5] L.M. Goncalves, C. Couto, P. Alpuim, A.G. Rolob, F. Völklein and J.H. Correia "Optimization of thermoelectric properties on Bi_2Te_3 thin films deposited by thermal co-evaporation" Thin Solid Films 518 (2010) 2816–2821.

[6] S.J. Kim, J.H. Wea, J.S. Kim, G.S. Kim and B.J. Cho "Thermoelectric properties of *P*-type Sb_2Te_3 thick film processed by a screen-printing technique and a subsequent annealing process" J. Alloys Compd. 582 (2014) 177–180.

[7] Z. Cao, E. Koukharenko, R.N. Torah, J. Tudor and S.P. Beeby "Flexible screen printed thick film thermoelectric generator with reduced material resistivity" Journal of Physics: Conference Series 557 (2014) 012016.

[8] J.H. Wea, S.J. Kim, G.S. Kim and B.J. Cho "Improvement of thermoelectric properties of screen-printed Bi_2Te_3 thick film by optimization of the annealing process" J. Alloys Compd. 552 (2013) 107–110.

[9] N.H. Trung, K. Sakamoto, N.V. Toan and T. Ono "Synthesis and evaluation of thick films of electrochemically deposited Bi_2Te_3 and Sb_2Te_3 thermoelectric materials" Materials 10 (2017) 1–17.

[10] H. Shen, S. Lee, J. Kanga, T.Y. Eom, H. Lee and S. Han "Thickness dependence of the electrical and thermoelectric properties of co-evaporated Sb_2Te_3 film" Appl. Surf. Sci. 429 (2018) 115–120.

[11] M. Mizoshiri, M. Mikami and K. Ozaki "*P*-Type Sb_2Te_3 and n-type Bi_2Te_3 films for thermoelectric modules deposited by thermally assisted sputtering method, Jpn. J. Appl. Phys. 52 (2013) 06GL071–06GL076.

[12] S. Shena, W. Zhua, Y. Denga, H. Zhaob, Y. Penga and C. Wanga, "Enhancing thermoelectric properties of Sb_2Te_3 flexible thin film through microstructure

control and crystal preferential orientation engineering" Applied Surface Science 414 (2017) 197–204.

[13] T. Chen, P. Fan, Z. Zheng, D. Zhang, X. Cai, G. Liang and Z. Cai, "Influence of substrate temperature on structural and thermoelectric properties of antimony telluride thin films fabricated by RF and DC cosputtering" Journal of ELECTRONIC MATERIALS Vol. 41, No. 4 (2012) 679-683.

[14] T. Khumtong, A. Sakulkalavek and R. Sakdanuphab, "Empirical modelling and optimization of pre-heat temperature and Ar flow rate using response surface methodology for stoichiometric Sb_2Te_3 thin films prepared by RF magnetron sputtering" Journal of Alloys and Compounds 715 (2017) 65-72.

[15] J-C. Yang, X-Q. Meng, C-T. Yang and Y. Zhang, "Influence of sputtering power on crystal quality and electricalproperties of Sc-doped AlN film prepared by DC magnetron sputtering" Applied Surface Science 287 (2013) 355– 358.

[16] F. Anjum, R. Ahmad, N. Afzal and G. Murtaza, "Characterization of InN films prepared using magnetron sputtering at variable power" Materials Letters 219 (2018) 23–28.

[17] T. Windbacher, V. Sverdlov and S. Selberherr, "Chapter 1 Classical Device Modeling" Institute for Microelectronics, Gußhausstraße 27–29/E360, 1040 Vienna, Austria.

[18] N. Ghafouri, "Bismuth Telluride and Antimony Telluride Based Co-evaporated Thermoelectric Thin Films:Technology, Characterization, and Optimization" Doctor of Philosophy (Electrical Engineering), The University of Michigan 2012.

[19] Z. Yu, "Fabrication and physical propertied of thermoelectric thin film" Master of Engineering by research, Institute for superconducting and electronic materials, University of Wollongong 2011.

[20] X. Wang, H. He, N. Wang, L. Miao, "Effects of annealing temperature on thermoelectric properties of Bi_2Te_3 films prepared by co-sputtering" Applied Surface Science 276 (2013), 539-542.

[21] M. Grundmann, "The Physics of Semiconductors an Introduction Including Nanophysics and Applications" Third Edition. Institut für Experimentelle Physik II Universität Leipzig Germany.

[23] S.O. Kasap, "Principles of electronic materials and devices" Third Edition. The McGraw-Hill companies, Univesity of Saskatchewon Canada.

[24] P. Wanarattikan, P. Jitthammapirom, R. Sakdanuphab and A. Sakulkalavek, "Effect of Grain Size and Film Thickness on the Thermoelectric Properties of Flexible Sb_2Te_3 Thin Films" Hindawi Advances in Materials Science and Engineering Vol. 2019 (2018).

[25] H. Liu, Y. Wang, D. Mei, Y. Shi and Z. Chen, “Design of a Wearable Thermoelectric
Generator for Harvesting Human Body Energy” In book: Wearable Sensors and Robots 55-66.

[26] N. M. Ravindra, B. Jariwala, A. Bañobre and A. Maske, “Thermoelectrics Fundamentals Materials Selection Properties and Performance” SpringerBriefs in Materials, Department of Physics New Jersey Institute of Technology Newark, NJ, United states of America.

[27] B. Fang, Z. Zeng, X. Yan and Z. Hu, “Effects of annealing on thermoelectric properties of Sb_2Te_3 thin films prepared by radio frequency magnetron sputtering” Journal of Materials Science Materials in Electronics 24 (2013) 1105–1111.

[28] J. Martin, Li Wang, L. Chen, G.S. Nolas, “Enhanced Seebeck coefficient through energy-barrier scattering in PbTe nanocomposites”. Physical Review B, 79 (11) (2009), 115311–. doi:10.1103/PhysRevB.79.115311.

[29] V. Teixeira, J. Carneiro, P. Ccrvalho, E. Silva, S. Azevedo and C. Batista, “High barrier plastics using nanoscale inorganic films” Woodhead Publishing Limited, University of Minho, Portugal 2011.

[30] T.R.R. Sing, H. Mcmillan, K. Mooney, A.Z. Alkilani and R.F. Donnelly, “Microneedles for drug delivery and monitoring” Woodhead Publishing Limited, Queens University Belfast, United Kinhdom 2013.

[31] K. Wasa, I. Kanno and H. Kotera, “Handbook of Sputter Deposition Technology Fundamentals and Applications for Functional Thin Films, Nanomaterials, and MEMS” Second Edition, William Andrew is an imprint of Elsevier 2012.

[32] K. Wasa, M. Kitabatake and H. Adachi, “THIN FILM MATERIALS TECHNOLOGY Sputtering of Compound Materials” William Andrew, Inc.

[33] E. Alfonso, J. Olaya and G. Cubillos, “Thin Film Growth through Sputtering Technique and Its Applications” Universidad Nacional de Colombia, Colombia

[34] R.M. Park, H.A. Mar and N.M. Salansky, “Molecular beam epitaxy growth of ZnSe on (100) GaAs by compound source and separate source evaporation: A comparative study” Journal of Vacuum Science & Technology B 3, (1985) 676-680.

[35] W. Stutius, “Organometallic vapor deposition of epitaxial ZnSe films on GaAs substrates” Applied Physics Letters 33, 656 (1978)

[36] J.A. Thornton, “Influence of apparatus geometry and deposition conditions on the structure and topography of thick sputtered coatings” Journal of Vacuum Science & Technology 11, (1974) 666-670.

[37] A. Enokihara, H. higashino, K. Setsune, T. mitsuyu and K. wasa, “Superconductivity in 2-μm Wide Strip Line of Gd-Ba-Cu-O Thin Film Fabricated by LowTemperature Processes” Japanese Journal of Applied Physics Vol. 27 No.8 (1998) L1521-L1523.

[38] MIT OpenCourseWare, “X-RAYS AND X-RAY DIFFRACTION” 3.091SC Introduction to Solid State ChemistryIntroduction to Solid State Chemistry, Lecture Notes No. 5 1-18.

[39] R. Guinebretière, “X-ray Diffraction by Polycrystalline Materials” published in Great Britain and the United States in 2007 by ISTE Ltd,.

[40] D. Semnani, “Geometrical characterization of electrospun nanofibers” Iran Elsevier Ltd. Isfahan University of Technology, Iran 2017.

[41] A. Chauhan, “Deformation and damage mechanisms of ODS steels under high-temperature cyclic loading” Doktor der Ingenieurwissenschaften der Fakultät für Maschinenbau Karlsruher Institut für Technologie (KIT) 2018.

[42] R.F. Egerton, “Physical Principles of Electron Microscopy An Introduction to TEM, SEM, and AEM” Springer Science+Business Media, Inc. Department of Physics, University of Alberta , Canada 2005.

[43] M. Balestrieri, “Transparent conductive oxides with photon converting properties in view of photovoltaic applications : the cases of rare earth-doped zinc oxide and cerium oxide” Université de Strasbourg, 2014.

[44] N. Ngo, H. Niu, P. Bharadwaj, H. Bhatti and S. Adhikari, “Van der Pauw Resisitivity Measurement” Technical Report 2017.

[45] ULVAC Group Companies, “Electric Resistance Measurement System ZEM- 3 series”

[46] H.J. Lee, S. Hyun , H.S. Park and S.W. Han “Thermoelectric properties of n-type Bi–Te thin films with various compositions” Microelectronic Engineering 88 (2011) 593–596.

[47] S-R. Jian, P H. Le, C-W. Luo and J-Y. Juang “Nanomechanical and wettability properties of Bi_2Te_3 thin films: Effects of post annealing” Journal of Applied Physics 121 (2017) 175302-1 - 175302-5.

[48] K. Takayama and M. Takashiri “Multi-layered-stack thermoelectric generators using *P*-type Sb_2Te_3 and n-type Bi_2Te_3 thin films by radio-frequency magnetron sputtering” Vacuum 144 (2017) 164-171.

[49] M.F. Eliana, J. Vieira, Figueira, L. Ana, J. Pires, Grilo, F. Manuel, A.M. Silva Pereira and L.M. Goncalves “Enhanced thermoelectric properties of Sb_2Te_3 and Bi_2Te_3 films for flexible thermal sensors” Journal of Alloys and Compounds 774 (2019) 1102-1116.

[50] S.J. Kim, J. H. Wea, J.S. Kim, G.S. Kim and B.J. Cho "Thermoelectric properties of *P*-type Sb_2Te_3 thick film processed by a screen-printing technique and a subsequent annealing process" Journal of Alloys and Compounds 582 (2014) 177–180.

[51] P. Markowski and A. Dziedzic "Experimental characterization of thermoelectric properties of thick film composites" International Microelectronics And Packaging Society JMEP, Vol. 3 No.2, 2nd Qtr 2006.

[52] C.L. Cramer "Thermoelectric properties of Si/Sic thin-film superlattices growth by Ion beam sputtering" the Degree of Master of Science Colorado State University Fort Collins, Colorado 2015.

[53] K.H. Lee, Y. Mune, H. Ohta and K. Koumoto "Thermal Stability of Giant Thermoelectric Seebeck Coefficient for $SrTiO_3/SrTi_{0.8}Nb_{0.2}O_3$ Superlattices at 900K" Applied Physics Express 1 (2008) 015007-1 - 015007-3.

[54] Tapan K. Gupta "Handbook of thick- and thin-film hybrid microelectronics" John Wiley & Sons, Inc. Hoboken, New Jersey. 2003.

[55] T.G. Novak, K. Kim and S. Jeon "2D and 3D nanostructuring strategies for thermoelectric materials" Nanoscale, 2019, 11, 19684–19699.

[56] B. Fang, Z. Zeng, X. Yan and Z. Hu "Effects of annealing on thermoelectric properties of Sb_2Te_3 thin films prepared by radio frequency magnetron sputtering" J Mater Sci: Mater Electron (2013) 24:1105–1111.

[57] M. Takashiri, S. Tanaka and K. Miyazaki "Improved thermoelectric performance of highly-oriented nanocrystalline bismuth antimony telluride thin films" Thin Solid Films 519 (2010) 619–624.

[58] J.C. Yang, X.-Q Meng, C.T Yang and Y. Zhang "Influence of sputtering power on crystal quality and electricalproperties of Sc-doped AlN film prepared by DC magnetron sputtering" Applied Surface Science 287 (2013) 355–358.

[59] H. Shena, S. Lee, J-G. Kanga, T-Y. Eom, H. Lee, and S. Han "Thickness dependence of the electrical and thermoelectric propertiesof co-evaporated Sb_2Te_3 films" Applied Surface Science Vol 429 (2018) 115-120.

[60] H. Shen, S. Lee, J-G. Kang, T-Y. Eom, H. Lee, C. Kang, and S. Han "Thickness effects on the microstructure and electrical/thermoelectric properties of co-evaporated Bi-Te thin films" Journal of Alloys and Compounds vol 767 (2018) 522-527.

[61] S. Jin Kim, J. Hyung Wea, J. Sang Kim, G. Soo Kim and B. Jin Cho "Thermoelectric Properties of *P*-type Sb_2Te_3 Thick Film Processed by a Screen-printing technique and a Subsequent Annealing Process" Journal of Alloys and Compounds Vol. 582 177-180.

[62] Z. Cao, E. Koukharenko, R.N. Torah, J. Tudor and S.P. Beeby "Flexible screen printed thick film thermoelectric generator with reduced material resistivity" Journal of Physics: Conference Series 557 (2014) 012016.

[63] O. Vigil-Galan, F. Cruz-Gandarilla, J. Fandino, F. Roy, J. Sastre-Hernandez and G. Contreras-Puente "Physical properties of Bi_2Te_3 and Sb_2Te_3 films deposited by close space vapor transport" SEMICONDUCTOR SCIENCE AND TECHNOLOGY 24 (2009) 025025 .

[64] M. Mizoshiri, M. Mikami and K. Ozaki "*P*-Type Sb_2Te_3 and n-Type Bi_2Te_3 Films for Thermoelectric Modules Deposited by Thermally Assisted Sputtering Method" Japanese Journal of Applied Physics 52 (2013) 06GL07.

[65] R. Rudež, P. Markowski, M. Presečnik, M. Košir, A. Dziedzic and S. Bernik "Development of thick-film thermoelectric micro generators based on *P*-type $Ca_3Co_4O_9$ and n-type $(ZnO)_5In_2O_3$ legs" Ceramics International 41 (2015) 13201–13209.

[66] K.-Y.Chan, and B.S. Teo, "Sputtering power and deposition pressure effects on the electrical and structural properties of copper thin films". Journal of Materials Science, 40(22), (2005) 5971–5981. doi:10.1007/s10853-005-1362-8.

[67] S. Kianwimol, P. Wanarattikan, R. Sakdanuphab, P. Pluengphon, T. Bovornratanaraks, and A. Sakulkalavek, "Experimental Study on Flexible Bismuth Telluride Thin Films Deposited by DC Sputtering at Different Powers" Journal of Electronic Materials (2019). doi:10.1007/s11664-019-07100-1.

[68] X. Duan, J. Yang, W. Zhu, X.A. Fan, S.Q. Bao, Thickness and temperature dependence of electrical resistivity of *P*-type $Bi_{0.5}Sb_{1.5}Te_3$ thin films prepared by flash evaporation method. Journal of Physics D: Applied Physics, 39(23) 5064–5068 (2006), https://doi:10.1088/0022-3727/39/23/024.

[69] A. Kosarian, M. Shakiba, and E. Farshidi "Role of sputtering power on the microstructural and electro-optical properties of ITO thin films deposited using DC sputtering technique". IEEJ Transactions on Electrical and Electronic Engineering, 13(1) (2017) 27–31. doi:10.1002/tee.22494.

[70] Xiao, W., Deng, H., Zou, S., Ren, Y., Tang, D., Lei, M., ... Chen, Y. (2018). Effect of roughness of substrate and sputtering power on the properties of TiN coatings deposited by magnetron sputtering for ATF. Journal of Nuclear Materials, 509, 542–549. doi:10.1016/j.jnucmat.2018.07.011.

[71] X. Zhang, Z. Zeng, C. Shen, Z. Zhang, Z. Wang, C. Lin, Z. Hu, Investigation on the electrical transport properties of highly (00l)-textured Sb_2Te_3 films deposited by molecular beam epitaxy. Journal of Applied Physics, 115(2), (2014).024307. https://doi:10.1063/1.4861394.

[72] G. D. Deshmukh, S. M. Patil, S. S. Patil, P. H. Pawar, Effect of Film Thickness on Structural and Optical Properties of Bi_2Te_3 Thin Films, J. Chem. Bio. Phy. Sci. Sec. C, (2015) Vol.5, No.3; 2769-2779.

[73] D.J. Li, M. Tan, G.Q. Liu, H. Liu, X. Sun, Preparation and characterization of ZrB_2/AlN multilayers by N^+ beam assisted deposition, Surf. Coat. Technol. 205 (2011), https://doi.org/10.1016/j.surfcoat.2011.01.028.

[74] H.-J. Lee, H. S.Park, S. Han, and J. Y.Kim, "Thermoelectric properties of n-type Bi–Te thin films with deposition conditions using RF magnetron co-sputtering". Thermochimica Acta, 542, 57–61 (2012). doi:10.1016/j.tca.2012.01.003.

[75] A. Chaoumead, Y. Sung, and D.-J. Kwak, "The Effects of RF Sputtering Power and Gas Pressure on Structural and Electrical Properties of ITiO Thin Film" Advances in Condensed Matter Physics (2012). 1–7. doi:10.1155/2012/651587.

[76] H. C. Kim, T.S. Oh, and D.B. Hyun, "Thermoelectric properties of the *P*-type Bi_2Te_3–Sb_2Te_3–Sb_2Se_3 alloys fabricated by mechanical alloying and hot pressing" Journal of Physics and Chemistry of Solids, 61(5), (2000) 743–749. doi:10.1016/s0022-3697(99)00269-3.

[77] Z. Yu, C. Yan, T. Huang, W. Huang, Y. Yan, Y. Zhang, and Y. Zhao, "Influence of sputtering power on composition, structure and electrical properties of RF sputtered $CuIn_{1-x}Ga_xSe_2$ thin films". Applied Surface Science, 258(13), (2012). 5222–5229. doi:10.1016/j.apsusc.2012.01.152.

[78] X. Han, Z. Zhang, Z. Liu, C. Xu, X. Lu, L. Sun, P. Jiang, Effects of thickness on thermoelectric properties of Bi0.5Sb1.5Te3 thin films, Applied Nanoscience. (2020) 10:2375–2381. https://doi.org/10.1007/s13204-020-01441-8.

[79] P. Fan, Z.H. Zheng, G.-X, Liang, D-P. Zhang, and X.M. Cai, "Thermoelectric characterization of ion beam sputtered Sb2Te3 thin films" Journal of Alloys and Compounds, 505(1), 278–280. (2010). doi:10.1016/j.jallcom.2010.06.046.

[80] T. Khumtong, P. Sukwisute, A. Sakulkalavek, R. Sakdanuphab, "Microstructure and Electrical Properties of Antimony Telluride Thin Films Deposited by RF Magnetron Sputtering on Flexible Substrate Using Different Sputtering Pressures" Journal of Electronic Materials, 46(5), 3166–3171 (2017). doi:10.1007/s11664-017-5303-5.

[81] S.Shengfei, Z. Wei, D. Yuan, Z. Huaizhou, P.Yuncheng, W. Chuanjun, "Enhancing thermoelectric properties of Sb_2Te_3 flexible thin film through microstructure control and crystal preferential orientation engineering" Applied Surface Science, 414, 197–204. (2017). doi:10.1016/j.apsusc.2017.04.074.

[82] P. Nuthongkum R. Sakdanuphab M. Horprathum A. Sakulkalavek "[Bi]:[Te] Control, Structural and Thermoelectric Properties of Flexible Bi_xTe_y Thin Films Prepared by RF Magnetron Sputtering at Different Sputtering Pressures" Journal of Electronic Materials, doi:10.1007/s11664-017-5671-x. (2017).

[83] L. Tantan, D. Hongmei, C. Huiyi, Z. Wenliang, Z. Jun, L. Jian, Y. Pingxiong, C. Junhao, "Structural, optical and electrical properties of Sb_2Te_3 films prepared by pulsed laser deposition" Journal of Crystal Growth, 416,78–81. (2015). doi:10.1016/j.jcrysgro.2015.01.022

[84] N. Somdock, S. Kianwimol, A. Harnwunggmoung, A. Sakulkalavek., R. Sakdanuphab, Simultaneous stoichiometric composition and highly (00l) orientation of flexible Bi_2Te_3 thin films via optimising the DC magnetron sputter-deposition process" Journal of Alloys and Compounds, 773, 78–85 (2019). doi:10.1016/j.jallcom.2018.09.216

[85] M. Kumari, Y.C. Sharma, Effect of alternate layers of Bi_2Te_3-Sb_2Te_3 on structural, optical and thermoelectric properties, Chalcogenide Letters, 17 (2) (2020) 59 – 67.

[86] H-J. Lee, H.S. Park, S. Han, J.Y. Kim, Thermoelectric properties of n-type Bi–Te thin films with deposition conditions using RF magnetron co-sputtering. Thermochimica Acta, 542, (2012) 57–61. https:// doi:10.1016/j.tca.2012.01.003.

[87] Z-H. ZhengJ-T. Luo, JF. Li, G-X. Liang, F. Ping, "Enhanced thermoelectric performance of *P*-type Sb_2Te_3 thin films through organic-inorganic hybridization on flexible substrate" Current Applied Physics, (2019). S156717391930029X–. doi:10.1016/j.cap.2019.01.019.

[88] V.D. Mote, Y. Purushotham, B.N. Dole, "Williamson-Hall analysis in estimation of lattice strain in nanometer-sized ZnO particles" Journal of Theoretical and Applied Physics, 6(1), (2012). doi:10.1186/2251-7235-6-6.

[89] J. Raj Mohamed, L. Amalraj, Effect of precursor concentration on physical properties of nebulized spray deposited In2S3 thin films. Journal of Asian Ceramic Societies, 4(3) (2016) 357–366. https:// doi:10.1016/j.jascer.2016.07.002.

[90] R. David Prabu, S. Valanarasu, V. Ganesh, M. Shkir, S. AlFaify, A. Kathalingam, Investigation of molar concentration effect on structural, optical, electrical, and photovoltaic properties of spray-coated Cu2O thin films. Surface and Interface Analysis, 50(3) (2018) 346–353. https:// doi:10.1002/sia.6374.

[91] L.M. Goncalves; C. Couto; P. Alpuim; A.G. Rolo; F. Völklein; J.H. Correia (2010). Optimization of thermoelectric properties on Bi_2Te_3 thin films deposited by thermal co-evaporation, Thin Solid Films 518(10), 2816–2821. doi:10.1016/j.tsf.2009.08.038.

[92] M. Tangi, A. De, S.M. Shivaprasad, Role of dislocations and carrier concentration in limiting the electron mobility of InN films grown by plasma assisted molecular beam epitaxy. Journal of Applied Physics, 123(1) (2018) 015701. https://doi:10.1063/1.5008903.

[93] L. M. Goncalves, P. Alpuim, A.G. Rolo, J.H. Correia, Thermal co-evaporation of Sb_2Te_3 thin-films optimized for thermoelectric applications. Thin Solid Films, 519(13) (2011) 4152–4157. https://doi:10.1016/j.tsf.2011.01.395.

[94] J-H. Kim, J-Y. Choi, J-M Bae, M-Y. Kim, T-S. Oh, "Thermoelectric Characteristics of n-Type Bi_2Te_3 and *P*-Type Sb_2Te_3 Thin Films Prepared by Co-Evaporation and Annealing for Thermopile Sensor Applications" MATERIALS TRANSACTIONS, 54(4), 618–625 (2013). doi:10.2320/matertrans.m2013010

[95] V. Balasubramanian, P. Naresh Kumar, D. Sengottaiyan, "Effect of the annealing temperature on the current-voltage and Hall effect studies of Bi_2S_3 thin films grown on glass substrates by using chemical bath deposition" Adv. Appl. Sci. Res. 6(4) (2015) 190-195

[96] L. Bin, H. Songbai, L. Wei, D. Xia, F. Lianghuan, Z. Jingquan, W. Lili, C. Yaping, L. Bing, L. Zhi, "Thin Films by Coevaporation. International Journal of Photo energy", 1–4 (2010). doi:10.1155/2010/476589

[97] T. Duong Van, Q. Nguyen Van, H. Nguyen Thi Minh, H. Nguyen Thi, C. Sunglae, T. Duong Anh, D. Dang Duc, T. Tran Van, "Optimizing the Carrier Density and Thermoelectric Properties of Sb_2Te_3 Films by Using the Growth Temperature" Journal of the Korean Physical Society, 72(8), (2018) 915–919. doi:10.3938/jkps.72.915

[98] R. Sathyamoorthy, J. Dheepa, Structural characterization of thermally evaporated Bi2Te3 thin films. Journal of Physics and Chemistry of Solids, 68(1) (2007) 111–117. https://doi:10.1016/j.jpcs.2006.09.014.

[99] T. Ming, D. Yuan, H. Yanming, "Enhanced thermoelectric properties and layered structure of Sb_2Te_3 films induced by special (00l) crystal plane" Chemical Physics Letters, 584, 159–164. (2013). doi:10.1016/j.cplett.2013.08.084

[100] Z. Yua, C. Yana, T. Huanga, W. Huanga, Y. Yana, Y. Zhanga, L. Liua, Y. Zhanga, Y. Zhao, Influence of sputtering power on composition, structure and electrical properties of RF sputtered $CuIn_{1-x}Ga_xSe_2$ thin films. Applied Surface Science, 258(13) (2012) 5222–5229.

[101] H.C. Kima, T.S. Oha, D.-B. Hyun, Thermoelectric properties of the *P*-type Bi_2Te_3–Sb_2Te_3–Sb_2Se_3 alloys fabricated by mechanical alloying and hot pressing. Journal of Physics and Chemistry of Solids, 61(5) (2000) 743–749. https://doi:10.1016/s0022-3697(99)00269-3.

[102] Y. Feng, A. Elquist,Y. Zhang, K. Gao, I. Ferguson, A. Tzempelikos, N. Lu, Temperature dependent thermoelectric properties of cuprous delafossite oxides. Composites Part B: Engineering, 156 (2019) 108–112. https://doi:10.1016/j.compositesb.2018.08.070.

[103] M.S. Dresselhaus, G. Chen, M.Y. Tang, R.G. Yang, H. Lee, D.Z. Wang, P. Gogna, New Directions for Low-Dimensional Thermoelectric Materials. Advanced Materials, 19(8) (2007) 1043–1053. https://doi:10.1002/adma.200600527.

[104] S. Ohta, T. Nomura, H. Ohta, and K. Koumoto, “High-temperature carrier transport and thermoelectric properties of heavily La- or Nb-doped $SrTiO_3$ single crystals” Journal of Applied Physics, 97(3) (2005) 034106. https://doi:10.1063/1.1847723.

[105] E. Jin Bae, Y. Hun Kang, K.S. Jang, S. Yun Cho, Enhancement of Thermoelectric Properties of PEDOT:PSS and Tellurium-PEDOT:PSS Hybrid Composites by Simple Chemical Treatment. Scientific Reports, 6, 18805 (2016). https://doi:10.1038/srep18805.

[106] A. Chen, D. Madan, P.K. Wright, J.W. Evans, Dispenser-printed planar thick-film thermoelectric energy generators. Journal of Micromechanics and Microengineering, 21(10), 104006– (2011). https://doi:10.1088/0960-1317/21/10/104006.

Author biography

Name Miss Prasopporn Junlabhut

Date of Birth 04 March 1987

Address 91/48 Moo. 3 Sothorn, Mueang chachoengsao, Chachoengsao, 24000, Thailand 24000.

Education Bachelor degree of Science in Applied Physics and Industrial Instrument, Faculty of Science, King Mongut's Institute of Technology Ladkrabang (KMITL), Bangkok, Thailand (2009).

Master of Science in Nanoscience and Nanotechnology, College of Nanotechnology, King Mongut's Institute of Technology Ladkrabang (KMITL), Bangkok, Thailand (2013).

Academic Publications:

[1] P. Junlabhut, P. Nuthongkum, R. Sakdanuphab, A. Harnwunggmoung, A. Sakulkalavek, Influence of Sputtering Power Density on the Thermoelectric and Mechanical Properties of Flexible Thermoelectric Antimony Telluride Films Deposited by DC Magnetron Sputtering. Journal of Electronic Materials, (2019). www.https//doi:10.1007/s11664-019-07692-8.

[2] P. Junlabhut, P. Nuthongkum, A. Sakulkalavek, A. Harnwunggmoung, P. Limsuwan, R. Sakdanuphab, Enhancing the thermoelectric properties of sputtered Sb_2Te_3 thick films via post-annealing treatment. Surface and Coatings Technology, 387, 125510– (2020). www.https //doi:10.1016/j.surfcoat.2020.125510.

Conferences:

[1] The 5th Southeast Asia Conference on Thermoelectrics (SACT2018), in Empress Angkor Resort & Spa, Siem Reap, Cambodia, on 14-17 December 2018

[2] The 38th International Conference on Thermoelectrics and The 4th Asian Conference on Thermoelectrics (ICT/ACT 2019), in International Convention Center (HICO), Gyeongju, South Korea, on June 30th to July 4th, 2019

[3] First virtual International Thermoelectric Conference (VCT 2020) –July 27, 2020

Journal of ELECTRONIC MATERIALS
https://doi.org/10.1007/s11664-019-07692-8

TOPICAL COLLECTION: INTERNATIONAL CONFERENCE ON THERMOELECTRICS 2019

Influence of Sputtering Power Density on the Thermoelectric and Mechanical Properties of Flexible Thermoelectric Antimony Telluride Films Deposited by DC Magnetron Sputtering

PRASOPPORN JUNLABHUT,[1] PILAIPON NUTHONGKUM,[1] RACHSAK SAKDANUPHAB,[2,3] ADUL HARNWUNGGMOUNG,[4] and APARPORN SAKULKALAVEK[1,3,5]

1.—Faculty of Science, King Mongkut's Institute of Technology Ladkrabang, Chalongkrung Rd. Ladkrabang, Bangkok 10520, Thailand. 2.—College of Advanced Manufacturing Innovation, King Mongkut's Institute of Technology Ladkrabang, Chalongkrung Rd. Ladkrabang, Bangkok 10520, Thailand. 3.—Thailand Center of Excellence in Physics, Commission on Higher Education, Bangkok 10400, Thailand. 4.—Faculty of Science and Technology, Rajamangala University of Technology Suvarnabhumi, Nonthaburi 11000, Thailand. 5.—e-mail: aparporn.sa@kmitl.ac.th

Antimony telluride (Sb_2Te_3) films were deposited on flexible polyimide substrates by DC magnetron sputtering technique using a 99.9% alloy Sb_2Te_3 target. We measured structural, electrical, thermoelectric and mechanical properties with sputtering power density in the range 30–50 W. X-ray diffraction confirmed that all Sb_2Te_3 films have high crystallinity with a significant preferential growth along the (015) plane. Surface morphologies were verified by scanning electron microscope: deposited film grain size increased with sputtering power density. The elemental composition was determined by energy dispersive x-ray spectroscopy. Electrical transport properties, carrier concentration, was measured by Hall effect measurement at room temperature. Electrical conductivity and Seebeck coefficient were simultaneously measured by a DC four-terminal method (ZEM-3). The power factor was strongly dominated by electrical conductivity, leading to a maximum of 1.95 mW/K^2m with sputtering power 45 W at 300°C. The wettability test, based on the contact angle, evaluated surface energy and hydrophilicity. Nanoindentation was measured on a NHT^2 CSM Instrument with diamond Berkovich indenter (B-P 31) at room temperature. The hardness and elastic modulus of deposited Sb_2Te_3 films increased with the power density.

Key words: Flexible thermoelectric, antimony telluride, DC magnetron sputtering, sputtering power density

INTRODUCTION

Thermoelectric (TE) materials have been extensively studied due to their important properties and their potential application for waste heat recovery and cooling. TE materials can directly convert thermal energy to electrical energy and vice versa through Seebeck and Peltier effects. Devices based on TE materials are interesting due to environmental friendliness, high durability, scalability and maintenance free operation. TE power generators and small-scale cooling systems have been developed for electronic devices and microelectronic components.[1–3] The TE efficiency of materials are often described by a thermoelectric figure of merit, $ZT = {S^2\sigma T}/{\kappa}$, where S is the Seebeck coefficient, σ is electrical conductivity, T is the absolute temperature and κ is the total thermal conductivity. The $S^2\sigma$

(Received June 12, 2019 ; accepted September 27, 2019)

Published online: 11 October 2019

term in this expression is the power factor. High performance TE materials combining high Seebeck coefficient and electrical conductivity as well as low thermal conductivity are desired. Recently, several research groups have studied thin films of TE materials, used to improve thermoelectric performance:[4–6] these materials enhance both density of Fermi level states and increase phonon scattering based on the quantum confinement effect.[7]

TE materials, based on general formula, $A_2^{V}B_3^{VI}$, are promising materials. Antimony telluride (where A = Sb, B = Te) is promising, with a narrow band gap, $E_g < 0.2$ eV. Sb_2Te_3 compounds have the rhombohedral crystal structure with five atoms per unit cell belonging to the space group, $R\bar{3}m$. This material has attracted attention because of its excellent figure of merit at 300 K. To form a flexible thermoelectric device, polyimide used as a substrate was chosen due to its low thermal conductivity (0.12 Wm^{-1}/K) and thermal expansion coefficient (12×10^{-6} K^{-1}) which closely matches that of the Sb_2Te_3 films. In addition, polyimide can reduce residual stress and increase adhesion in the film.[8] Several techniques have been investigated for deposition of Sb_2Te_3 films including evaporation,[9] chemical vapor deposition,[10] pulse laser deposition,[11] co-evaporation[12] and sputtering.[13] Among these deposition techniques, direct current (DC) magnetron sputtering has been widely used because it produces high quality films, extremely high adhesion and excellent uniformity over a large substrate area. Several researchers have described the deposition of the sputtered Sb_2Te_3 films.[13–16] The compositional, structural, electrical and thermoelectric properties of the deposited films depend on parameters such as working gas pressure, working distance, sputtering time and substrate temperature. However, there has been little discussion on the sputtering power density of Sb_2Te_3 deposited films. Sputtering power density is an important factor in Sb_2Te_3 film deposition; it affects the plasma density and particle energy during the deposition.[17]

Several previous researchers have studied the structural, electrical and thermoelectric properties of TE materials.[4–6] We also assessed the reliability of flexible Sb_2Te_3 films: wettability, suface energy and nanoidentation were measured, because the surface properties affect the mechanical integrity of the device, in particular, the metalized contact layer durability and hardness. The mechanical properties are crucial factors when designing and fabricating TE devices. Assessed Sb_2Te_3 films with various grain sizes and found that mechanical properties were size-dependent.[18] Hydrophobicity or hydrophilicity of the resultant surface was also governed by chemical composition and microstructure of the deposited films.[19]

We deposited Sb_2Te_3 films on flexible polyimide substrates using the direct current magnetron sputtering and measured the effect of the sputtering power density associated with the plasma density and particles energy during film deposition on the structural, electrical and thermoelectric properties. Changes in crystallinity, chemical composition, grain size, and film thickness were attributed to the wettability and mechanical properties.

EXPERIMENTAL PROCEDURE

Sb_2Te_3 films were deposited on flexible 0.025 mm thick polyimide substrates (DuPont Kapton) using DC magnetron sputtering. Firstly, the polyimide substrates were attached to a glass slide and then ultrasonically cleaned in order with methanol and de-ionized water for 10 min, these substrates were dried with nitrogen. A 75 mm antimony telluride alloy target (Sb_2Te_3 purity: 99.9%, Stanford Advanced Materials) was used as sputtering target. Before the deposition process, the electrode distance was set to 50 mm. The base pressure in the deposition chamber was kept below 2.0×10^{-5} mbar using a diffusion pump backed by a rotary vane pump. The Ar gas working pressure during sputtering was kept at 2.6×10^{-2} mbar. Before the shutter was opened to expose the film, sputtering power density was applied for 10 min to remove contamination and the oxide layer on the target surface. After that, substrate pre-heat temperature was set to 400°C for 15 min. Finally, the various sputtering power densities, from 30 W to 50 W, were applied for 6 min to generate deposited Sb_2Te_3 films.

The structural properties of the Sb_2Te_3 films, including crystallinity, crystal size, micro strain and dislocation were investigated by x-ray diffraction (PANalytical Empyrean) operated with Cu-Kα (λ = 0.154 nm) radiation. The data was recorded in the 10°–70° of 2θ range. The surface morphology and thickness of the Sb_2Te_3 deposited films were obtained by scanning electron microscope (EVO MA10). The elemental composition of the deposited films was estimated from energy-dispersive x-ray spectroscopy (Oxford Instruments X-Max 20). The electrical property, carrier concentration, was measured by Hall effect measurement at room temperature (Ecopia, HMS3000). The temperature-dependent Seebeck coefficient and electrical conductivity were also measured by ZEM-3 (ULVAC-RIKO) at 50–300°C. The wettability was measured with a contact angle OCA 20 machine for a 10 μL de-ionized water droplet placed on the film surface equipped and monitored with a CCD camera at ambient temperature with three different positions for each sample. The hardness (or nanoindentation) was measured on a NHT^2 CSM Instrument with diamond Berkovich indenter (B-P 31) at room temperature, averaged over three different positions for each sample, which leading to the hardness and elastic modulus.

RESULTS AND DISCUSSION

The x-ray diffraction patterns of Sb_2Te_3 films deposited at different sputtering power densities are shown in Fig. 1: the films showed a polycrystalline structure, belonging to the $R\bar{3}m$ space group of Sb_2Te_3 films (JCPDS No. 15-0874). The four main diffraction peaks at 17.44°, 28.24°, 38.28° and 44.59° corresponded to the (006), (015), (1010) and (1015) planes, respectively. XRD results show that a significant preferential growth along the (015) plane developed with increased sputtering power density. Especially when the power rose to 45 W, the (015) peak became very strong. Increasing sputtering power density led to higher kinetic energy of the deposited atoms. During ion bombardment, their kinetic energy was dissipated and converted to vibration of the ions. When the atoms accumulated sufficient vibration energy, they ejected from the target surface, rearranged the crystal structure and increasing surface migration on the substrate.[1,2] However, when the sputtering power was increased to 50 W, it is seen that the (015) peak intensity dropped and the crystallinity dropped further.[3,4] Variation of the power density of the films can be correlated with the accumulation of surface and strain energy during the coating process.[5] As the power density were increased, a preferred orientation along (015) shifted slightly toward a lower angle as seen in Fig. 1. The peak shifting was related to the change in the d spacing of the deposited films, which indicated a variation of the lattice size as shown in the Fig. 2. It shows that the lattice parameters of the a-axis are little changed, while those of the c-axis increase with the power density. It is well known that the lattice parameters increase, when the antisite defect increases, since Sb has a larger atomic radius than Te as seen in Fig. 2. The lattice parameter is altered, leading to crystal imperfection.[5] The XRD peaks shifted corresponding to Te gradually decrease as the power density increases as seen the elemental composition

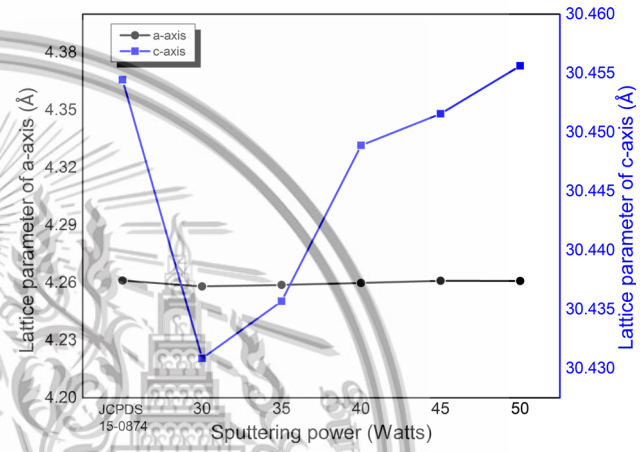

Fig. 2. Lattice parameter of Sb_2Te_3 films versus sputtering power.

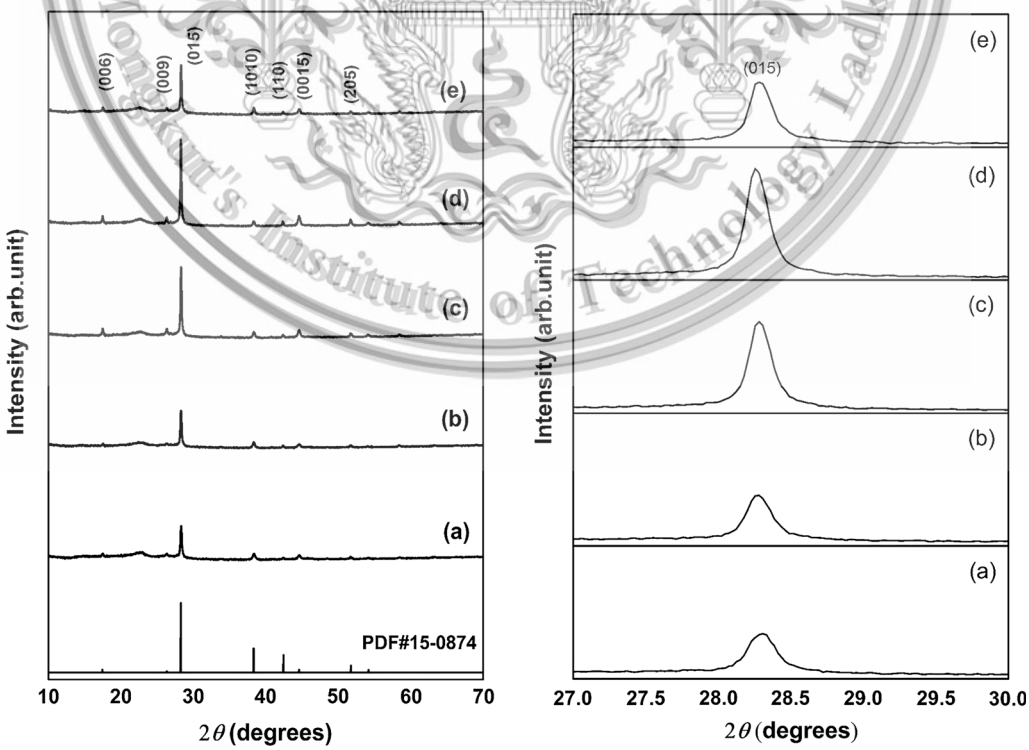

Fig. 1. Sb_2Te_3 film XRD patterns on polyimide substrates versus sputtering power density-(015) plane (a) 30 W (b) 35 W (c) 40 W (d) 45 W and (e) 50 W.

Table I. Electrical and thermoelectrical properties of Sb_2Te_3 versus sputtering power density at room temperature

Sputtering power (W)	Te content (at.%)	Carrier concentration: η ($\times 10^{19}$ cm^{-3})	Carrier mobility: μ (cm^2/Vs)	Electrical conductivity: σ ($\times 10^4$ S/m)	Seebeck coefficient: S (μV/K)	Power factor: PF (mW/K^{2}m)
30	62.3	3.2	50.4	2.57	173	0.77
35	60.0	4.3	47.6	3.28	185	1.12
40	58.7	4.8	54.7	4.18	167	1.16
45	58.6	4.4	61.9	4.32	168	1.22
50	58.5	2.3	36.7	1.35	182	0.43

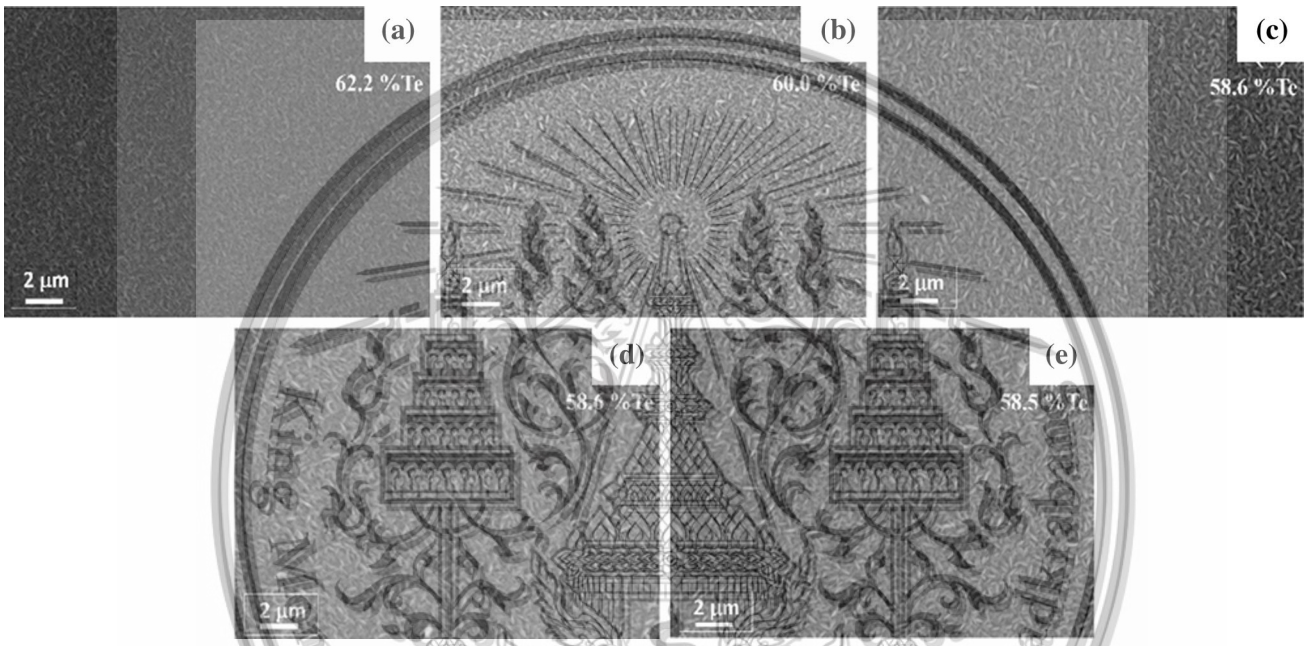

Fig. 3. Surface morphology and Te atomic fraction of Sb_2Te_3 films versus sputtering power (a) 30 W (b) 35 W (c) 40 W (d) 45 W and (e) 50 W.

of Te in Table I. It can be seen that where the power density was increased the Te vacancy defects in the Sb_2Te_3 films increased. The deviation of Te composition of the films produces holes, which increase the carrier concentration.

The surface morphology and atomic concentration of Te (Te at.%) in Sb_2Te_3 films deposited at different sputtering power densities were investigated by SEM and EDS, and the results are shown in Fig. 3. All deposited films exhibited a homogeneous grain distribution which are almost free of cracks. Larger grains formed as the power density increased due to coalescence of small grains and diffusion of atoms. The elemental composition of Sb_2Te_3 deposited films was considered to be the stoichiometric relationship of the power density. The results indicated that Te content decreased with increasing the power density. The stoichiometric film was obtained at a sputtering power of 35 W. The composition is very important for the electrical property. Te-rich film was observed for low sputtering power (30 W). Excess Te content affects the low conductivity.[20] As the power was increased to 50 W, the deposited films became significantly Te deficient, i.e., the degree of non-stoichiometry increased. At high sputtering power density, the thermal transport in thin film increased and affected Te evaporation from the film, due to the differential vapor pressure, Te compared with Sb.[4,21] The film thicknesses were measured by SEM on cross-section and the thickness was used in calculation of the electrical property. The deposited films have thicknesses between 600 nm and 1000 nm depending on the sputtering power density.[17,22]

The deposition rate and thickness of the Sb_2Te_3 films show almost a linear relationship with the sputtering power density in the power range from 30 W to 50 W as seen in Fig. 4. The deposition rate increased with the power density could be associated with increased flux of atoms. An increase in the power density enhances the probability of ejection of atoms from the compound target. It was concluded that the sputtering power density was a major factor affecting the sputtering yield of a target, which, in turn, affected the film thickness.

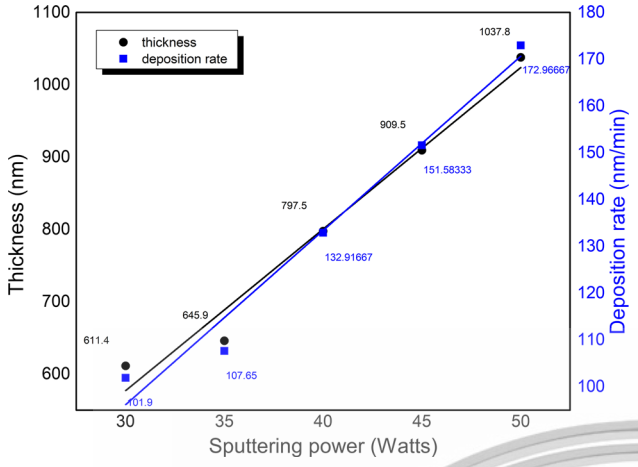

Fig. 4. Thickness and deposition rate of Sb_2Te_3 films versus sputtering power.

Electrical properties at room temperature of Sb_2Te_3 films are summarized in Table I. All deposited Sb_2Te_3 films present as p-type semiconductors due to the positive mobility. As seen in Table I, the carrier concentration (n) increased with increasing sputtering power up to 45 W. Then, it decreased slightly as the sputtering power was increased to 50 W. Typically, the carrier concentration is sensitive to chemical composition and lattice defects: excess Te content led to higher resistivity.[20] Secondly, the Te deficiency led to weak Van der Walls bonding between Te(1)–Te(1) layers—Sb_2Te_3 structure. Te vacancies $V_{Te}^{\cdot\cdot}$ were produced by increasing sputtering power density, which vaporized Te. The antisite defects are occupied by Sb atoms. The Sb atoms will enter Te vacancies due to the small difference in electronegativity. The antisite defects, $Sb_{Te}^{'}$, were produced and led to the formation of $V_{Sb}^{'''}$. The interaction of antisite defects and vacancies is shown by Ref. 23.

$$Sb_2Te_3 = 2Sb_{Te}^{'} + V_{Te}^{\cdot\cdot} + 2V_{Sb}^{'''} + \frac{3}{2}Te_{(g)}\uparrow + 2h^{\cdot}, \quad (1)$$

where $h^{\cdot}$ denotes the produced hole and $\uparrow$ denotes the loss of Te. The deviation from stoichiometry of the films produces holes which increase the carrier concentration.

The electrical conductivity (σ) of the Sb_2Te_3 deposited films increased with sputtering power up to 45 W. Up to this point, the power density affected film crystallinity. The films were more uniform with less defects which led to enhanced electrical conductivity. As the power reached 50 W, the resistivity noticeably increased due to the reduction of carrier concentration and excessive crystallization. The resistivity dramatically increased and reaching a maximum of 7.40×10^{-5} Ωm. The resistivity is determined by carrier concentration and carrier mobility following, $\rho = 1/\mu qn$. The electrical conductivity increased considerably with increasing the sputtering power density. The highest electrical conductivity of 4.32×10^4 S/cm was obtained with sputtering power 45 W. The change of electrical conductivity with increasing the power density expected to increase the crystallinity, increase the deposition rate and increase the grain size as evidenced from XRD and SEM images.[7,24] A large electrical conductivity is required in thermoelectric efficiency. However, as sputtering power density was increased to 50 W, the reduced crystallinity and increased defect concentration caused a decrease of conductivity. The carrier mobility (μ) of the deposited films was increased according to the larger grain growth with increasing sputtering power density.

The Seebeck coefficient (S) for the films with increased sputtering power density demonstrated that all films are p-type semiconductors which was confirmed by ZEM-3. The maximum Seebeck coefficient, 185 μV/K, was observed with 35 W sputtering power matching the expected stoichiometric ratio.[25] When the sputtering power density were increased, the Seebeck coefficient declined slightly and then stabilized as seen in Table I. According to the theory, the Seebeck coefficient, S, is inversely related to the carrier concentration:

$$S(T) = \frac{\pi^2 k_B^2 T}{3e}\left[\frac{N(E)}{n} + \left(\frac{\partial \ln \mu(E)}{\partial E}\right)_{E=E_F}\right], \quad (2)$$

where k_B denotes the Boltzmann's constant, e denotes the electron charge, $N(E)$, denotes the density of states, η denotes the carrier concentration and T denotes the temperature. The Seebeck coefficient is inversely proportional to the charge carrier concentration. The power factors of Sb_2Te_3 films was based on two factors, i.e., electrical conductivity and the Seebeck coefficient—$PF = S^2\sigma$. The highest power factor at room temperature was 1.22 mW/K^{2}m. Khumthong et al. reported that the Sb_2Te_3 film fabricated on polyimide substrate using RF magnetron sputtering and obtained PF = 1.06 × 10 4 W/K^{2}m.[15] Shen et al. reported that a maximum PF = 5.2×10^6 W/K^{2}m was obtained for the film fabricated on polyimide substrate using DC magnetron sputtering with in situ annealing for 20 min.[26] Our measurements led to the highest power factor with high crystallinity films, which led to high electrical conductivity and high Seebeck coefficient.

The temperature dependence of conductivity, Seebeck coefficient and power factors are presented in Fig. 5 as a function of applied temperature and as a parameter of sputtering power density. Figure 5a shows that the conductivity of films increased with applied temperature, which indicates a typical semiconductor-like behavior, with a maximum of $\sim 4.90 \times 10^4$ S/m at 300°C, with the sputtering power in the range of 40 W and 45 W. The maximum conductivity corresponded to the maximum

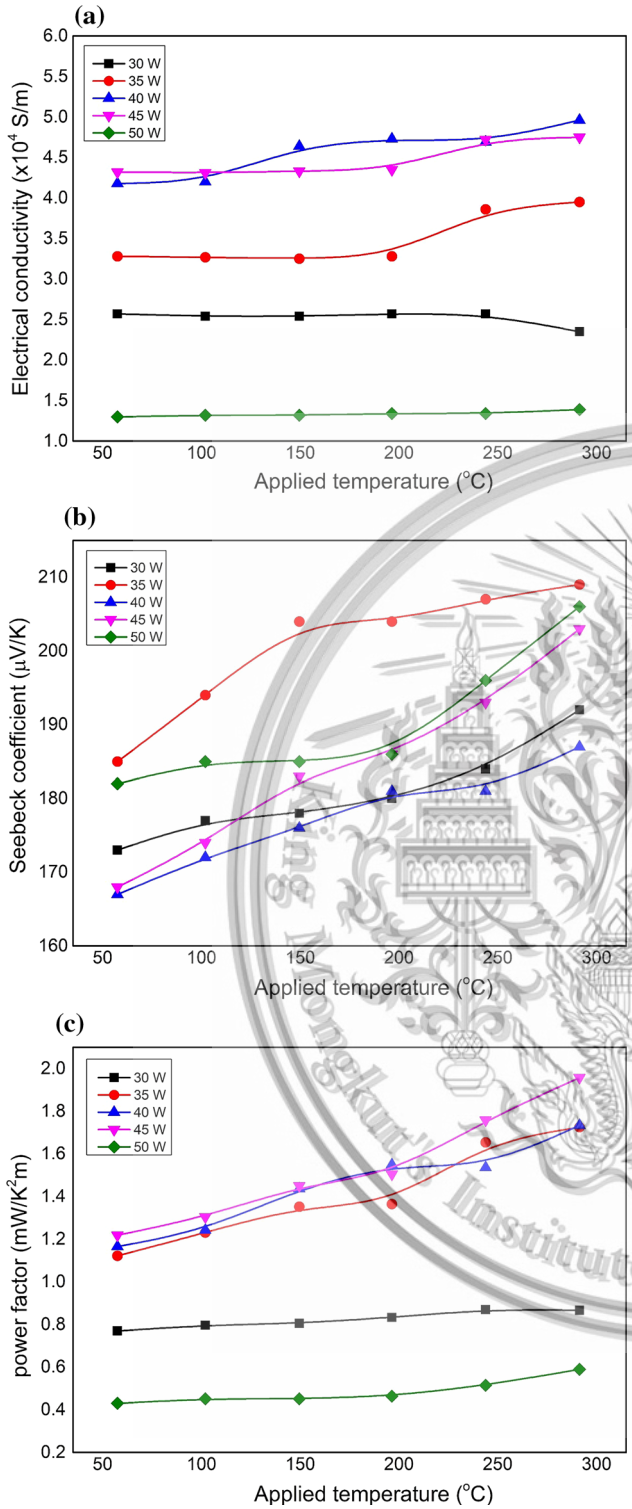

Fig. 5. (a) Electrical conductivity (b) Seebeck coefficient and (c) power factor for Sb_2Te_3 films versus applied temperature as a parameter of sputtering power density.

crystallinity and consequently the increase of carrier mobility in the film with increasing the power density. The temperature dependence of Seebeck coefficient is shown in Fig. 5b. A maximum Seebeck coefficient of ~ 209 μV/K with 35 W sputtering

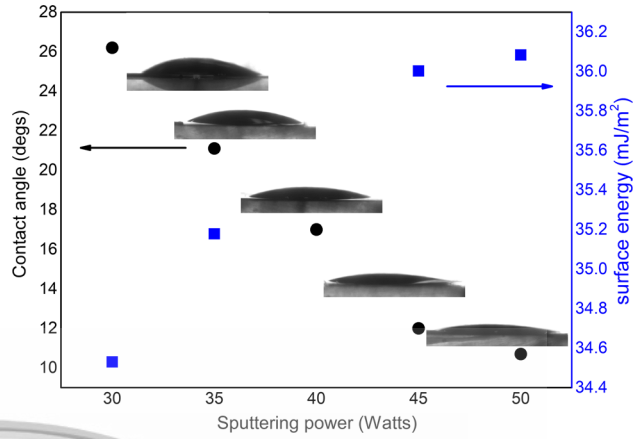

Fig. 6. Contact angle (black filled circle) and surface energy (blue filled square) for Sb_2Te_3 films versus sputtering power density. Images of water droplets on the film surface are placed next the corresponding black filled circle at a level matching the contact angle on the left axis (Color figure online).

power (i.e., close to the ideal stoichiometry of Sb_2Te_3) at 300°C was obtained. In the theory, S directly depends on the temperature (T) and inversely depends on the carrier concentration.[27] Figure 5c shows the temperature dependence of power factors. The power factor describe the ability of a material to produce electrical power from a given temperature difference. Our results show that the power factors are strongly dominated by electrical conductivity, leading to a maximum PF = 1.95 mW/K^{2}m with 45 W sputtering power at 300°C.

Wettability of Sb_2Te_3 films was measured by the static water contact angle method are shown in Fig. 6. The contact angle was taken as an average of three points of deposited at different sputtering power densities. The contact angle gradually decreased from 26.2° to 10.7° as the power was increased. It can be seen that the water droplets completely spread over the surface of the films at the higher sputtering power. This indicated that the highly hydrophilic states were obtained at the higher power density. The change of the wettability depends on the grain size with increasing power density. With the larger grains, the water could fill the grooves of the rougher surface, making it more hydrophilic.[19] Typically, the wettability test is used to determine the surface energy, which can be calculated using the Fowkes–Girifalco–Good (FGG) relation. The interaction of the dispersive force or the Van der Waals force between liquid and solid interface give information about the different surface energies. Following FGG,[28] γ_{ls} is the surface energy corresponding to the liquid solid interface calculated from

$$\gamma_{ls} = \gamma_s + \gamma_l - 2\sqrt{\gamma_s^d \gamma_l^d}, \quad (3)$$

where γ_s and γ_l are the surface energies measured for the solid and liquid and γ_s^d and γ_l^d are the

Table II. Nano indentation results of Sb_2Te_3 films versus sputtering power density

Sputtering power (W)	Average hardness (MPa)	Hardness uncertainty	Average modulus (GPa)	Modulus uncertainty
30	237	0.14	8.0	1.70
35	304	0.13	8.9	0.77
40	313	0.10	8.9	1.00
45	377	0.06	9.1	1.80
50	408	0.09	9.1	2.30

dispersive portions of the surface tension for the liquid and solid surface, respectively.

Young's equation quantifies the surface energy by measuring the angle of the cross-section of a liquid droplet when contacting a solid surface[28] and given by:

$$\gamma_s = \gamma_{ls} + \gamma_l \cos\theta, \tag{4}$$

where θ is the contact angle between the liquid and solid. Using Young's equation, combined with Eq. 3, and, employing de-ionized water (72.8 mJ/m^2) as a testing liquid, $\gamma_l^d = \gamma_l$.[28] Equation 4 becomes and the surface energy of the calculated materials, γ_s^d is:

$$\gamma_s^d = \frac{1}{4}\gamma_l(\cos\theta + 1). \tag{5}$$

The calculated surface energies of the Sb_2Te_3 films with increasing sputtering power density and decreasing contact angles were 34.5 mJ/m^2, 35.1 mJ/m^2, 35.6 mJ/m^2, 36.0 mJ/m^2 and 36.1 mJ/m^2. The surface energy is very important in a number of industrial applications, such as bonding, coating, sealing and cleaning.

Hardness values (H) were obtained from the applied indentation load divided by the projected contact area:

$$H = \frac{P_m}{A_p} \tag{6}$$

where P_m denotes a perfectly sharp Berkovich indenter and A_p denotes the projected contact area between the indenter and the sample surface ($A_p = 24.56\ h_c^2$ for Berkovich indenter and h_c is the true contact depth). Following Oliver and Pharr,[29] the elastic modulus of the specimen, E, can be calculated from reduced elastic modulus E^* in Eq. 7

$$E^* = \frac{S}{2\beta\sqrt{A_p/\pi}}, \tag{7}$$

where β denotes the geometric constant ($\beta = 1.034$ for Berkovich indenter) and the elastic modulus E is computed from:

$$\frac{1}{E^*} = \frac{1-\upsilon^2}{E} + \frac{1-\upsilon'^2}{E'}, \tag{8}$$

where υ is the Poisson's ratio of the indenter ($\upsilon = 0.07$). υ' are the Poisson's ratio of the film ($\upsilon' = 0.25$). and $E' = 1141$ GPa is the elastic modulus of the indenter.

The hardness and elastic modulus of the Sb_2Te_3 films are shown in Table II. The hardness increased with sputtering power density while the elastic modulus slightly changed only with the power density.

The SEM images indicated that the grain size has a significant effect on the mechanical properties of the Sb_2Te_3 films. The increased sputtering power density results in the increase of the grain size and film density from the kinetics of film agglomeration. The larger grain with high density films used more energy during nano indentation, which led to a higher surface stress.[21,30,31]

CONCLUSION

Flexible antimony telluride, Sb_2Te_3, films were deposited on polyimide substrates using DC sputtering. Sputtering power density had a significant effect and controlled the structural, stoichiometry, electrical, thermoelectric, wettability and hardness properties of the films. The deposited film had larger grains and crystallinity improved as the power density increased. However, the stoichiometry of the deposited films slightly changed due to Te revaporation as thermal transport increased. As well as chemical composition, Te evaporation effected carrier concentration and number of lattice defects which led to reduced Seebeck coefficient. The largest Seebeck coefficient, 209 μV/K at 300°C, was seen at sputtering power density of 35 W due to the nearly stoichiometric composition. The maximum power factor, 1.95 mW/K^{2}m, was found at 45 W sputtering power at 300°C. Wettability tests indicated that hydrophilicity, which showed the interaction between liquid and solid interface, depended on the grain size which increased with sputtering power density. The calculated surface energy, hardness, and elastic modulus of the Sb_2Te_3 is very important in a number of industrial applications, such as bonding, coating, sealing or cleaning.

ACKNOWLEDGMENTS

This work has partially been supported by Faculty of Science, King Mongkut's Institute of Tech-

nology Ladkrabang (KMITL) for financial support. Authors would like to thank Rajabhat Rajanagarindra University (RRU) for student fund support. Authors gratefully acknowledge the support Optical Thin-Film Technology Laboratory, NSTDA for Hall measurement, John Morris, KRIS and Prof. Pichet Limsuwan, Faculty of Science, KMITL, who edited this paper for us.

REFERENCES

1. J.-C. Yang, X.-Q. Meng, C.-T. Yang, and Y. Zhang, *Appl. Surf. Sci.* 287, 335 (2013).
2. A. Kosarian, M. Shakiba, and E. Farshidi, *IEEE J. Trans. Electr. Electron.* 13, 27 (2018).
3. W. Xiao, H. Deng, S. Zou, Y. Ren, D. Tang, M. Lei, C. Xiao, X. Zhou, and Y. Chen, *J. Nucl. Mater.* 509, 542 (2018).
4. F. Anjum, R. Ahmad, N. Afzal, and G. Murtaza, *Mater. Lett.* 219, 23 (2018).
5. G.D. Deshmukh, S.M. Patil, S.S. Patil, and P.H. Pawar, *J. Chem. Biol. Phys. Sci.* 5, 2769 (2015).
6. R. Sathyamoorthy and J. Dheepa, *J. Phys. Chem. Solids* 68, 111 (2007).
7. Z. Yua, C. Yana, T. Huanga, W. Huanga, Y. Yana, Y. Zhanga, L. Liua, Y. Zhanga, and Y. Zhao, *Appl. Surf. Sci.* 258, 5222 (2012).
8. L.M. Goncalves, P. Alpuim, A.G. Rolo, and J.H. Correia, *Thin Solid Films* 519, 4152 (2011).
9. N.G. Patel and P.G. Patel, *J. Mater. Sci.* 26, 2543 (1991).
10. R. Venkatasubramanian, T. Colpitts, E. Watko, M. Lamvik, and N. El-Masry, *J. Cryst. Growth* 170, 817 (1997).
11. T. Liu, H. Deng, H. Cao, W. Zhou, J. Zhang, J. Liu, P. Yang, and J. Chu, *J. Cryst. Growth* 416, 78 (2015).
12. H. Shen, S. Lee, J.-G. Kang, T.-Y. Eom, H. Lee, and S. Han, *Appl. Surf. Sci.* 429, 115 (2012).
13. B. Fang, Z. Zeng, X. Yan, and Z. Hu, *J. Mater. Sci. Mater. Electron.* 24, 4 (2013).
14. M. Mizoshiri, M. Mikami, and K. Ozaki, *Jpn. J. Appl. Phys.* 52, 06FL07 (2012).
15. T. Khumtong, P. Sukwisute, A. Sakulkalavek, and R. Sakdanuphab, *J. Electron. Mater.* 46, 5 (2017).
16. N.-W. Park, W.-Y. Leel, J.-E. Hong, T.-H. Park, S.-G. Yoon, H. Im, H.S. Kim, and S.-K. Lee, *Nanoscale Res. Lett.* 10, 20 (2015).
17. K.-Y. Chan and B.-S. Teo, *J. Mater. Sci.* 40, 5971 (2005).
18. H.J. Lee, S. Hyun, H.S. Park, and S.W. Han, *Microelectron. Eng.* 88, 593 (2011).
19. M. Zenkiewicz, *J. Achiev. Mater.* 24, 1 (2007).
20. H.-J. Lee, H.S. Park, S. Han, and J.Y. Kim, *Thermochim. Acta* 542, 57 (2012).
21. C.-H. Tasi, Y.-C. Tseng, S.-R. Jian, Y.-Y. Liao, C.-M. Lin, P.-F. Yang, D.-L. Chen, H.-J. Chen, C.-W. Luo, and J.-Y. Juang, *J. Alloys Compd.* 619, 834 (2015).
22. A. Chaoumead, Y.-M. Sung, and D.-J. Kwak, *Adv. Condens. Matter. Phys.* 2012, 1 (2012).
23. H.C. Kima, T.S. Oha, and D.-B. Hyun, *J. Phys. Chem. Solids* 61, 743 (2000).
24. T. Chen, P. Fana, Z. Zheng, D. Zhang, X. Cai, G. Liang, and J. Chi, *J. Adv. Mater.* 194–196, 2400 (2011).
25. P. Fan, Z.-H. Zheng, G.-X. Liang, D.-P. Zhang, and X.-M. Cai, *J. Alloys Compd.* 505, 278 (2010).
26. S. Shena, W. Zhua, Y. Denga, H. Zhaob, Y. Penga, and C. Wang, *Appl. Surf. Sci.* 414, 197 (2017).
27. P. Nuthongkum, R. Sakdanuphab, M. Horprathum, and A. Sakulkalavek, *J. Electron. Mater.* 46, 11 (2017).
28. M.S. Angelo, B.E. McCandless, R.W. Birkmire, S.A. Rykov, and J.G. Chen, *Prog. Photovolt: Res. Appl.* 15, 93 (2007).
29. S.-R. Jian, P.H. Le, C.-W. Luo, and J.-Y. Juang, *J. Appl. Phys.* 121, 175302 (2017).
30. J. Wang, Z. Huang, H. Duan, S. Yu, X. Feng, G. Wang, W. Zhang, and T. Wang, *Acta Mech. Solida Sin.* 24, 1 (2011).
31. A.M. Abazari, S.M. Safavi, G. Rezazadeh, and L.G. Villanueva, *Sensors* 15, 28543 (2015).

Surface & Coatings Technology 387 (2020) 125510

Contents lists available at ScienceDirect

Surface & Coatings Technology

journal homepage: www.elsevier.com/locate/surfcoat

Enhancing the thermoelectric properties of sputtered Sb_2Te_3 thick films via post-annealing treatment

Prasopporn Junlabhut[a], Pilaipon Nuthongkum[b], Aparporn Sakulkalavek[a], Adul Harnwunggmoung[c], Pichet Limsuwan[a], Rachsak Sakdanuphab[d,*]

[a] Faculty of Science, King Mongkut's Institute of Technology Ladkrabang, Chalongkrung Rd. Ladkrabang, Bangkok 10520, Thailand
[b] Faculty of Science and Technology, Rajabhat Rajanagarindra University, Chachoengsao 24000, Thailand
[c] Faculty of Science and Technology, Rajamangala University of Technology Suvarnabhumi, Nonthaburi 11000, Thailand
[d] College of Advanced Manufacturing Innovation, King Mongkut's Institute of Technology Ladkrabang, Chalongkrung Rd. Ladkrabang, Bangkok 10520, Thailand

ARTICLE INFO

Keywords:
Antimony telluride
Thick film
Heat treatment
Annealing
DC magnetron sputtering

ABSTRACT

Sb_2Te_3 films of more than 10 μm in thickness were deposited on flexible polyimide substrates by heat treatment-assisted DC magnetron sputtering. The post-annealing parameters including the temperature (150–350 °C) and time (15–60 min) were varied to investigate the microstructure, chemical composition, porosity and thermoelectric properties of the thick films. X-ray diffraction showed that both the as-deposited and post-annealed films were polycrystalline with significant preferential growth along the (015) plane. The films showed slightly off-stoichiometric compositions after post-annealing treatment. Increasing the annealing temperature and annealing time led to an increase in crystalline size and a decrease in porosity of the thick films. This was related to grain growth, agglomeration and surface improvement. The electrical transport and thermoelectric properties including carrier concentration, carrier mobility, electrical conductivity and Seebeck coefficient were investigated using Hall effect measurements and a ZEM-3 apparatus. A maximum power factor of 1.7 mW/K^{2}m was obtained following annealing at 350 °C for 30 min.

1. Introduction

Global warming and climate change are major problems for the world. Strategies for dealing with these problems include increasing the use of renewable energy and improving energy efficiency. One way to improve energy efficiency and minimize wasted heat is to use energy harvesting technology. This technology can directly convert thermal energy to electrical energy through thermoelectric materials (TEs), given a suitable temperature. The conversion efficiency of TEs is expressed by the thermoelectric figure of merit (ZT). Antimony telluride (Sb_2Te_3) is a well-known TE that has attracted much attention for its potential application in microelectronics [1]. Sb_2Te_3 lattice consist of layers. Each layer comprises five atomic planes oriented perpendicular to the *c*-axis according to …Te^1-Sb-Te^2-Sb-Te^1… Te^1-Sb-Te^2-Sb-Te^1. There are the van der Waals gaps between Te^1 atoms [2]. Typically, the excellence ZT of Sb_2Te_3 is typically achieved at near room temperature [3,4] which is conveniently close to the temperature of the human body. Devices integrated into the human body can access this heat source day and night. There are two kinds of thermoelectric devices: bulk and thin film. In bulk thermoelectric devices, a temperature difference (ΔT) between the two sides of the device can be easily achieved and results in a relatively high electrical power [5]. However, it is difficult to reduce the size of bulk thermoelectric devices, due to adhesion problems and limited flexibility. The cost of bulk thermoelectric devices is also high because of the batch process required for their manufacturing. Thin film thermoelectric devices involve lesser amounts of materials, are easily integrated into compact circuits, and can be deposited on flexible heat sources [6]. However, it is challenging to produce a satisfactory temperature difference across the thin film [7]. An attractive strategy is to combine the advantages of bulk and thin film thermoelectric devices. A flexible thermoelectric thick film could potentially induce a large temperature difference. There are an attractive approach because of their ability and suitability to power miniature electrical devices for wearable applications.

Screen printing [7–9], electro chemical [10], thermal evaporation [11], and magnetron sputtering [12] have been extensively investigated to deposit the Sb_2Te_3 thick film. Screen printing [7–9] has been commonly used due to the short process time, low fabrication cost and large coating area. However, these is requiring a mixing powder, binder, glass powder and solvent along with a precursor, leads to weak

* Corresponding author.
E-mail address: rachsak.sa@kmitl.ac.th (R. Sakdanuphab).

https://doi.org/10.1016/j.surfcoat.2020.125510
Received 1 November 2019; Received in revised form 28 January 2020; Accepted 22 February 2020
Available online 24 February 2020

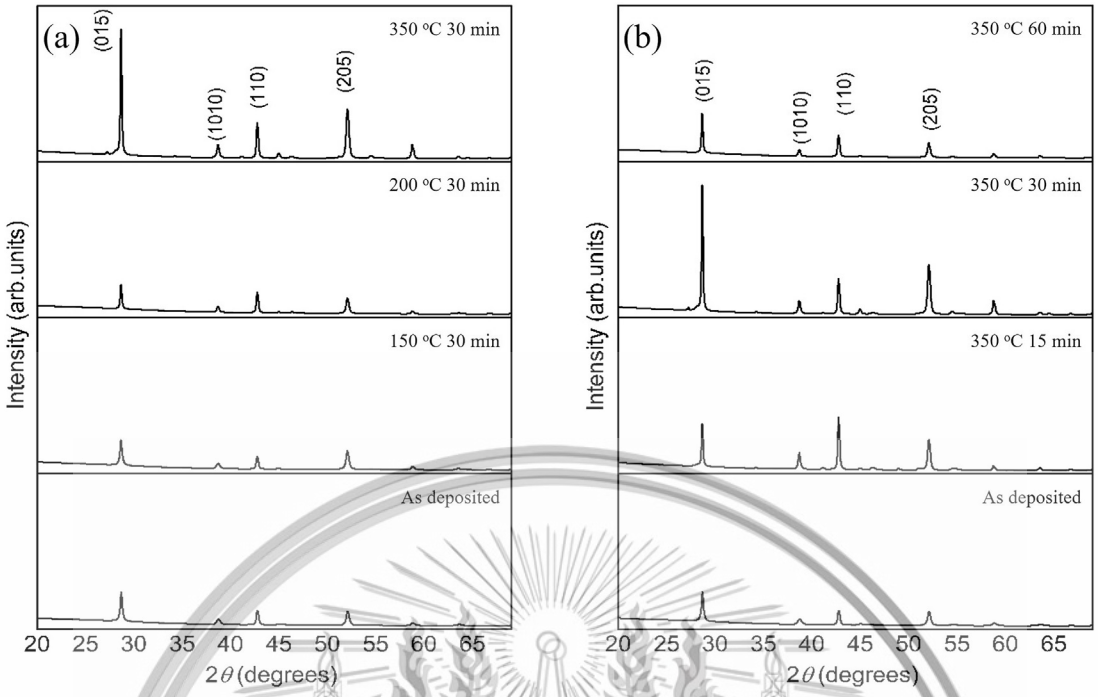

Fig. 1. XRD patterns of Sb_2Te_3 thick films at different (a) annealing temperature and (b) annealing time.

Table 1
Summary table of calculated strain, average grain sizes and percentage of Te of Sb_2Te_3 thick films.

Annealing conditions		β cosθ	Strain (ε) $\times 10^{-3}$	W-H crystalline size (nm)	%Te
Temp. (°C)	Time (min)				
As deposited	-	0.0037	3.29	72	59.28
150 °C	30	0.0036	3.21	137	59.21
250 °C	30	0.0031	3.08	141	57.34
350 °C	30	0.0028	2.29	182	57.10
350 °C	15	0.0030	2.22	144	57.30
350 °C	30	0.0028	2.29	182	57.10
350 °C	60	0.0029	2.37	163	56.22

contact between particles and highly porous products. There have been few studies on sputtering thick films using a single Sb_2Te_3 target. Magnetron sputtering is commonly used to provide uniform high purity films with large areas. Polyimide was chosen as a substrate because of its low thermal conductivity (0.12 W/Km) and its thermal expansion coefficient (12×10^{-6} K^{-1}) closely matching the thermal expansion coefficient of Sb_2Te_3 thick film, which reduces residual stress and increasing adhesion [13]. However, increasing film thickness during deposition generally leads to weak contacts between particles, high porosity and consequently, higher resistivity compared with thin films [8]. Heat treatment and annealing process has been shown to yield the better connections between the particles and thus improved films crystallinity [14]. Strongly electrical transport and good thermoelectric properties were reportedly obtained following annealing. Little effort appears to have been made on the effects of annealing on the structural and electrical transport properties of sputtered Sb_2Te_3 thick films. The annealing temperature and annealing time also require optimizing.

In this study, Sb_2Te_3 thick films were directly deposited on flexible polyimide by heat treatment-assisted DC magnetron sputtering. The annealing temperature and annealing time were optimized to enhance thermoelectric properties. The influence of heat treatment and annealing process on the structural, electrical and thermoelectric properties of Sb_2Te_3 flexible thick films were investigated.

2. Material and method

P-type Sb_2Te_3 thick films were grown on flexible 25-μm-thick polyimide substrates (DuPont Kapton) by DC magnetron sputtering technique using the alloy Sb_2Te_3 (purity: 99.9%, Stanford Advanced Materials) with a diameter of 3 in. Before deposition, a 25 × 75 mm of polyimide were attached to a glass slide (glass transition temperature (T_g) = 557 °C and 1 mm thickness) and ultrasonically cleaned in methanol and then de-ionized water (each for 10 min) and then dry under a N_2 gas flow. The distance between the target-substrate was 40 mm. Before deposition, the chamber base pressure was maintained below 2.7×10^{-5} mbar using a diffusion pump backed by a rotary vane pump before deposition. A flow of Ar gas was then introduced into the chamber and the deposition pressure was maintained at 2.6×10^{-2} mbar and DC power was maintained at 45 W. Before the shutter was opened to expose the film, the target was pre-sputtered for 10 min to remove the contaminations. The substrate pre-heat was applied at 400 °C for 15 min under the substrate with the same vacuum chamber. The process was repeated 6 times to reach the designated film thickness. Finally, thick films were annealed using halogen lamp in Ar atmosphere of approximately 2.6×10^{-2} mbar at temperature 0, 150, 250 and 350 °C for 30 min. To investigate the effect of annealing time, the thick films were also annealed at 350 °C for 15, 30 and 60 min, respectively. The crystal structure, including crystal orientation and average crystalline size was characterized by X-ray diffraction (XRD) using a Rigaku diffractometer (Smartlab). XRD patterns were recorded in the 2θ range of 10–70° at 40 kV and 20 mA with a scanning rate of 10°/min. The elemental composition was examined by energy-dispersive X-ray spectroscopy (EDX, Oxford Instruments X-Max 20) over a large film area. The surface morphology and thickness were observed by field-emission scanning electron microscopy (FE-SEM, EVO MA10) operated at 10 kV. The electrical properties and carrier concentration were obtained by Hall effect measurements at room temperature (Ecopia, HMS3000). The temperature-dependent Seebeck coefficient and electrical conductivity were measured using a ZEM-3 apparatus (ULVAC-RIKO) at 50–300 °C.

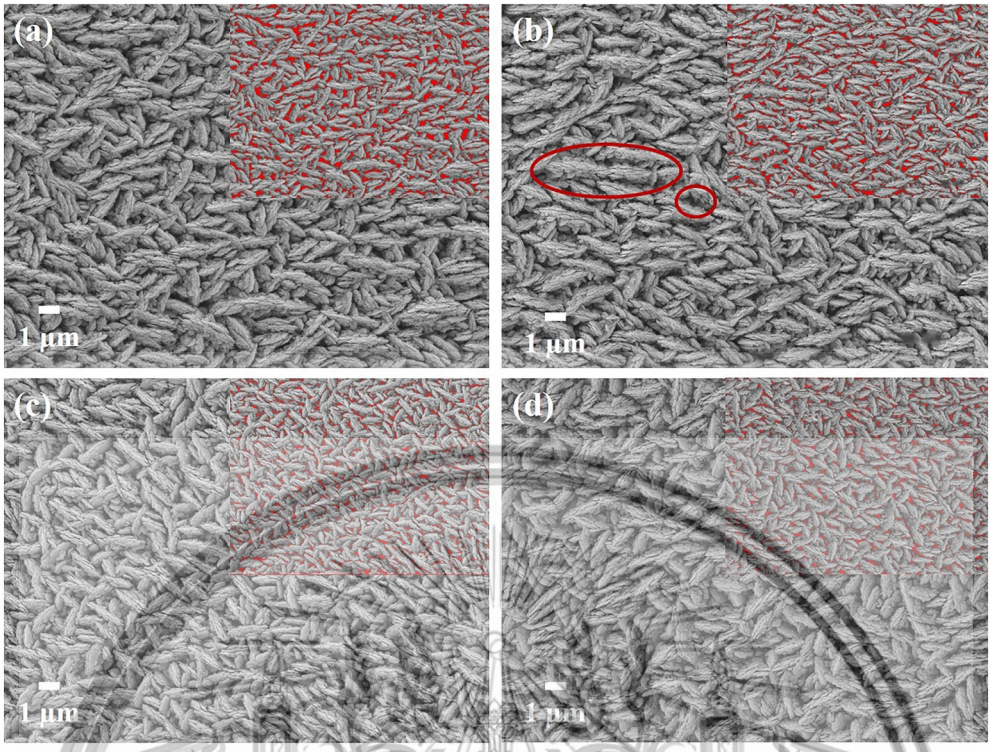

Fig. 2. FE-SEM images showing surface morphology of Sb_2Te_3 thick films (a) As-deposited and annealed at (b) 150 °C (c) 250 °C (d) 350 °C for 30 min. Inset show the porosities as red areas. (For interpretation of the references to colour in this figure legend, the reader is referred to the web version of this article.)

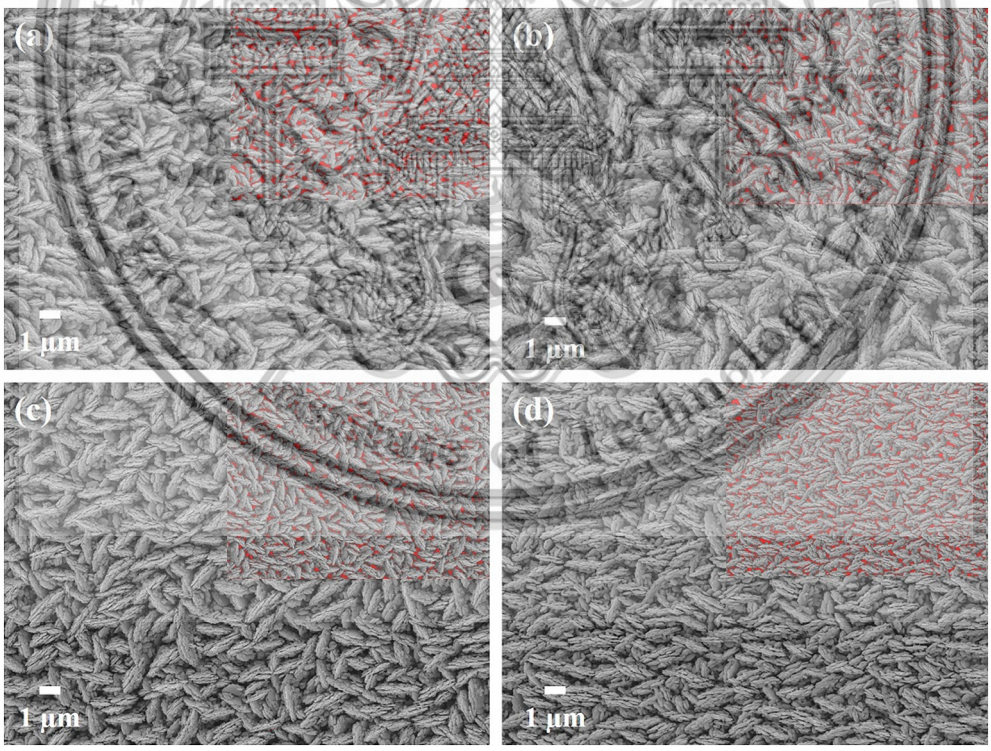

Fig. 3. FE-SEM images showing surface morphology of Sb_2Te_3 thick films (a) As-deposited and annealed for (b) 15 min (c) 30 min (d) 60 min at 350 °C. Inset shows the porosities as red areas. (For interpretation of the references to colour in this figure legend, the reader is referred to the web version of this article.)

3. Results and discussion

The crystal phases of the as-deposited and annealed Sb_2Te_3 thick film are exhibited in the XRD pattern Fig. 1(a). The XRD patterns are characteristic of the rhombohedral crystal structure with a space group of $R\bar{3}m$ (JCPDS card no. 15-0874) [15]. The polycrystalline Sb_2Te_3 thick films show XRD peaks at 28.24°, 38.27°, 42.36° and 51.69° which are corresponding to (015), (1010), (110) and (205) plane orientation, respectively. The growth process and heat treatment at substrate are related to the mobility of the adatoms during film growth. In other

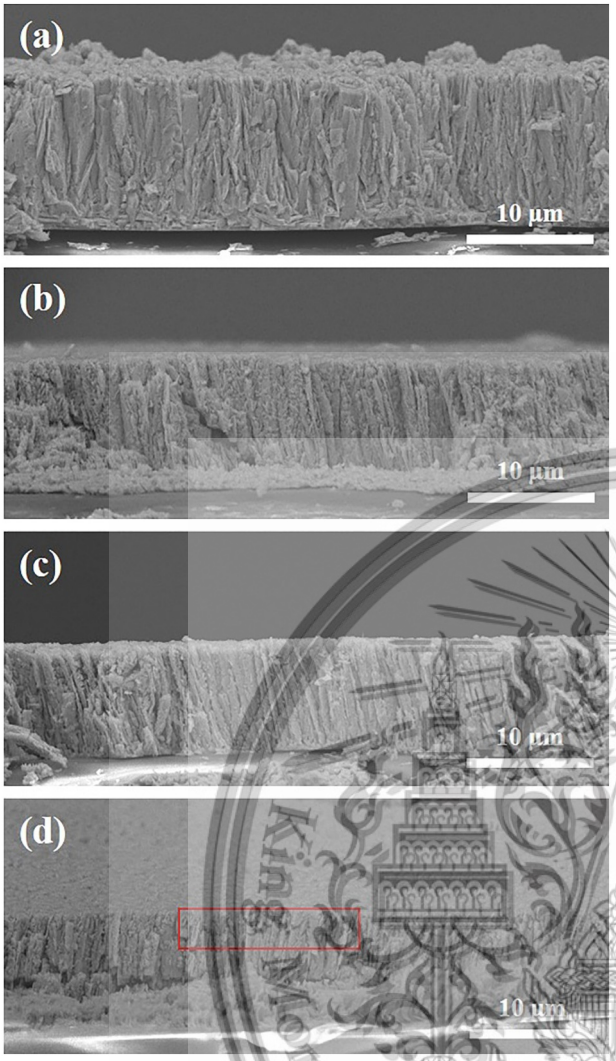

Fig. 4. Cross-sectional FE-SEM images of Sb_2Te_3 thick films (a) As-deposited and annealed for (b) 15 min (c) 30 min (d) 60 min at 350 °C.

words, the increasing of substrate temperature, the adatom have sufficient energy to overcome the surface diffusion barriers to preferential orientation. The sufficient substrate temperature was leading to the nucleation in the in-plane crystal growth along *c*-axis [15,16]. An increase in annealing temperature results in higher diffusion of the adatoms, which leads to grain growth and higher crystallinity [1]. To achieve the designated film thickness, low mobility atoms arrive at the surface of substrate with various angles of incidence. The annealing process was incorporated with the aim of improving crystal growth. As the annealing temperature increases from 0 to 350 °C, the atoms of the Sb_2Te_3 thick film have more energy to diffuse, agglomerate, and finally rearrange into a crystal structure [5]. The intensity of a preferred orientation (015) plane increases with increasing annealing temperature. This implies that thick films are obtained with highly orientated crystallinity following annealing at 350 °C for 30 min. XRD patterns of thick films annealed at 350 °C for 15, 30 and 60 min are shown in Fig. 1(b). The average crystalline size and the atomic composition are shown in Table 1. The results suggest that that annealing for 30 min leads to the highest crystal growth, which potentially improves the power factor of the film [17]. The (015) XRD peak of annealed film is sharper and narrower than that of the as-deposited film. This suggests that high quality thick films with good crystallinity and a large grain size are formed as the annealing temperature increases. Crystal imperfection in the film as evidenced from the lattice strain was also examined. Size-induced and strain-induced of Sb_2Te_3 thick films under the different annealing conditions can be considered by Williamson-Hall formula [18]:

$$\beta cos\theta = \frac{k\lambda}{D} + 4\varepsilon sin\theta \quad (1)$$

where, D is the average crystalline size, λ is wavelength of X-ray radiation (0.154 nm), β is the integral breadth of the diffraction peak, θ is Bragg diffraction angle, and ε is microscopic strain. The average crystalline size and strain of Sb_2Te_3 thick films increases from 72 to 182 nm with increasing annealing temperature. The highest crystalline size of 182 nm is obtained after annealing at 350 °C for 30 min, as shown in Table 1. The results indicated that the post-annealing is significantly related to the lattice strain. The lattice strain decreased slightly with increased annealing temperature. The decreased lattice strain at larger crystalline size was due to reduction of lattice imperfection, which indicated the formation of a high crystalline film. The variation of strain was related to the change in the d-spacing of the film, which indicated a variation of the lattice structure [19].

The atomic composition of thick films was measured by EDX. Table 1 shows the atomic percentage of Te (%Te) for thick films annealed at different temperatures. The %Te slightly decreases from 59.28% to 57.10% as annealing temperature increase. This is cause by the re-evaporation of volatile element Te during annealing. Atomic bonds of the thick films are not equivalent in all the directions at the surface, which leads to the evaporation of Te [1,13]. In order to further optimize the annealing time, the annealing temperature was performed at 350 °C. The %Te slightly decreases with increasing annealing time; this result shows that the annealing time does not significantly change the %Te.

FE-SEM images of the surface morphology of Sb_2Te_3 thick films annealed at 0, 150, 250, and 350 °C for 30 min are shown in Fig. 2. FE-SEM images of the as-deposited film show loose and vertical flakes, and the surface appears rough and incompact. Flakes with a larger lateral size are observed when the annealing temperature increases to 150 °C, as indicated by the red circles in Fig. 1(b). The size distribution, grain density and surface smoothness increase as the annealing temperature increases to 250 °C and then to 350 °C. The flakes are well crystallized because of the high film surface energy. Annealing provides sufficient energy to allow the diffusion of condensing particles, leading to lattice points that form an ordered crystalline structure. This is consistent with the XRD results. The film porosity reduces with increasing annealing temperature, which potentially benefits carrier transport and phonon scattering. Fig. 3 shows FE-SEM images of thick films annealed at 350 °C for 15, 30 and 60 min. The size distribution, grain density and surface smoothness increase with increasing annealing time. During deposition of the thick film, weak contacts between particles generally result in high porosity and higher resistivity [20]. Post-annealing can improve the particle connections. In support of this, FE-SEM images were processed using the ImageJ software package to calculate the area ratio of the surface pores [7].

Fig. 2 insets and Fig. 3 insets show the porosity of the Sb_2Te_3 thick film (as red areas) for the various annealing conditions. The porosities are 15.26, 13.19, 11.74 and 10.39% for the as-deposited thick film and films annealed at 150, 250, and 350 °C, respectively. The decrease in number of pores at higher annealing time is also confirmed by porosity tests. The film annealed at 350 °C for 15 min has a porosity of 12.18%. However, the porosity of the film slightly decreases to 10.39% after annealing for 30 min and then increases to 13.28% after annealing for 60 min.

Cross-sectional FE-SEM images of the Sb_2Te_3 films annealed for different times are shown in Fig. 4. Columnar-shaped growth is apparent. The film thickness slightly decreases with increasing annealing time because of the evaporation of Te. A smooth surface is obtained at higher annealing times. A crack is observed across the columns of the film annealed for 60 min. The crack would lead to an increase in

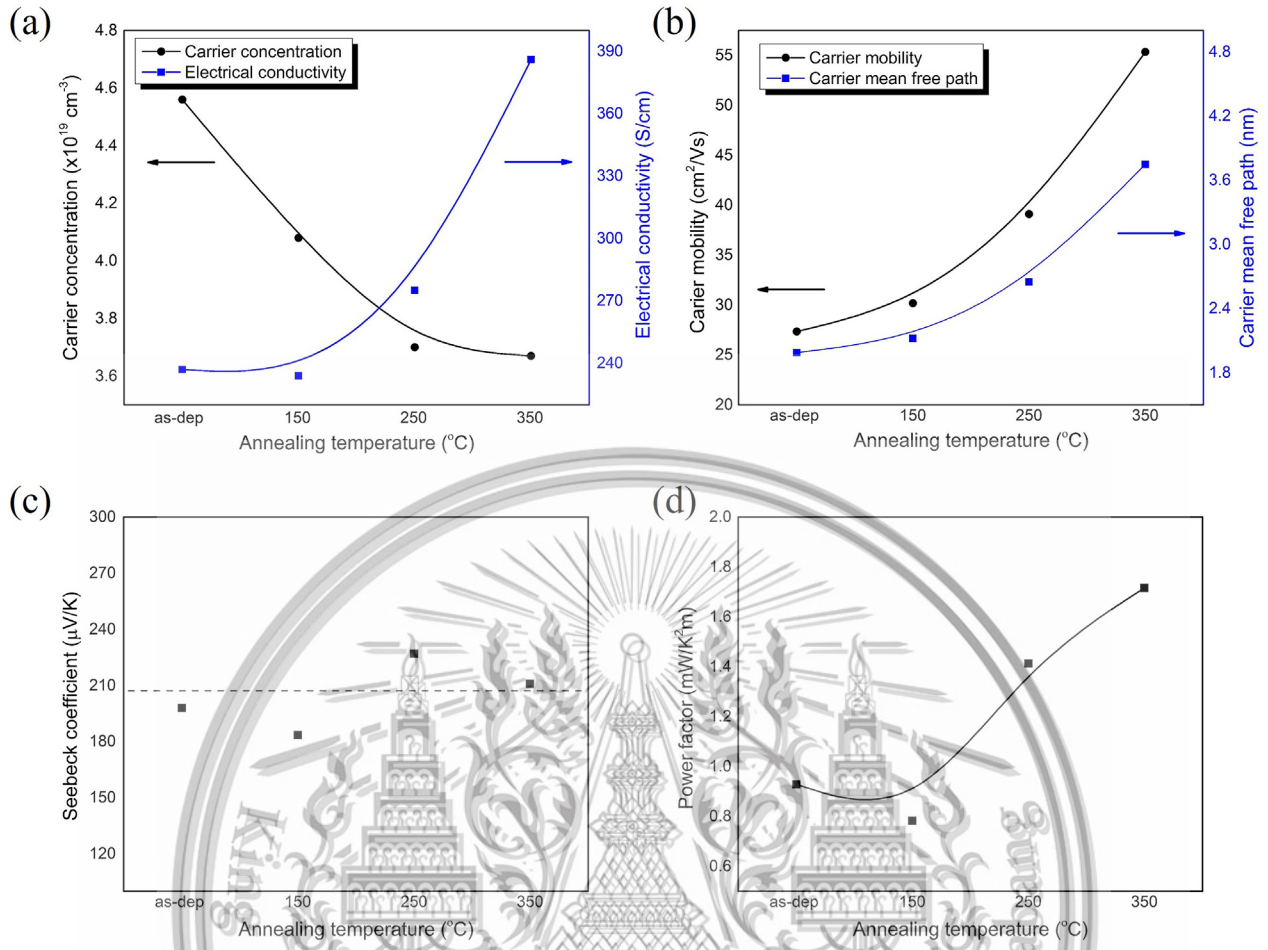

Fig. 5. Annealing temperature dependence on (a) carrier concentration and electrical conductivity, (b) carrier mobility, (c) Seebeck coefficient, and (d) power factor of the Sb_2Te_3 thick films.

trapped carriers in the grain boundaries, an increase in resistivity. The microstructure of the films was analyzed by XRD spectrum and SEM cross-sectional images. Typically, there is the relationship between the crystallinity and microstructural morphology of the films. The higher intensity XRD peaks indicate the more crystallinity and the larger crystalline size. It is related to the morphology of films that is continuous, compact and large grain size. For annealing at 350 °C for 60 min film, it was observed discontinuous lateral crack in a columnar film. The crack affects the lower peak intensity and smaller crystalline size of the films. Sb_2Te_3 thick film with a highly orientated crystalline structure is obtained after annealing at 350 °C for 30 min. Annealing for 60 min leads to a decrease in film crystallinity, as shown in Fig. 1(b).

Fig. 5 shows the annealing temperature dependence on the in-plane electrical transport properties and thermoelectric properties of the Sb_2Te_3 films measured at room temperature. All films have a positive carrier concentration, implying that the majority carriers in the thick films are holes. As seen in Fig. 5(a), the carrier concentration (n) of the films slightly decreases from 4.56×10^{19} to 3.67×10^{19} cm^{-3} and the electrical conductivity (σ) dramatically increased from 237 to 386 S/cm as annealing temperature increase from 0 to 350 °C. During deposition, the Sb_2Te_3 thick films contains many point defect including vacancies and antisite defect. The carrier concentration is related to defect inside the films. Post-annealing reduces the amount of point defects which decreases the carrier concentration [21]. The decrease in carrier concentration with increasing annealing temperature has been previously reported for the Sb_2Te_3 films [12,22,23]. The results indicated that the significant reduction of carrier concentration in the Sb_2Te_3 films.

Besides the reduction of the point defect of the thick films, the increase in carrier mobility (μ) from 27.35 to 55.36 cm^2/Vs with increasing annealing temperature is attributed to grain growth. Post-annealing leads to a slight change in surface morphology, as seen in Fig. 2. The transfer of carriers is mainly affect by grain boundaries leading to an increase in mobility. The low electrical conductivity of the as-deposited films could be attributed to the lower mobility owing to the low crystallinity, small crystalline size and non-compact grain. The Sb_2Te_3 film becomes more compact with better crystallinity as increasing annealing temperature, so the electrical conductivity is improved. It is assumed that the increased electrical conductivity is largely attributed to the improved crystal orientation, larger crystalline size, low porosities grains and increased carrier mobility. The mean free path of the films is collectively affected by the internal crystal structure, which strong influences the carrier mobility. According to the value of carrier concentration and carrier mobility, the mean free path of carriers of thick films can be estimated using the formula [24]:

$$l = \frac{h}{2e}\left(\frac{3n}{\pi}\right)^{\frac{1}{3}}\mu \quad (2)$$

where l is the mean free path of the carriers, h is plank's constant and e is te electron charge. The l increases with increasing annealing temperature due to the decreased film porosity, as shown in Fig. 4(b). The in-plane Seebeck coefficients (S) of the Sb_2Te_3 films are positive, indicating that all deposited films are p-type. The S does not significantly change with increasing annealing temperature, as shown in Fig. 5(c). This is because there is little change in carrier concentration, as shown earlier. The power factor ($PF = S^2\sigma$) is shown in Fig. 5(d). The power factor of the thick film increases with increasing annealing

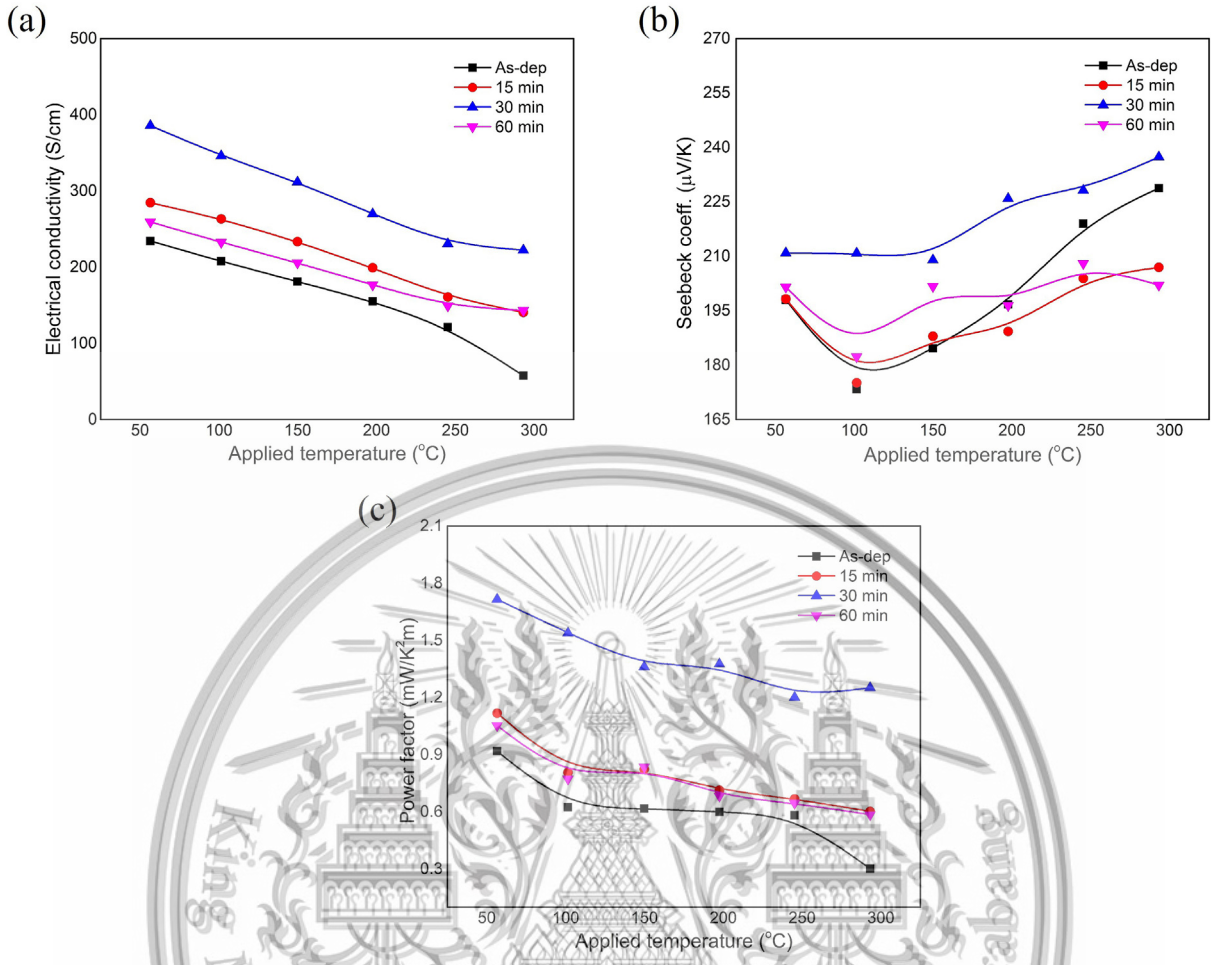

Fig. 6. Temperature dependence of the in-plane (a) electrical conductivity (b) Seebeck coefficient and (c) power factor of Sb_2Te_3 thick film annealed at 350 °C with different annealing time.

temperature, reaching 1.72 mW/K^{2}m after annealing at 350 °C for 30 min. This is attributed to the competition of the decreased carrier concentration, increased mobility and largely constant Seebeck coefficient with increasing annealing temperature.

The thermoelectric properties of the Sb_2Te_3 thick films annealed at 350 °C for 15–60 min. Fig. 6 shows the electrical conductivity, Seebeck coefficient, and power factor of Sb_2Te_3 thick films annealed at 350 °C for different annealing time. The values are shown as a function of applied temperature. The electrical conductivity was slowly decrease with increasing applied temperature range from 50 to 300 °C, reaching a maximum of 386 S/cm at 50 °C. This indicates typical metallic transport behavior. When at sufficient temperature, the electrical transport across the grain boundaries/interfaces can be expressed by thermionic emission expression:

$$\sigma(T) \sim T^{-1/2} exp[-E_B/kT] \quad (3)$$

where E_B is the height of the grain boundary/interface potential barrier. For certain temperature and grain boundary/interface potential barriers, $\Delta\sigma/\Delta T$ ratio can become negative or positive, which is consistent with the previous reports [3,12,20]. The conductivity of Sb_2Te_3 thick films increases with increasing annealing time up to 30 min. When the annealing time increase to 60 min, the crystallinity, fracture cross section, and chemical composition of samples decreased, which reduces the electrical conductivity.

The maximum Seebeck coefficient of 237 μV/K K is obtained at an applied temperature of 300 °C after annealing at 350 °C for 30 min. The increase in Seebeck coefficient of the Sb_2Te_3 thick films could be attributed to the decrease in the carrier concentration [5]. The temperature dependence of thermoelectric power factors of the Sb_2Te_3 films as a function of annealing time is calculated from the value of S and σ. The thermoelectric power factor slightly decreased with increasing applied temperature 50 to 300 °C. A maximum power factor of 1.72 mW/K^{2}m is obtained at an applied temperature of 50 °C. This is lower than that reported by H. Shen et al. [11] 2.5 mW/K^{2}m for co-evaporated 10-μm-thick Sb_2Te_3 films at room temperature. The current value is comparable to that reported by M. Mizoshiri et al. [12] of 1.6 mW/K^{2}m for 100-μm-thick Sb_2Te_3 Deposited by Thermally Assisted Sputtering Method at room temperature. The current value is higher than that reported by O. Vigil-Galan et al. [25] of 0.38 mW/K^{2}m for 15-μm-thick Sb_2Te_3 films deposited by close space vapor transport at substrate temperatures 450 °C. The results indicated that the suitable Sb_2Te_3 thick films deposited by DC magnetron sputtering at low power density and post-annealed at 350 °C for 30 min has enhanced thermoelectric properties, with a maximum power factor of 1.7 mW/K^{2}m.

4. Conclusion

We enhanced the thermoelectric properties of Sb_2Te_3 thick films by post-annealing treatment. The crystalline size and atomic composition of thick films depends on the annealing temperature and annealing time. The largest crystalline size with a slightly decreased %Te is observed for the film annealed at 350 °C for 30 min. The correlation between porosity and carrier transport/phonon scattering was illustrated using the ImageJ software package. The pore surface area significantly decreases with increasing annealing temperature and annealing time. A maximum power factor of 1.7 mW/(K^{2}m) at 50 °C is obtained.

CRediT authorship contribution statement

Prasopporn Junlabhut: Conceptualization, Methodology. **Pilaipon Nuthongkum:** Formal analysis. **Aparporn Sakulkalavek:** Formal analysis. **Adul Harnwunggmoung:** Validation. **Pichet Limsuwan:** Supervision. **Rachsak Sakdanuphab:** Writing - review & editing.

Declaration of competing interest

The authors declare that they have no known competing financial interests or personal relationships that could have appeared to influence the work reported in this paper.

Acknowledgments

This work was financially supported by the College of Advanced Manufacturing Innovation, King Mongkut's Institute of Technology Ladkrabang (KMITL), Thailand and Thailand Research Fund (TRF) ID code RSA6180013. The authors thank Rajabhat Rajanagarindra University (RRU) for student fund support. The authors acknowledge the Optical Thin-Film Technology Laboratory, NSTDA, Thailand, for carrying out Hall measurements.

References

[1] X. Duan, Y. Jiang, Annealing effects on the structural and electrical transport properties of n-type $Bi_2Te_{2.7}Se_{0.3}$ thin films deposited by flash evaporation, Appl. Surf. Sci. 256 (2010) 7365–7370, https://doi.org/10.1016/j.apsusc.2010.05.069.

[2] T. Plechacek, J. Horak, Point defects in Pb-doped Sb_2Te_3 single crystals, J. Solid State Chem. 145 (1999) 197–203, https://doi.org/10.1006/jssc.1999.8242.

[3] M. Tan, Y. Deng, Y. Hao, Enhanced thermoelectric properties and layered structure of Sb_2Te_3 films induced by special (00l) crystal plane, Chem. Phys. Lett. 584 (2013) 159–164, https://doi.org/10.1016/j.cplett.2013.08.084.

[4] K. Rajasekar, L. Kungumadevi, A. Subbarayan, R. Sathyamoorthy, Thermal sensors based on Sb_2Te_3 and $(Sb_2Te_3)_{70}(Bi_2Te_3)_{30}$ thin films, Ionics 14 (2008) 69–72, https://doi.org/10.1007/s11581-007-0146-3.

[5] K. Takayama, M. Takashiri, Multi-layered-stack thermoelectric generators using p-type Sb_2Te_3 and n-type Bi_2Te_3 thin films by radio-frequency magnetron sputtering, Vacuum 144 (2017) 164–171, https://doi.org/10.1016/j.vacuum.2017.07.030.

[6] E. Vieira, J. Figueira, A. Pires, J. Grilo, M. Silva, A. Pereira, L. Goncalves, Enhanced thermoelectric properties of Sb_2Te_3 and Bi_2Te_3 films for flexible thermal sensors, J. Alloys Compd. 774 (2019) 1102–1116, https://doi.org/10.1016/j.jallcom.2018.09.324.

[7] S.J. Kim, J.H. Wea, J.S. Kim, G.S. Kim, B.J. Cho, Thermoelectric properties of P-type Sb_2Te_3 thick film processed by a screen-printing technique and a subsequent annealing process, J. Alloys Compd. 582 (2014) 177–180, https://doi.org/10.1016/j.jallcom.2013.07.195.

[8] Z. Cao, E. Koukharenko, R.N. Torah, J. Tudor, S.P. Beeby, Flexible screen printed thick film thermoelectric generator with reduced material resistivity, J. Phys. Conf. Ser. 557 (2014) 012016, , https://doi.org/10.1088/1742-6596/557/1/012016.

[9] J.H. Wea, S.J. Kim, G.S. Kim, B.J. Cho, Improvement of thermoelectric properties of screen-printed Bi_2Te_3 thick film by optimization of the annealing process, J. Alloys Compd. 552 (2013) 107–110, https://doi.org/10.1016/j.jallcom.2012.10.085.

[10] N.H. Trung, K. Sakamoto, N.V. Toan, T. Ono, Synthesis and evaluation of thick films of electrochemically deposited Bi_2Te_3 and Sb_2Te_3 thermoelectric materials, Materials 10 (2017) 1–17, https://doi.org/10.3390/ma10020154.

[11] H. Shen, S. Lee, J. Kanga, T.Y. Eom, H. Lee, S. Han, Thickness dependence of the electrical and thermoelectric properties of co-evaporated Sb_2Te_3 films, Appl. Surf. Sci. 429 (2018) 115–120, https://doi.org/10.1016/j.apsusc.2017.09.037.

[12] M. Mizoshiri, M. Mikami, K. Ozaki, p-Type Sb_2Te_3 and n-type Bi_2Te_3 films for thermoelectric modules deposited by thermally assisted sputtering method, Jpn. J. Appl. Phys. 52 (2013) 06GL071–06GL076, https://doi.org/10.7567/JJAP.52.06GL07.

[13] L.M. Goncalves, C. Couto, P. Alpuim, A.G. Rolob, F. Völklein, J.H. Correia, Optimization of thermoelectric properties on Bi_2Te_3 thin films deposited by thermal co-evaporation, Thin Solid Films 518 (2010) 2816–2821, https://doi.org/10.1016/j.tsf.2009.08.038.

[14] B. Fang, Z. Zeng, X. Yan, Z. Hu, Effects of annealing on thermoelectric properties of Sb_2Te_3 thin films prepared by radio frequency magnetron sputtering, J. Mater. Sci. Mater. Electron. 24 (2013) 1105–1111, https://doi.org/10.1007/s10854-012-0888-1.

[15] T. Liu, H. Deng, H. Cao, W. Zhou, J. Zhang, J. Liu, P. Yang, J. Chu, Structural, optical and electrical properties of Sb_2Te_3 films prepared by pulsed laser deposition, J. Cryst. Growth 416 (2015) 78–81, https://doi.org/10.1016/j.jcrysgro.2015.01.022.

[16] N. Somdock, S. Kianwimol, A. Harnwunggmoung, A. Sakulkalavek, R. Sakdanuphab, Simultaneous stoichiometric composition and highly (00l) orientation of flexible Bi_2Te_3 thin films via optimising the DC magnetron sputter-deposition process, J. Alloys Compd. 773 (2019) 78–85, https://doi.org/10.1016/j.jallcom.2018.09.216.

[17] Z. Zheng, J. Luo, F. Li, G. Liang, P. Fan, Enhanced thermoelectric performance of P-type Sb_2Te_3 thin films through organic-inorganic hybridization on flexible substrate, Curr. Appl. Phys. 19 (2019) 470–474, https://doi.org/10.1016/j.cap.2019.01.019.

[18] V.D. Mote, Y. Purushotham, B.N. Dole, Williamson-Hall analysis in estimation of lattice strain in nanometer-sized ZnO particles, J. Theor. Appl. Mech.-Pol. 8 (2012) 2251–7235, https://doi.org/10.1186/2251-7235-6-6.

[19] G. Deshmukh, S. Patil, S. Patil, P. Pawar, Effect of film thickness on structural and optical properties of Bi_2Te_3 thin films, J. Chem. Biol. Phys. Sci. 5 (9) (2015) 2769–2779.

[20] J. Martin, L. Wang, L. Chen, G.S. Nolas, Enhanced Seebeck coefficient through energy-barrier scattering in PbTe nanocomposites, Phys. Rev. B 79 (2009) 115311, , https://doi.org/10.1103/PhysRevB.79.115311.

[21] J.H. Kim, J.Y. Choi, J.M. Bae, M.Y. Kim, T.S. Oh, Thermoelectric characteristics of n-type Bi_2Te_3 and p-type Sb_2Te_3 thin films prepared by co-evaporation and annealing for thermopile sensor applications, Mater. Trans. 54 (2013) 618 to 625, https://doi.org/10.2320/matertrans.M2013010.

[22] B. Lv, S. Hu, W. Li, X. Di, L. Feng, J. Zhang, L. Wu, Y. Cai, B. Li, Z. Lei, Preparation and characterization of Sb_2Te_3 thin films by coevaporation, Int. J. Photoenergy (2010) 1–4, https://doi.org/10.1155/2010/476589.

[23] D.V. Thiet, Optimizing the carrier density and thermoelectric properties of Sb_2Te_3 films by using the growth temperature, J. Korean Phys. Soc. 72 (2018) 915–919, https://doi.org/10.3938/jkps.72.915.

[24] S. Shena, W. Zhua, Y. Denga, H. Zhaob, Y. Penga, C. Wanga, Enhancing thermoelectric properties of Sb_2Te_3 flexible thin film through microstructure control and crystal preferential orientation engineering, Appl. Surf. Sci. 414 (2017) 197–204, https://doi.org/10.1016/j.apsusc.2017.04.074.

[25] O. Vigil-Galan, F. Cruz-Gandarilla, J. Fandino, F. Roy, J. Sastre-Hernandez, G. Contreras-Puente, Physical properties of Bi_2Te_3 and Sb_2Te_3 films deposited by close space vapor transport, Semicond. Sci. Technol. 24 (2009) 025025, , https://doi.org/10.1088/0268-1242/24/2/025025.